THÈSE

En vue de l'obtention du

DOCTORAT DE L'UNIVERSITÉ DE TOULOUSE

Délivré par : *l'Université Toulouse 3 Paul Sabatier (UT3 Paul Sabatier)*

Présentée et soutenue le *05/07/2018* **par :**

Maxime Dupont

Dynamics and disorder in quantum antiferromagnets

JURY

Michel Caffarel	Directeur de recherche	Président du Jury
Frédéric Mila	Professeur	Rapporteur
Christian Rüegg	Professeur	Rapporteur
Claudine Lacroix	Directrice de recherche	Examinateur
Guillaume Roux	Maître de conférences	Examinateur
Mladen Horvatić	Directeur de recherche	Examinateur
Sylvain Capponi	Professeur des universités	Directeur de thèse
Nicolas Laflorencie	Chargé de recherche	Directeur de thèse

École doctorale et spécialité :
SDM : Physique de la matière - CO090
Unité de Recherche :
Laboratoire de Physique Théorique de Toulouse
Directeur(s) de Thèse :
Sylvain Capponi et *Nicolas Laflorencie*
Rapporteurs :
Frédéric Mila et *Christian Rüegg*

À Maman, Papa, Alexis et Clémentine.
À mes grands-parents.
☺

Acknowledgments

First and foremost, I would like to thank Sylvain Capponi and Nicolas Laflorencie, my Ph. D. advisors, who made these three years *the most* enjoyable they could have been. I am extremely thankful to them for their availability, guidance, and good teaching.

I am grateful to Mladen Horvatić and his NMR team from Grenoble, France, with whom I had invaluable collaborations that guided most of my works. I also thank you for accepting to be part of my Jury, as well as Claudine Lacroix, Guillaume Roux and Michel Caffarel. Especially, I am grateful to Christian Rüegg and Frédéric Mila for accepting to be referees for my thesis.

I cannot say enough how much I have appreciated my years at the lab. The great atmosphere prevailing, both scientifically and for everyday life, is largely due to its people. Hence, a very special gratitude goes out to all down at the lab, and in particular to people of the "strongly correlated systems" group: Matthieu, Pierre, Fabien, Didier, Revaz, Zoran, Aleksandra, and again, Sylvain and Nicolas. I would also like to acknowledge Gabriel with whom I started to work at the end of my thesis.

A very special mention goes to all Ph. D. students and postdocs (*Bah!*) that I had the chance to meet. You made the life inside (coffee and tea breaks, lunch times and sometimes scientific discussions) and outside (restaurants, bars, concerts and untold events) of the lab the most pleasant. Starting with those who left before I did, thanks to Frédéric (who still thinks he is better than me at Civilization®), Xavier, Juan Pablo, Thibaut, Medha, David, Wei-Lin, Bertrand, Guillaume and Lionel. Continuing now with people that will leave after me, I thank from the heart Benjamin (Senior), Olivier (we shared the office in an unexpected quiet way), Benjamin (Junior), (Comrade) Hugo, Jordan (pronounced in a very French way), Julie (our feminine *touch*), Nicolas (you managed to make either vegetarianism or Ramonville-Saint-Agne trendy, pick one), Francesca (your Italian pasta are the best) and Marc (I am still amazed by the fact you started a Ph. D. once retired!).

I am also thankful to Christian Miniatura who made it possible for me to come to Singapore, and to Anders Sandvik whom I visited for three months at Boston University during my thesis.

Finally, but not least, I would like to mention and thank all the people outside this very scientific environment, starting with my parents, my brother, my sister, my grandparents, and everyone else from the family. I also thank Vianney, Hélène, Audrey, Samantha, Florian, Stéphane, Clément... and those that I unwittingly forgot...

Table of contents

List of abbreviations

AF — Antiferromagnetic

BEC — Bose-Einstein Condensation

BG — Bose-Glass

BZ — Brillouin Zone

DIMPY — $(C_7H_{10}N)_2CuBr_4$

DMRG — Density Matrix Renormalization Group

DTN — Dichlorotetrakis-Thiourea-Nickel, $NiCl_2$-$4SC(NH_2)_2$

DTN*X* — $Ni(Cl_{1-x}Br_x)_2$-$4SC(NH_2)_2$

EPR — Electron Paramagnetic Resonance

ESR — Electron Spin Resonance

FM — Ferromagnet

INS — Inelastic Neutron Scattering

MBL — Many-Body Localized

MF — Mean-Field

MPO — Matrix Product Operator

MPS — Matrix Product States

NMR — Nuclear Magnetic Resonance

QMC — Quantum Monte Carlo

RPA — Random Phase Approximation

SAC — Stochastic Analytic Continuation

SDRG — Strong Disorder Renormalization Group

SVD — Singular Value Decomposition

SW — Spin-Waves

TEBD — Time Evolution Block Decimation

TLL — Tomonaga-Luttinger Liquid

Introduction

The work within this manuscript deals with quantum magnetism, or more broadly with condensed matter physics and strongly correlated systems. In these systems, the many-body interactions and correlations between particles cannot be neglected; otherwise, the models would simply fail to capture the relevant physics at play and phenomena ensuing. Although the work presented thereafter is all theoretical, it is worth noting that it is substantially connected with experiments. In fact, a great deal of it has been performed in a fruitful collaboration with the nuclear magnetic resonance group at the high magnetic fields facility[1] in Grenoble, France. This allows for both a better understanding of experimental observations and an appropriate experimental checking of theoretical predictions regarding new quantum phases of matter.

I. Strongly correlated systems and quantum magnetism

Understanding the effects of many-body interactions in quantum systems is a long-standing challenge of modern physics. Basically, describing $\sim 10^{23}$ coupled degrees of freedom poses a cumbersome problem, impossible to solve exactly in most cases. What makes it curiously interesting though, is that this intractable description is usually based on models that are extremely simple to write down and understand. Despite their apparent simplicity, they faithfully capture and describe a wide range of properties and phenomena taking place in realistic materials. This goes from the least to most exotic phases of matter (like superconductivity or the quantum Hall effect) to phase transitions (like the changes of state of water).

1. Mott insulator and quantum magnetism

All in all, quantum condensed matter physics is mainly concerned with electronic systems and electronic properties in materials. Usually, we are interested in crystalline solids: the atoms are arranged in an ordered microscopic structure, forming a periodic crystal *lattice*.

[1] Laboratoire National des Champs Magnétiques Intenses

Often, the very first question is whether a given material is a conductor or an insulator. This can be understood for many materials within band theory by means of the nearly-free electron or tight-binding models. In the first case, the valence electrons are treated as free particles, weakly perturbed by the periodic potential caused by the nuclei and core electrons of the atoms. In the second approach, valence electrons are tightly bound to the atom to which they belong, and the atoms in the solid are nearly independent. In other words, the atoms can be pictured as rather spatially well-separated but not quite enough to make the atomic description relevant. Both models seem reasonable and cover relatively different cases. However, they neglect electron-electron interactions. Although it may sound purely academic, it still predicts results very close to the mark for many systems[2]. As we will only briefly discuss the tight-binding approach in the following, one can refer to chapter 9 of Ref. 5 for more details about the nearly-free electron model. Without loss of generality, one can write down the total Hamiltonian as

$$\mathcal{H}(\mathbf{r}) = \sum_{\mathbf{R}} \mathcal{H}_{\text{atom}}(\mathbf{r} - \mathbf{R}) + \Delta V(\mathbf{r}), \tag{1}$$

where $\mathcal{H}_{\text{atom}}$ is the Hamiltonian describing a single isolated atom and the sum runs over each atomic position $\mathbf{R}$ of the lattice. Because the atoms are not independent and some of their electronic orbitals might overlap, $\Delta V(\mathbf{r})$ accounts for all the necessary corrections. Yet, $\Delta V(\mathbf{r})$ is small enough to be treated perturbatively. Hence, the atomic orbitals $\phi_n(\mathbf{r} - \mathbf{R})$, which are eigenfunctions of the $\mathcal{H}_{\text{atom}}$ of a single isolated atom at position $\mathbf{R}$,

$$\mathcal{H}_{\text{atom}}(\mathbf{r} - \mathbf{R})\phi_n(\mathbf{r} - \mathbf{R}) = E_n\phi_n(\mathbf{r} - \mathbf{R}), \tag{2}$$

should provide a good starting basis. Neglecting electron-electron interactions and using second quantization formalism with the atomic orbital as a basis state, the electronic Hamiltonian reads

$$\mathcal{H} = -\sum_{i,j}\sum_{m,n}\sum_{\sigma=\uparrow,\downarrow} t_{i,j}^{m,n}\left(c_{i,m,\sigma}^{\dagger}c_{j,n,\sigma} + c_{j,n,\sigma}^{\dagger}c_{i,m,\sigma}\right), \tag{3}$$

where $c_{i,m,\sigma}^{\dagger}$ and $c_{j,n,\sigma}$ are respectively creation and annihilation operators of an electron with spin σ in the orbitals m and n of the atoms centered around the vertices i and j of the lattice. The operators obey the fermionic anticommutation relation $\{c_{i,m,\sigma}, c_{j,n,\sigma'}^{\dagger}\} = \delta_{ij}\delta_{mn}\delta_{\sigma\sigma'}$ with at most one electron of given spin σ in the orbital m because of Pauli's principle. The hopping integral $t_{i,j}^{m,n}$ can be determined by computing the overlap between orbitals, i.e.,

$$t_{i,j}^{m,n} = \int \mathrm{d}\mathbf{r}\ \phi_m^*(\mathbf{r} - \mathbf{R}_i)\Delta V(\mathbf{r})\phi_n(\mathbf{r} - \mathbf{R}_j). \tag{4}$$

With the knowledge of the matrix elements $t_{i,j}^{m,n}$[3], one can then construct the Hamiltonian matrix (3) and attempt to solve the Schrödinger equation. It leads to the

[2]This would probably deviate us too much from the goal of this section, but the reason why neglecting electron-electron interactions work so well, especially to describe metallic phases can be understood by the phenomenological Fermi liquid theory [1–4]. It states that the properties of a large number of interacting electrons is basically those of non-interacting ones with parameters renormalized by the interactions. This is for example the case of the electron mass $m_e \to m_e^*$.

[3]This can be achieved by means of standard, yet non trivial, quantum chemistry calculations.

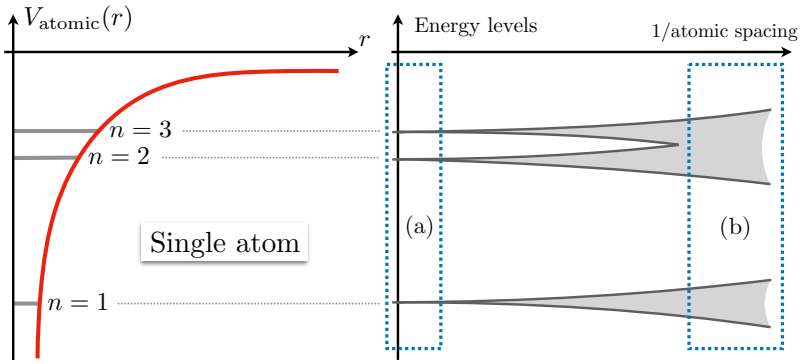

Figure 1: The left-hand side panel corresponds to a very simplified picture of the potential of a single atom, with its discretized electronic energy levels labeled by $n = 1, 2...$ The right-hand side panel displays these energy levels as a function of one over the distance between atoms in the crystal. The region (a) is the atomic limit where the atoms are well-separated from each others. The energy levels are $\mathcal{N}_{\text{atoms}}$-fold degenerated. As the atoms are moved closer to each others, they become perturbed by their neighboring atoms, which lifts the degeneracy. Finally in (b), since there are about $\mathcal{N}_{\text{atoms}} \sim 10^{23}$ atoms in the crystal, the energy levels form a continuum with band structures. This figure has been reproduced from Ref. 5.

simplified picture displayed in Fig. 1, with the neighboring atoms perturbing the atomic limit and leading to a band-like structure of the energy spectrum. The low-temperature properties are then obtained by filling the energy levels (bands) with the $\mathcal{N}_e$ electrons, starting at the bottom. We call valence band the last one fully filled and conduction band the one just above, with possibly a gap in between. The highest energy level filled with an electron is known as the *Fermi level* and its position sets the cursor between three different cases,

(i) If the conduction band contains electrons, then the system is a conductor because there are accessible states at arbitrarily low-energy;

(ii) If the conduction band is empty but there is no gap with the valence band, the system is also a conductor;

(iii) If the conduction band is empty and there is a finite gap with the valence band, then the system is an insulator[4].

After introducing band theory and before getting to the point of this section, let us simplify the Hamiltonian (3) a bit more. First, as the distance between atoms $|\mathbf{R}_i - \mathbf{R}_j|$ becomes large, we expect the hopping integral to be zero and we consider nonzero matrix elements for nearest-neighbor only, noted $\langle i, j \rangle$. We will focus on the case (i) with the conduction band containing electrons. To describe the low-temperature properties in this case, we assume that only this band needs to be taken into account. This is because the electrons within other bands are strongly bound

[4]The difference between an insulator and semi-conductor is the width of the gap. A semi-conductor is a "bad insulator" with a gap energy that is at least of the order of the temperature T. This means that electrons can access states from the conduction band through thermal fluctuations.

and it would require a huge amount of energy to excite them. As for empty bands of higher energy, they are too far away, energetically speaking. It follows,

$$\mathcal{H}_{\text{tight-binding}} = -t \sum_{\langle i,j \rangle} \sum_{\sigma=\uparrow,\downarrow} \left(c^\dagger_{i,\sigma} c_{j,\sigma} + c^\dagger_{j,\sigma} c_{i,\sigma} \right), \tag{5}$$

with only four possible states by site: $|0\rangle$, $|\uparrow\rangle$, $|\downarrow\rangle$ and $|\uparrow\downarrow\rangle$. If treating a material in the non-interacting limit predicts the right conductor/insulator behavior in most cases, it also fails sometimes. Indeed, some materials, while experimentally insulating are conductors within band theory, the so-called *Mott insulators* [6]. As the biggest assumption made was neglecting the electron-electron (Coulomb) interaction, it is natural to suspect that it actually plays a role and takes the form of an additional term next to the tight-binding Hamiltonian,

$$\mathcal{H}_{\text{Hubbard}} = -t \sum_{\langle i,j \rangle} \sum_{\sigma=\uparrow,\downarrow} \left(c^\dagger_{i,\sigma} c_{j,\sigma} + c^\dagger_{j,\sigma} c_{i,\sigma} \right) + U \sum_i n_{i\uparrow} n_{i\downarrow}, \tag{6}$$

where $n_{i,\sigma} = c^\dagger_{i,\sigma} c_{i,\sigma}$ is the density operator. The second term is the screened Coulomb potential which accounts for the electrostatic repulsion ($U > 0$) between electrons on the same site, while the interaction between electrons on different sites has been neglected[5]. This model is known as the Hubbard model [7], and it is the starting point when studying strongly correlated systems. This is because at low-temperature, the system will attempt to minimize its energy from two competing contributions. On the one hand, the hopping term ($t > 0$) will favor a delocalized behavior whereas the Coulomb repulsion will favor a localized behavior. It is easy to imagine that $t/U \gg 1$ will lead to a metallic phase and $t/U \ll 1$ to an insulating one, namely a Mott insulating phase, which cannot be explained otherwise than by the interactions.

We are now interested in the low-energy properties of the Mott insulating phase at half-filling: with the model allowing at most two electrons per site, it means that $\sum_{i,\sigma} \langle n_{\text{i},\sigma} \rangle / \mathcal{N}_{\text{sites}} = 1$. One can get some insights by using perturbation theory since there is a small parameter in the Hamiltonian, $t/U \ll 1$ [8, 9]. Considering only the Coulomb potential term ("zeroth-order"), all states that have exactly one electron per site correspond to the degenerate manifold of the ground states. With null first-order corrections in t/U, one needs to go to the second-order. It gives an effective Hamiltonian that can be written in terms of spin-1/2 operators (up to irrelevant additional constants) when comparing matrix elements,

$$\mathcal{H}_{\text{Heisenberg}} = J \sum_{\langle i,j \rangle} \mathbf{S}_i \cdot \mathbf{S}_j, \qquad \text{with } J = \frac{4t^2}{U}. \tag{7}$$

This corresponds to a magnetic lattice model, called the Heisenberg model, with spin $\mathbf{S}_i = (S^x_i, S^y_i, S^z_i)$ degrees of freedom. The spin operators obey the usual commutation relation $[S^\alpha_i, S^\beta_j] = i\varepsilon_{\alpha\beta\gamma}\delta_{ij}S^\gamma_i$ [9]. There is definitely a lot to say about the Heisenberg Hamiltonian, and I will come back to it at the very beginning of the first chapter. It is a paradigm model when it comes to quantum magnetism and it will govern the low-temperature properties of many Mott insulating materials.

[5] The Coulomb potential has a long-range nature, i.e., $V_{\text{Coulomb}}(\mathbf{r}) \propto 1/|\mathbf{r}|$, so it is a priori not justified to restrict its effect on-site. However, though it might require a more careful treatment, one can imagine that it is screened by other electrons.

2. A zest of phase transitions

As a big part of the work in this manuscript is concerned with phase transitions, it seems appropriate to make a quick introduction with the main ideas and right terminology. A more thoroughgoing introduction can be read in Refs. 10, 11 and 12 to cite but a few. Essentially, a phase transition is a global and sudden change in the physical properties of a system by tuning an external parameter, e.g., temperature or pressure.

If you consider the temperature T and, let us say, any everyday life magnet, it is only a magnet below a specific temperature $T < T_c$ (which happens to be higher than the room temperature), called the critical temperature — or in the case of ferromagnets, the Curie temperature. The phenomena occurring at T_c is a phase transition from a featureless paramagnetic phase to a ferromagnetic phase. Microscopically, the magnetic moments (spins $\mathbf{S}$) are the relevant degrees of freedom which get *spontaneously* aligned along the same direction below T_c, while they look completely disordered at higher temperature. Hence, each phase is respectively referred as *ordered* and *disordered*. A successful attempt to build a general theory for continuous phase transitions was done by Landau in the middle of the twentieth century [13]. It states that a phase transition follows a spontaneous *symmetry breaking* from the disordered to the ordered phase. In our example, the disordered phase has a global rotation symmetry because the spins can point in any direction in space whereas in the ferromagnetic phase it has been broken since the spins are aligned in a given direction. The point is that the (classical or quantum alike) Hamiltonian or Lagrangian describing the system do have the symmetry that is being spontaneously broken below T_c, and that this breaking is not induced by an external parameter. The spontaneous breaking of a symmetry can be quantified by means of the *order parameter*, usually a scalar number $m(T)$ that is finite in the ordered phase and zero otherwise,

$$m(T) \begin{cases} = 0 \text{ for } T > T_c, \\ > 0 \text{ for } T < T_c. \end{cases} \tag{8}$$

It is related to the microscopic model in some way, and it would be the magnetization in our example,

$$m(T) = \left| \lim_{\mathcal{N}_{\text{spins}} \to +\infty} \sum_{\mathbf{r}} \langle \mathbf{S}_{\mathbf{r}} \rangle / \mathcal{N}_{\text{spins}} \right| \tag{9}$$

where $\langle \cdot \rangle$ is the thermodynamic average. Another observable that can detect order is the correlation function $C(T, \mathbf{r}) = \langle \mathbf{S}_{\mathbf{r}} \cdot \mathbf{S}_{\mathbf{0}} \rangle$, in the limit of long distances, $\mathbf{r} \to \infty$. It is closely related to the order parameter and accounts for its spatial fluctuations. It takes the general form,

$$C(T, \mathbf{r}) \underset{r \to +\infty}{\sim} \frac{1}{|\mathbf{r}|^{D-2+\eta}} \exp\left(-\frac{|\mathbf{r}|}{\xi(T)} \right) + m^2(T), \tag{10}$$

with D the dimensionality of the system and η some exponent. When approaching the *critical point*, $T \to T_c$, the system is characterized by a diverging correlation length, $\xi \sim |T - T_c|^{-\nu}$ with $\nu > 0$, which indicates that the order parameter fluctuations do not display a characteristic length scale. Therefore, fluctuations exist on all length

scales and the system look "similar" on all length scales as well. This is called *scale-invariance* and it results in a power-law dependence of physical quantities close to the transition: this is because an algebraic dependence is the only one that can be scale-invariant and respect dimensional analysis of observables[6]. The exponents of the power-laws dependence such as η or ν (more exists, e.g. $C(T) \sim |T - T_c|^{-\alpha}$ for the specific heat or $m(T) \sim |T - T_c|^{\beta}$ for the order parameter) are called the *critical exponents* and fully characterize the system at the transition. This last statement can actually be made stronger by introducing the concept of *universality class*. It regroups together systems with the same dimensionality and which undergo the same symmetry breaking at the transition, independently of the microscopic details[7]. Remarkably, within the same universality class, systems that can microscopically be quite different, will behave in exactly the same way at the transition, that is to say, with exactly the same exponents. Another important result regarding phase transitions is the Mermin-Wagner theorem [17–20]. It states that the spontaneous breaking of a continuous symmetry is allowed at finite temperature for three-dimensional (and in higher dimensional) systems but only allowed at $T = 0$ in the two-dimensional case. As for one-dimensional systems, there cannot be spontaneous long-range order with a continuous symmetry breaking, even at zero temperature.

So far, I have only discussed classical phase transitions which are driven by thermal fluctuations. There also exists quantum phase transitions (see Refs. 21 and 22), driven by quantum fluctuations, and which happen at absolute zero temperature ($T = 0$). Again, it corresponds to a sudden and global change in the ground state properties of a system by tuning one of the Hamiltonian parameters, $\mathcal{H}(g)$, with for example $g = t/U$ in the Hubbard model that I discussed in the previous section. Looking at the eigenenergies of $\mathcal{H}(g)$ versus g, a quantum phase transition will be defined as a point $g = g_c$ of non-analyticity in the ground state energy. This can either come from a level-crossing with an excited state or an "avoided level-crossing" as displayed in Fig. 2 (a). This implies that the energy spectrum will play a role in a quantum phase transition and we define a characteristic energy scale Δ for g close to g_c. This could be the energy between the first excited state and the ground state if there is an energy gap between them. Or in the case of a gapless spectrum[8], this could be the scale at which there is a qualitative change in the nature of the frequency spectrum. In any case, it should scale as,

$$\Delta \sim |g - g_c|^{z\nu}, \tag{11}$$

with z the *dynamic exponent*, only nonzero for a quantum phase transition. The product $z\nu$ of two exponents comes from the fact that, similarly to classical phase transitions, the correlation length behaves as $\xi \sim |g - g_c|^{-\nu}$, which leads to $\Delta \sim \xi^{-z}$. Indeed, in quantum mechanics, energy and time are related through Heisenberg's

[6] A scaling transformation on the spatial coordinates of the system takes the form $\tilde{\mathbf{r}} \to b\mathbf{r}$, with $b \in \mathbb{R}$, and such a transformation should leave the physical properties invariant. With the fact that close to the critical point, the correlation length is the only relevant length scale in the system with $\xi \sim |T - T_c|^{-\nu}$, this is the starting point of the *scaling hypothesis* and can be justified a posteriori by renormalization group arguments [14–16]. For example, the scaling hypothesis suggests that the correlation function of Eq. (10) takes the general form $C(\mathbf{r}) = |\mathbf{r}|^{-D+2-\eta}\, \mathcal{G}_{C(\mathbf{r})}\left(|\mathbf{r}|/\xi\right)$ with $\mathcal{G}_{C(\mathbf{r})}$ a universal scaling function.

[7] It might also depend on the short/long-range nature of the interactions.

[8] Unlike a gapped spectrum with a finite energy difference between the ground state and the first excited state, a gapless spectrum has such an energy difference equal to zero.

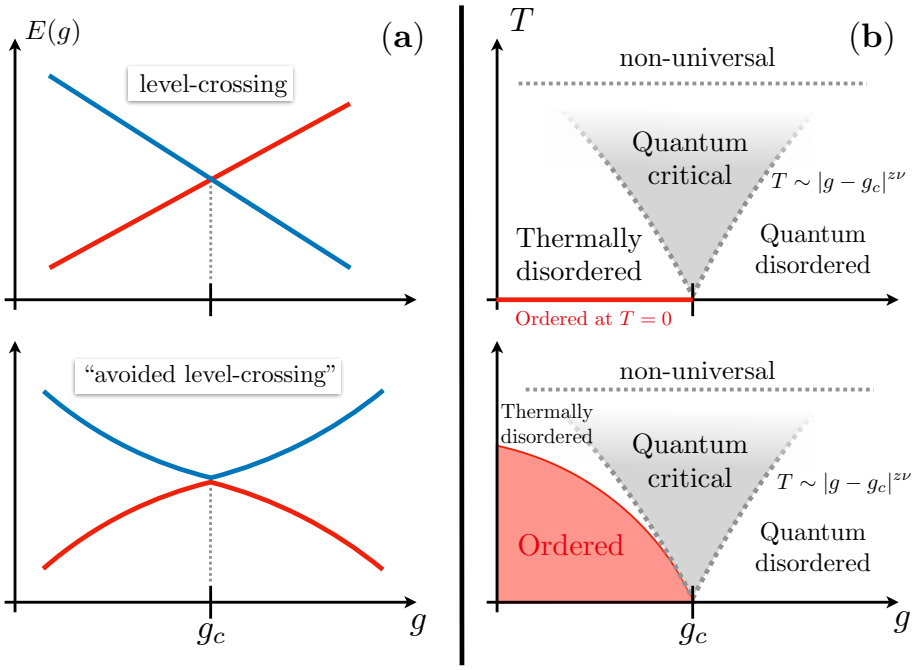

Figure 2: (a) Simplified picture of the spectrum $E(g)$, eigenenergies of the Hamiltonian $\mathcal{H}(g)$, with only the ground state and first excited state energies. The top panel corresponds to a level crossing and the bottom one to an "avoided level-crossing" at $g = g_c$. In both cases, g_c is a point of non-analyticity, which defines a quantum phase transition. This figure has been reproduced from Ref. 21. **(b)** Schematic phase diagram in the vicinity of a quantum critical point. The top panel displays an ordered phase (red line), in the sense of spontaneous symmetry breaking, only at $T = 0$ and the bottom panel an ordered phase at finite T (red region). In both cases, we have above the quantum critical point g_c a quantum critical region (grey region), bounded by dashed crossover lines $T \sim |g - g_c|^{z\nu}$, in which one can observe at finite temperature the universal properties of the quantum phase transition. At high temperature, the system properties are non-universal. This figure has been reproduced from Ref. 22

principle[9], $\Delta \cdot \tau \sim 1$, which gives $\tau \sim \xi^z$. Therefore, in addition a diverging length scale ξ as $g \to g_c$, we have a diverging characteristic time τ, the correlation time[10]. A quantum phase transition might sound all theoretical since no experiment really takes place at absolute zero temperature. There exists however, what is called a *quantum critical* regime at finite temperature, bounded by crossover lines $T \sim |g - g_c|^{z\nu}$ on each side of the quantum critical point g_c, as displayed in Fig. 2 (b). It hosts the universal high-temperature regime of the field theory describing the quantum critical point. It is the region of the phase diagram being probed by experiments and which exhibits universal properties of the quantum phase transition at finite temperature.

Phase transitions are of first importance in condensed matter physics as it connects

[9]Unless specified otherwise, all physical constants are taken equal to unity in the following, $\hbar = c = k_B = 1$.

[10]In a nutshell, and one can refer to Refs. 21 and 22 for more details, this is the imaginary correlation time — although this is related to the "real time" by a Wick rotation $\tau \to it$. It naturally arises when expanding the partition function with $\beta = 1/T \to \infty$ with a Suzuki-Trotter decomposition to map a quantum D-dimensional problem onto a $(D + z)$-dimensional classical problem.

very different phases of matter with different properties and the transition itself between phases exhibits universality. One challenging task is thus to characterize the phases and the nature of the transition by getting the critical exponents, and a large part of the work in this manuscript will be dedicated to that.

3. Numerical tools and methods

Independently of the quantum problem one is looking at, it will require at some point to solve the time-independent Schrödinger equation

$$\mathcal{H}|\Psi\rangle = E|\Psi\rangle. \tag{12}$$

This is a standard academic problem for a two-level system since the Hilbert space dimension will be 2, but is generally intractable in condensed matter physics if one wants to describe $\sim 10^{23}$ degrees of freedom. For instance, in the case of spin-1/2 systems (each spin can have the states $|\uparrow\rangle$, $|\downarrow\rangle$), this would lead to a Hilbert space of dimension $2^{10^{23}}$. This is because the Hilbert space dimension scales, in most cases, *exponentially* with the system size. Nonetheless, many analytical tools have been developed to address this problem, such as field theories and various approximations. Yet, not every problem can be solved exactly and approximations remain approximations, and do not necessarily capture the right physical properties. With the advent of computational resources, numerical methods have been developed in the last decades to handle efficiently many-body problems, and I want to give a glimpse, not to the methods themselves — to which I will come back all along this manuscript —, but to a few general ideas. Furthermore we will see that it is not necessary to simulate 10^{23} degrees of freedom to capture the relevant physics, and depending on the numerical method and model, one is nowadays able to simulate from tens to thousands degrees of freedom.

Exact diagonalization (up to the numerical precision of 10^{-16}) is the solely unbiased method and implemented in every linear algebra library. It constructs numerically and iteratively the matrix U holding the eigenvectors of $\mathcal{H}$, i.e. $\mathcal{H} \rightarrow U^\dagger \mathcal{H} U$. This algorithm complexity scales as $\mathcal{O}(N^3)$ with N the dimension of the Hilbert space. One can expect to diagonalize matrices of size $\sim 10^4 \times 10^4$ in a reasonable amount of time. For spin-1/2 systems, this corresponds to about fourteen spins. Beside the algorithm complexity, memory (RAM) is also very important, and each of the N^2 elements of the matrix requires 8 octets of memory. To give some numbers, this corresponds to $\simeq 6.4$ Gb for $N = 10^4$ and $\simeq 640$ Gb for $N = 10^5$, and this does not take into account the intermediary tables required for the algorithm, or the table holding the basis states. In order to overcome these limitations, I want to highlight the importance of symmetries. If $\mathcal{S}_A$ is a symmetry operator that commutes with the Hamiltonian, i.e., $[\mathcal{H}, \mathcal{S}_A] = 0$, it is a conserved quantity labeled by a quantum number s_A. This can effectively reduce the size of the matrix by partitioning it into blocks labeled by $\{s_A\}$ that can be diagonalized independently. If there are multiple symmetries $\mathcal{S}_A$, $\mathcal{S}_B$, $\mathcal{S}_C$... that commute with the Hamiltonian and each others, one can divide further the Hamiltonian into blocks labeled by a set of quantum numbers $\{s_A, s_B, s_C ...\}$, see Fig. 3. For example, standard symmetries include translations, rotations of the lattice, particles number... With their use, one can expect to simulate from twenty to thirty $S = 1/2$ spins. This might not seem

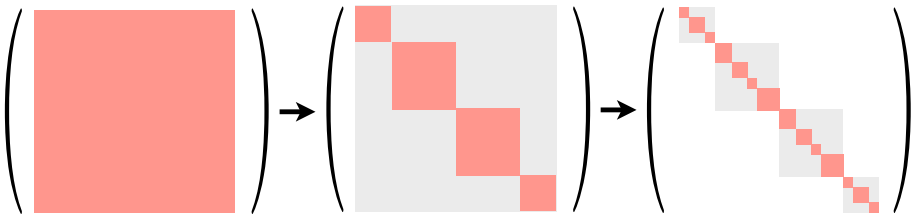

Figure 3: On the left-hand side, we have the Hamiltonian matrix written as a single block. The sketch in the middle represents the Hamiltonian matrix divided into independent diagonal blocks by the use of a symmetry $\mathcal{S}_A$ of the Hamiltonian. Each block is labeled by a quantum number s_A. Finally, on the right-hand side panel, the blocks $\{s_A\}$ have been divided further by the use of an additional symmetry $\mathcal{S}_B$. The blocks are now labeled by a set of quantum numbers $\{s_A, s_B\}$.

like a huge gain, but again, the Hilbert space dimension scales exponentially with the system size.

Another point that I want to mention is the variational principle which takes the following form in quantum mechanics,

$$E\Big[|\Psi\rangle\Big] = \frac{\langle\Psi|\mathcal{H}|\Psi\rangle}{\langle\Psi|\Psi\rangle} \geq E_0, \tag{13}$$

where E is the energy of the state $|\Psi\rangle$ and E_0 the ground state energy of the system. It means that no matter what state $|\Psi\rangle$ is considered, its energy will be larger than the ground state energy of the system, except if the state is the ground state itself. Since we are mostly interested in the low-energy properties, or in other words the ground state, we need to minimize the energy by optimizing the wave function coefficients $|\Psi\rangle = \sum_n^N a_n|n\rangle$, where the sum runs over the basis states. This is, computationally speaking not easier than diagonalizing the Hamiltonian. However, the interaction between degrees of freedom in most physical systems is *local*, resulting in a very sparse Hamiltonian matrix with about $\sim N$ nonzero elements compared to the N^2 matrix elements. This makes matrix-matrix or matrix-vector multiplications little demanding and interesting operations one can take advantage of. Let illustrate this with the power method. It starts with a random vector $|\Psi_0\rangle$ in the eigenbasis $\{|m\rangle\}$ with eigenvalues λ_m of $\mathcal{H}$,

$$|\Psi_k\rangle = \mathcal{H}^k|\Psi_0\rangle = \sum_m^N c_m\mathcal{H}^k|m\rangle = \lambda_1^k\left[c_1|1\rangle + c_2\left(\frac{\lambda_2}{\lambda_1}\right)^k|2\rangle + \ldots\right], \tag{14}$$

where the eigenvalues are sorted in ascending order $|\lambda_1| > |\lambda_2|$[11]... Therefore, in the limit $k \to \infty$, $|\Psi_k\rangle$ converges to the leading eigenvector $|1\rangle$ up to a multiplicative constant (we assume that $c_1 \neq 0$). In this limit, and by considering two consecutive steps k and $k+1$, one has access to the leading eigenvalue, $\lambda_1 = |\mathcal{H}^{k+1}|\Psi_{k+1}\rangle/\mathcal{H}^k|\Psi_k\rangle|$. In practice, more sophisticated methods, more stable and which converge faster, are used like the Arnoldi, Lanczos or Jacobi-Davidson algorithms. Nevertheless, they are based on the power method idea of matrix-vector multiplication to get the ground

[11] One has to make sure that $|\lambda_1|$ will be the largest eigenvalue of the Hamiltonian, and that λ_1 will be the smallest. This can be achieved by shifting the whole Hamiltonian by the right constant c, i.e., $\mathcal{H} \to (\mathcal{H} - Ic)$ at the beginning where I is the identity matrix.

state, and can be used on top of the symmetries block-diagonalizing $\mathcal{H}$, allowing one to simulate up from twenty to fifty $S = 1/2$ spins [23–28].

Next, I want to discuss the basic idea behind the Monte Carlo methods: the sampling the partition function in the canonical ensemble at temperature T,

$$\mathcal{Z}(T) = \mathrm{Tr}\ \mathrm{e}^{-\mathcal{H}/T}. \tag{15}$$

If one were to compute $\mathcal{Z}(T)$ naively, it would require for a quantum system i) the exponentiation of the Hamiltonian matrix $\mathcal{H}$, involving its diagonalization, and then ii) to perform an exponentially large sum with the system size. For a classical system, the problem reduces to an exponentially large summation with the system size since the energy of any configuration $\{\sigma\}$ can be trivially computed. This summation is still very limiting though, and the idea of Monte Carlo methods is to avoid its full computation by building a *Markov chain*. Although I am interested in quantum systems, the sampling concept can be understood for classical systems (like the Ising model) just the same. The Boltzmann probability of a given configuration $\{\sigma\}$ reads,

$$\mathcal{P}\left(\{\sigma\}\right) = \frac{1}{\mathcal{Z}(T)}\, W\left(\{\sigma\}\right) \quad \text{with } W\left(\{\sigma\}\right) = \mathrm{e}^{-E(\{\sigma\})/T}, \tag{16}$$

and the idea is to generate a sequence of N configurations $\{\sigma_1\}, \{\sigma_2\}, \ldots \{\sigma_N\}$ whose probability to appear in this sequence is equal to $\mathcal{P}\left(\{\sigma\}\right)$ as in Eq. (16) in the limit of $N \to \infty$. If one knows how to generate this sequence, each of its configurations can be used to compute the system properties and then do the average over all the sequence configurations. This should give a result close to the exact one, with a sampling error of the order $\mathcal{O}(1/\sqrt{N})$. The best-known way to achieve this is by the Metropolis algorithm [29], based on the *detailed balance principle*. It states that starting from a random initial configuration $\{\sigma_{\text{init}}\}$ and fulfilling the condition

$$W\left(\{\sigma_A\}\right) \mathcal{P}\Big(\{\sigma_A\} \to \{\sigma_B\}\Big) = W\left(\{\sigma_B\}\right) \mathcal{P}\Big(\{\sigma_B\} \to \{\sigma_A\}\Big), \tag{17}$$

should lead after a warming-up (thermalization) to a sequence of good configurations that one can use; $\mathcal{P}\left(\{\sigma_A\} \to \{\sigma_B\}\right)$ is the probability to go from configuration $\{\sigma_A\}$ to $\{\sigma_B\}$. In addition, we require that the sampling must be *ergodic*: any configuration $\{\sigma_C\}$ with a nonzero weight $W(\{\sigma_C\})$ must be reachable in a finite number of moves starting from an arbitrary configuration. In practice, one suggests a configuration $\{\sigma_{k+1}\}$ resulting from some change in the current configuration $\{\sigma_k\}$, like a spin flip on a random spin of the system. The move is accepted with probability $\min\left[\mathcal{P}\left(\{\sigma_k\} \to \{\sigma_{k+1}\}\right), 1\right]$, and rejected otherwise, where

$$\mathcal{P}\Big(\{\sigma_k\} \to \{\sigma_{k+1}\}\Big) = \exp\left\{\Big[E(\{\sigma_k\}) - E(\{\sigma_{k+1}\})\Big]\Big/T\right\}. \tag{18}$$

It is now obvious why this procedure cannot work for quantum systems without some workaround since a direct correspondence between a state and a probability W cannot be made except in the eigenbasis of $\mathcal{H}$, which is unknown. Moreover, even if the eigenbasis was known, it is definitely not straightforward to think of some local moves from one eigenstate to another.

As a last remark, it is unavoidable to perform a *finite-size scaling analysis* when doing numerical simulations in condensed matter physics. Rather than just studying

the physical properties of the largest system one can simulate, a systematic study is performed on different system sizes $N_1,\ N_2, \dots N_{\max}$ and the scaling of observables in the *thermodynamic limit*, $1/N \to 0$, is extrapolated.

I have implemented and used various state-of-the-art numerical methods to tackle the quantum many-body problems in this manuscript. This includes exact diagonalization, quantum Monte Carlo and matrix product states algorithms like the powerful density matrix renormalization group, based on the variational principle. I will discuss thoroughly these last two methods in the following chapter now that the basic ideas have been set up.

II. Organization of the manuscript

Chapter A The first chapter will be a natural follow-up of this introduction where I will exhaustively go through the class of quantum spin systems I have been studying. Specifically, it will focus on (quasi-)low-dimensional quantum antiferromagnets. A system geometrically one-dimensional such as a chain or a ladder is by definition *low-dimensional*. Now, any lattice in higher dimension will also be considered as such, as long as the couplings between degrees of freedom, lying on the vertices, are at well-separated energy scales. As an example, take a simple cubic lattice with first-neighbor couplings $J_{a,b,c}$ in the a, b and c spatial directions. A system with $J_a \gg J_{b,c}$ will be qualified quasi-one-dimensional and made of weakly coupled chains, hence "quasi". What sets the cursor for the relevant energy scale of the system is the temperature T. Therefore we might expect a temperatures range $T \sim J_a \gg J_{b,c}$ around which universal one-dimensional features will manifest. As the temperature gets lowered however, with $T \sim J_{b,c}$, the system will unavoidably meet specific three-dimensional phenomena such as a phase transition with a spontaneous symmetry breaking towards an ordered phase, e.g., the Néel order for an antiferromagnet. I will show that in numerous antiferromagnets subject to an external magnetic field, the Néel phase is analog to a Bose-Einstein condensation with all its enthralling properties and experimental fingerprints, like the lambda anomaly in the specific heat at the transition. In addition to the many great examples I will discuss, an entire section will be dedicated to a specific quasi-one-dimensional compound, made of weakly coupled $S = 1$ chains called "DTN". Moreover, I will get back in its own section on how the ordering process of the three-dimensional system is modulated with reduction of dimensionality. I will also introduce beforehand the numerical tools that have been implemented and used.

Chapter B The second chapter will be dedicated to the dynamical properties of quantum spin systems which are accessed experimentally by means of inelastic neutron scattering and nuclear magnetic resonance through the so-called spin-lattice relaxation rate $1/T_1$. The quantities measured experimentally can be related to time-dependent correlation functions such as $\langle \mathbf{S_r}(t) \cdot \mathbf{S_0}(0) \rangle$ where in the Heisenberg picture $\mathbf{S_r}(t) = \mathrm{e}^{-i\mathcal{H}t}\mathbf{S_r}\mathrm{e}^{i\mathcal{H}t}$, with $\mathcal{H}$ the Hamiltonian describing the system and t the time. The computation of such observables is theoretically *very* challenging. An entire part of this chapter will introduce the numerical tools and methods that I

have implemented and used to reliably access the real-time dynamics of pure (zero temperature) and mixed (finite temperature) quantum states. The main question that will be addressed here is about the dimensional crossover of these dynamical quantities in quasi-one-dimensional spin systems as function of temperature. Especially, I want to define the temperature window in weakly coupled chain type compounds inside which the universal one-dimensional features can be experimentally probed. This range is defined for low-enough temperature such that the low-energy physics are visible, but not too low either as we do not want to approach too much the phase transition towards long-range ordering that might spoil the genuine one-dimensional properties. I will precisely define what I mean by *low-enough* but *not too low either*.

Chapter C The third chapter will focus on the interplay between interactions and disorder in quantum antiferromagnets. In condensed matter physics, disorder and interactions lead to non-trivial low-energy physics, which goes beyond non-interacting Anderson localization, where quantum interference of electronic waves due to multiple scattering processes induced by the impurities, can completely block the transport, thus driving a metal-to-insulator phase transition. In that respect, doped quantum antiferromagnets offer a unique playground to address this subtle interplay between impurities and many-body effects. The disorder is induced by chemical doping by randomly substituting one atom by another and drive the "clean system" toward new magnetic quantum phases of matter with a total change of its physical properties. Specifically, I will be interested in two different phases that I will introduce and briefly review in the first part: namely the *random singlet phase* and the *Bose-glass* phase. A first work that I will present will focus on the dynamical properties of the random singlet phase in one-dimensional Heisenberg spin chains with random antiferromagnetic exchange couplings. As we will see, one main inspiration is to motivate inelastic neutron scattering and nuclear magnetic resonance experiments by presenting state-of-the-art numerical results in these systems. In the last part of this chapter, I will present a series of works on the chemically doped "DTN" compound at high magnetic fields, which has been proposed in prior publications as the first experimental realization of the elusive Bose-glass phase in a quantum magnet. The starting point of our works was an experimental study of the putative high magnetic fields Bose-glass phase by nuclear magnetic resonance. Unexpected observations hinted that something else than a Bose-glass was at play. We theoretically showed that the disorder itself is actually getting ordered, forming a Bose-Einstein condensation through a novel order-by-disorder mechanism that I will discuss. Moreover, we provide a complete picture of the phase diagram "high magnetic fields *vs.* doping concentrations *vs.* temperatures". At low doping there is still room for a Bose-glass phase and we study the critical properties of the Bose-Einstein condensation to Bose-glass transition. The theoretically predicted disorder-induced revival of Bose-Einstein condensation in "DTN" was afterwards experimentally detected by nuclear magnetic resonance.

— Chapter A —

(Quasi-)Low-dimensional quantum antiferromagnets

Overall, this first chapter is organized as a more specialized introduction than the *real* introduction (namely, the previous part) of this manuscript. I will introduce more thoroughly the class of quantum spin systems I have been studying as well as their — sometimes — peculiar physical properties, theoretical tools to describe them, and efficient numerical methods to investigate them.

Section I I will first discuss generic one-dimensional antiferromagnets [30] whose low-energy properties can be effectively described by the Tomonaga-Luttinger liquid theory [31–33]. I will present this universal model, which can account for the many-body interactions in various one-dimensional quantum systems: fermions, bosons, or spins alike [34–39]. Besides that, I will review some remarkable experiments checking for the accuracy of this description, favoring magnetic examples.

Section II In the second section, I will move to coupled spin chains in a three-dimensional fashion. Specifically it is known that at low temperature, the three-dimensional Néel ordering following the spontaneous symmetry breaking in numerous quantum antiferromagnets subject to an external magnetic field is analogous to a Bose-Einstein condensation as in — best known for — cold atoms experiments [40–42]. I will review this fascinating property and go through how it manifests itself in several quantum antiferromagnets [43, 44], eventually building up a dictionary translating from boson to spin language, or vice-versa. I will also provide and discuss recent experimental realizations.

Section III I will in the next section discuss numerical methods to investigate the quantum systems discussed before. Well-suited for one-dimensional systems, I will first present the Matrix Product States formalism [45, 46] along with the variational Density-Matrix Renormalization Group method [47, 48] to obtain, in the most efficient way up to date, ground-state properties of interacting quantum systems. I will then introduce quantum Monte Carlo in its stochastic series expansion formulation [49, 50], whose basic idea is to sample the partition function of a quantum system.

Section IV Mermin-Wagner theorem [17–20] states that the spontaneous breaking of a *continuous* symmetry is deeply related to the dimensionality of a system. In antiferromagnets, the Néel order associated with spontaneous breaking of

SU(2) or U(1) symmetry is allowed at any temperature for three-dimensional systems but allowed only at zero temperature for purely two-dimensional systems (and cannot happen in one-dimensional systems, even at zero temperature). I will discuss in this section on how the ordering process of such a three-dimensional system is modulated with reduction of dimensionality towards the two-dimensional limit.

Section V Finally, as another example for the first two sections, I will focus on a realistic antiferromagnetic quantum $S = 1$ spin compound "DTN" [51]. This material has an interesting double hatting. On one side, it is three-dimensional and displays a Bose-Einstein condensation upon applying a sufficiently large magnetic field at low temperature. On the other side, its weak three-dimensional couplings make possible experimental investigations for universal Tomonaga-Luttinger liquid properties at intermediate temperature, i.e., above the critical temperature below which the system undergoes a phase transition towards antiferromagnetic order.

I. One-dimensional antiferromagnets

When it comes to quantum magnetism, the paradigm model is the one-dimensional $S = 1/2$ Heisenberg model that we derived in the introduction,

$$\mathcal{H}_{\text{Heisenberg}} = J \sum_i \mathbf{S}_i \cdot \mathbf{S}_{i+1}. \tag{A.1}$$

It is a lattice model, where the sum is run over each site i of the chain lattice which each holds a spin $\mathbf{S}_i = (S_i^x, S_i^y, S_i^z)$ degree of freedom. The model is SU(2) invariant, which means that both the total spin $\mathbf{S}_{\text{tot}} = \sum_i \mathbf{S}_i$ and the total z-component $S_{\text{tot}}^z = \sum_i S_i^z$ are conserved quantities and commute with the Hamiltonian. Depending on the sign of J, the model can describe different magnetic phases. In order to minimize the system energy, it is obvious that $J < 0$ will favor neighboring spins pointing in the same direction (ferromagnet) whereas $J > 0$ will favor neighboring spins pointing in opposite directions (antiferromagnet). It is instructive to rewrite the model by introducing the raising and lowering operators expressed as $S^{\pm} = S^x \pm iS^y$,

$$\mathcal{H}_{\text{Heisenberg}} = J \sum_i \left[\frac{1}{2} \left(S_i^+ S_{i+1}^- + S_i^- S_{i+1}^+ \right) + S_i^z S_{i+1}^z \right]. \tag{A.2}$$

It becomes obvious that in the ferromagnetic case, the basis state $|\uparrow\uparrow \cdots \uparrow\rangle$ is indeed an eigenstate that will minimize the energy. The same cannot be said for the classical Néel state $|\uparrow\downarrow\uparrow\downarrow \cdots \uparrow\downarrow\rangle$ because of the spin flips induced by the raising and lowering operators $S_i^{\pm} S_{i+1}^{\mp}$. However, the one-dimensional antiferromagnetic Heisenberg model is integrable by means of Bethe ansatz [52, 53], a powerful technique of mathematical physics. This provides a goldmine of information on its ground state properties and makes it one of the few many-body quantum models with a known exact solution. For instance, its ground state is unique (non degenerated), of total spin $\mathbf{S}_{\text{tot}} = 0$ (singlet), $S_{\text{tot}}^z = 0$ [54, 55], and despite the antiferromagnetic nature of the model, its staggered magnetization is zero, i.e., $\sum_i (-1)^i \langle \mathbf{S}_i \rangle = 0$. Its energy spectrum

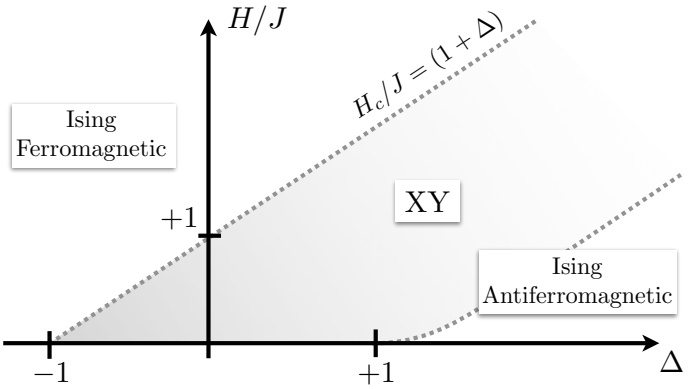

Figure A.1: Phase diagram of the $S = 1/2$ XXZ model in Eq. (A.4) as a function of the dimensionless external magnetic field H/J and the Ising anisotropy Δ, both along the z-component of the spin degrees of freedom. The phase diagram is symmetrical with respect to the horizontal axis given that the transformation $S_i^z \to -S_i^z$ restores the initial model formulation for $H/J < 0$. There are three distinct phases, including two "classical Ising" limits: the Ising ferromagnetic and the Ising antiferromagnetic phases, which are gapped, and the XY phase which can be described by Tomonaga-Luttinger liquid theory. This figure has been reproduced from Ref. 30.

is *gapless* [56] and the lowest excitations states are spin triplets with a spin wave spectrum $\varepsilon(q) = \pi|\sin q|/2$ [57] where q is the momentum. Besides, the spin-spin correlation at long distance reads [58],

$$\langle \mathbf{S}_i \cdot \mathbf{S}_{i+r} \rangle \underset{r\to+\infty}{\sim} (-1)^r \frac{3}{2\pi^{3/2}} \frac{\sqrt{\ln r}}{r}, \tag{A.3}$$

where the alternating sign accounts for the antiferromagnetic properties of the model. Ultimately, there is no long-range order, but the correlations are not short-ranged either due to the power-law dependence; we refer in the literature to such a ground state as *quasi long-range* ordered or *critical*, although there is no transition involved.

The one-dimensional S=1/2 XXZ model Before going further and to be more general in the following, it is interesting to introduce a descendant of the Heisenberg model,

$$\mathcal{H}_{\text{XXZ}} = J \sum_i \left[\frac{1}{2} \left(S_i^+ S_{i+1}^- + S_i^- S_{i+1}^+ \right) + \Delta S_i^z S_{i+1}^z \right] - H \sum_i S_i^z, \tag{A.4}$$

called the XXZ model, because of the anisotropy Δ induced along the z-component of the interactions, which reduces the model symmetry from SU(2) to U(1)[1]. We also have introduced an external magnetic field H which couples to the spin degrees of freedom, along the same direction as the anisotropy, and which lifts the spin inversion symmetry $S_i^z \to -S_i^z$ for $H \neq 0$. The phase diagram of this model is displayed in Fig. A.1, with three different phases, including two "classical Ising" limits. The Ising ferromagnetic ground state has its N spins pointing in the same z (or $-z$) direction with a magnetization density $m^z = \sum_i \langle S_i^z \rangle / N = \pm 1/2$. It spontaneously breaks the discrete spin inversion symmetry $S_i^z \to -S_i^z$ of the model for $H/J = 0$

[1]Now, only the total spin z-component is conserved, i.e. $[\mathcal{H}, S_{\text{tot}}^z] = 0$.

by randomly choosing a direction. For $H/J \neq 0$ the symmetry is lifted anyway and the ferromagnetic ground state will be stabilized along the magnetic field direction. The low-lying excitations are *magnons* (one spin flip), gapped $S^z = \pm 1$ modes with dispersion relation $\varepsilon(q) = J(\cos q - \Delta) + H$. The Ising antiferromagnetic ground state breaks the discrete translation symmetry to two lattice spacing with a zero magnetization and a finite staggered magnetization density $\sum_i (-1)^i \langle S_i^z \rangle / N \neq 0$. Its value depends on Δ and H and is only maximum in the limit $\Delta \to +\infty$. For instance, along the $H/J = 0$ line, it smoothly decreases from $1/2$ in the true classical limit to zero at $\Delta = 1$ to recover the isotropic Heisenberg model properties. This dependence is due to quantum fluctuations (raising and lowering operators) since the classical Néel *is not* the ground state, although it looks more and more like it towards the classical limit. The gapped excitations of domain-wall type [59, 60] can be better understood starting from this limit and using perturbation theory. The last region of the phase diagram, the XY phase is of the same type as the isotropic Heisenberg model: gapless, critical and can be described by the Tomonaga-Luttinger liquid theory and bosonization techniques [37, 61].

To proceed, it is interesting to map the initial spin model to spinless fermions via the non local Jordan-Wigner transformation [56, 62],

$$S_j^+ = c_j^\dagger \prod_{l=1}^{j-1} \mathrm{e}^{i\pi n_l}, \quad \text{and } S_j^z = n_j - \frac{1}{2}, \tag{A.5}$$

where $n_j = c_j^\dagger c_j$ and $c_j^\dagger$ (c_j) are creation (annihilation) operators of a spinless fermion on site j. The exponential string ensures that the fermionic operators obey the right anticommutation relation. The transformation leads to,

$$\mathcal{H}_{\text{t-V}} = \sum_i \left[-t \left(c_i^\dagger c_{i+1} + c_{i+1}^\dagger c_i \right) + V n_i n_{i+1} \right] - \mu \sum_i n_i, \tag{A.6}$$

up to additional irrelevant constants with $t = J/2$, $V = J\Delta$ and $\mu = (H + J\Delta)$. It is called the t-V model, and it is very similar to the Hubbard model in the writing: a hopping term t, a density-density interaction V and a chemical potential μ. In one dimension, the correspondence with the XXZ spin-1/2 model remains local despite the exponential strings, which happen to cancel out. For $V = 0$ we are left with a tight-binding model of free fermions which can be diagonalized going to Fourier space with the substitution $c_r = \sum_q \mathrm{e}^{iqr} c_q / \sqrt{N}$,

$$\tilde{\mathcal{H}} = \sum_q \varepsilon(q) c_q^\dagger c_q, \quad \text{with } \varepsilon(q) = -2t \cos q - \mu, \tag{A.7}$$

and $q = 2\pi n/N$ with $n = 1, 2 \ldots N$ where N is number of sites. The $\binom{N}{N_f}$ eigenstates are constructed by filling the N levels with N_f fermions, and the ground state by specifically filling the N_f lowest energy levels up to the Fermi level q_F, i.e., $|\text{gs}\rangle = \prod_q^{q_F} c_q^\dagger |0\rangle$, with $|0\rangle$ the vacuum. As for any non interacting system that can be "easily" diagonalized, one can compute many of its properties at zero or finite temperature since the partition function factorizes into the single-particle partition function. For instance, the spin-spin correlations of the ground state in the initial spin language at zero magnetic field reads,

$$\langle S_i^\pm S_{i+r}^\mp \rangle \sim (-1)^r / \sqrt{r} \quad \text{and } \langle S_i^z S_{i+r}^z \rangle = -1/2(\pi r)^2, \tag{A.8}$$

where the longitudinal (zz) correlation is only non zero for odd distances [56]. The computation of the transverse ($\pm\mp$) correlation is a bit more involved because of the exponential strings, but can eventually be reduced to the computation of a determinant [63]. Similarly to the isotropic case, we find a power-law dependence, but with a different exponent values. For the general case in the XY phase, one can derive the following scalar field Hamiltonian in the continuum limit[2] [37, 61],

$$\mathcal{H}_{\mathrm{TLL}} = \frac{1}{2\pi}\int \mathrm{d}r\ \left\{uK\left[\partial_r\theta(r)\right]^2 + \frac{u}{K}\left[\partial_r\phi(r)\right]^2\right\}, \tag{A.9}$$

where $\theta(r)$ and $\phi(r)$ are canonically commuting bosonic fields, $[\phi(x), \partial_y\theta(y)/\pi] = i\delta(x-y)$ and r the spatial variable. In a geometrical interpretation, these fields can be viewed as the two angles required to define a spin as a classical vector, and quantum nature comes from the commutation relation. The model only relies on two parameters, u, the propagation velocity of the bosonic excitations through the system and K, the dimensionless Tomonaga-Luttinger liquid parameter which measures "the degree of quantum fluctuations" in the system. At that point, it is worth mentioning that the better known Landau's Fermi Liquid theory [1–4] fails to describe strongly interacting one-dimensional quantum systems, which require a specific treatment known as *Tomonaga-Luttinger liquid theory*. Landau's idea is to recast the problem in terms of low-energy excitations called quasiparticles that are only weakly interacting, bringing us back to the more comfortable case of free particles. In one dimension however, particles behave in a highly cooperative way and are governed by collective excitations rather than individual ones. This leads to very peculiar and unique physical properties for one-dimensional quantum systems such as Peierls instabilities [64, 65] or spin-charge separation in electronic models [37]. The Tomonaga-Luttinger liquid theory is much more general than what it might look and can actually describe from spin, fermionic and bosonic degrees of freedom alike, to the edge states in the quantum Hall effect [66–68].

At zero magnetic field, the XXZ model is integrable and the value of the u and K are known from Bethe ansatz equations as a function of the Ising anisotropy Δ [71],

$$K = \frac{\pi}{2\arccos(-\Delta)}, \quad \text{and } u = \frac{J\pi\sqrt{1-\Delta^2}}{2\arccos(\Delta)}, \tag{A.10}$$

and are displayed in Fig. A.2. Since they fully characterize the system, they are related to physical observables such as the static susceptibility χ and the spin stiffness ρ_s — or respectively to the compressibility and the superfluid density in the bosons language. The latter corresponds to the variation of the ground state energy e_0 of the system in response to a twist of the boundary conditions, $|\Psi_{j=N+1}\rangle = \mathrm{e}^{i\Phi}|\Psi_{j=1}\rangle$. These quantities take the form,

$$\chi = \frac{\mathrm{d}m^z}{\mathrm{d}H} = \frac{K}{u\pi} \quad \text{and } \rho_s = \frac{\mathrm{d}^2 e_0(\Phi)}{\mathrm{d}\Phi^2}\bigg|_{\Phi=0} = \frac{uK}{\pi}. \tag{A.11}$$

[2] The derivation of the Tomonaga-Luttinger liquid model uses the fermionic representation of Eq. (A.6) as a starting point. Its exact and rigorous derivation is however quite demanding and lengthy. I will skip it in this manuscript and redirect interested readers to the reference books 37 and 61.

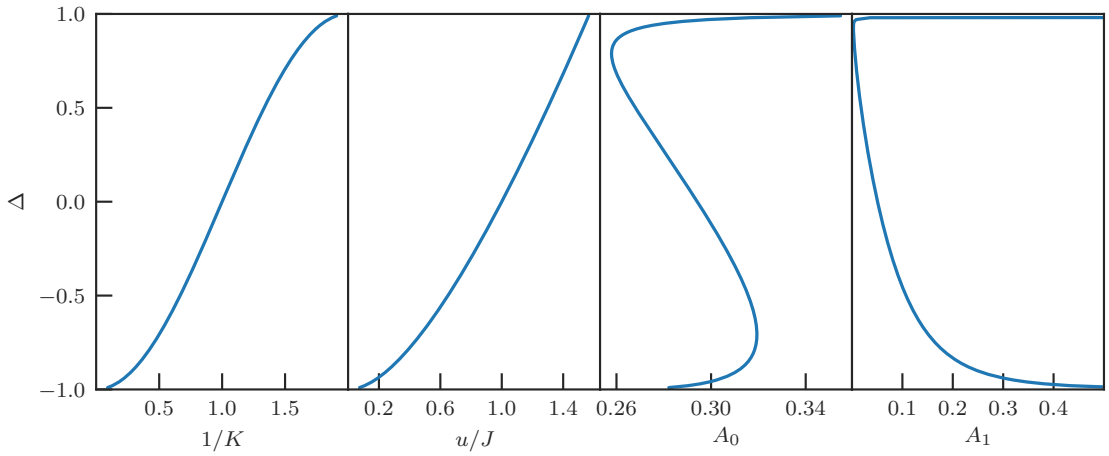

Figure A.2: Tomonaga-Luttinger Liquid parameters at zero magnetic field $H = 0$ as a function of the Ising anisotropy Δ for the XXZ Hamiltonian of Eq. (A.4). u and K are computed from Eq. (A.10) and the prefactors A_0, A_1 of the correlation functions of Eq. (A.13) are obtained from the expressions in Refs. 69 and 70.

The parameter K will also govern the critical behavior of the correlation functions which have the asymptotic form at long distance $r \to \infty$,

$$\langle S_i^{\pm} S_{i+r}^{\mp} \rangle \sim (-1)^r \left[\frac{A_0}{|r|^{\frac{1}{2K}}} - \tilde{A}_0 \frac{\cos(2\pi m^z |r|)}{|r|^{\frac{1}{2K}+2K}} \right], \tag{A.12}$$

and

$$\langle S_i^z S_{i+r}^z \rangle - \langle S_i^z \rangle \langle S_{i+r}^z \rangle \sim (-1)^r A_1 \frac{\cos(2\pi m^z |r|)}{|r|^{2K}} - \frac{K}{2\pi^2 |r|^2}, \tag{A.13}$$

where A_0, $\tilde{A}_0$ and A_1 prefactors which depend on the Hamiltonian parameters, with known exact expressions versus the Ising anisotropy Δ at zero magnetic field for A_0 and A_1 plotted in Fig. A.2 [69, 70]. At zero magnetic field, the free fermions case with $K = 1$, computed independently in Eq. (A.8) is recovered, and at the isotropic point $\Delta = 1$, longitudinal and transverse correlation functions become equivalent. However, because of the presence of a marginally irrelevant operator in the fields theory at the Heisenberg point, logarithmic corrections appear in several quantities. This includes the correlation function [58, 72–74], with a correcting factor $\sqrt{\ln r}$ in the magnetic susceptibility behavior at low-temperature, $2\pi\chi(T) \sim 2 + \ln^{-1}(T_0/T) + \mathcal{O}(\ln^{-3} T)$ [75], where T_0 is a given constant, which was experimentally observed in the $S = 1/2$ chain compound Sr_2CuO_3 [76–78]. Another evidence of the Tomonaga-Luttinger Liquid regime is the linearity of the specific heat, $C = T\pi/3u$, which was observed under magnetic field in the quasi-one-dimensional spin-chain antiferromagnet $BaCo_2V_2O_8$ material [79] and in the metal-organic, two-leg, spin-ladder system[3] $(C_5H_{12}N)_2CuBr_4$ [80].

[3] We discuss in the next section that upon applying a sufficiently strong external magnetic field, a two-leg spin-ladder can be described by a Tomonaga-Luttinger-Liquid theory.

Half-odd integer versus integer one-dimensional spin systems So far, I have only been discussing $S = 1/2$ spin chains and one would naively think that $S \geq 1$ should give very similar properties for the Heisenberg model of Eq. (A.1). It is half true, in the sense that a distinction between half-odd integer and integer spin chains must be made. The former $S = 1/2,\ 3/2,\ 5/2\ldots$ are all critical with a gapless energy spectrum, and display comparable properties, although only the first one is integrable. Haldane showed in his seminal work [81,82] with semi-classical arguments on the non-linear sigma model that $S = 1,\ 2\ldots$ spin chains have a gapped spectrum and that the spin-spin correlations are short-ranged $\langle \mathbf{S}_i \cdot \mathbf{S}_{i+r} \rangle \sim \mathrm{e}^{-|r|/\xi}$ with ξ the correlation length. It was a hot topic in the late eighties and nineties to verify these predictions and study the $S = 1$ spin chain since no exact solution exists for $S \geq 1$. The enthusiasm and excitement was mainly because at the time, most results relied on spin-wave theory [83–85], which develops series expansions in powers of $1/S$ for the low-energy parameters and this method works best close to the classical limit ($S \to \infty$); therefore, there was no reason to think that the case $S > 1/2$, would be different. Numerical methods have played a major role, and the exponential decay of the correlations was observed in quantum Monte Carlo [86,87] and density matrix renormalization group [47] simulations with $\xi \simeq 6.03$. The value of the energy gap between the ground state and the first excited state was computed with high precision as well, $\Delta_g/J \simeq 0.41050\ldots$ [88] and observed by inelastic neutron scattering experiments in $S = 1$ quasi-one-dimensional compounds $AgVP_2S_6$ [89,90], $CsNiCl_3$ [91] and $Ni(C_2H_8N_2)_2NO_2ClO_4$ [92]. The presence of this gap strongly dominates the low-temperature properties, $T \ll \Delta_g$, of integer spin chains with activated laws $\sim \mathrm{e}^{-\Delta_g/T}$ for physical quantities such as the specific heat or the magnetic susceptibility as observed from nuclear magnetic resonance frequency shift measurements in $AgVP_2S_6$ [93]. From Haldane work, the gap of integer spin S chains should follow $\Delta_g(S) \sim \mathrm{e}^{-\alpha S}$ with $\xi \sim 1/\Delta_g$ and α some positive constant, to accord the half-integer and integer behaviors in the classical limit.

It was soon realized that open $S = 1$ spin chains hold effective $S = 1/2$ degrees of freedom at the boundaries [94], as observed in the $Ni(C_2H_8N_2)_2NO_2ClO_4$ material from ESR and EPR experimental measurements [95–97], in $Y_2BaNi_{1-x}Mg_xO_5$ [98] by NMR measurements and in quantum Monte Carlo simulations [99]. It was later observed by magnetization measurement in the doped $CsNi_{1-x}Mg_xCl_3$ compound [100]. The Ni^{2+} ions carry a $S = 1$ and the Mg^{2+} are non magnetic impurities cutting the interacting $S = 1$ chain into finite-sized ones with open boundaries. The susceptibility is exponentially suppressed at low temperature for $x = 0$ whereas for finite x, there is a crossover to a diverging Curie behavior $\chi \sim 1/T$ arising from the free and non interacting effective $S = 1/2$ spins. To better understand this, the idea is that a spin-1 can be decomposed into two effective $S = 1/2$ spins. Yet, the reverse operation of combining two $S = 1/2$ spins can give rise to $S = 0$ and $S = 1$ spins and the first one has to be projected out since we want to describe a spin-1 chain in the end. An ansatz for the ground state is pictured in Fig. A.3, with effective $S = 1/2$ spins from neighboring sites forming singlets. It is obvious that the effective boundary $S = 1/2$ spins are dangling by not taking part to a singlet. This is not the exact ground state of the Heisenberg $S = 1$ chain but one of its descendant, the AKLT model [101–103] describing a one-dimensional $S = 1$ spin chain with a Heisenberg interaction and an additionnal first-neighbor biquadratic interaction of the form $\frac{1}{3}(\mathbf{S}_i \cdot \mathbf{S}_{i+1})^2$. Turning off the biquadratic term $\frac{1}{3} \to 0$ does not induce

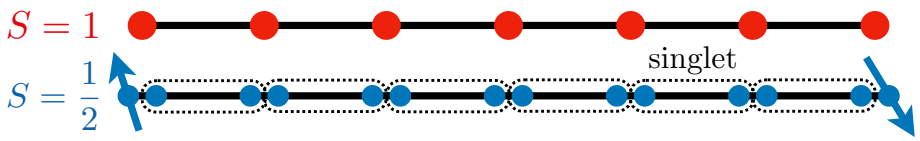

Figure A.3: Picture of the exact ground state for the $S = 1$ Heisenberg spin chain with an additional first-neighbor biquadratic interaction of the form $\frac{1}{3}(\mathbf{S}_i \cdot \mathbf{S}_{i+1})^2$, called the AKLT model. The initial $S = 1$ spins are divided into two effective $S = 1/2$ spins which form singlets with neighboring spins. There are dangling free effective $S = 1/2$ spins at the boundaries which cannot form a singlet. Since the AKLT ground state belongs to the same phase as the purely Heisenberg chain, both are connected and share properties, including these effective free $S = 1/2$ spins, observed in experiments, see text.

a quantum phase transition, which means that the AKLT and the exact $S = 1$ Heisenberg ground states are adiabatically connected, belong to the same phase and share properties such as the effective free $S = 1/2$ spins at the boundaries, so-called *edge states*.

Symmetry protected topological phase and entanglement entropy In this AKLT picture (Fig. A.3), effective neighboring spins within a singlet have an opposite $S^z = \pm\frac{1}{2}$ component. This implies that for the original $S = 1$ degrees of freedom, there cannot be two consecutive spins with the same z-component ± 1, even though there can be as many spins with $S^z = 0$ in between them. In other words, only basis states with consecutive z-component ± 1 and ∓ 1 (with as many $S^z = 0$ as we want in between) are non zero in this description. This leads to some kind of non local long-range antiferromagnetic order [104] where the non local correlation function $\langle S^\alpha_j \cdot \prod_{n=j+1}^{j+r-1} \mathrm{e}^{i\pi S^\alpha_n} \cdot S^\alpha_{j+r} \rangle$ with $\alpha = x, y, z$ takes a finite value at long distance, as for long-range ordered systems. Later, it was realized that the edge states and non-local order are fingerprints of what is now known as symmetry protected topological (SPT) phases [105–110].

A more robust fingerprint of SPT phases is the exact double degeneracy of the entanglement spectrum between two parts A and B of the system when cut in half in real space. With $|\Psi_{AB}\rangle$ a pure ($T = 0$) state describing a quantum system, the quantity of interest is the reduced density matrix,

$$\rho_A = \mathrm{Tr}_B\Big(|\Psi_{AB}\rangle\langle\Psi_{AB}|\Big), \tag{A.14}$$

where the partial trace runs over degrees of freedom from the B region, see Fig. A.4. The eigenvalues of ρ_A define the entanglement spectrum of the subsystem A with the other subsystem B. The amount of entanglement between these two subsystems can be measured through Von Neumann entanglement entropy,

$$S_{\mathrm{vN}}(\rho_A) = -\mathrm{Tr}\Big(\rho_A \ln \rho_A\Big), \tag{A.15}$$

with the property $S_{\mathrm{vN}}(\rho_A) = S_{\mathrm{vN}}(\rho_B)$. Entanglement-related quantities have proven to be a powerful tool for investigating quantum many-body systems, and especially in condensed matter physics (see Ref. 111 for a review). For instance it provides major information on the nature of the ground state of a system, like criticality, and gives access to the central charge for critical one-dimensional quantum systems

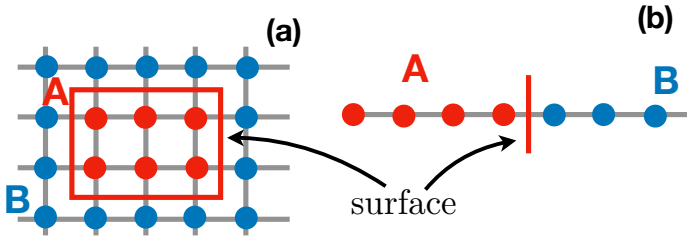

Figure A.4: Real space bipartition of a **(a)** two-dimensional ($D = 2$) and a **(b)** one-dimensional ($D = 1$) quantum many-body systems into two parts A and B. The area law states that the entanglement entropy of the subsystem A with B scales with the surface of A, see text.

described by conformal field theory [112–114]. It is also the corner stone of tensor network algorithms [46, 115, 116] through the *area law*, a general statement telling you that the entanglement entropy between two parts A and B of the ground state of a system (Fig. A.4) grows with the surface of the subsystem A and not its volume, i.e., $S_{\text{vN}}(\rho_A) \sim L^{D-1} + \dots$ for a D-dimensional system [113, 117–119]. The fact that the leading algebraic dependance with L becomes constant in one dimension ($D = 1$) is, as we shall see, the reason why Matrix Product States work so well to describe one-dimensional quantum systems.

II. Magnetic field-induced Bose-Einstein condensation in quantum antiferromagnets

To remove any ambiguity straight away, unlike what may imply the chapter's title, a *low-dimensional* quantum antiferromagnet is *not* a necessary condition to obtain a Bose-Einstein condensation in a magnetic insulator. Yet, it happens that many realistic materials — including the one that we will thoroughly investigate by the end of this chapter — are anisotropic with stronger energy couplings along favored spatial directions, and ultimately qualify as quasi-low-dimensional. Thus, although this section could be on its own, it still slightly fits in here.

Now, if one says Bose-Einstein condensation, what comes in mind first is *cold atoms* related physics, definitely not antiferromagnets. But before moving to that, let us review this phenomenon in the instructing academic case of a non-interacting bosons gas in D dimensions, inside a volume L^D. The prediction of this phenomenon was done by Einstein and Bose in 1924 [120–122] in three dimensions but only observed many years later (1995) in trapped ultracold Bose-condensed gases of alkali atoms [123, 124]. We consider free particles with a generic dispersion relation $\varepsilon(\mathbf{q}) = \mathbf{q}^z$, and the states labeled by the momentum $|\mathbf{q}\rangle$. The occupation number $n_{\mathbf{q}}$ of particles in a given state follows Bose–Einstein statistics and the density of particles is simply

$$n = \frac{1}{L^D} \sum_{\mathbf{q}} n_{\mathbf{q}} = \frac{1}{L^D} \sum_{\mathbf{q}} \frac{1}{\mathrm{e}^{[\varepsilon(\mathbf{q})-\mu]/T} - 1}, \tag{A.16}$$

with $\mu < 0$ the chemical potential which controls it and T the temperature. One can then substitute the sum by an integral,

$$n = \frac{1}{(2\pi)^D} \int_0^\infty \mathrm{d}\mathbf{q}\, \frac{1}{\mathrm{e}^{[\mathbf{q}^z - \mu]/T} - 1} = \frac{2T^{\frac{D}{z}}}{z\Gamma\left(\frac{D}{2}\right)(4\pi)^{\frac{D}{2}}} \Gamma\left(\frac{D}{z}\right) \mathrm{Li}_{\frac{D}{z}}\left(\mathrm{e}^{\mu/T}\right). \tag{A.17}$$

To get the second term, we first move to generalized spherical coordinates in D dimensions and then make the variable substitution $q^z/T \to \tilde{q}$. $\Gamma(x)$ is the Euler gamma function and $\mathrm{Li}_s(x) = \sum_{n=1}^\infty x^n/n^s$ is the polylogarithm function: a monotonous increasing function in x, and thus in μ for $s > 0$. Since $\mu \to 0$ is the limiting value, the density seems bounded, which is *not physical*. A workaround is to introduce a critical temperature corresponding to $\mu = 0$,

$$T_c = n^{z/D} \left(\frac{z 2^{D-1} \pi^{D/2} \Gamma(D/2)}{\Gamma(D/z)\zeta(D/z)} \right)^{z/D}, \tag{A.18}$$

where $\zeta(x)$ is the Riemann zeta function. Still, there seems to be a flaw in the theory and it is not clear what happens below T_c and how it is related to the boundedness of the density. In fact, the flaw comes from the substitution of the sum in Eq. (A.16) by an integral in Eq. (A.17), which implies some uniformity in the density of states and is not true anymore for $T < T_c$: the limiting $\mathbf{q} = \mathbf{0}$ ground state needs to be explicitly written in this case,

$$n = \frac{1}{L^D} \frac{1}{\mathrm{e}^{-\mu/T} - 1} + \cdots \tag{A.19}$$

where the second omitted term is the same as Eq. (A.17). Above the critical temperature $T > T_c$, this first term vanishes in the thermodynamic limit ($L \to \infty$), and we recover the expression (A.17) for the density. Below the critical temperature with $\mu \to 0$, it follows that the fraction of particles in the ground state is,

$$\frac{n_0}{n} = 1 - \left(\frac{T}{T_c} \right)^{D/z}. \tag{A.20}$$

This means that a macroscopic fraction of particles occupies the same (lowest) energy state below a critical temperature T_c, known as the *Bose-Einstein condensation* (BEC) phenomena. More generally, T_c is a critical point marking a phase transition with a spontaneous symmetry breaking. It is not obvious what symmetry is broken at T_c yet: let us define the wavefunction

$$\Psi_{\mathbf{q}=\mathbf{0}} = \sqrt{n_0} \mathrm{e}^{i\theta}, \tag{A.21}$$

describing the condensate fraction[4], with $|\Psi_{\mathbf{q}=\mathbf{0}}|^2 = n_0$ and θ some generic phase factor. For $T > T_c$, it is zero in the thermodynamic limit for any value of θ. Below T_c however, the finiteness of the condensate fraction sets θ to some arbitrary value which breaks the continuous U(1) symmetry of the Hamiltonian. The condensate wavefunction (A.21) plays the role of the order parameter for the transition and is a complex number. The mindful reader would have noticed that there seems to exist a critical temperature (and therefore long-range order) in any dimension, which

[4] At finite temperature, the whole system is not described by a pure state but a mixed state. However, a single microstate, $\mathbf{q} = \mathbf{0}$ here, can be described as such.

goes against Mermin-Wagner theorem. I have purposely overlooked the computation of the density in Eq. (A.17). Indeed, the polylogarithm function only converges for $D/z > 1$ if the chemical potential approaches zero. For a standard quadratic dispersion relation with $z = 2$, we find that indeed, there can only be long-range order at finite temperature for $D > 2$. For massless relativistic particles ($z = 1$), condensation can takes place in $D = 2$, but only in $D = 3$ for finite-mass bosons (m) with a dispersion relation $\varepsilon(\mathbf{q}) = \sqrt{m^2c^4 + c^2\mathbf{q}^2}$ with c the light velocity [125].

Closely related, although different, the *superfluidity* phenomena was observed in 1937 in liquid ^{4}He [126, 127] and the connection with BEC was quickly realized [128, 129]. It is the curious property of a fluid to have exactly zero viscosity. For instance, when stirred, a superfluid forms vortices that continue to rotate indefinitely, without loss of kinetic energy. To mathematically define superfluidity, we need to distinguish between dynamical (time-dependent) aspects and the response of the system to an infinitesimally small perturbation [130, 131]. The second is used as customary definition for the superfluid density ρ_s and can be related to the second derivative of the free energy density of the system $\mathcal{F}$ with respect to a Galilean transformation of velocity $\mathbf{v}$ to the system,

$$\rho_s = \frac{1}{V}\lim_{\mathbf{v}\to\mathbf{0}} \nabla^2_{\mathbf{v}}\mathcal{F}(\mathbf{v}) \equiv \frac{1}{V}\lim_{\Phi\to 0}\frac{\mathrm{d}^2\mathcal{F}(\Phi)}{\mathrm{d}\Phi^2} \tag{A.22}$$

where $\nabla^2_{\mathbf{v}}$ is the Laplacian operator. The second expression in Eq. (A.22) equivalently relates the superfluid density to the response of the free energy to a boundary phase twist Φ. The interested reader can refer Ref. 132 where a rigorous and pedagogical derivation can be found.

At zero temperature, liquid helium is 100% superfluid, but less than 10% of the atoms are actually in the BEC [133, 134] — unlike the case of free bosons where the whole condensed fluid is also superfluid. Indeed, due to interactions, most of the particles are expelled from the condensate and spread over a wide range of momenta $\mathbf{q} \neq \mathbf{0}$. This is known as the quantum *depletion* of the BEC and was microscopically explained by Bogoliubov's theory in 1947 [135]. This points out the importance of interactions in realistic systems: e.g., for interactions characterized by a scattering length a, the condensed fraction at zero temperature at leading order $\sqrt{na^3} \ll 1$ corrects to $n_0/n \simeq 1 - (8/3)\sqrt{na^3/\pi}$ [136], which was verified by both Monte Carlo simulations [137] and Bragg spectroscopy experiments [138].

If it is usual to introduce Bose–Einstein condensation for cold atomic gases, the phenomenon can also take place with quasiparticles, i.e., effective particles describing collective excitations in physical systems. Indeed, some have integer spins and obey Bose–Einstein statistics like standard particles. Such systems include semiconductor microcavities, in which photons are confined and strongly coupled to electronic excitations, leading to the creation of exciton-polaritons [139–141], bosonic quasiparticles that can display BEC signatures. Similarly, triplons have shown condensation for the first time in the antiferromagnetic $TlCuCl_3$ compound [142–144]. The quasiparticles density can be controlled by an external magnetic field, acting as a chemical potential, to cover the limit from a dilute to a strongly interacting bose gas. Nowadays, it is widely known that a large numbers of quantum antiferromagnets display a BEC [43, 44], on which we shall now focus.

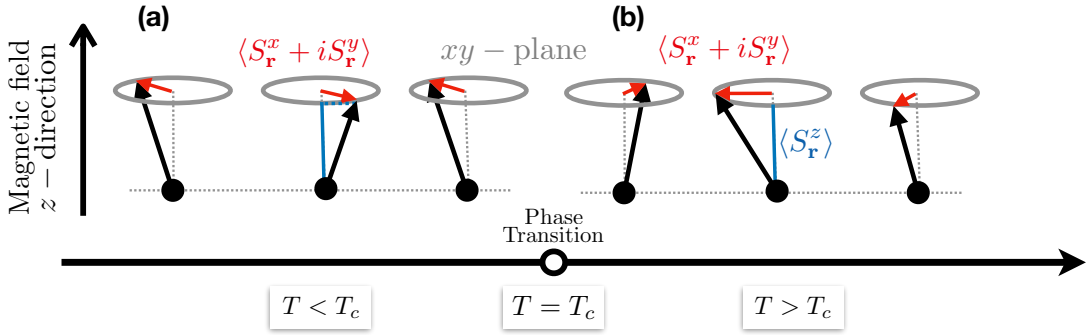

Figure A.5: Sketch of a quantum antiferromagnet with a U(1) symmetry and subject to an external magnetic field along the z direction. The system has a magnetization $m^z = \sum_{\mathbf{r}} \langle S^z_{\mathbf{r}}\rangle / \mathrm{N}$. **(a)** The system is antiferromagnetically ordered in the XY plane for $T < T_c$ and the spins component in the XY plane are ordered in an antiferromagnetic way. The order is characterized by a complex order parameter of Eq. (A.24). **(b)** The system is disordered with $T > T_c$ and the spins component in the XY plane is featureless with a random organization.

1. Equivalence between Bose-Einstein condensation and antiferromagnetic XY order

I want to establish the connection between the usual BEC properties that we just reviewed for bosonic degrees of freedom with what is happening at low temperature in some quantum antiferromagnets, described by spin degrees of freedom on a lattice. This section will mostly resume ideas from Refs. 43 and 44, and the next section will be dedicated to experimental examples that I will skip in the first place. It is actually straightforward to make the connection between spins and bosons through the Holstein–Primakoff [145] or Matsubara–Matsuda [146] transformations. For $S = 1/2$ degrees of freedom, a down spin maps to an empty site and an up spin to an occupied site by a boson. Unlike traditional bosons however, the maximum occupancy needs to be constrained to one, and the bosons thus qualify as "*hard-core*". In this case, the transformation simply reads,

$$S^+_j = b^\dagger_j, \quad \text{and } S^z_j = b^\dagger_j b_j - \frac{1}{2}, \tag{A.23}$$

which indeed verifies the usual spin and boson commutation relations, i.e., $[b_i, b^\dagger_j] = \delta_{ij}$. There are now two required conditions to have a system that could potentially display a BEC. The first one is a three-dimensional system for the phase transition to happen at finite temperature and the second is a U(1) symmetric system, since it is the symmetry being spontaneously broken for $T < T_c$ in a BEC. The last requirement is necessary but not sufficient. For instance, coupled XXZ chains in the ferromagnetic or antiferromagnetic Ising phases have a U(1) symmetry but it is not the one that is being spontaneously broken (see Fig. A.1 and associated discussions above). An extra requirement would be to have the ordered phase characterized by a complex order parameter, as the BEC one. This is the case of magnets with antiferromagnetic order in the XY plane,

$$m^{\mathrm{AF}} = \lim_{N\to+\infty} \frac{1}{N} \sum_{\mathbf{r}} \mathrm{e}^{i\mathbf{r}\cdot\mathbf{q}_{\mathrm{AF}}} \langle S^x_{\mathbf{r}} + iS^y_{\mathbf{r}}\rangle, \quad \text{with } \mathbf{q}_{\mathrm{AF}} = (\pi,\pi,\pi)\,, \tag{A.24}$$

—	**Boson language**	**Spin language**
	Particles density n	Magnetization m^z
	Chemical potential μ	Magnetic field H
	Superfluid density ρ_s	Transverse spin stiffness ρ_s
Order parameter	$\Psi_{\mathbf{q}=\mathbf{0}} = \sqrt{n_0}\mathrm{e}^{i\theta}$	$m^{\mathrm{AF}} = \lim_{N\to+\infty} \sum_{\mathbf{r}} \mathrm{e}^{i\mathbf{r}\cdot\mathbf{q}_{\mathrm{AF}}} \langle S^x_{\mathbf{r}} + iS^y_{\mathbf{r}}\rangle/N$
Kind of order	BEC	XY ordering

Table A.1: Translation dictionary of physical quantities from the boson to spin language and vice-versa. It uses notations introduced in the text.

which is zero for $T > T_c$ and non zero otherwise. A schematic representation of this XY order is shown in Fig. A.5. Below the critical temperature, the spins are antiferromagnetically ordered in the XY plane, which can be seen as a complex plane $(S^x_{\mathbf{r}}, S^y_{\mathbf{r}})$, with a randomly picked and locked value for the phase $\theta = \arg\left(m^{\mathrm{AF}}\right)$. To make the connection with the order parameter of the BEC in Eq. (A.21) plain, the condensed fraction is related to the modulus squared of the XY order, $n_0 = |m^{\mathrm{AF}}|^2$. Moreover, we show in Tab A.1 the correspondence of physical quantities in boson and spin language.

The simplest magnetic systems that can realize BEC are coupled XXZ chains which are individually in the XY phase (see Fig. A.1)[5]. More generally, one-dimensional U(1) spin systems which display a critical XY phase that can be described by Tomonaga-Luttinger liquid theory, will stabilize the quasi-long-range order to plain XY long-range order at finite temperature when coupled together in three dimensions [147–149]. Upon applying a sufficiently large magnetic field to close the singlet–triplet spin gap, this includes, for example, coupled spin-ladders and coupled $S = 1$ chains. Generically, these systems exhibit two quantum critical points $H_{c1,2}$, with some gapped phase below H_{c1}, a trivial ferromagnetic phase above H_{c2} (also gapped) and a gapless XY phase in between. As already discussed in the previous section, the one-dimensional Heisenberg $S = 1$ model displays an energy gap $\Delta_g \equiv H_{\mathrm{c1}}$ between its (singlet) ground state and its first (triplet) excited state. Subject to an external magnetic field $H \geq H_{\mathrm{c1}}$, the system becomes gapless and can be described as a Tomonaga-Luttinger liquid [150, 151]. When coupled, this leads to XY long-range order as observed in inelastic neutron scattering experiments on the $SrNi_2V_2O_8$ material [152]. Two-leg $S = 1/2$-ladder systems can be seen as two coupled spin chains with two different energy scales coupling neighboring spins: along the chains with J_{leg} and within the rungs with J_{rung}. The limit $J_{\mathrm{rung}} = 0$ carries the system to two independent single chains and the opposite one, $J_{\mathrm{leg}} = 0$, generates independent two spins (dimer) systems. In both cases, the presence of a small parameter makes possible analytical investigations, and one can show that weak and strong-coupling ladders are adiabatically connected and part of the same phase. They have a gapped energy spectrum for $J_{\mathrm{rung}}/J_{\mathrm{leg}} > 0$ [153, 154], whose value smoothly depends on the couplings ratio, from $\Delta_g = 0$ for $J_{\mathrm{rung}} = 0$ to $\Delta_g = J_{\mathrm{rung}}$ for $J_{\mathrm{leg}} = 0$. Analogously to the $S = 1$ chain, an external magnetic field $H \geq \Delta_g$ can close this gap and brings the system to the Tomonaga-Luttinger liquid class [155, 156].

[5] This is a valid statement except at the isotropic point $\Delta = 1$, $H = 0$ where the coupled chains will display Néel ordering with a spontaneous SU(2) symmetry breaking below T_c. This is different of the XY order and the BEC discussed here.

Furthermore, to make the equivalence between antiferromagnetic XY long-range order and BEC complete, it is important to point out that the temperature-driven transitions in both cases from the disordered to ordered phases with the spontaneous U(1) symmetry breaking belong to same universality class (known as 3D XY in three dimensions). Therefore, the critical behavior of all physical quantities around T_c happens with exactly the same exponents.

Lastly, after making the equivalence plain and introducing explicitly which kind of magnetic systems can display a BEC and under which conditions, I want to make a few more comments before moving to experimental examples. At zero temperature, and for a magnetic field $H > H_{c2}$, the system is fully polarized with all its spins pointing in the field direction. As the magnetic field strength is reduced, one, and then more spin flips will occur to eventually reach a zero magnetization. These spin flips are known as magnons, bosonic $S^z = -1$ quasiparticles. In the simplest $S = 1/2$ XXZ case (this can be easily extended to other systems), a single spin flip from the ferromagnetic state at $H = H_{c2}$ has a dispersion relation $\varepsilon(\mathbf{q}) = J(1 + \cos \mathbf{k})$ with a minimum at $\mathbf{q} = \mathbf{q}_{\mathrm{AF}} = (\pi, \pi, \pi)$. Around the antiferromagnetic wave-vector, it can be approximated by $\varepsilon(\mathbf{q} \to \mathbf{q}_{\mathrm{AF}}) \simeq J|\mathbf{q} - \mathbf{q}_{\mathrm{AF}}|^2/2$, which is the dispersion relation of a free particle with an effective mass $m = 1/J$. Since BEC can take place without interactions, we have just shown that (non-interacting) magnons can condense at $\mathbf{q} = \mathbf{q}_{\mathrm{AF}}$ and that the external magnetic field controls their density. A next and more realistic step that we will skip, would be to write an effective model for these quasiparticles to take into account their interactions as in Refs. 147 and 143. Another remark is that the knowledge of the quasiparticle dispersion relation close to the quantum critical point H_{c2} provides the value of the dynamical exponent $z = 2$ for the quantum phase transition between the ferromagnetic and XY ordered phases (also known as the superfluid/insulator transition [157])[6]. It is reasonable to believe that this value will actually stand for more than a single spin flip (i.e. in a small region around H_{c2}), as long as the magnons remain extremely diluted that we can neglect interactions. Finally, the spontaneous breaking of the continuous U(1) symmetry below T_c leads to gapless Nambu-Goldstone modes [158, 159] with a linear dispersion above the BEC ground state around the antiferromagnetic wave vector, i.e. $\varepsilon(\mathbf{q}) \sim v_s|\mathbf{q} - \mathbf{q}_{\mathrm{AF}}|$ with v_s the spin-wave velocity. These modes have been experimentally observed in the dimerized $S = 1/2$ $TlCuCl_3$ compound by inelastic neutron scattering experiments, see Refs. 160, 144, 161 and references therein.

2. Fingerprints of Bose-Einstein condensation in quantum antiferromagnets and selected examples

To evince that BEC in quantum antiferromagnets is not a remote phenomena, I show in the left-hand side of Fig. A.6 experimental measurements of the phase boundary $T_c(H)$ between the disordered and long-range ordered XY phases in several three-dimensional compounds. We notice that the maximum critical temperature is

[6] In a periodic system, the momentum $\mathbf{q}$ is defined within a Brillouin zone where its components are $q_i = 2n_i\pi/L_i$ with $n_i = 1, 2 \ldots L_i$ and L_i a linear size along a given direction i. Close to a transition, the only relevant length is the correlation length ξ, hence $\varepsilon(\mathbf{q}) = \mathbf{q}^2 \sim \xi^{-2}$. Moreover at a quantum phase transition, the characteristic energy Δ scales as $\Delta \sim \xi^{-z}$, suggesting that $z = 2$ if one believes that the dispersion relation is indeed the characteristic energy close to H_{c2}.

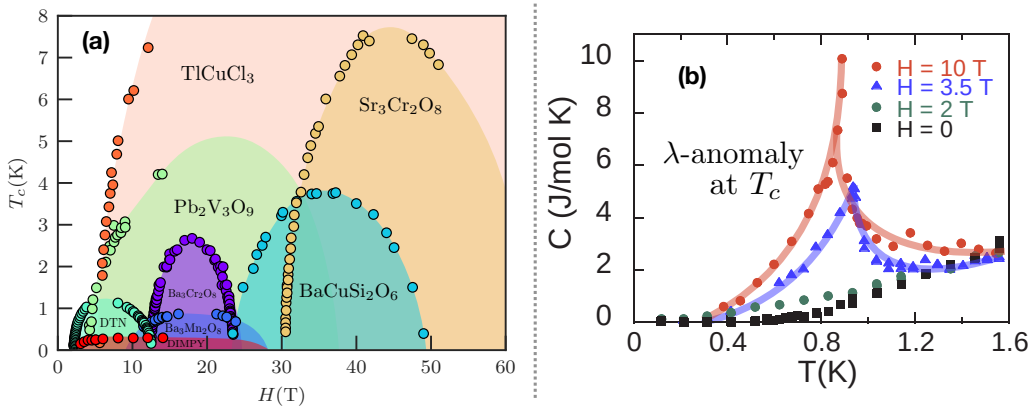

Figure A.6: The left panel **(a)** shows the phase diagram $T_c(H)$ of numerous magnetic Mott insulators which display a Bose-Einstein condensation (inside the shaded regions), including $BaCuSi_2O_6$ [162], $NiCl_2$-4SC$(NH_2)_2$ (DTN) [163], $Ba_3Mn_2O_8$ [164], $TlCuCl_3$ [165], $(Hpip)_2CuBr_4$ [166, 167], $Pb_2V_3O_9$ [168], $Sr_2Cr_3O_8$ [169], $Ba_3Cr_2O_8$ [170] and $(C_7H_{10}N)_2CuBr_4$ (DIMPY) [171]. This figure has been reproduced from Ref. 44 and the data have been captured from various experimental measurements in the above references. The right hand side figure **(b)** shows experimental measurements of the specific heat versus temperature for various magnetic field values in the $S = 1$ $NiCl_2$-4SC$(NH_2)_2$ (DTN) compound. It displays the characteristic λ-anomaly at the transition for $H = 3.5$ T and $H = 10$ T, but not for the two other fields which are in the gapped phase below the first critical field H_{c1}. This figure has been adapted from Ref. 163.

large compared to what is required to obtain a condensate in cold atoms experiments ($T_c \sim \mu$K), about six orders of magnitude larger in fact. The downside is that these experimental candidates require a very large magnetic field to close the spin gap and get beyond H_{c1}, and an ever larger magnetic field to be able to map the whole phase boundary, experimentally inaccessible for a few of them. Nevertheless, they allow the experimental study of the critical properties of the transition, with the advantage that these materials are in the thermodynamic limit and have a high degree of spatial homogeneity due to the crystalline lattice. On the contrary, cold atoms experiments are carried out with only a few thousands of them, and the confining trap potential makes it difficult to obtain a high degree of homogeneity. Yet, this comparison is to be contrasted, because spin compounds are far from being ideal systems as they have additional interactions (crystalline anisotropies, dipolar interactions, spin-orbit coupling...) that might weakly break the required U(1) symmetry and modify the physics in the vicinity of the transition. Although such additional terms should be taken into account to rigorously describe the system, especially at very low temperature where these effects might become prominent, most systems provide a clean "magnetic field/temperature" window where physical quantities and critical properties can be neatly measured and studied. Also, the orientation of the external magnetic field is in some cases crucial and it is tricky to ensure that it does not unduly break the U(1) symmetry of the system (other than spontaneously below the critical temperature). A precursor for the phase transition is the cusp observed in the specific heat at the critical temperature, which can be used to map the phase boundary $T_c(H)$ between disordered and ordered phases. Experimental measurements on the

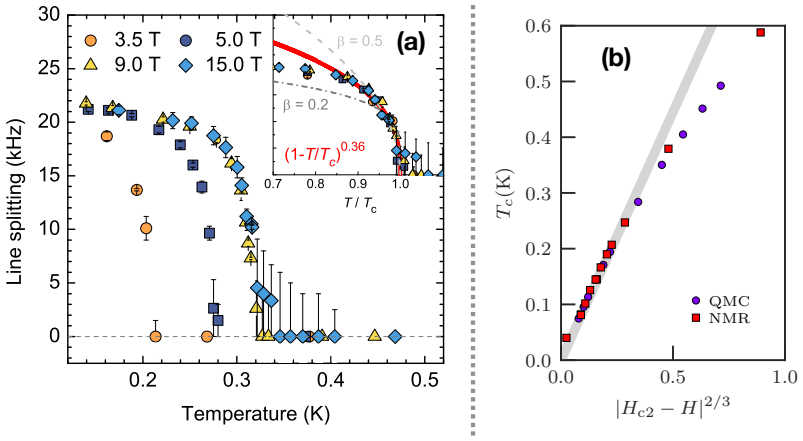

Figure A.7: The left panel **(a)** shows the value of the line splitting in the ^{14}N NMR spectra of the $(C_7H_{10}N)_2CuBr_4$ (DIMPY) compound as a function of the temperature for different magnetic fields value. It is proportional to the modulus of the order parameter m^{AF} which allows for the checking of the critical behavior $|m^{\mathrm{AF}}| \sim |1 - T/T_c|^{\beta}$ with β the order parameter exponent. The figure is from Ref. 173. The right hand side panel **(b)** shows the linear behavior (grey line) of the critical temperature versus the rescaled magnetic field $|H_{c2} - H|^{2/3}$ close to the second critical field H_{c2}, for the coupled $S = 1$ chains $NiCl_2$-$4SC(NH_2)_2$ (DTN) material. The red square symbols are experimental data obtained by NMR measurements and the purple dots are obtained by quantum Monte Carlo simulations on the spin model describing this material. The data have been taken from Ref. 174.

coupled $S = 1$ chains compound $NiCl_2$-$4SC(NH_2)_2$ (DTN) are reported in the right panel of Fig. A.6, with a striking λ-anomaly at the transition for $H = 3.5$ T and $H = 10$ T, as observed in liquid ^{4}He [172].

One experimental fingerprint that the transition observed at T_c belongs to the same universality class as the BEC one comes from the critical behavior of the order parameter. The left hand side panel of Fig. A.7 shows the value of the line splitting in the ^{14}N NMR spectra of the antiferromagnetic spin ladder compound $(C_7H_{10}N)_2CuBr_4$ (DIMPY) as a function of the temperature for various magnetic field values [173]. This is directly proportional to the magnetization in the XY plane, or in other words, to the modulus of the complex order parameter m^{AF}[7]. Close to the transition, its critical behavior is governed by the order parameter exponent β,

$$\text{Line splitting} \propto \quad |m^{\mathrm{AF}}| \sim |1 - T/T_c|^{\beta}\,, \tag{A.25}$$

whose value is $\beta = 0.3486(1)$ for the 3D XY universality class [175]. The rescaling of the experimental data with respect to T_c gives the inset of Fig. A.7 (a), and the best fit results in an exponent $\beta = 0.36$, very close to the one expected for this transition.

Another experimental checking is the critical behavior of T_c in the vicinity of the quantum critical point H_{c2}. This corresponds, as already discussed, to the limit of extremely diluted condensed bosonic quasiparticles with a quadratic dispersion relation which gives a dynamical exponent $z = 2$. Moreover, in dimension $D > 2$,

[7] Although m^{AF} is complex, only its modulus is accessible in most, if not all, cases (experimentally and numerically). Thereby, I will often abusively refer to $|m^{\mathrm{AF}}|$ as m^{AF} in the following.

the magnetization (≡ particles density) scales linearly with the magnetic field, i.e. $1 - m^z \propto (H_{c2} - H)$ [147, 176–178]. Close to a quantum critical point, the scaling relation generically reads,

$$T_c \sim |H_{c2} - H|^{\phi}, \tag{A.26}$$

with ϕ a critical exponent that we can actually relates to $\phi = z/D$. Indeed, going back to the calculations of the density versus the critical temperature for non interacting bosons, we found that $T_c \sim n^{z/D}$ in Eq. (A.18). I plot in the right panel of Fig. A.7 the scaling of the critical temperature for the coupled $S = 1$ chains $NiCl_2$-$4SC(NH_2)_2$ (DTN) compound in the vicinity of the upper critical field H_{c2}. The data are from Ref. 174 and include experimental NMR measurements and quantum Monte Carlo simulations on the underlying model describing the material; overall they are in very good agreement with the expected scaling $\phi = 2/3$. To be fully consistent, it is important to mention that the upper critical dimension for the XY transition is $D_c = 4$. Above D_c, the critical exponents of the theory describing the system become the same as for the mean-field treatment for this theory. Around the quantum critical point H_{c2}, the effective dimension is $D + z = 5 > D_c$ and thus, the mean field exponents apply. This is why the magnetization is proportional to the magnetic field for instance. This also explains why the hyperscaling relation $z\nu = \phi$ with ν the correlation length exponent does not stand anymore[8].

III. Numerical methods

After introducing the quantum magnetic systems I am interested in, I now want to present numerical methods to investigate them. First, I will focus on the Matrix Product States formalism for one-dimensional systems. It is an ansatz to represent an intractable wave function in practice — exponentially large with the system size N — as a more practical product of N matrices (or more generally tensors). Every one of them will be associated to a degree of freedom on the lattice and their elements will hold information as would do the global wave function, but with some very reasonable approximations to make the description tractable. I will then introduce quantum Monte Carlo in its stochastic series expansion formulation whose idea is to expand the partition function $\mathcal{Z} = \mathrm{Tr}\ \mathrm{e}^{-\beta\mathcal{H}}$ as the Taylor expansion of the exponential in powers of the inverse temperature $\beta = 1/T$. There is plethora of complete reviews on the two subjects from which I took great inspiration, Refs. 179, 115, 45 and 46 for Matrix Product States and Refs. 180 and 181 regarding quantum Monte Carlo, including references therein for both methods.

[8] At a quantum phase transition, we can define a characteristic energy scale $\Delta \sim |\mathrm{H}_{c2} - H_c|^{z\nu}$ and also for $D \geq 3$, we have the scaling of the critical temperature $T_c \sim |H_{c2} - H_c|^{\phi}$. The critical temperature T_c is also a characteristic energy scale, leading to the hyperscaling relation $\phi = z\nu$.

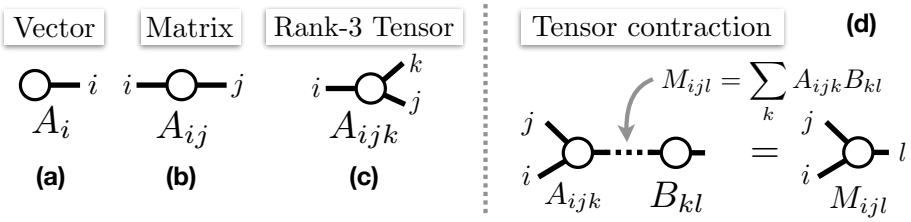

Figure A.8: Graphical notation for tensors as a closed shape, a circle in this case. The panels **(a)**, **(b)** and **(c)** respectively shows the graphical representation of rank-1 (vector), rank-2 (matrix) and rank-3 tensors. The elements of a rank-N tensor are labelled by N indices and each index of the tensor is represented by a line emanating from it. The panel **(d)** shows the graphical representation of the contraction operation which generalizes standard vector-vector, matrix-vector, matrix-matrix multiplications for higher rank tensors. To indicate that pairs of indices are shared amongst two tensors and that they can be contracted, they are joined together by a line.

1. Matrix Product States

A state describing a quantum system comprised of N degrees of freedom is usually written as a vector $|\Psi\rangle$ in a given work basis $\{|\sigma\rangle\} = \{|\sigma_1\sigma_2\cdots\sigma_N\rangle\}$,

$$|\Psi\rangle = \sum_{\sigma_1}\sum_{\sigma_2}\cdots\sum_{\sigma_N} c_{\sigma_1\sigma_1\cdots\sigma_N}|\sigma_1\sigma_2\cdots\sigma_N\rangle, \tag{A.27}$$

where σ_μ can take d different values, each representing a state of the degree of freedom, e.g. for a spin-1/2 chain $\sigma_\mu = \uparrow, \downarrow$ and $d = 2$, which leads to a 2^N components wavefunction to describe the system. We will restrict ourselves to one-dimensional lattice[9] models with degrees of freedom living on the vertices, in such a way that σ_μ and $\sigma_{\mu+1}$ are neighbors in real space.

A rank-N tensor is a mathematical object holding data whose elements are labelled by $i, j, k, \ldots$ indices (N in total), e.g. $A_{ijk\ldots}$ and its total number of elements is the product of the maximum index value taken by each one of the indices, i.e., $N_{\text{elts}} = i_{\max} j_{\max} k_{\max} \ldots$. It is the generalization of vectors and matrices, which are respectively rank-1 and 2 tensors. More advanced, tensor networks are made of multiple "connected" tensors and traditional tensor notation quickly becomes unwieldy: it is helpful to use a graphical notation [183]. The basic graphical notation for a tensor is to represent it as a closed shape such as a square or a circle, although there is no standard convention and it is sometimes useful to use different shapes to represent different kind of tensors. Each index of the tensor is represented by a line emanating from it, with as many lines as indices. In Fig. A.8 (a,b,c) I show the graphical representation of rank-1 (vector), 2 (matrix) and 3 tensors. The contraction of two tensors is the mathematical operation that generalizes the better

[9] Actually, Matrix Product States are also used to simulate two-dimensional systems by representing the 2D lattice as a one-dimensional path at the price of introducing long-range interactions, see Ref. 182. However, as we shall discuss, all the benefits of one-dimensional systems with local interactions resulting from the area law are lost, making simulations very difficult and demanding. Generalization of MPS in two-dimensions are known as Projected Entangled Pair States (PEPS), but are definitely not as efficient as MPS, although a lot of work has been dedicated to them in the past few years. See Ref. 46 for an introduction to PEPS.

known matrix-vector or matrix-matrix multiplications, e.g. $\sum_j A_{ij}B_j = C_i$ and $\sum_k A_{ik}B_{kj} = M_{ij}$. Basically, the elements of the two tensors that are labelled by the same indices are first multiplied element-wise and then summed. Graphically, to indicate that pairs of tensor indices are contracted they are joined together by a line, as in Fig. A.8 (d). This is an example of a contraction between a rank-3 tensor and a matrix sharing a common index and which results in a rank-3 tensor, i.e. the number of unpaired lines left over. If no index lines remain unpaired the result is a scalar. We will usually drop the index labelling in the graphical notation since they can be distinguished by their location in the diagram.

Wave functions and Hamiltonians as tensor networks Ultimately, we want to describe a quantum system as a collection of tensors, one for every degree of freedom. It seems natural that the tensors will share indices at some point since the degrees of freedom σ_μ are coupled and entangled. Concretely, the vector Ψ_i with $i = 1, 2 \dots d^N$ describing a quantum system can be reshaped into a rank-N tensor $\Psi_{\sigma_1,\sigma_2\dots\sigma_N}$ where each index σ_μ can take d values without any loss of information since it has exactly the same number of elements, see Fig. A.9 (a). This way of representing a state is actually more natural — but probably less practical — since setting a value of each of the index defines a basis state and provides its weight $c_{\sigma_1\sigma_1\cdots\sigma_N}$ in the wave function. This object is still too big to be dealt with and the idea is to crack it into smaller pieces. A well-suited mathematical operation to do that is the singular-value decomposition (SVD), a generalization of the eigendecomposition of a positive semi-definite normal matrix to any rectangular matrix M,

$$M_{ij} = U_{ik}\Lambda_{kk}V^\dagger_{kj}, \qquad \text{with } U^\dagger U = V^\dagger V = I, \tag{A.28}$$

with M of size $m \times n$, Λ a diagonal square matrix of linear size $\min(m, n)$ holding the singular values and U, V holding the left-singular and right-singular vectors. However, this operation applies on for a matrix, not for a tensor. Though it might be tedious, this is not a problem in practice: a tensor can be mapped to a matrix by merging indices and vice-versa by splitting an index. This is just a different way to label the same elements of the object by more or less indices. The steps to crack the rank-N tensor are explained in Fig. A.9 and provide at the end a tensor network, also known as a Matrix Product State (MPS),

$$|\Psi\rangle = \sum_{\sigma_1}\sum_{\sigma_2}\cdots\sum_{\sigma_N} \underbrace{A^{\sigma_1}_{a_1} A^{\sigma_2}_{a_1 a_2} \cdots A^{\sigma_N}_{a_{N-1}}}_{c_{\sigma_1\sigma_2\cdots\sigma_N}} |\sigma_1\sigma_2\cdots\sigma_N\rangle, \tag{A.29}$$

where each tensor $A^{\sigma_\mu}_{a_{\mu-1},a_\mu}$ is associated to a degree of freedom σ_μ with a_μ a virtual index shared between neighboring tensors. Note that the contraction of all the A tensors along their common virtual indices would give back the object rank-N tensor of Fig. A.9 (a). Obviously, at this point there is no gain and it is still intractable to rewrite the wave function within a tensor network formulation compared to the standard vector form. In practice, we do not want to *rewrite* the wave function differently but directly start from the MPS formulation. For instance, the cumbersome process of finding the ground state of a given Hamiltonian by optimizing its coefficients $c_{\sigma_1\sigma_2\cdots\sigma_N}$ through a variational principle translates to optimizing the tensors elements and can be carried tensor after tensor. We will see that this can be done *very* efficiently using the Density Matrix Renormalization Group algorithm, with some control parameter in the number of elements to optimize by imposing a maximum D

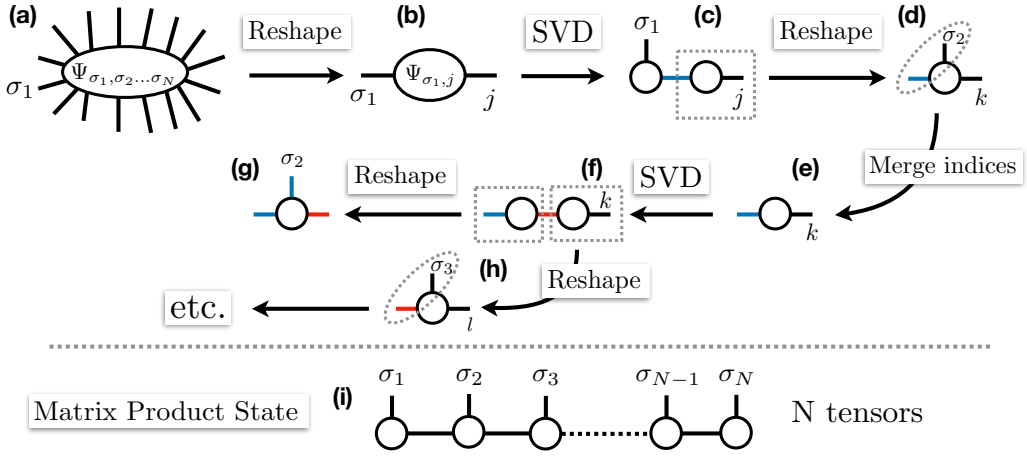

Figure A.9: The steps **(a)** to **(h)** explain the procedure to crack down the rank-N tensor of panel **(a)** into N tensors, one for each degree of freedom σ_μ of the system. The tensor is first reshaped into a matrix in **(b)** isolating σ_1 from the rest where $j = 1, 2 \dots d^{N-1}$. We then perform in **(c)** a singular value decomposition (SVD) on the matrix to factorize the matrix, the singular values have been absorbed in $V^\dagger$, see Eq. (A.28) for notations and surrounding discussion. Note that this operation has introduced a virtual index (in blue) which does not hold a physical degree of freedom. We focus on the right-hand side matrix and reshape it in **(d)** to a rank-3 tensor by isolating the degree of freedom σ_2 from the index j where $k = 1, 2 \dots d^{N-2}$. In **e**, the indices σ_2 and the virtual index outgoing from the previous SVD are merged together to obtain a matrix. Again, a SVD is performed on this matrix in **(f)** with the singular values absorbed in the right-hand side matrix. The left-hand side matrix is reshaped into a rank-3 tensor in **g** by splitting the blue index to explicitly show the index σ_2 that was absorbed earlier on for the purpose of the SVD. The right-hand side matrix of step **(f)** is reshaped in **(h)**, isolating the index σ_3, with $l = 1, 2 \dots d^{N-3}$. The following operations are the same as the previous ones, starting from step **(d)**. In the end, we get the tensor network shown in panel **(i)**, which represents a Matrix Product State (MPS) with N tensors, one for each degree of freedom. Neighboring tensors share a common virtual index resulting from the successive SVD performed.

value for the virtual indices. The total number of elements in the MPS formulation is ND^2d, to be compared with the exponentially large number of coefficients d^N of the traditional wave function. A variational principle is based on some Hamiltonian describing the system for which we want to find the ground state. Similarly to a MPS, we can write a Hamiltonian matrix in a local form, known as a Matrix Product Operator (MPO) [184–187],

$$\mathcal{H} = \sum_{\sigma_1,\sigma_1'} \cdots \sum_{\sigma_N,\sigma_N'} \underbrace{W_{b_1}^{\sigma_1\sigma_1'} W_{b_1 b_2}^{\sigma_2\sigma_2'} \cdots W_{b_{N-1}}^{\sigma_N\sigma_N'}}_{=\langle\sigma_1\sigma_2\cdots\sigma_N|\mathcal{H}|\sigma_1'\sigma_2'\cdots\sigma_N'\rangle} |\sigma_1\sigma_2\cdots\sigma_N\rangle\langle\sigma_1'\sigma_2'\cdots\sigma_N'|, \tag{A.30}$$

where each tensor $W[\sigma_\mu] \equiv W_{b_{\mu-1},b_\mu}^{\sigma_\mu\sigma_\mu'}$ is associated to a degree of freedom σ_μ with b_μ a virtual index shared between neighboring tensors. The fact that interactions remain localized around neighboring degrees of freedom and are generally two-body make it possible for most Hamiltonian to encode exactly, quite easily, and surprisingly,

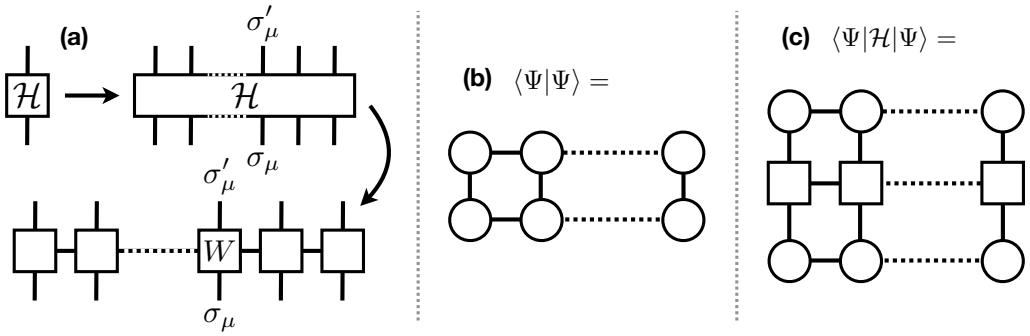

Figure A.10: **(a)** Matrix Product Operator formulation of the Hamiltonian matrix $\mathcal{H}$. Each degree of freedom σ_μ is associated to a rank-4 tensor W. Surprisingly, the tensors W take a very simple, small and compact form that can be written exactly in most cases, see text for discussion. **(b)** Overlap between the wave function $|\Psi\rangle$ and its conjugate transpose in the MPS formulation. To obtain the conjugate transpose of a MPS, we take the complex conjugate of each entry. The result of the contraction of all the tensors is naturally a scalar. **(c)** Expectation value of the operator $\mathcal{H}$ in the MPS/MPO formulation. The tensors have to be contracted altogether to get the resulting scalar.

in a compact form the tensors $W[\sigma_\mu]$. This is to be stressed since in practice, performing the steps of Fig. A.10 (a) to go from the standard matrix form to an MPO is impossible because the Hamiltonian $\mathcal{H}$ is exponentially large with the system size. Considering our favorite one-dimensional XXZ model, the tensors $W[\sigma_\mu]$ read,

$$W[\sigma_\mu] = \begin{bmatrix} I & 0 & 0 & 0 & 0 \\ S^+ & 0 & 0 & 0 & 0 \\ S^- & 0 & 0 & 0 & 0 \\ S^z & 0 & 0 & 0 & 0 \\ -HS^z & (J/2)S^- & (J/2)S^+ & \Delta J S^z & I \end{bmatrix}, \tag{A.31}$$

where each of its element is an operator acting on the degree of freedom σ_μ[10]. Consequently, it is easy in practice to implement the MPO of the XXZ model which consists of rank-4 tensors with a total number of elements equal to 5^2d^2. Knowing how to represent a wave function and an operator in this tensor network representation, the next step is to compute expectation values. This could not be more straightforward as shown in Fig. A.10 (b,c), the task simply consists of tensor contractions. The only caution is about the order in which the tensors are being contracted because we do not want to end up with intermediate tensors that would be far too large to be handled — remember that the number of elements in a tensor is the product of the size of all its indices. Theoretically, we could make the contraction in any order and the resulting scalar would be the same, but in practice we want to make it efficient. The best way to achieve this is to start on one end of the tensor network and contract the first column of tensors, and we contract this new tensor with the ones next to it, and so on, like the fasten of a zipper.

The Density Matrix Renormalization Group algorithm I now want to briefly explain the idea behind the Density Matrix Renormalization Group algorithm to

[10] The rank-3 tensors for the first and last sites are respectively given by $W[\sigma_1] = [0\ 0\ 0\ 0\ 1]^{\mathrm{T}} W[\sigma_\mu]$ and $W[\sigma_N] = W[\sigma_\mu][1\ 0\ 0\ 0\ 0]$. with $W[\sigma_\mu]$ from Eq. (A.31).

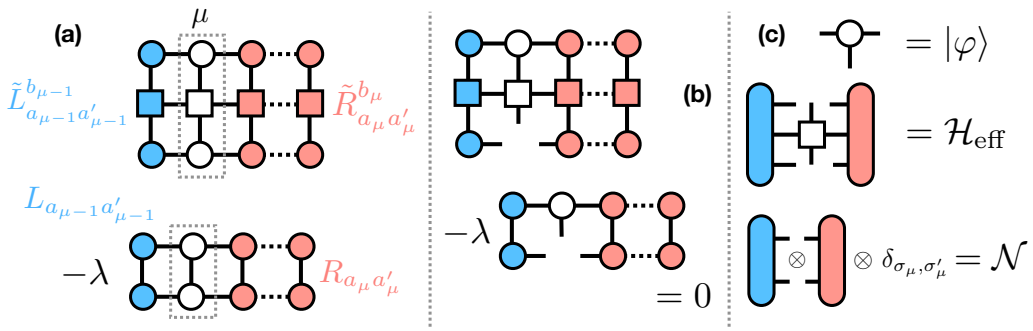

Figure A.11: **(a)** In the Density Matrix Renormalization Group (DMRG) algorithm, we optimize the elements of each tensor independently, focusing on one (degree of freedom μ) and keeping the others on its left (in blue) and right (in red) constant. These left and right tensors, once contracted altogether provide an effective environment (tensors L, $\tilde{L}$, R and $\tilde{R}$) in which to carry the optimization problem. **(b)** Taking the extremum of Eq. (A.32) with respect to the tensor $(A^{\sigma_\mu}_{a_{\mu-1}a_\mu})^*$ gives rise to dangling indices in the tensor network. **(c)** Solving the equation of the previous panel can be recast to a generalized eigenvalue problem $\mathcal{H}_{\text{eff}}|\varphi\rangle - \lambda\mathcal{N}|\varphi\rangle = 0$ by reshaping the different tensors to matrices and vectors. The goal is now to find the lowest eigenstate $|\varphi_0\rangle$ that will be reshaped back to a rank-3 tensor to replace the old $A^{\sigma_\mu}_{a_{\mu-1}a_\mu}$ tensor. This optimization procedure is repeated back and forth for each tensor until convergence (of the ground-state energy for example).

obtain reliably the ground state of a one-dimensional system up to several hundred degrees of freedom. Unlike what the name of the algorithm suggests we have never introduced any density matrix in this section. This is because the first formulation of the algorithm was done using a density matrix by White in early nineties [47, 48] whereas tensor networks in the context of condensed matter have been developed about ten years later. We thus present here the Density Matrix Renormalization Group (DMRG) in the age of Matrix Product States[11]. The problem we want to solve comes down to extremizing

$$\langle\Psi|\mathcal{H}|\Psi\rangle - \lambda\langle\Psi|\Psi\rangle, \tag{A.32}$$

with λ a Lagrangian multiplier to ensure that $|\Psi\rangle$ is normalized. As already emphasized, this is impossible in practice in a standard quantum mechanics formulation, because the number of coefficients in $|\Psi\rangle$ is exponentially large with the system size. In the tensor network formulation, we will solve this problem by optimizing the coefficients tensor by tensor, keeping the others constant. Let us optimize the tensor $A^{\sigma_\mu}_{a_{\mu-1}a_\mu}$ associated to the degree of freedom σ_μ that we keep explicitly written in the two terms of the expression (A.32) to extremize,

$$\langle\Psi|\Psi\rangle = L_{a_{\mu-1}a'_{\mu-1}} \left(A^{\sigma_\mu}_{a_{\mu-1}a_\mu}\right)^* A^{\sigma_\mu}_{a_{\mu-1}a_\mu} R_{a_\mu a'_\mu}, \tag{A.33}$$

and

$$\langle\Psi|\mathcal{H}|\Psi\rangle = \tilde{L}^{b_{\mu-1}}_{a_{\mu-1}a'_{\mu-1}} \left(A^{\sigma_\mu}_{a_{\mu-1}a_\mu}\right)^* W^{\sigma_\mu\sigma'_\mu}_{b_{\mu-1}b_\mu} A^{\sigma_\mu}_{a_{\mu-1}a_\mu} \tilde{R}^{b_\mu}_{a_\mu a'_\mu}, \tag{A.34}$$

[11] This is actually the title of the review 45 by U. Schollwöck that I heartily recommend.

where the L, $\tilde{L}$, R and $\tilde{R}$ are the contractions of all the tensors to the left (L) and to the right (R) of the degree of freedom σ_μ, see Fig. A.11 (a). We have also implicitly assumed the summation over all the indices to lighten writing. Taking the extremum of Eq. (A.32) with respect to $(A^{\sigma_\mu}_{a_{\mu-1}a_\mu})^*$,

$$\frac{\partial}{\partial (A^{\sigma_\mu}_{a_{\mu-1}a_\mu})^*}\Big[\langle\Psi|\mathcal{H}|\Psi\rangle - \lambda\langle\Psi|\Psi\rangle\Big] = 0, \tag{A.35}$$

gives rise to the tensor network of Fig. A.11 (b) with dangling indices because of the derivative with respect to the tensor $(A^{\sigma_\mu}_{a_{\mu-1}a_\mu})^*$. From this point, the problem can be recast to a generalized eigenvalue problem as shown in Fig. A.11 (c) where we have isolated each element,

$$\mathcal{H}_{\text{eff}}|\varphi\rangle - \lambda\mathcal{N}|\varphi\rangle = 0. \tag{A.36}$$

Solving this equation for the lowest eigenvalue λ_0 gives the ground state $|\varphi_0\rangle$ of the effective Hamiltonian, which can be reshaped to a rank-3 tensor $A^{\sigma_\mu}_{a_{\mu-1}a_\mu}$ and inserted back into the tensor network. The matrices $\mathcal{H}_{\text{eff}}$ and $\mathcal{N}$ are hermitian and of linear size dD^2. It is in general too large for an exact diagonalization, but since we are interested in finding the lowest energy state, we can use iterative Lanczos or Jacobi-Davidson algorithms. The optimization scheme is carried by sweeping from left to right for each tensor and then right to left, and so on until convergence (of the ground-state energy for instance). I want to make a few general remarks on the algorithm that I presented in its most simple form:

- Solving numerically a generalized eigenvalue problem is quite demanding. Fortunately, we can ensure that the MPS is left-normalized up to site $\mu-1$ and right-normalized from site $\mu+1$ onwards, i.e. the blue and red tensors at the bottom of Fig. A.11 (c) are identity matrices, which implies that $\mathcal{N} = I$. With this condition, the problem reduces to a simpler eigenvalue equation $\mathcal{H}_{\text{eff}}|\varphi\rangle - \lambda|\varphi\rangle = 0$.

- Since the DMRG optimizing scheme is local, one might wonder if we wont't get stuck into local minima or if we are guaranteed to find the global minimum, i.e. the ground state in its MPS representation. As for any optimization algorithm, there is no such guarantee but this can be easily checked by computing the variance $\langle\mathcal{H}^2\rangle - \langle\mathcal{H}\rangle^2$ which should be zero for an eigenstate of the Hamiltonian — not necessarily its ground state, but chances that we would get stuck in an arbitrary eigenstate are small. In practice, we do not locally update one tensor at a time but two next to each others to whittle convergence issues. Another helper is to encode the symmetries of the Hamiltonian within MPS in order to have a block-diagonal structure [188–190]. It ensures that the state will have the good quantum numbers and this will also speed up calculations.

Why is the MPS representation efficient? The most recurrent operations when dealing with MPS are contractions and SVD. For example, contract two neighboring tensors in a MPS, $K^{\sigma_\mu\sigma_{\mu+1}}_{a_{\mu-1}a_{\mu+1}} = \sum_{a_\mu} A^{\sigma_\mu}_{a_{\mu-1}a_\mu} A^{\sigma_\mu+1}_{a_\mu a_{\mu+1}}$, on which we perform an arbitrary operation that could not have been performed on both tensors independently. Once the task is done, we want to get back to the local form with one tensor for each degree of freedom σ_μ and $\sigma_{\mu+1}$. Hence, we perform a SVD by first reshaping K into a $dD \times dD$ matrix. The factorization leads to $K = U(\Lambda V^\dagger)$ with Λ of size

$dD \times dD$ holding the singular values. The matrices U and $(\Lambda V^\dagger)$ are then reshaped back to tensors with a new common virtual index of dimension dD compared to before when it was of dimension D only. It was not obvious up to now, but SVD are making the resulting factorized tensors grow, and that needs to be controlled. The singular values are real positive numbers and by keeping only the D largest ones, $\tilde{K} = U\tilde{\Lambda}V^\dagger$ is the best approximation of the initial K matrix which minimizes the Frobenius norm of the difference between $\tilde{K}$ and K, with $\tilde{K}$ truncated and of dimension $D \times D$. I want to explain in a few words why the MPS representation of a one-dimensional ground state with a finite D value is actually so accurate, not to say exact. This understanding comes from the physical meaning of the singular values $\lambda_i \in \Lambda$ emerging when performing a SVD between two neighboring sites μ and $\mu+1$, cutting the systems in two parts A and B. The rescaled singular values $\tilde{\lambda}_i = \lambda_i^2 / \sum_i^D \lambda_i^2$ correspond to the entanglement spectrum and govern the degree of entanglement between parts A and B of size L_A and L_B through the entanglement entropy, $S_{\text{vN}}(N_{A,B}) = -\sum_i^D \tilde{\lambda}_i \ln \tilde{\lambda}_i$. As a function of the system size, one might naively expect D to scale exponentially to retain a high accuracy. However, as mentioned before, the area law states that the entanglement entropy of the ground state of a local, gapped and one-dimensional Hamiltonian does not depend on the subsystem size $N_{A,B}$ but is constant $S_{\text{vN}}(N_{A,B}) \sim \text{cst}$ [113,117–119,191]. This implies that there is only a finite number of $\tilde{\lambda}_i$ that will actually contribute to an accurate description of the ground state, independently of the system size, hence totally justifying the truncation. The entanglement entropy of the ground state of a local one-dimensional *critical* Hamiltonian will not be constant but grows logarithmically with the subsystem size $S_{\text{vN}}(N_{A,B}) \sim \ln N_{A,B}$, keeping the description tractable and accurate up to relatively large systems.

In the following, all presented works including numerical Matrix Product States simulations are based on the ITensor library [192].

2. Quantum Monte Carlo

The stochastic series expansion formulation of the quantum Monte Carlo (QMC) algorithm is based on the Taylor expansion of the partition function in powers of the inverse temperature $\beta = 1/T$ [49,50],

$$\mathcal{Z} = \text{Tr}\, \mathrm{e}^{-\beta\mathcal{H}} = \sum_{n=0}^{\infty} \frac{(-\beta)^n}{n!} \text{Tr}\, \mathcal{H}^n = \sum_{\{|\sigma\rangle\}} \sum_{n=0}^{\infty} \frac{(-\beta)^n}{n!} \langle\sigma|\mathcal{H}^n|\sigma\rangle, \tag{A.37}$$

with $\mathcal{H}$ the Hamiltonian describing the system and with the trace expressed in the work basis $\{|\sigma\rangle\} = \{|\sigma_1\sigma_2\cdots\sigma_N\rangle\}$ in the second term. The powers of $\mathcal{H}$ can be rewritten as all possible products of all the terms in the Hamiltonian. To provide an example and without loss of generality, consider a pairwise interaction between degrees of freedom at positions $b = [i,j]$ described by $\mathcal{H}(b)$. The total Hamiltonian reads,

$$\mathcal{H} = \sum_b \mathcal{H}(b), \quad \text{with } \mathcal{H}(b) = \sum_{\text{terms } a} \mathcal{H}(a,b). \tag{A.38}$$

For a spin system described by our favorite XXZ Hamilotnian, $a = 1$ can label the diagonal interaction $\mathcal{H}(1,b) = J\Delta S_i^z S_j^z - H(S_i^z + S_j^z)$ and $a = 2,3$ the off-diagonal

ones $\mathcal{H}(2,b) = \frac{J}{2} S_i^+ S_j^-$ and $\mathcal{H}(3,b) = \frac{J}{2} S_i^- S_j^+$. In this formulation, at a given power n of the Hamiltonian in the Taylor expansion emerges products of n terms that we readily represent by a sequence S_n,

$$\mathcal{Z} = \sum_{\{|\sigma\rangle\}} \sum_{n=0}^{\infty} \sum_{\{S_n\}} \frac{(-\beta)^n}{n!} \langle\sigma| \prod_{p=0}^{n} \mathcal{H}(a,b) |\sigma\rangle, \tag{A.39}$$

where we have introduced the position p of the term $\mathcal{H}_p(a,b)$ in the sequence S_n. For a given sequence, the indices a and b are redundant with p but it will be useful in the following to have them explicitly written. Note the sum over all possible sequences in the partition function. In the Taylor expansion, the sum over n runs up to infinity and leads to infinitely large sequences S_n of operators, which cannot be numerically handled. Since we simulate finite size systems at finite temperature, it is reasonable to think that only sequences of finite size n will give significative contributions to the partition function[12]. Therefore, we impose a cutoff M for the maximum value of n, such that configurations labelled with $n > M$ are negligible. Without going into the details, its optimal value can be determined dynamically during the thermalization process. For practical reasons, sequences $n < M$ will be artificially enlarged by adding $M - n$ identity operators into it. There are $\binom{M}{M-n} = \frac{M!}{(M-n)!n!}$ different ways to add these identity operators to a sequence of size n. When this is included into the definition of the partition function to avoid multiple counting of a same sequence,

$$\mathcal{Z} = \sum_{\{|\sigma\rangle\}} \sum_{\{S_M\}} \frac{(-\beta)^n (M-n)!}{M!} \langle\sigma| \prod_{p=0}^{M} \mathcal{H}_p(a,b) |\sigma\rangle, \tag{A.40}$$

with n the number of non-identity operators in the sequence. The identity terms are now labelled by $a = 0$, furthermore, an identity term does not act on a particular pair of sites b, which will be referred in this case as $b = 0$. This formulation of the partition function clarifies what is a Monte Carlo configuration: it is defined by a basis state $|\sigma\rangle$ and a sequence of operators S_M with a weight given by,

$$W(\{|\sigma\rangle, S_M\}) = \frac{(-\beta)^n (M-n)!}{M!} \langle\sigma| \prod_{p=0}^{M} \mathcal{H}_p(a,b) |\sigma\rangle, \tag{A.41}$$

which is directly related to the Boltzmann probability associated to a given configuration, $\mathcal{P}(\{|\sigma\rangle, S_M\}) = W(\{|\sigma\rangle, S_M\})/\mathcal{Z}$. For it to be interpreted as a probability, it must be real and positive. There is in general no guarantee of that, although we can easily manage it for spin or bosonic models on a bipartite lattice[13]. The number of non-identity operators is $n = n_1 + n_{2,3}$ with n_1 the number of diagonal operators and $n_{2,3}$ the number of off-diagonal ones in the sequence. We can write $(-\beta)^n = \beta(-1)^{n_1+n_{2,3}}$, and by ensuring that every one of the diagonal operators induce a minus sign in the product, we can cancel n_1 of them. This is easily done by shifting the whole Hamiltonian by a dummy constant, and make sure that all matrix elements involving a diagonal operator are negative, i.e. $\mathcal{H}_p(1,b) \to \mathcal{H}_p(1,b) + \varepsilon$

[12] We indeed show at the end of this section that in average $\langle n \rangle = -\beta E$ with E the energy of the system, extensive quantity with the system size.

[13] A lattice is bipartite if it can be divided in two sublattices A and B with degrees of freedom of the sublattice A only interacting with those of the sublattice B.

with ε an appropriate constant shift. The remaining $n_{2,3}$ minus signs have to do with off-diagonal operators. There is no problem when describing a ferromagnetic system with $J < 0$ which indeed leads to $n_{2,3}$ negative matrix elements involving the terms $\frac{J}{2} S_i^{\pm} S_j^{\mp}$. For an antiferromagnetic system with $J > 0$ the idea to overcome this is to carry out a unitary transformation of the spin operators on one of the sublattices, such that $S_j^+ \to -S_j^+$ and $S_j^- \to -S_j^-$ (and no change for the operator S_j^z). The commutation relations of the spin operators remain unchanged by this transformation. Hence, it does not affect the spectrum of the model, even though the sign in front of the off-diagonal terms change to "$-$". This is enough to cancel the remaining $n_{2,3}$ minus signs of all the possible weights (A.41) of the configuration space. The minus sign in the weights gives rise to the so-called "sign problem" that can be worked around for specific models as we just showed. When no simple trick exists to skirt the sign problem, the model cannot be simulated. One can refer to Ref. 193 for a more complete introduction on this.

With everything fine, the stochastic computation of the partition function can be performed with movements in the configuration space $\{|\sigma\rangle, S_M\}$ as long as we verify the detailed balance. Although the Hilbert space dimension is exponentially large, as for the number of different possible sequences S_M, a single configuration is easily represented: $|\sigma\rangle$ is simply a basis state and the operator string can simply be represented by a list of integers:

$$S_M = \Big[(a,b)_1, (a,b)_2, \dots (a,b)_p, \dots (a,b)_M\Big] \tag{A.42}$$

with a the type of the term (0 for identity, 1 for diagonal and 2, 3 for off-diagonal) and b labelling the two sites on which the term acts; for a nearest-neighbor interaction it simply labels the bonds of the lattice. In this formulation, it is actually easy to visualize a given configuration of the $\{|\sigma\rangle, S_M\}$ space, where the action of the operator string $\prod_{l=0}^{p} \mathcal{H}_l(a,b)$ on a given initial state of the system can be interpreted as the propagation of this initial state along the operator string itself, see Fig A.12 (a): at a given slice p, the state $|\sigma(p)\rangle$ is obtained after the action of the first p operators of the string on $|\sigma\rangle \equiv |\sigma(0)\rangle$,

$$|\sigma(p)\rangle = \prod_{l=0}^{p} \mathcal{H}_l(a,b)|\sigma(0)\rangle \tag{A.43}$$

with the periodic condition $|\sigma(M)\rangle = |\sigma(0)\rangle$ due to the cyclic invariance of the trace. This notation is useful to isolate the action of a single operator at a given slice p from the state at the previous slice $p-1$, e.g.

$$\langle\sigma(0)| \prod_{l=0}^{M} \mathcal{H}_l(a,b)|\sigma(0)\rangle = \langle\sigma(p-1)|\mathcal{H}_p(a,b)|\sigma(p)\rangle, \tag{A.44}$$

where the first $p-1$ operators of the string have been applied on the bra $\langle\sigma(0)|$ and the operators onwards $p+1$ on the ket $|\sigma(0)\rangle$.

Monte Carlo updates As in any Monte Carlo algorithm, we now need to start from an initial configuration $\{|\sigma\rangle, S_M\}$ and suggest updates to accept or refuse with a transition probability from the old configuration to the new satisfying detailed balance. The ergodicity is encoded in the fact that all the weights (A.41) are strictly positive. Again, as in any Monte Carlo algorithm there is a lot of different possible

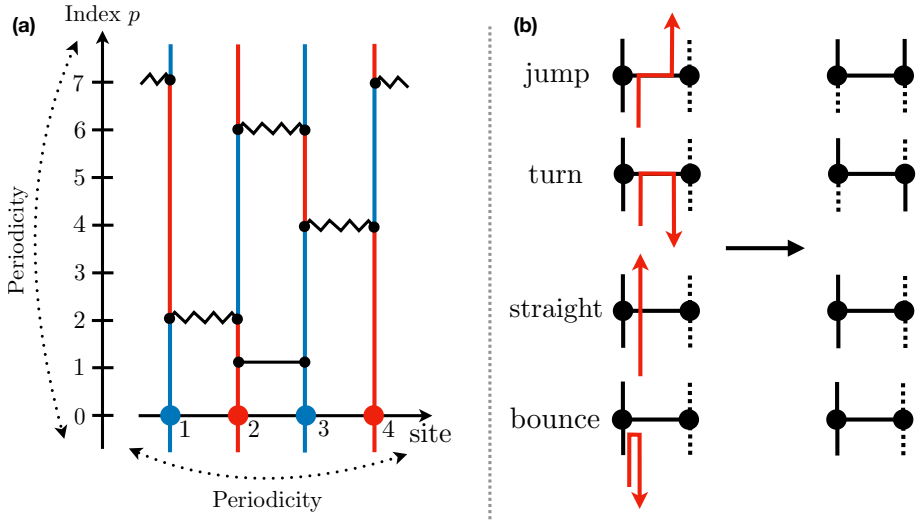

Figure A.12: (a) Graphical representation of one Monte Carlo configuration for a one-dimensional four spin-1/2 system with a first-neighbor interaction. The colors blue and red correspond respectively to a state $|\sigma_i\rangle = |\pm\frac{1}{2}\rangle$. The cutoff $M = 7$ and there are $n = 5$ non-identity operators. The diagonal operator is represented by a straight line between two sites and an off diagonal operator by a zig-zag line. The identity operators have been omitted in this representation. **(b)** Different possible movements for the worm (red line) on a vertex, depending on the relative position between the entrance and exit legs. Their names are quite explicit: the jump, the turn, the straight and the bounce. These movements are related to the update of the operator on the vertex.

updates but we want the most efficient ones. A good candidate that I will present is known as the directed loops algorithm with two types of updates. The first one is the *diagonal update* which tries to exchange an identity operator by diagonal operator, and vice-versa, in the sequence S_M, i.e. $(0,0) \leftrightarrow (1,b)$ [49, 50, 194]. The other type of update is the *loop operator update* that attempts to exchange an off-diagonal operator by another off-diagonal operator or a diagonal one, and vice-versa, i.e. $(m,b) \leftrightarrow (n,b)$ with $m,n = 1,2,3$ [195].

The diagonal update runs through all operators of the sequence. If $a = 2,3$ (off-diagonal term), we do nothing and move to the next one. If an identity operator ($a = 0$) is encountered, a pair of sites b is randomly picked amongst all the N_b possible ones and the exchange of the identity operator by a diagonal one $(0,0)_p \leftrightarrow (1,b)_p$ is proposed with probability of acceptance,

$$\mathcal{P}\Big[(0,0)_p \to (1,b)_p\Big] = \min\left(1, \frac{N_b \beta \langle \sigma(p-1)|\mathcal{H}_p(1,b)|\sigma(p)\rangle}{M-n}\right), \tag{A.45}$$

and similarly for the reverse move $(1,b)_p \leftrightarrow (0,0)_p$ if a diagonal operator is encountered in the sequence,

$$\mathcal{P}\Big[(1,b)_p \to (0,0)_p\Big] = \min\left(1, \frac{M-n+1}{N_b \beta \langle \sigma(p-1)|\mathcal{H}_p(1,b)|\sigma(p)\rangle}\right). \tag{A.46}$$

During a diagonal update, the number n of non-identity operators changes, but it should not reach the cutoff value M that we introduced for the Taylor expansion. To ensure that its value is large enough, it is dynamically updated during a thermalization

process. In practice, we start with a random basis state $|\alpha\rangle$ and an empty sequence (filled with identity operators) of small size M. We then perform diagonal updates until some convergence. Namely, if $n > \frac{4}{5}M$, we extend the sequence size to $M \to \frac{5}{4}n$ by adding identity operators and extend the size of the sequence as many times as necessary until the average $\langle n \rangle$ value does not fluctuate too much when performing updates and remain smaller than M. We will see by the end of this section that the average value of non-identity operators is related to physical observables such as the energy of the system and justifies that $\langle n \rangle \propto \beta N$ with N the number of degrees of freedom in the system.

Diagonal updates are used in the thermalization process and used alongside loop operator updates for the usual sampling movements. This second movement is trickier than the first one because a simple substitution of a diagonal operator by an off-diagonal one in the sequence would give a configuration with a zero contribution to the partition function since the matrix element $\langle \sigma(p-1)|\mathcal{H}_p(m,b)|\sigma(p)\rangle$ would vanish with $m = 2, 3$. To overcome this problem we introduce the non-local loop update. The idea is to represent every one of the n non-identity operators acting on sites $[i, j]$ as 4-legs vertices labelled by $k = 1, 2, 3, 4$. At a given pth vertex, there is a state associated to each leg, i.e.

$$\begin{array}{rcl} |\sigma(k=1)\rangle & = & |\sigma_i(p-1)\rangle \\ |\sigma(k=2)\rangle & = & |\sigma_j(p-1)\rangle \\ |\sigma(k=3)\rangle & = & |\sigma_i(p)\rangle \\ |\sigma(k=4)\rangle & = & |\sigma_j(p)\rangle \end{array} \tag{A.47}$$

In this representation, the update runs as follow. First, one of the n vertices is randomly chosen, as well as one of its legs, the "entrance leg" k_{in}. Then, an exit leg k_{out} is chosen on the same vertex together with new states $|\sigma(k_{\text{in}})\rangle$ and $|\sigma(k_{\text{out}})\rangle$ for the entrance and exit legs respectively, according to a certain probability table satisfying detailed balance. In agreement with these new proposed states, we replace the old operator at this vertex by a new one that would initiate the proposed change if we were to simply follow the propagation lines. The allowed new states are only those corresponding to non-zero matrix elements,

$$\langle \sigma(k=1)\sigma(k=2)|\mathcal{H}_p(a,b)|\sigma(k=3)\sigma(k=4)\rangle, \tag{A.48}$$

where a can take the values $1, 2$ or 3. The next step consists of following the propagation line on the same site as the exit leg until a new vertex is met. The update procedure is exactly the same as for the first vertex. The operation is carried until a closed loop is formed, by going back to the initial vertex through the first same entrance leg that we picked and with the exact same initial updated state $|\sigma(k_{\text{in}})\rangle$. Note that due to the periodicity $|\sigma(p=0)\rangle = |\sigma(p=M)\rangle$, if the loop goes through the boundary, the initial state will be changed. By going from one vertex to another from an exit leg to an entrance leg the update process can be pictured as a *worm* moving in the configuration space [196, 197]. Depending on the relative position of the entrance and exit legs on a vertex, there are four possible movements for the worm as shown in Fig. A.12 (b): jumping, turning, going straight or bouncing. The jumping and turning movements bring the worm on a different site and are associated to off-diagonal operators. By going straight, the worm stays on the same site and the operator on the vertex should be diagonal. The last movement is the bounce which keeps the vertex unchanged. There are actually different ways to build

the probability table for the worm movements/vertex updates. A generic solution is to consider that the probability to change one vertex to another is proportional to the weight of the matrix element (A.48) after the update, independently of the entrance leg. However, this choice turns out to be inefficient in many cases because of "bounce" movements which do nothing and that we want to avoid. A more efficient probability table can be constructed by minimizing the probability of bouncing, and is known as the *directed* loop update since it explicitly depends on the entrance leg [198–202].

Computation of physical observables The stochastic series expansion formulation of the QMC algorithm makes it quite easy to compute observables, and as I don't want to present a catalog of observables here, I refer the interested reader to Ref. 180. To justify a posteriori the truncation M introduced in the Taylor expansion at the beginning, one can show that the total energy E of the system is given by

$$E = -\frac{\partial \ln Z}{\partial \beta} = -\frac{\langle n \rangle}{\beta}, \tag{A.49}$$

where the shift constant ε inserted in the first place to avoid a sign problem has been subtracted already. Here, the symbol $\langle \cdot \rangle$ stands for the average number n of non-identity operators over many sampling configurations. The energy being an extensive quantity, the energy density is $e = E/N$; which justifies the cutoff M with $\langle n \rangle \propto \beta N$ being finite. Also, I want to mention that for magnetic systems displaying long-range XY order that I discussed in the previous section, the complex order parameter m^{AF} cannot be entirely computed, only its square modulus $|m^{\mathrm{AF}}|^2$ is accessible, with no information on its argument $\theta = \arg(m^{\mathrm{AF}})$. This is because its computation is based on the transverse correlation function,

$$|m^{\mathrm{AF}}|^2 = \lim_{N \to +\infty} \frac{1}{2N^2} \sum_{i,j} \Big(\langle S_i^+ S_j^- \rangle + \langle S_i^- S_j^+ \rangle \Big). \tag{A.50}$$

Besides, if one were able to compute the complex order parameter m^{AF}, it would be zero since a continuous symmetry cannot be spontaneously broken on a finite size system. Quantum Monte Carlo is an *exact* numerical method within error bars, in the sense that we did no approximation. The error bars result from the stochastic sampling in the configuration space and scale as $\mathcal{O}(1/\sqrt{N_{\mathrm{m}}})$ with N_{m} the number of measurements performed, and the reduction of the error bars simply implies longer simulation times. However, one cannot just evaluate the error bars as the standard deviation of all the measurements performed, because consecutive measurements do not result from strictly independent Monte Carlo configurations, but from updated ones. Owing to the non zero auto-correlation time between consecutive measurements, the standard deviation would actually underestimate the errorbars and a faithful estimation is obtained by a resampling of the measurements using jackknife or bootsrap methods [203].

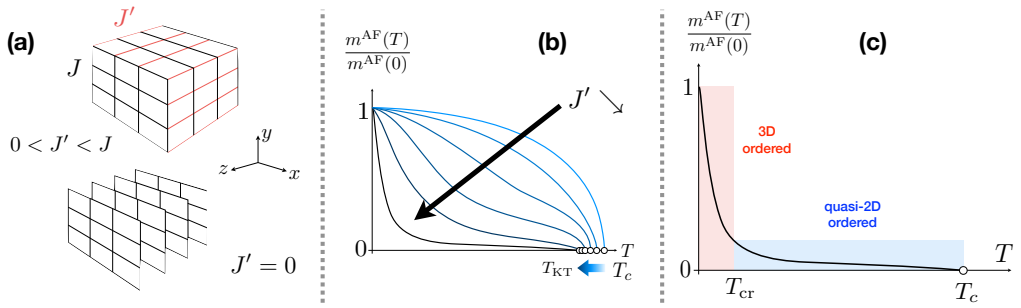

Figure A.13: **(a)** Upper panel, a three-dimensional spin system on a tetragonal lattice. Black and red bonds represent the Heisenberg exchange interactions J and J' between neighboring spins respectively. When the exchange interaction J' along the z axis is gradually switched off, it converges to a two-dimensional spin system on layered squared lattices as shown in the lower panel. **(b)** Possible scenario of suppression of the XY ordering by the reduction of dimensionality from 3D (lighter blue) to quasi-2D (darker blue). Note that the critical temperature remains finite even in the quasi-2D limit. **(c)** A schematic distinction of the quasi-2D and the 3D ordered phases. The quasi-2D ordered phase is spread near the critical temperature T_c and associated by the suppressed but nonzero spontaneous order $m^{\mathrm{AF}}(T)$. The quasi-2D ordered phase inherits the critical behavior of the 2D Kosterlitz-Thouless critical phase. The 3D ordered phase is a rather conventional ordered phase with a well developed interlayer correlation. Those phases are roughly separated at a crossover temperature T_{cr}.

IV. Dimensional modulation of the ordering process in weakly coupled spin chains

Adapted from the work Phys. Rev. B **94**, 144403 (2016)

Shunsuke C. Furaya, **Maxime Dupont**[14], Sylvain Capponi, Nicolas Laflorencie, and Thierry Giamarchi

Spontaneous symmetry breaking is deeply related to dimensionality of a system [17–20]. The XY antiferromagnetic order going with spontaneous breaking of U(1) symmetry is safely allowed at any temperature for three-dimensional systems but allowed only at zero temperature for purely two-dimensional systems. In this work, we closely investigated how smoothly the ordering process of the three-dimensional system is modulated into that of the two-dimensional one with reduction of dimensionality. The critical temperature is kept finite even in the two-dimensional limit although the long-range order is greatly suppressed for low-dimensionality. This feature of the critical temperature is highly nontrivial and dictates how the order parameter is squashed under the reduction of dimensionality. We investigated this dimensional modulation of the order parameter using analytical tools and numerical methods. Magnetic insulators are particularly interesting from the viewpoint of dimensionality since one can control it with their temperature. Let us take as an

[14] In this theoretical collaboration, I carried out the numerical simulations, which include DMRG and quantum Monte Carlo calculations.

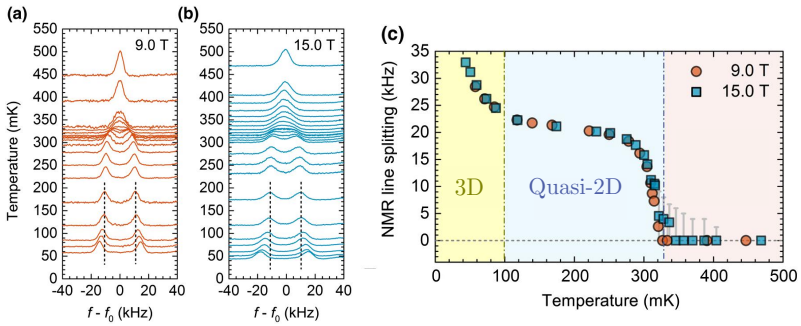

Figure A.14: ^{14}N NMR spectra as a function of the temperature in an applied field of **(a)** $H = 9.0$ T and **(b)** 15.0 T. Dashed vertical lines correspond to the first saturation of the line splittings at around $T = 150$ mK on cooling. **(c)** The line splitting, proportional to the modulus of the order parameter $|m^{\mathrm{AF}}|$, as a function of the temperature, where three different regimes are identified and presented using different background colors and separated by the vertical dash-dotted lines. Adapted from Ref. 204.

example a spatially anisotropic quantum Heisenberg antiferromagnet on a three-dimensional cubic lattice whose exchange interactions are J in the x and y directions and J' in the z direction as shown in Fig. A.13 (a). For $J' \ll J$, this system is effectively identical to two-dimensional (2D) quantum spin systems when the temperature T is high enough to mask the interplane correlation due to J'. On the other hand, when $T \ll J'$, the interplane coupling J' is non-negligible and leads to spontaneous XY order. In short, the Heisenberg antiferromagnet on weakly coupled square lattices behaves two-dimensionally for $T \gg J'$ and three-dimensionally for $T \ll J'$. There must be a dimensional phase transition or crossover at a moderate temperature in between these two distinctive regions. The Heisenberg quantum antiferromagnet on the spatially anisotropic cubic lattice has a spontaneous XY order $m^{\mathrm{AF}}(T)$ below a critical temperature T_c for $J'/J \simeq 1$. It is well known that $m^{\mathrm{AF}}(T)$ exhibits a domical temperature dependence represented by the lightest-blue curves in Fig. A.13 (b). On the other hand, it exhibits spontaneous XY order only at zero temperature for $J'/J = 0$. Here we ask the question of how the $m^{\mathrm{AF}}(T)$ curve is modified when reducing J'/J and how it dictates the existence of a quasi-2D ordered phase where the system behaves two-dimensionally except for the suppressed but nonzero $m^{\mathrm{AF}}(T)$ breaking the U(1) symmetry, see Fig. A.13 (c).

This work is greatly motivated by experimental measurements on the strong-leg spin-ladder compound $(C_7H_{10}N)_2CuBr_4$, also known as DIMPY. As already discussed, a two-leg spin ladder has a gapped singlet phase at low field where a nonzero excitation gap exists. A strong magnetic field closes it and allows the field-induced TLL phase. The system of 3D coupled antiferromagnetic spin ladders exhibits long-range XY order on the low-temperature side of the field-induced TLL phase. NMR measurements of the order parameter versus temperature, reported in Fig. A.14 show two different regimes labelled quasi-2D and 3D and interpreted as such [204]. More broadly, DIMPY has recently been under active experimental and theoretical investigations [171, 173, 205–209] because it is the first spin-ladder compound with strong leg interactions $J_{\mathrm{leg}}/J_{\mathrm{rung}} = 1.7$. Since coupled spin chains and coupled spin-ladders subject to a magnetic field can both realize a 3D XY ordered phase at low-temperature, results should be independent of the underlying model. That is

why we slightly move away from the realistic description of DIMPY by considering more generic spin-1/2 degrees of freedom on the vertices of an orthorhombic lattice with spatially anisotropic couplings J, J_1' and J_2' such that $J \gg J_1' \gg J_2'$. The 1D nature of the underlying model is masked by well developed interchain correlations in the quasi-2D or 3D ordered phases and thus not essential for our claim of the dimensional modulation. Still, it is technically convenient for theoretical analyses. The model is described by the following Hamiltonian,

$$\mathcal{H} = J \sum_{\langle ij \rangle_0} \left[\frac{1}{2} \left(S_i^+ S_j^- + S_i^- S_j^+ \right) + \Delta S_i^z S_j^z \right] - H \sum_i S_i^z + \mathcal{H}_{\text{3D}}$$
$$\text{with } \mathcal{H}_{\text{3D}} = J_1' \sum_{\langle ij \rangle_1} \mathbf{S}_i \cdot \mathbf{S}_j + J_2' \sum_{\langle ij \rangle_2} \mathbf{S}_i \cdot \mathbf{S}_j, \tag{A.51}$$

with $\langle ij \rangle_n$ restricting the sum to nearest-neighbors in the three different n spatial directions.

1. Analytical approaches

Mean-Field treatment The simplest way to deal with a phase transition is a mean field approach. It has proven to be often precise enough to determine the phase boundary of the XY ordered phase of various compounds such as the weakly coupled spin-1/2 Heisenberg antiferromagnetic ladders $CuBr_4(C_5H_{12}N)_2$ by treating the three-dimensional coupling in a mean-field way [166, 171, 210]. In the ordered phase, the antiferromagnetic order develops in the XY plane and is measured by the order parameter $m^{\text{AF}} = \lim_{N \to +\infty} \sum_{\mathbf{r}} m_{\mathbf{r}}^{\text{AF}} / N$ with $m_{\mathbf{r}}^{\text{AF}} = \mathrm{e}^{i \mathbf{q}_{\text{AF}} \cdot \mathbf{r}} \langle S_{\mathbf{r}}^x + i S_{\mathbf{r}}^y \rangle$ and $\mathbf{q}_{\text{AF}} = (\pi, \pi, \pi)$ the antiferromagnetic wavevector. For convenience, we rotate the XY spin components such that $\langle S_{\mathbf{r}}^y \rangle = 0$, which brings the XY ordering solely along the x component. Doing that is like imposing the angle $\theta = \arg(m^{\text{AF}})$ to be zero, while it is normally *spontaneously* locked to a random value due to the phase transition. However, as we only seek to describe the ordered phase here, it is fine to choose its value. The mean-field Hamiltonian is derived by rewriting the operators of the interchain coupling Hamiltonian $\mathcal{H}_{\text{3D}}$ in (A.51) as $S_j^\mu = \langle S_j^\mu \rangle + (S_j^\mu - \langle S_j^\mu \rangle)$ where $\langle \cdot \rangle$ denotes the average value on the ground state. Neglecting quadratic terms and up to an irrelevant constant we get,

$$\mathcal{H}_{\text{3D}} \to \mathcal{H}_{\text{MF}} = (z_1 J_1' + z_2 J_2') \sum_j \left[m^{\text{AF}} S_j^x + m^z S_j^z \right]. \tag{A.52}$$

where $z_{1,2} = 2$ is the number of neighboring chains coupled through $J_{1,2}'$. Note that we have assumed an homogeneous system with $m^{\text{AF}} = (-1)^j \langle S_j^x \rangle$ and $m^z = \langle S_j^z \rangle$, valid for any site j. Ultimately, the mean-field Hamiltonian describes a single chain subject to an effective longitudinal magnetic field $\propto m^z$ and an effective staggered transverse magnetic field $\propto m^{\text{AF}}$ accounting for the XY order.

Generically, the order parameter is given in linear response by $m^{\text{AF}} = \chi^{xx} h_{\text{stag}}$ with χ^{xx} the transverse susceptibility of the full system (A.51) and h_{stag} a staggered magnetic field. Likewise, we get for a single chain described by the mean-field Hamiltonian which is explicitly subject to a staggered field itself,

$$m^{\text{AF}} = \chi_{\text{1D}}^{xx} \left[h_{\text{stag}} + (z_1 J_1' + z_2 J_2') m^{\text{AF}} \right]. \tag{A.53}$$

Isolating the order parameter from the above expression, we finally get,

$$\chi^{xx} = \frac{\chi^{xx}_{1\mathrm{D}}}{1 - (z_1 J_1' + z_2 J_2')\chi^{xx}_{1\mathrm{D}}}, \tag{A.54}$$

known as the random phase approximation (RPA) [211, 212]. The 1D susceptibility $\chi^{xx}_{1\mathrm{D}}$ in the Tomonaga-Luttinger Liquid phase can be computed exactly [37, 155, 210] and is given by

$$\chi^{xx}_{1\mathrm{D}} = \frac{A_0 \sin\left(\frac{\pi}{4K}\right)}{u} \left(\frac{2\pi T}{2u}\right)^{\frac{1}{2K}-2} B^2\left(\frac{1}{8K}, 1 - \frac{1}{4K}\right), \tag{A.55}$$

with $B(x, y) = \Gamma(x)\Gamma(y)/\Gamma(x + y)$ the Beta function and $\Gamma(z)$ the Gamma function. u and K are the Tomonaga-Luttinger Liquid parameters and A_0 the prefactor of the transverse correlations. The RPA formula (A.54) tells us that the phase transition occurs when the susceptibility diverges, i.e. $1 - (z_1 J_1' + z_2 J_2')\chi^{xx}_{1\mathrm{D}} = 0$. This equation has a unique solution,

$$T_c = \frac{u}{2\pi} \left[\frac{A_0(z_1 J_1' + z_2 J_2') \sin\left(\frac{\pi}{4K}\right) B^2(\frac{1}{8K}, 1 - \frac{1}{4K})}{2u}\right]^{\frac{2K}{4K-1}}. \tag{A.56}$$

The RPA analysis we just performed tells us the fate of the critical temperature in the 2D limit $J_2'/J_1' \to 0$: even when $J_2' = 0$, the susceptibility (A.54) diverges at a certain finite temperature known the Berezinky-Kosterlitz-Thouless transition temperature T_{KT} [213–215]. Note that the susceptibility is divergent everywhere in the Kosterlitz-Thouless phase [216]. Let us see our system as a weakly coupled 2D systems with an infinitesimal interlayer coupling J_2' as in Fig. A.13 (a). Performing the RPA calculation with respect to J_2', we obtain the susceptibility,

$$\chi^{xx} = \frac{\chi^{xx}_{2\mathrm{D}}}{1 - z_2 J_2' \chi^{xx}_{2\mathrm{D}}}, \tag{A.57}$$

where $\chi^{xx}_{2\mathrm{D}}$ is the transverse susceptibility in the 2D limit $J_2'/J_1' = 0$. The above susceptiblity χ^{xx} is divergent at a temperature T_c which is a solution of

$$\chi^{xx}_{2\mathrm{D}}|_{T=T_c} = \frac{1}{z_2 J_2'}. \tag{A.58}$$

Since the right hand side of the above equation is large but finite, the 2D susceptibility at T_c on the left hand side must be finite as well. Therefore it immediately follows that $T_{\mathrm{KT}} < T_c$ for any $J_2'/J_1' > 0$. The relation of the critical temperature and the Kosterlitz-Thouless temperature indicates that the critical temperature converges to a finite value, which is T_{KT} in the quasi-2D limit (another argument, developed in Ref. 217, leads to the same conclusion regarding the fate of T_c as $J_2'/J_1' \to 0$). Therefore, the RPA analysis supports the dimensional reduction scenario sketched in Fig. A.13 (b). We will develop in the following further evidences by studying the shape of the order parameter m^{AF} versus the temperature through various approaches

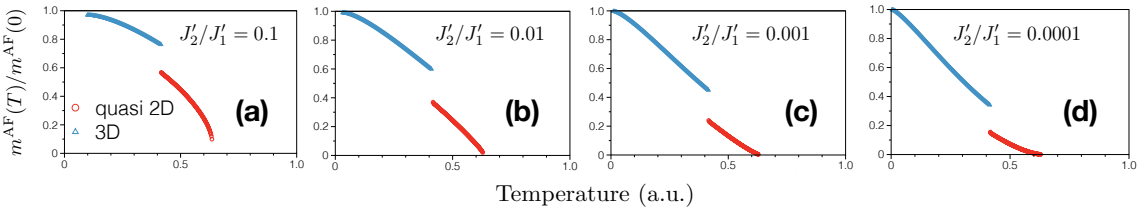

Figure A.15: Normalized XY order parameter plotted agains the temperature (arbitrary units) for several ratios of J_2'/J_1'. The variational method allows the computation of the order parameter in two limits: deep in the ordered phase (blue triangles) and close to the critical temperature (red circles).

Variational method The variational method is designed to build a quadratic action that best approximates the nonlinear action of the original theory. Using the bosonization representation of the spins [37] the Hamiltonian of the system in the ordered XY phase leads to the Euclidean action[15],

$$\mathcal{S} = \sum_{\mu,\nu}\Bigg\{\frac{K}{2\pi u}\int \mathrm{d}\tau\mathrm{d}x\Big[(\partial_\tau\theta_{\mu,\nu})^2 + u^2\,(\partial_x\theta_{\mu,\nu})^2\Big] \\ - J_1' A_0\int \mathrm{d}\tau\mathrm{d}x\,\cos\left(\theta_{\mu,\nu}-\theta_{\mu+1,\nu}\right) - J_2' A_0\int \mathrm{d}\tau\mathrm{d}x\,\cos\left(\theta_{\mu,\nu}-\theta_{\mu,\nu+1}\right)\Bigg\}, \quad \text{(A.59)}$$

The $\theta_{\mu,\nu}\equiv\theta_{\mu,\nu}(\tau,x)$ field describes the antiferromagnetic XY order with $m^{\rm AF}(T) = \sqrt{A_0}\langle\cos\theta_{\mu,\nu}\rangle$. Note that when $J_1' = J_2' = 0$, the action represents a set of mutually independent Tomonaga-Luttinger Liquids. The basic idea of the variational method is to search for a quadratic variational action, that will make the computation of observables possible (especially the order parameter here), of the form

$$\mathcal{S}_{\rm v} = \frac{T}{2\Omega}\sum_{\omega_n,\mathbf{q}} G_{\rm v}^{-1}(i\omega_n,\mathbf{q})|\theta(i\omega_n,\mathbf{q})|^2, \quad \text{(A.60)}$$

that approximates best the original action with $G_{\rm v}(i\omega_n,\mathbf{q})$ the Green's function to determine. Here ω_n are the Matsubara frequencies and Ω is the volume of the system. The field $\theta(i\omega_n,\mathbf{q})$ is the Fourier transform of $\theta_{\mu,\nu}(\tau,x)$. To find the optimum approximation of the Green's function, we use the variational principle over the free energy [218]. The free energy is defined as $\mathcal{F} = -T\ln\mathcal{Z}$, where $\mathcal{Z}$ is the partition function, $\mathcal{Z} = \int\mathcal{D}[\theta_{\mu,\nu}]\mathrm{e}^{-\mathcal{S}}$ where $\mathcal{D}[\theta_{\mu,\nu}]$ denotes the integration over all paths. The variational principle reads $\mathcal{F}\leq\mathcal{F}_{\rm var}$ where $\mathcal{F}_{\rm var}$ is the variational free energy defined as

$$\mathcal{F}_{\rm var} = \mathcal{F}_{\rm v} + T\langle(\mathcal{S}-\mathcal{S}_{\rm v})\rangle_{\rm v}. \quad \text{(A.61)}$$

Here $\mathcal{F}_{\rm v}$ is the free energy of the variational action (A.60) and the average $\langle\cdot\rangle_{\rm v}$ is taken with respect to it. The optimal $\mathcal{S}_{\rm v}$ is determined so as to minimize the variational free energy from the saddle-point equation $\delta\mathcal{F}_{\rm var}/\delta G_{\rm v} = 0$. An expression of the Green's function versus the temperature and the couplings J_2'/J_1' is then be obtained, but the underlying equations that need to be solved self-consistently can

[15] The other field $\phi_{\mu,\nu}$, dual to $\theta_{\mu,\nu}$ can be discarded in the description of the XY ordered phase characterized by $\theta_{\mu,\nu}$ only.

only be handled in basically two limits: deep in the ordered phase and close to the critical temperature. Fig. A.15 shows the order parameter in the whole temperature range for $J_2'/J_1' = 0.1,\ 0.01,\ 0.001$ and 10^{-4}, where the discontinuity between the red and blue symbols is a technical artifact resulting from the two limits considered for calculations. For $J_2'/J_1' \ll 1$, we clearly see a rapid growths of the XY ordering below a certain crossover temperature $T_{\rm cr}$ separating the quasi-2D phase (red symbols) from the 3D phase (blue symbols) with a change of curvature, supporting scenario of Fig. A.13 (b).

Classical approximation In order to describe the ordering process coherently in the entire region of the ordered phase, trying to accord the two limiting cases of Fig. A.15, we discard the imaginary-time dependence of the fields $\theta_{\mu,\nu}(\tau, x) \simeq \theta_{\mu,\nu}(x)$, which replaces the original $(3+1)$-dimensional quantum system to the $(3+0)$-dimensional classical one. This classical approximation works well near the critical temperature [21] and, although it is challenging to specify its precise range of validity, we can expect that it is very wide in the 2D limit $J_2'/J_1' \to 0$ because the system stays at the critical line at low temperatures $T < T_{\rm KT}$. Moreover, it is reasonable to think that in the ordered phase, the field fluctuations of neighboring chains μ and $\mu+1$ within a same 2D layer are going to be much more smaller than those from neighboring chains on different 2D layers (ν and $\nu+1$) if $J_1' \gg J_2'$. Hence, we expand the cosine term of the interchain interaction up to second order as $\cos(\theta_{\mu,\nu} - \theta_{\mu+1,\nu}) \simeq 1 - \frac{1}{2}(\theta_{\mu,\nu} - \theta_{\mu+1,\nu})^2$. Dropping the constant, we move to the continuum limit in the μ direction, $(\theta_{\mu,\nu} - \theta_{\mu+1,\nu})^2 \to (\partial_y \theta_\nu)^2$ where the classical field now depends on the 2D layer ν and the continuous variables x and y as $\theta_\nu(x, y)$. Straightforwardly, the new action reads

$$\mathcal{S}_{\rm cl} = \sum_\nu \Bigg\{ \frac{K}{2\pi u T} \int {\rm d}x{\rm d}y \Big[u^2 (\partial_x \theta_\nu)^2 + v_y^2 (\partial_y \theta_\nu)^2 \Big] - \frac{J_2' A_0}{T} \int {\rm d}x{\rm d}y \, \cos(\theta_\nu - \theta_{\nu+1}) \Bigg\} \quad \text{with } v_y^2 = \frac{u^2 J_1' A_0}{2K}, \tag{A.62}$$

where we have used $\int {\rm d}\tau = 1/T$ and the substitution $\sum_\mu \to \int {\rm d}y$ resulting from the continuum limit with lattice spacings set to unity. For convenience, we also make the following rescalings $y = v_y \tau'$, $K' = v_y K/T$ and $\tilde{J}_2' = v_y J_2'/T$, which leads to

$$\mathcal{S} = \sum_\nu \Bigg\{ \frac{K'}{2\pi u} \int {\rm d}x{\rm d}\tau' \Big[u^2 (\partial_x \theta_\nu)^2 + (\partial_{\tau'} \theta_\nu)^2 \Big] - \tilde{J}_2' A_0 \int {\rm d}x{\rm d}\tau' \, \cos(\theta_\nu - \theta_{\nu+1}) \Bigg\}. \tag{A.63}$$

By comparing this form of the action with the original one, it is clear that it can be seen as the description of a $(2+1)$-dimensional quantum system, i.e. quantum spin chains with Tomonaga-Luttinger parameters K' and u, coupled in a two-dimensional fashion through $\tilde{J}_2'$ and where $K' \propto 1/T$. Along with a renormalization group analysis of the couplings, one way to go further into the calculations (other than numerically, see next section) is to make a mean-field approximation of the $\tilde{J}_2'$ interaction in the action (A.63). This reduces the problem to a single chain in a staggered field.

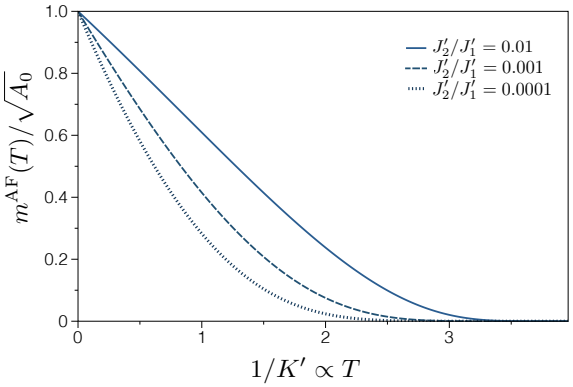

Figure A.16: Order parameter in the strongly 2D case for various values of the couplings ratio J_2'/J_1' computed in the mean-field approximation of the $(2+1)$-dimensional action (A.63), leading effectively to a $(1+1)$-dimensional model described by the integrable sine-Gordon theory. The horizontal axis represents the temperature $1/K' \propto T$

The resulting action is known as the sine-Gordon theory and is integrable. One can get an expression for the order parameter $m^{\mathrm{AF}}(T)$, shown in Fig. A.16 for different values of J_2'/J_1', where the curves are qualitatively consistent with the results of the variational calculations of Fig. A.15.

2. Numerical study

We are at the stage of supporting our results obtained thus far with unbiased numerical calculations. The initial 3D model of Eq. (A.51) with $J \gg J_1' \gg J_2'$ is numerically out of reach due to the strong anisotropy required between couplings which makes the quantum Monte Carlo simulations too demanding to reach low enough temperatures to capture the relevant physics. Indeed, a rough estimate based on the RPA formula (A.56) gives a critical temperature $T_c \sim \mathcal{O}(J_1')$ and we have to go far below this temperature to capture the quasi-2D and then 3D regime for the order parameter[16]. However, the classical approximation, which has proven to give reasonable results consistent with the variational method, makes it possible to simulate the underlying Hamiltonian associated to the action (A.63). Indeed, simulating weakly coupled spin chains in two-dimensions at zero temperature is substantially less demanding. In this section we provide numerical evidences to support previous analytical results by reproducing the order parameter $m^{\mathrm{AF}}(T)$ curve of Fig. A.16. Especially, the numerical analysis allows us to go beyond the simple mean-field approximation with respect to $\tilde{J}_2'$ that we have made and test the validity of the mean-field approximation. The Tomonaga-Luttinger Liquid (TLL) is a universal description, basically independent of the microscopic details. Thus, in order to test the analytical results, we can use any 1D lattice system as long as it is described by TLL theory at zero temperature. In practice, we will use the simplest

[16] We did attempt to simulate the 3D system described by the Hamiltonian (A.51) with $J_1' = J/10$ and $J_2' = J_1'/10$. While being at the limit of what one can expect to compute, we could not observe the quasi-2D regime of the order parameter. We believe that the factor 10 between the couplings was not large enough to actually observe it.

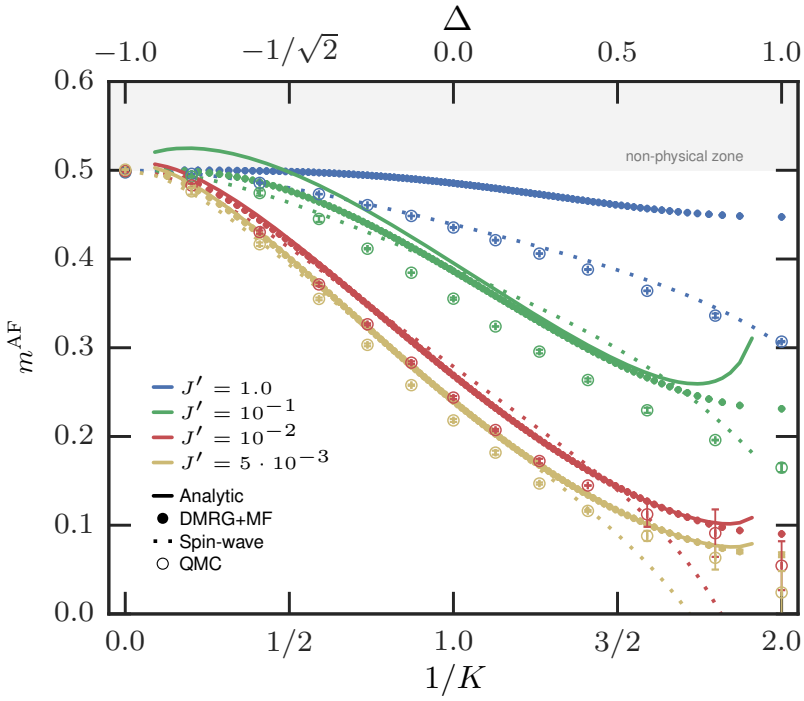

Figure A.17: Order parameter m^{AF} as a function of the TLL parameter $1/K \propto T$ plotted for various interchain couplings J'/J for the different approaches: analytic mean-field, numerical mean-field DMRG, spin-waves, and quantum Monte Carlo (infinite size extrapolations).

example, namely coupled XXZ spin-1/2 chains described by the Hamiltonian

$$\mathcal{H} = \sum_{i,n} \left\{ J \left[\frac{1}{2} \left(S^+_{i,n} S^-_{i+1,n} + S^-_{i,n} S^+_{i+1,n} \right) + \Delta S^z_{i,n} S^z_{i+1,n} \right] + J' \mathbf{S}_{i,n} \cdot \mathbf{S}_{i,n+1} \right\}, \quad \text{(A.64)}$$

where i and n label the sites along and perpendicular to the chains. $\Delta \in [-1, 1]$ is the Ising anisotropy governing the TLL parameter of isolated XXZ chains [71], and J' controls the strength of the transverse 2D interchain coupling[17]. In the following, the intrachain coupling is set to unity $J = 1$. The goal is to numerically investigate the ground-state order parameter as a function of the TLL parameter K in order to compare it with various analytical approaches. We first discuss mean-field approximations, both analytically and within a numerical scheme [219] based on DMRG calculations. We also compare these results with a spin-wave theory. Lastly, quantum Monte Carlo simulations are used to deal with the exact quantum mechanical problem and to compute the order parameter of weakly coupled XXZ chains in the limit of small interchain coupling J'.

Analytical mean-field treatment Rewriting the 2D interchain coupling of the Hamiltonian (5), similarly to what we did in the beginning of this section, we obtain a model describing a single one-dimensional chain in a staggered magnetic field $\propto m^{\mathrm{AF}}$ along the x spin component. The associated fields theory corresponds to the

[17] In our published work, there was also an Ising anisotropy Δ along the z spin component in the transverse 2D interchain coupling. However, we showed that its value played no role in the zero temperature order parameter value and simply keep the transverse coupling SU(2) symmetric.

integrable sine-Gordon theory [37, 69, 212, 220] from which the order parameter can be computed (details are in previous references),

$$m^{\mathrm{AF}} = \sqrt{A_0}\frac{\frac{8K\pi^2}{(8K-1)\sin\left(\frac{\pi}{8K-1}\right)}\left[\frac{\Gamma\left(1-\frac{1}{8K}\right)}{\Gamma\left(\frac{1}{8K}\right)}\right]^{\frac{8K}{8K-1}}}{\left[\Gamma\left(\frac{4K}{8K-1}\right)\Gamma\left(\frac{16K-3}{16K-2}\right)\right]^2}\left(\frac{\pi A_0 J'}{u}\right)^{\frac{1}{8K-2}}. \tag{A.65}$$

It is plotted against $1/K$ in Fig. A.17 and discussed in the following.

Numerical mean-field treatment One can also simulate the mean-field Hamiltonian describing a 2D array of coupled chains self-consistently. Specifically, numerical simulations can be performed in a self-consistent way using the DMRG algorithm at $T = 0$. To do so we start with a nonzero initial guess for the order parameter m^{AF} in the Hamiltonian and (tar)get the system ground state. Once we have it, a new value of the order parameter is measured and a new Hamiltonian is built accordingly. The procedure is repeated until two consecutive measures of the m^{AF} appear to be converged. As visible in Fig. A.17, both analytical and numerical mean-field approaches agree better for smaller J'. The numerical mean-field is more controlled than the analytical approach when J' is not very small, giving $m^{\mathrm{AF}} \leq 0.5$, as it should be, in particular close to the ferromagnetic point $1/K \to 0$. Nor does it predict any divergence for m^{AF} close to $1/K \to 2$, attributed to the divergence of the prefactor $\propto \sqrt{A_0}$ in Eq. (A.65).

Spin-wave As known for a long time, back to the seminal work by Anderson [83], spin-wave theory gives excellent estimates at the $1/S$ order for the order parameter of $D \geq 2$ spin-S quantum antiferromagnets, even for the most quantum case of $S = 1/2$. The question of weakly coupled chains, where spatial anisotropy enhances quantum fluctuations is more delicate, as discussed in several works [219, 221–223]. After making a rotation in order to align the quantization axis with the classical order along the x direction, we use the Dyson-Maleev representation of the spin-S operators in the rotated frame,

$$S_i^x = S - n_i, \quad S_i^y = \frac{1}{2i}\left[(2S - n_i)b_i^\dagger - b_i^\dagger\right], \\ \text{and } S_i^z = -\frac{1}{2}\left[(2S - n_i)b_i^\dagger + b_i^\dagger\right], \tag{A.66}$$

where the operators $b_i^\dagger$ and b_i follow bosonic commutation relations. At this point we make two things: first, we introduce a transverse field $-\Gamma\sum_{i,n} S_{i,n}^x$ (along the order direction) that will be useful to compute the order parameter; then, we make the operators substitution for spin $S = 1/2$, keeping only $\mathcal{O}(S)$ and $\mathcal{O}(S^2)$ terms,

$$\mathcal{H}_{\mathrm{sw}} = \frac{1}{4}\sum_{i,n}\Bigg\{2(n_{i,n} + n_{i+1,n}) - 1 + \sum_{+-}\pm(1 \pm \Delta)\left(b_{i,n}^\dagger b_{i+1,n} + \mathrm{h.c.}\right) \\ + J'\left[2(n_{i,n} + n_{i,n+1}) - 1 + 2\left(b_{i,n}^\dagger b_{i+1,n} + \mathrm{h.c.}\right)\right] - 2\Gamma\left(1 - n_{i,n}\right)\Bigg\}. \tag{A.67}$$

This Hamiltonian can easily be diagonalized using a standard Bogoliubov transformation in Fourier space $\mathbf{q} = (q_x, q_y)$ with $q_n = 2\pi m/L_n$ with $m \in [0, 1, \ldots L_n - 1]$.

Here L_n is the system size in the $n = x, y$ spatial direction with $N = L_x L_y$ degrees of freedom. Up to an irrelevant constant we get,

$$\tilde{\mathcal{H}}_{\rm sw} = \sum_{\mathbf{q}} \Omega_{\mathbf{q}} \alpha^{\dagger}_{\mathbf{q}} \alpha_{\mathbf{q}}, \quad \text{with } \Omega_{\mathbf{q}} = \sqrt{A^2_{\mathbf{q}} - B^2_{\mathbf{q}}}, \tag{A.68}$$

where $\Omega_{\mathbf{q}}$ is known as the spin-wave excitation spectrum with

$$\begin{aligned} A_{\mathbf{q}} &= (1 + J' + \Gamma) - \frac{(\Delta - 1)}{2} \cos q_x, \\ \text{and } B_{\mathbf{q}} &= \frac{(\Delta + 1)}{2} \cos q_x + J' \cos q_y. \end{aligned} \tag{A.69}$$

In the absence of the external symmetry breaking field Γ, the dispersion has a zero mode at $\mathbf{q} = (q_x = 0, q_y = 0)$[18]. The order parameter can be computed using the Hellman-Feynman theorem $\langle \partial_\Gamma \mathcal{H}(\Gamma) \rangle = \partial_\Gamma \langle \mathcal{H}(\Gamma) \rangle$ as [224],

$$m^{\rm AF} = 1 - \frac{1}{2N} \frac{\partial E}{\partial \Gamma}\Big|_{\Gamma=0} = 1 - \frac{1}{2N} \sum_{q_x, q_y} \frac{A_{\mathbf{q}}}{\Omega_{\mathbf{q}}}, \quad \text{with } E = \sum_{\mathbf{q}} \Omega_{\mathbf{q}} \tag{A.70}$$

where the sum is performed over all $\mathbf{q} \neq (0, 0)$ to avoid the diverging term $A_{\mathbf{0}}/\Omega_{\mathbf{0}}$ in the sum. Spin-wave results are plotted together with MF estimates as well as with exact QMC results in Fig. A.17. In the repulsive TLL regime ($1/K > 1$), the spin-wave $m^{\rm AF}$ is strongly depleted for increasing anisotropy (decreasing J'), and deviates from mean-field results. On the other hand, for the attractive TLL regime ($1/K < 1$), the agreement with mean-field is remarkable, in particular for smaller values of J'. Nevertheless, we cannot expect the spin-wave theory to be reliable for extremely small J' for any $1/K > 0$ because the spin-wave expansion is not justified in the 1D limit $J' \to 0$.

Quantum Monte Carlo treatment In order to go beyond the mean-field approximation and take exactly into account the 2D interchain coupling J', we use QMC through the stochastic series expansion algorithm [198, 225]. Since we are interested in ground state properties, we need to perform QMC simulations at temperatures well below the finite size gap of our finite size system, the lowest spin-wave gap being dictated by the weak coupling J'. Note also that one needs to perform a very careful finite size scaling analysis in order to reach the thermodynamic limit. We work on finite size systems with $N = L^2/r$ spins, where L is the length of the L/r coupled chains and r is the aspect ratio of the 2D system. Finite size systems with aspect ratio $r > 1$ have been used before to reduce finite size effects for the anisotropic case [226] and surprisingly, also for isotropic case [227]. For the present study, we performed simulations for different 2D couplings $J' = 1$ ($r = 8$), $J' = 0.1$ ($r = 16$), $J' = 0.01$ ($r = 16$) and $J' = 0.005$ ($r = 32$) for multiple Ising anisotropy values covering the whole range $\Delta \in [-1, 1]$. In order to ensure that we are probing only the ground state, we have performed QMC simulations both at temperatures $T = 2J'/L$ and $T = J'/L$ and checked that it provided the same results. We compare QMC results in Fig. A.17 for four values of J'. We notice that the order parameter value

[18] The zero mode is not at the AF wavevector (π, π) because we carried out a unitary transformation of the spin operators on one of the sublattices to perform spin-waves calculations, i.e. $S^+ \to -S^+$ and $S^- \to -S^-$ on Hamiltonian (5).

given by QMC is always smaller than that by numerical mean-field, which is expected as the mean-field approximation overestimates the order by discarding fluctuations. Note that the error bars do not reflect the QMC errors, which are much smaller, but rather gives an idea on the uncertainty due to the infinite size extrapolation procedure.

3. Summary and discussions

In this work, we discussed the dimensional modulation of magnetic ordering process in spatially anisotropic quantum antiferromagnets. Taking advantage of the small interchain and interlayer interactions, we performed several complementary analyses which all led to the dimensional reduction scenario sketched in Fig. A.13 (b). Because the critical temperature converges to the Kosterlitz-Thouless transition temperature T_{KT} in the 2D limit $J_2'/J_1' \to 0$, the quasi-2D ordered phase emerges in the range $T_{\mathrm{cr}} < T < T_c$, where T_{cr} represents the crossover temperature to the 3D phase, see Fig. A.13 (c). Since $T_c \to T_{\mathrm{KT}}$ and $T_{\mathrm{cr}} \to 0$ in the 2D limit, the quasi-2D ordered phase is smoothly connected to the Kosterlitz-Thouless phase. As we saw in the variational approach (Fig. A.15), the XY order $m^{\mathrm{AF}}(T)$ is strongly suppressed near the critical temperature when $J_2'/J_1' \ll 1$. We note that the same $m^{\mathrm{AF}}(T)$ curve is also derived with the aid of the classical approximation, see Fig. A.16. This agreement shows that our system in the quasi-2D ordered phase is well approximated by the classical system, for which we have provided a clear numerical confirmation based on quantum Monte Carlo simulations of an equivalent quantum system, compared to mean-field and spin-wave approximations. This characteristic of the quasi-2D ordered phase is inherited from the Kosterlitz-Thouless phase in the 2D limit.

V. Study of the S=1 antiferromagnetic quantum spin-chain compound "DTN"

Adapted from the work Phys. Rev. B **95**, 020404(R) (2017)

Rémi Blinder, **Maxime Dupont**[19], Sutirtha Mukhopadhyay, Mihael S. Grbić, Nicolas Laflorencie, Sylvain Capponi, Hadrien Mayaffre, Claude Berthier, Armando Paduan-Filho, and Mladen Horvatić

This section is dedicated to the spin-1 antiferromagnetic insulator compound $NiCl_2$-$4SC(NH_2)_2$ also known as Dichlorotetrakis-Thiourea-Nickel or "DTN" for short, that we investigated during my thesis in a fruitful collaboration with the NMR group at the high magnetic fields facility in Grenoble, France. Several works regarding this compound will be reported throughout this manuscript, especially in the last chapter

[19] In this experimental/theoretical collaboration, I performed the theoretical analysis, including the numerical simulations relying on DMRG and quantum Monte Carlo methods.

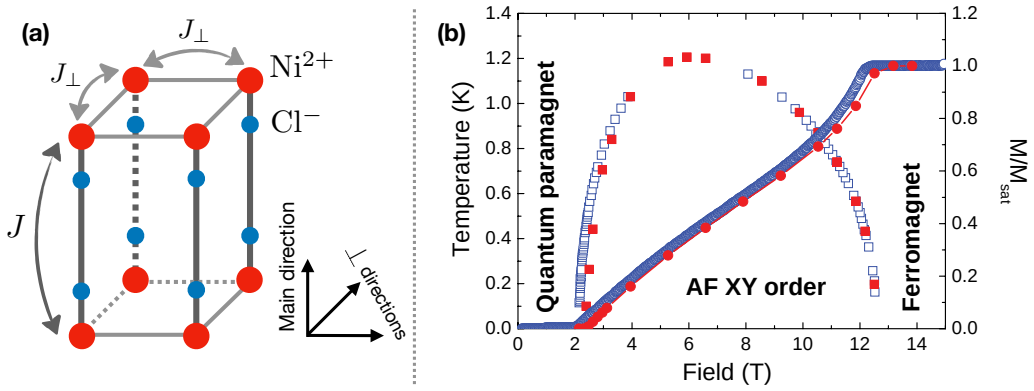

Figure A.18: (a) Crystallographic structure of the DTN compound. The $S = 1$ are carried by the Ni^{2+} ions (red dots) and the Chlorine atoms (blue dots) makes the compound spatially anisotropic (tetragonal lattice). **(b)** Temperature *vs.* magnetic field phase diagram of the XY AF ordered phase obtained from magnetocaloric effect measurements (open squares), see text for discussions about the different phases. The magnetization curve at $T = 16$ mK (open circles) is also displayed. Results of the quantum Monte Carlo simulations of the phase-diagram boundaries and the magnetization are denoted by solid squares and circles respectively. Adapted from Ref. 163.

dedicated to the interplay between interactions and disorder at high magnetic fields in this material, when chemically doped with Bromine impurities. Therefore, it is only natural to start this section with a self-consistent — if not exhaustive — overview about this compound to better seize its physical properties. The disorder-free case will be considered here, and the doped case saved for later. Being made of weakly coupled $S = 1$ chains, the question of one-dimensional based approaches to capture the relevant physics at play will be addressed in the second section.

1. Introduction to the DTN compound

The magnetic properties of the DTN compound are described by $S = 1$ degrees of freedom, borne by Ni^{2+} ions, forming a tetragonal lattice — a cubic lattice with two equivalent and one inequivalent spatial direction[20]. Two Chlorine atoms are present in between two Ni^{2+} along the crystallographic axis c (referred as the main or chain direction) and are responsible of the spatial anisotropy as shown in Fig. A.18 (a). The other atoms do not play a particular role in the magnetic description and are

[20] Actually, the situation is somewhat more complex than a simple tetragonal lattice. In fact, the DTN compound is a *body-centered tetragonal* lattice, corresponding to two interpenetrating tetragonal subsystems shifted by half of the tetragonal unit cell [228]. This frustrated coupling makes the theoretical study more difficult or even impossible in the case of quantum Monte Carlo simulations. However, its strength is supposed to be the smallest energy scale of the system ($J_f = 0.08$ K) [229] and can be safely neglected, especially regarding the nature of the ordered phase, because a perfectly frustrated coupling between the two subsystems should have no effect at all at the mean-field level, i.e. $J_\perp \sim \tilde{J}_\perp + J_f$ since it is treated on the same level as a non-frustrated transverse coupling $\tilde{J}_\perp$. Plus, this additional coupling does not induce any symmetry breaking in the system, see discussions.

not considered. The $S = 1$ interact through the following Hamiltonian [163, 230],

$$\mathcal{H} = \sum_i \Bigg\{ \sum_m \Big[J\mathbf{S}_{i,m} \cdot \mathbf{S}_{i+1,m} + D\left(S^z_{i,m}\right)^2 - g\mu_B H S^z_{i,m} \Big] + \sum_{\langle m,n \rangle} J_\perp \mathbf{S}_{i,m} \cdot \mathbf{S}_{i,n} \Bigg\}, \tag{A.71}$$

where the first index of the spin operator refers to the spin position on the chain to which it belongs, labeled by the second index. The $\langle \cdot \rangle$ symbol in the last sum restricts it to nearest-neighbor chains. The spin-spin exchange interactions are of the Heisenberg type with $J = 2.2$ K along the chain direction and $J_\perp = 0.18$ K in the transverse directions. In addition, every spin is subject to a strong easy-plane anisotropy $D = 8.9$ K. An external magnetic field H which couples to the spin degrees of freedom is applied in the same direction as the D anisotropy such that the Hamiltonian remains U(1) invariant, where the gyromagnetic factor $g = 2.31$[21]. It is quite unusual to note that all energy couplings are exactly known for this compound, with the applied magnetic field being the only tunable parameter here.

The ratio $J_\perp/J \simeq 0.08$ makes the system look like weakly coupled spin-1 chains, and in the first approximation we neglect the three-dimensional coupling ($J_\perp = 0$) to study the zero temperature phase diagram versus the magnetic field. Starting from the limit $H \to +\infty$, the ground state is a trivial ferromagnet, with all the spins aligned along the magnetic field direction $|\uparrow\uparrow \cdots \uparrow\rangle$ with energy $E_N = JN + DN - g\mu_B HN$ where N is the total number of spins in the system. As the magnetic field strength is reduced, the ferromagnetic phase will subsist until the first spin is flipped from $|\uparrow\rangle$ to $|0\rangle$. More precisely, the change of the ground state will occur if the energy of the single flipped spin state $E_{N-1} = E_N - D - 4J + g\mu_B H$ becomes smaller than E_N. The magnetic field value for which this change occurs defines the critical point H_{c2}^{1D},

$$H_{c2}^{1D} = (D + 4J)/g\mu_B = 11.4 \text{ T}. \tag{A.72}$$

In the other limit at $H = 0$, the ground state is in the so-called large-D phase [235] and *is not* of the Haldane type. This is because $D/J \simeq 4$ in DTN, which is larger than the critical value $D_c/J = 0.968$ [236] above which the ground state is in a trivial paramagnetic gapped phase (called large-D). It is only below this critical point — at which the gap closes — that the system undergoes a transition towards the better known topological Haldane gapped phase of the bare Heisenberg $S = 1$ chain. In the large-D phase, the ground state corresponds to a "dressed" state where all the spins

[21] Depending on the work one refers to, the value of the critical fields H_{c1} and H_{c2} determined experimentally vary from 2.05 to 2.15 T for the first one [231] and from 12.2 to 12.6 T [230, 232] for the second. This can be explained by magnetic field calibration problems or a non-meticulous sample orientation compared to the external magnetic field that would explicitly break the U(1) symmetry. Moreover, magneto-elastic couplings have been highlighted in DTN by magnetostriction and ultrasounds experiments [233, 234]; due to these couplings, the pressure applied on the sample to hold it tight can affect the critical fields [231]. Since the critical fields can be related to the microscopic parameters of the Hamiltonian (see text), they are used to determine the coupling constants. In our works on DTN, we have used the most common set of parameters $J = 2.2$ K, $J_\perp = 0.18$ K and $D = 8.9$ K and decided to tune the value of the gyromagnetic factor such that the theoretical value of the upper critical field H_{c2} fits with our experimental determination. Hence $g = 2.31$, although independent ESR measurements give $g = 2.26$ with accuracy better than 0.5% [163].

have a zero z-component $|00\cdots0\rangle$. Note that this is the exact ground state only in the $D/J \to +\infty$ limit. It is clear that the first excitation must be a spin flip, which will eventually occur upon applying a sufficiently large magnetic field $H \geq H_{c1}^{1D}$ to close the gap, given in perturbation theory by [237],

$$H_{c1}^{1D} = \left[D - 2J - \frac{J^2}{D} + \frac{J^3}{2D^2} + \mathcal{O}\left(\frac{J^4}{D^5}\right)\right]/g\mu_B = 2.6 \text{ T}. \tag{A.73}$$

The intermediate region in between H_{c1}^{1D} and H_{c2}^{1D} corresponds to a gapless Tomonaga-Luttinger Liquid phase, that can only describe a purely one-dimensional quantum system. Therefore, it will not subsist when plugging back the 3D coupling of the true DTN Hamiltonian, but will turn into antiferromagnetic XY order with the spontaneous breaking of the U(1) symmetry, robust to finite temperature up to T_c. On the contrary, the two gapped phases at low and high fields are only slightly affected, with shifted critical points $H_{c1} = H_{c1}^{1D} - 4J_\perp/g\mu_B = 2.1$ T and $H_{c2} = H_{c2}^{1D} + 8J_\perp/g\mu_B = 12.3$ T. The phase diagram is shown in Fig. A.18 (b), and the ordered phase corresponds to a so-called "Bose-Einstein Condensation" in a quantum antiferromagnet, discussed earlier, with $T_c^{\max} \sim 1.2$ K. The gapped nature of the large-D and ferromagnetic phases is characterized by the magnetization plateaus displayed on Fig. A.18 (b) for $H \notin [H_{c1}, H_{c2}]$.

2. "How one-dimensional is the DTN compound?"

If the previous section was more of an introduction on the DTN compound, I will now be more specific and summarize the work of our experimental-theoretical collaboration on the DTN compound. On the experimental side, this work holds the first measurement of the *absolute* value of the order parameter at very low temperature ($T = 0.12$ K). On the theoretical side, the main idea is to check on the accuracy of Tomonaga-Luttinger Liquid (TLL) approaches to capture the three-dimensional properties of the XY ordered phase of DTN such as the critical temperature and the order parameter. For reference, these TLL-based methods (the random phase approximation and the sine-Gordon model) are identical to those introduced in the previous part "Dimensional modulation of the ordering process in weakly coupled spin chains".

Tomonaga-Luttinger Liquid parameters The various TLL-based approaches treating the 3D coupling in a mean-field way, through the random phase approximation for the critical temperature or the sine-Gordon model for the order parameter, see Eqs. (A.65) and (A.56) of the previous part, required the knowledge of the Tomonaga-Luttinger Liquid parameters value A_0, K and u of the model. If analytical expressions relate them to the microscopic model for the XXZ spin-1/2 chain thanks to Bethe ansatz, this is not a general statement holding for any model. Then, the main part of the work consists of determining these values using numerical simulations. Indeed, the TLL parameters appear in various physical quantities such as the magnetic susceptibility, $\pi\chi = K/u$ or the correlation functions $\langle S_i^{\pm} S_{i+r}^{\mp}\rangle \sim (-1)^r A_0/|r|^{\frac{1}{2K}}$ that can be computed within DMRG and fitted afterwards.

Numerical simulations were carried out on a lattice chain of size $N = 200$ by imposing a total magnetization $S_{\text{tot}}^z = 1, 2 \ldots N-1$ on the system to determine

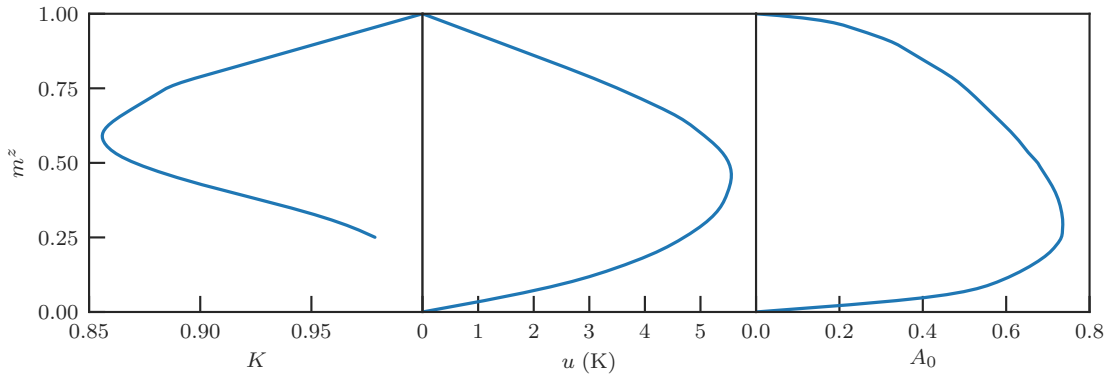

Figure A.19: Tomonaga-Luttinger Liquid parameters K, u and A_0 as a function of the magnetization m^z of the one-dimensional DTN compound described by the Hamiltonian (6) with $J = 2.2$ K, $D = 8.9$ K and $J_\perp = 0$. The parameters have been calculated using DMRG simulations, see text. Values for K at $m^z \to 0$ are not represented as the behavior of K in that region could not be precisely defined.

the TLL parameters in each of the magnetization sectors. From the ground state energy $E_0(S^z_{\text{tot}})$ of a given magnetization sector, one is able to reconstruct the global magnetization curve versus the external magnetic field H by the Legendre transformation $m^z(H) = \min\left[E_0(S^z_{\text{tot}}) - g\mu_B H S^z_{\text{tot}}\right]/N$. Taking its numerical derivative $\mathrm{d}m^z(H)/\mathrm{d}H$, one has access to the ratio $K/\pi u$. The correlation function $\langle S^{\pm}_i S^{\mp}_{i+r}\rangle$ is also computed in each of the magnetization sector and fitted with the right form versus r to extract K and A_0 [238, 239]; from the knowledge of K, u can be safely deduced from the susceptibility. The TLL parameters of DTN are reported in Fig. A.19, but their determination becomes increasingly difficult when approaching critical fields, in the $m^z \to 0$, 1 limits and we made use of the expected analytical behaviors to correct the obtained values: $u(m^z)$ and $A_0(m^z)$ are approaching zero linearly and as a square root, respectively. $K(m^z)$ is linearly approaching 1 on both sides, but its $m^z \to 0$ behavior could not be precisely defined.

Order parameter Our work constitutes on the experimental side to the first measurements of the *absolute* value of the amplitude of the order parameter m^{AF} of the ordered phase in DTN at $T = 0.12$ K[22]. To compare with the experimental measurements, I performed QMC simulations of the $S = 1$ Hamiltonian (6) at the same temperature as the measurements on finite size systems counting $N = L^3/64$ spins

[22]In order to determine value of the order parameter in the BEC phase, nitrogen spectra were recorded by NMR at $T = 0.12$ K and at different magnetic fields 9 T $< H < H_{c2}$. In the ordered phase, a transverse spin component appears in the ^{14}N spectra, corresponding to the order parameter. Since the spins are antiferromagnetically ordered, it creates a staggered local field at the nuclei, which results in a splitting of each NMR line. In canonical systems, the antiferromagnetic order induces a doubling of the unit cell, which results in a splitting of each line into 2, since the local field takes only 2 possible values, as seen in previous NMR studies [166, 173]. However, due to the body-centered tetragonal lattice of DTN, each NMR line splits into $2 \times 2 = 4$ lines when entering an AF ordered phase. This line splitting can be successfully tracked in ^{14}N spectra and converted into the order parameter. The main issue is to infer hyperfine tensors relating the spin polarization m^{AF} to the observed local hyperfine field δH induced at a given nuclear position by the surrounding magnetic moments. It is a highly nontrivial task as explained more thoroughly in our work and its supplemental material [174]

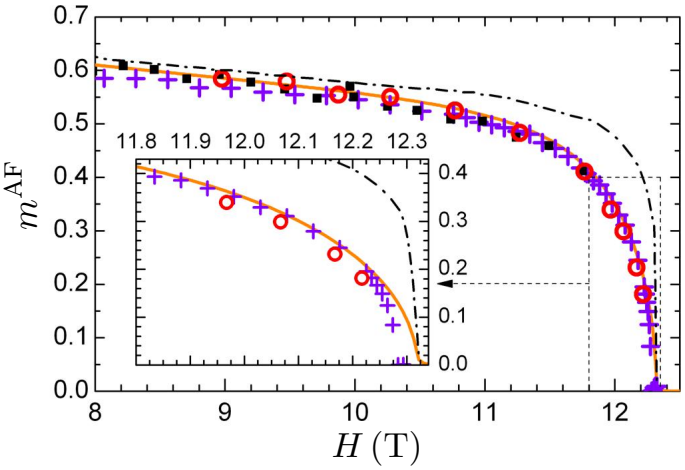

Figure A.20: The order parameter in the BEC phase of DTN at $T = 0.12$ K determined by NMR (circles) and by QMC simulations (crosses). NMR points are overlapped by neutron diffraction data from Ref. 229 downscaled by -25% (squares). The orange solid line and dashed-dotted black curve are the $T = 0$ prediction by DMRG+MF and by the sine-Gordon theory, respectively. The inset shows a zoom close to H_{c2}.

where L is the number of consecutive $S = 1$ spins along the chains direction. In order to adapt the simulation to the quasi-one-dimensional character of the Hamiltonian, only $L/8$ spins are then taken in each transverse directions (aspect ratio $r = 8$). A careful finite-size scaling analysis needs to be performed in order to determine the order parameter value in the thermodynamic limit. As shown in Fig. A.20 (a), the extrapolated QMC data agree remarkably well with the experiments.

For a quasi-one-dimensional system, a second, computationally less demanding approach to describe the order parameter at $T = 0$, is to take into account the inter-chain coupling within a mean-field (MF) approximation, neglecting spin fluctuations. This leads to a model of a single DTN chain in an effective magnetic field having a transverse staggered component due to AF ordering and a longitudinal component due to the magnetization by the external field, see Eq. (A.52) above. This model can be solved numerically in a self-consistent way using the DMRG algorithm to find the ground-state ($T = 0$) order parameter. The values obtained in this way and shown in Fig. A.20 (a) are very close to those from QMC calculated at 0.12 K; the apparent overestimate of m^{AF} by this DMRG+MF method, of about 3%, is partly due to the difference in the corresponding temperatures. Another possibility to solve this effective one-dimensional model is by rewriting it as a sine-Gordon field theory from which the order parameter can be computed from Eq. (A.65) in the previous section. In Fig. A.20 (a) we see that this estimates considerably deviate from the DMRG+MF results, especially close to H_{c2}, while the two results should be identical in the $J_\perp/J \ll 1$ limit. Apparently, as regards $m^{AF}(T = 0)$, the value $J_\perp/J \simeq 0.08$ *is not small enough* to consider DTN as a system of *weakly* coupled spin chains, in particular when the *total* interchain coupling $4J_\perp$ becomes larger than the intrachain energy scale u close to H_{c2}. This is to be compared with other "more one-dimensional" compounds, such as the weakly coupled spin-1/2 ladders $(C_5H_{12}N)_2CuBr_4$ where the sine-Gordon-based description of m^{AF} was remarkably

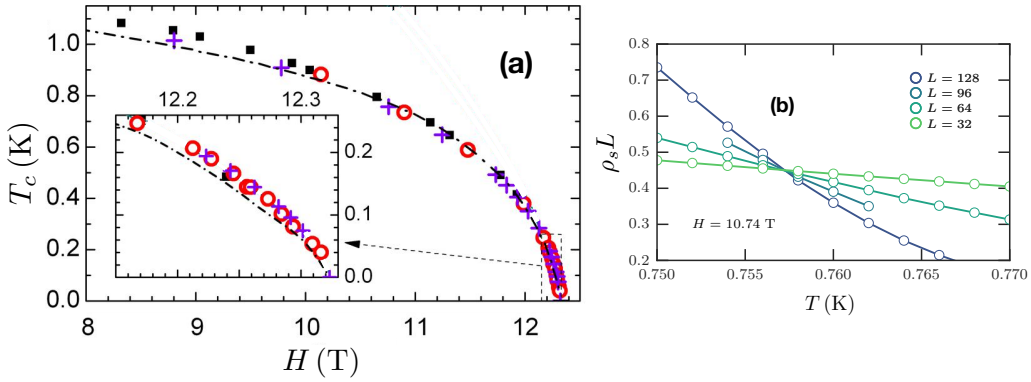

Figure A.21: **(a)** NMR data (red circles) for the critical temperature T_c compared with theoretical predictions: QMC data points are shown as crosses and the TLL prediction for T_c by the dash-dotted line (see the text). The squares correspond to the magnetocaloric effect data from Ref. 230 (with the field values downscaled by -2.3% to overlap the slightly different H_{c2} values). The inset shows a zoom close to H_{c2}. **(b)** Example at $H = 10.74$ T of the crossing of the spin stiffness ρ_s times the longitudinal system size L to determine the critical temperature $T_c = 0.7572(1)$ K according to the scaling law of Eq. (A.74).

accurate and fully consistent with the numerical DMRG+MF treatment[23] [166, 210].

Critical temperature We now turn our attention to the phase boundary $T_c(H)$. By NMR the precise critical temperature value is detected from the position of the maximum position of the corresponding critical spin fluctuations, which was measured as the corresponding peak of the transverse nuclear spin-spin relaxation rate $1/T_2$. NMR data, shown in Fig. A.21 (a), are in excellent agreement with the QMC simulations: for various system sizes and temperatures, we compute the spin stiffness [194, 240] and the order parameter, which both reveal a finite temperature transition using a standard finite-size scaling analysis,

$$\rho_s(L) = L^{2-D}\, \mathcal{G}_{\rho_s}\left[L^{1/\nu}\,(T - T_c)\right], \tag{A.74}$$

and,

$$m^{\mathrm{AF}}(L) = L^{-\beta/\nu}\, \mathcal{G}_{m^{\mathrm{AF}}}\left[L^{1/\nu}\,(T - T_c)\right], \tag{A.75}$$

where $D = 3$ is the dimensionality. The 3D XY critical exponents [175, 241, 242] $\nu = 0.6717$ (the correlation length exponent) and $\beta = 0.3486$ (the order parameter exponent) are used to extract the critical temperature T_c, after a Bayesian scaling analysis [243, 244]; see Fig. A.21 (b) for an example based on the spin stiffness. One can also include corrections to scaling of the form $\mathcal{G}\left[L^{1/\nu}(T - T_c)(1 + cL^{-\omega})\right]$, where ω is a subleading exponent of the order of one accounting for a finite-size drift, which gives similar values within the error bars. Our final T_c estimates in Fig. A.21 (a) are averages of the individual T_c from ρ_s and m^{AF} crossings, with and without irrelevant corrections, while the given error bars (actually smaller than the symbols size) reflect uncertainty between various estimates.

[23] Out of curiosity, we also compared the DMRG+MF treatment with the sine-Gordon based approach on a modified DTN Hamiltonian with $J_\perp = 0.01$, and which led to a better comparison between the two MF approaches and comfort us on the reason why the sine-Gordon estimate of m^{AF} fails for the true DTN Hamiltonian.

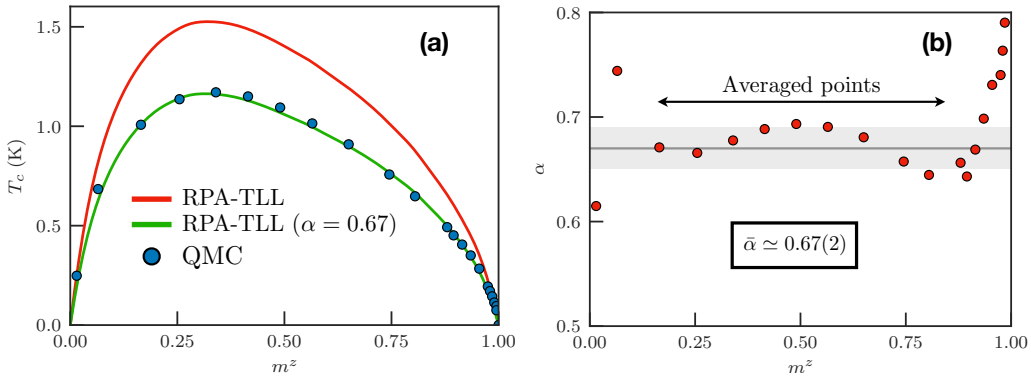

Figure A.22: (a) Critical temperature of the DTN compound versus the system magnetization. The RPA-TLL prediction clearly overestimates the critical temperature compared to the unbiased QMC except if one rescales the transverse coupling $J_\perp \to \alpha J_\perp$ of the RPA-TLL based approach. **(b)** Rescaling factor α of the three-dimensional coupling versus the magnetization of the system to make the critical temperature estimate from the mean-field RPA equal to the QMC estimate. The value of α is quite independent of the system magnetization except close to the critical points $m^z \to 0, 1$, where the MF description fails anyway. Moreover, note that we were not able to actually determine accurately the TLL parameter K for the DTN spin chain for $m^z \to 0$. The average value of the rescaling parameter $\bar{\alpha} = 0.67(2)$ is evaluated excluding these points.

The critical temperature can also be described by the analytical expression based on the random phase approximation of the susceptibility of a single TLL as in Eq. (A.56) and plotted in Fig. A.21 (a). Note that here, we have explicitly included a renormalization parameter α to take into account the effects of spin fluctuations beyond the mean-field treatment of interchain interaction, i.e. $J_\perp \to \alpha J_\perp$, see Fig. A.22 (a) to observe the difference with and without this rescaling factor. This was first discussed analytically for the Heisenberg spin chain in zero field in Ref. 245 and then precisely verified numerically in Ref. 246, where $\alpha = 0.695$ was obtained. A slightly different value, $\alpha = 0.74$ was successfully applied in describing $T_c(H)$ of the $(C_5H_{12}N)_2CuBr_4$ compound [167, 210], while for our DTN data we find $\alpha = 0.67(2)$, pointing to a quite universal value of this correction. For a given magnetic field, we determine the value of α such that $T_c^{\mathrm{QMC}}(H) = T_c^{\mathrm{RPA}}(H)$ as shown in Fig. A.22 (b).

Summary and discussions On the experimental side, the order parameter and the critical temperature of the high-field part of the antiferromagnetic ordered phase in the quasi-one-dimensional quantum magnet DTN were investigated by NMR. We compared them using several theoretical approaches. Especially, quantum Monte Carlo simulations for the standard spin-1 DTN model provide excellent fit to the data, and we used them as a reference to discuss the applicability of approximate techniques and their sensitivity to the strength of the three-dimensional coupling. For a moderately one-dimensional system such as DTN with $J_\perp/J \simeq 0.08$, we find that analytical TLL-based predictions are still very good for T_c as long as the renormalization of mean-field interaction is taken into account $J_\perp \to \alpha J_\perp$ with $\alpha \simeq 0.67$. The TLL treatment of the mean-field Hamiltonian results for DTN in an order parameter m^{AF} that deviates too much from the expected value. However, the

exact treatment of the chain mean-field approximation using DMRG turns out to be precise and in agreement with the expected value.

— Chapter B —

Dynamical properties of antiferromagnets

The computation of time-dependent quantities or the response of a quantum system over time to an initial perturbation are challenging problems to all fields of physics and especially condensed matter theory. It is however essential to understand these effects since they relate to most of the experimental probes involved in order to investigate quantum systems.

Section I For instance, I will be concerned in this chapter with spectral functions obtained through inelastic neutron scattering experiments [247,248] and with the nuclear magnetic resonance spin-lattice relaxation rate, the so-called $1/T_1$ [249–251]. These are both standard experimental tools in the condensed matter community to study quantum spin systems. I will present them in the first introductory section, mostly adopting a "theoretical point of view" by briefly explaining the underlying physics and quickly relate what is experimentally measured to what actually needs to be computed to have a direct comparison.

Section II In the following section, I will discuss the general numerical methods to capture time-dependent phenomena in quantum systems based on the Matrix Product States formalism and on the stochastic series expansion formulation of the quantum Monte Carlo algorithm that were both introduced in the previous chapter. *All* numerical methods suffer from some limitations that will also be discussed.

Section III Tomonaga-Luttinger Liquids are very peculiar systems. In the low-temperature limit, their nuclear magnetic resonance spin-lattice relaxation rate is expected to behave versus temperature with a power-law dependence [147], whose exponent is a function of the dimensionless parameter K. The first work of this chapter aims at defining properly the crossover "low-temperature limit" between a non-universal high temperature regime and the universal one-dimensional properties at low-temperature in quantum spin chains.

Section IV In a realistic compound, spin chains are always coupled to each others at some point. As already discussed in the previous chapter, the three dimensional coupling strength compared to the one-dimensional one $J_\perp/J$ makes the system look more or less one-dimensional and the temperature effectively controls the dimension. Being a natural follow-up of the previous work, we will be concerned here with the dimensional crossover in the spectral functions and the nuclear magnetic

resonance spin-lattice relaxation rate in two and three dimensional spin systems. We will employ both numerical and analytical calculations to address the dynamical properties of these systems versus the temperature.

Section V Lastly, I have studied the $S = 1$ Heisenberg chain, with a finite spin gap $\Delta_g \simeq 0.41J$, known as the Haldane gap, from which we simply expect an activated law for the nuclear magnetic resonance spin-lattice relaxation rate $\sim \exp(-\gamma\Delta_g/T)$. This work was motivated by conflicting predictions based on field theory of the nonlinear O(3) sigma model, $\gamma = 1$ or $\gamma = 3/2$ [252, 253], while both have been experimentally observed. In this work, we numerically investigated the $S = 1$ model in order to reconcile and settle the different analytical predictions as well as the experimental observations.

I. Introduction

Throughout this chapter, we will be interested in the dynamical properties of quantum antiferromagnets at finite temperature described by some generic U(1) symmetric Hamiltonian $\mathcal{H}$ in D dimensions where the anisotropy stands along the z spin component. Those are captured by the time-dependent correlation function,

$$S^{\mu\upsilon}_{\mathbf{q}}(t) = \langle S^{\mu}_{-\mathbf{q}}(t) S^{\upsilon}_{\mathbf{q}}(0)\rangle - \langle S^{\mu}_{-\mathbf{q}}(t)\rangle\langle S^{\upsilon}_{\mathbf{q}}(0)\rangle, \tag{B.1}$$

where $\langle\rangle$ indicates the thermal average, $S^{\mu}_{\mathbf{q}}(t) = \mathrm{e}^{i\mathcal{H}t} S^{\mu}_{\mathbf{q}} \mathrm{e}^{i\mathcal{H}t}$ is the time-dependent spin operator in the Heisenberg picture and the index $\mu, \upsilon \in [x, y, z]$ is the spin component. The spin operator in momentum space is related through a discrete Fourier transform to the real space by $S^{\mu}_{\mathbf{q}}(t) = \sum_{\mathbf{r}} \mathrm{e}^{i\mathbf{q}\cdot\mathbf{r}} S^{\mu}_{\mathbf{r}}(t)/\sqrt{N}$ with N the total number of spins in the system. Depending on the system dimension, $\mathbf{r}$ and $\mathbf{q}$ are D-dimensional vectors where each of the momentum components are $\in]-\pi, \pi]$[1]. The Fourier transform from time t to frequency ω gives the dynamical spin structure factor also known as the spectral function,

$$S^{\mu\upsilon}_{\mathbf{q}}(\omega) = \int_{-\infty}^{+\infty} \mathrm{d}t\, \mathrm{e}^{i\omega t} S^{\mu\upsilon}_{\mathbf{q}}(t), \tag{B.2}$$

which is the main quantity of interest and is somehow related to experimental probes such as inelastic neutron scattering (INS) measurements, the electron spin resonance (ESR) spectrum [254] or the nuclear magnetic resonance (NMR) spin-lattice relaxation rate $1/T_1$. What is known as the static spin structure factor is recovered when integrating over frequencies,

$$S^{\mu\upsilon}_{\mathbf{q}} = \frac{1}{\pi} \int_{-\infty}^{+\infty} \mathrm{d}\omega\; S^{\mu\upsilon}_{\mathbf{q}}(\omega), \tag{B.3}$$

with $\sum_{\mathbf{q}} S^{\mu\upsilon}_{\mathbf{q}} = \delta_{\mu\upsilon}/4$ fulfilling the sum rule. For a two or three-dimensional system, it also relates to the modulus square of the complex order parameter, i.e. $|m^{\mathrm{AF}}|^2 =$

[1] In all directions, lattice spacing has been set to unity.

$S^{xx}_{\mathbf{q}_{\mathrm{AF}}} + S^{yy}_{\mathbf{q}_{\mathrm{AF}}}$, accounting for spontaneous antiferromagnetic order in the XY plane with $\mathbf{q}_{\mathrm{AF}} = (\pi, \pi, \pi)$ the antiferromagnetic wave-vector. For convenience and due to the U(1) symmetry of the Hamiltonian considered here, the transverse part to the anisotropy along the z spin component can be isolated and written using raising and lowering operators,

$$S^{xx}_{\mathbf{q}} + S^{yy}_{\mathbf{q}} = \frac{1}{2}\Big(S^{+-}_{\mathbf{q}} + S^{-+}_{\mathbf{q}}\Big). \tag{B.4}$$

1. Inelastic Neutron Scattering

Inelastic neutron scattering is a spectroscopy technique that can directly relate to the spectral function (10). The wave vector $\mathbf{q}$ is the momentum transferred to the sample between incoming and outgoing wave vectors $\mathbf{k}'$ and $\mathbf{k}$ of the neutrons, and ω the kinetic energy transferred to the system due to the collision. More precisely, INS experiments measure the partial differential cross section [247, 248],

$$\frac{\mathrm{d}^2\sigma(\mathbf{q},\omega)}{\mathrm{d}\Omega\mathrm{d}\omega} = \frac{|\mathbf{k}'|}{|\mathbf{k}|} F^2_{\mathbf{q}} \sum_{\mu\upsilon} \left(\delta_{\mu\upsilon} - \frac{q_\mu q_\upsilon}{\mathbf{q}^2}\right) S^{\mu\upsilon}_{\mathbf{q}}(\omega), \tag{B.5}$$

with q_μ the projection of the wave vector $\mathbf{q}$ on the spin component μ. The prefactor of the dynamical spin structure factor in the sum ensures that only the spin components normal to $\mathbf{q}$ contribute to the cross section. The magnetic form factor $F_{\mathbf{q}}$ is the Fourier transform of the spatial density of the scatterer, i.e. the electrons holding the relevant spin degrees of freedom in our case. The ratio $|\mathbf{k}'|/|\mathbf{k}|$ and the form factor are known quantities that can be factored out of the experimental data. Furthermore, the spectral function is only non zero if $\mu = \upsilon$ for the Hamiltonian considered, which gives the corrected scattering intensity,

$$I = \sum_{\mu} \left(1 - \frac{q^2_\mu}{\mathbf{q}^2}\right) S^{\mu\mu}_{\mathbf{q}}(\omega) = I^{\perp} + I^{\parallel}, \tag{B.6}$$

where the intensity has been divided into longitudinal and transverse parts due to the U(1) symmetry of the Hamiltonian. Moreover, the q_μ-dependent prefactors can be calibrated in experimental setups and will be set to unity in the following, which results in

$$I^{\parallel} = S^{zz}_{\mathbf{q}}(\omega), \quad \text{and} \quad I^{\perp} = \frac{1}{2}\Big[S^{+-}_{\mathbf{q}}(\omega) + S^{-+}_{\mathbf{q}}(\omega)\Big]. \tag{B.7}$$

2. Nuclear Magnetic Resonance relaxation rate

In NMR experiments, the nuclear spins of the sample are polarized through an external magnetic field and then perturbed by an electromagnetic pulse. One can select and target specific nuclei by choosing the right frequency ω_0 corresponding to the level splitting of the picked nuclei due to Zeeman effect. Following the perturbation, the nuclear spins precess around the magnetic field direction and relax over time with an energy transfer to the external environment, the lattice and specifically the electrons holding the electronic spin described by the Hamiltonian

$\mathcal{H}$ [249–251]. The return of magnetization M to equilibrium over time reads $1 - M(t) \propto \mathrm{e}^{-t/T_1}$, where $1/T_1$ is known as the spin-lattice relaxation rate and can be related to the dynamical correlation function in crystalline magnets,

$$\frac{1}{T_1} = \frac{\gamma^2}{2} \sum_{\mathbf{q}} \sum_{\mu\nu} \left[A^{\mu\nu}_{\mathbf{q}} \right]^2 S^{\mu\nu}_{\mathbf{q}}(\omega_0), \tag{B.8}$$

with γ the gyromagnetic ratio and $A^{\mu\nu}_{\mathbf{q}}$ the hyperfine tensor describing the hyperfine and dipolar interactions between nuclear and electronic spins. Its $\mathbf{q}$-dependence provides a kind of form factor which can modify the sensitivity of $1/T_1$ to different wave vector components of the spin dynamics [255–257], although for simplicity, we will consider it to be independent of $\mathbf{q}$ and equal to unity in the following, just as $\gamma^2/2 = 1$. Thereby, the sum over $\mathbf{q}$ simplifies to the local ($\mathbf{r} = 0$) dynamical correlation function in real space,

$$\frac{1}{T_1} = \sum_{\mu\nu} S^{\mu\nu}_{\mathbf{r}=\mathbf{0}}(\omega_0) = \frac{1}{T_1^{\perp}} + \frac{1}{T_1^{\parallel}}, \tag{B.9}$$

As for the scattering intensity, we can separate the longitudinal and transverse contributions,

$$\frac{1}{T_1^{\parallel}} = S^{zz}_{\mathbf{r}=\mathbf{0}}(\omega_0), \quad \text{and} \quad \frac{1}{T_1^{\perp}} = \frac{1}{2}\Big[S^{+-}_{\mathbf{r}=\mathbf{0}}(\omega_0) + S^{-+}_{\mathbf{r}=\mathbf{0}}(\omega_0) \Big]. \tag{B.10}$$

It is theoretically justified to take the limit $\omega_0 = 0$ since the NMR frequency is of a few tens or hundreds of MHz, corresponding to temperatures of the order of mK, often making it the smallest energy scale of the problem. However, taking this limit assumes some smoothness in the local spectral function $S^{\mu\nu}_{\mathbf{r}=\mathbf{0}}(\omega)$, with no sharp contribution at $\omega \to 0$ that would not be captured by the actual NMR measurements due to the finiteness of ω_0[2]. The $\omega \to 0$ limit makes it also convenient to express the $1/T_1$ components directly as the integral over time of the dynamical correlation functions,

$$\frac{1}{T_1^{\perp}} = \mathrm{Re} \int_{-\infty}^{+\infty} \mathrm{d}t \, \langle S^{\pm}_{\mathbf{r}}(t) \, S^{\mp}_{\mathbf{r}}(0) \rangle = 2\mathrm{Re} \int_{0}^{+\infty} \mathrm{d}t \, \langle S^{\pm}_{\mathbf{r}}(t) \, S^{\mp}_{\mathbf{r}}(0) \rangle, \tag{B.11}$$

and similarly,

$$\frac{1}{T_1^{\parallel}} = 2\mathrm{Re} \int_{0}^{+\infty} \mathrm{d}t \, \Big[\langle S^{z}_{\mathbf{r}}(t) \, S^{z}_{\mathbf{r}}(0) \rangle - \langle S^{z}_{\mathbf{r}}(t) \rangle \langle S^{z}_{\mathbf{r}}(0) \rangle \Big]. \tag{B.12}$$

II. Numerical methods

Here comes the volume two regarding the numerical methods developed and implemented during my thesis where I will use the same notations as before. The real

[2] As a side remark, the local ($\mathbf{r} = \mathbf{0}$) spectral functions $S^{+-}_{\mathbf{r}=\mathbf{0}}(\omega_0)$ and $S^{-+}_{\mathbf{r}=\mathbf{0}}(\omega_0)$ become equivalent in the $\omega_0 \to 0$ limit [258] and one can compute whichever is the most convenient.

time evolution of quantum systems is computationally a very challenging problem as *all* methods suffer from severe limitations. In Matrix Product States (MPS) algorithms, the major drawback is the rapid growth of entanglement entropy of the system during the time evolution. This implies to keep a larger and larger bond dimension D in the MPS if one wants to be accurate, limiting in practice numerical simulations to short times. Exact diagonalization of the Hamiltonian to compute the evolution operator $\mathrm{e}^{-i\mathcal{H}t}$ is limited by the exponential size of the Hilbert space with the system size, though recent progress was made to compute dynamics in the Krylov space, allowing slightly larger systems. The two methods have been successfully used for one-dimensional systems so far, with only few options left for higher dimensions, like quantum Monte Carlo (QMC). However, QMC algorithms have the major caveat that dynamical data are obtained in imaginary time τ $(= -it)$ so that analytic continuation is needed a posteriori. This is an ill-posed problem due to the intrinsic sampling statistical error of the measured observables, resulting in an infinite number of solutions from imaginary time to real time. To overcome this issue, a standard workaround is the "maximum entropy" method which imposes an entropic prior (as in information entropy) in the analytic continuation to satisfy the principle of maximum entropy [259], but often results in distortions and broadening of the spectra. Recent developments introduced a stochastic analytic continuation, which performs stochastic samplings of all possible results and average those that fit the QMC data equally well, with very promising results [260–262]. The simulation of quantum mixed state (finite temperature) of dynamical quantities is directly part of QMC algorithms but requires extra work for MPS techniques with the introduction of auxiliary degrees of freedom (ancillas), acting as a thermal bath and artificially doubling the system size.

1. Matrix Product States

As we are interested in real-time dynamics, it is only natural to start by presenting an efficient way to apply the evolution operator $\mathrm{e}^{-i\mathcal{H}t}$ on a quantum state $|\Psi\rangle$ written as an MPS. I will then show how to represent and deal with a mixed state within the MPS language, which is known as the purification method. Lastly, I will describe a recently introduced method to compute spectral function directly in frequency space via a Chebyshev polynomials expansion. For entanglement entropy related issues, we shall discuss as well why all these methods are, at the very most, suitable for one-dimensional systems.

a. Time evolution

We will be general and consider the case with a Hamiltonian consisting of nearest-neighbor interactions only as it is the case for the XXZ model or the one-dimensional DTN Hamiltonian introduced before, i.e. $\mathcal{H} = \sum_j \mathcal{H}_{j,j+1}$. Ultimately, we want to time-evolve a wave function represented by an MPS up to a time t. In general this is done by applying the evolution operator $\mathrm{e}^{-i\mathcal{H}t}$ on the state but intractable in practice because it requires to diagonalize $\mathcal{H}$ to exponentiate it. The idea behind the Trotter decomposition is to first discretize the time using small time steps τ such

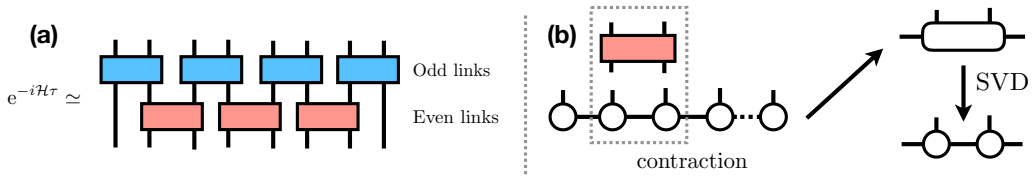

Figure B.1: **(a)** Tensor network representation of a first Trotter decomposition step of odd and even bonds $\mathcal{H}_{j,j+1}$ of the evolution operator $e^{-i\mathcal{H}\tau}$, which becomes exact in the limit $\tau \to 0$. A blue (red) tensor corresponds to an odd (even) bond evolution operator. **(b)** Applying the Trotter decomposed evolution operator to an MPS is quite straightforward. Successively, the two involved tensors of the MPS are first contracted together with the associated evolution gate. Then, a simple SVD on the rank-4 tensor gives back the original local MPS form. When performing the SVD, we only keep the largest singular values to control the bond dimension D of the system.

that $t = N\tau$, leading to $e^{-i\mathcal{H}t} = \prod^N e^{-i\mathcal{H}\tau}$. Now, if the time step τ is small enough, a first or higher[3] order Trotter decomposition can be performed,

$$e^{-i\mathcal{H}\tau} \simeq \prod^N e^{-i\mathcal{H}_{\text{even}}\tau} \prod^N e^{-i\mathcal{H}_{\text{odd}}\tau} + \mathcal{O}(\tau^2) \tag{B.13}$$

where $\mathcal{H}_{\text{even}}$ and $\mathcal{H}_{\text{odd}}$ respectively correspond to the sum of all even and odd bond Hamiltonians $\mathcal{H}_{j,j+1}$ only acting on two nearest-neighbor spins. The decomposition is possible because even (odd) bond Hamiltonians commute with each others. But it is not exact and leads to an error in τ due to the fact that the commutator $[\mathcal{H}_{j-1,j}, \mathcal{H}_{j,j+1}] \neq 0$. The advantage is that the bond Hamiltonians can easily be diagonalized and exponentiated since they are only $d^2 \times d^2$ matrices, see Fig. B.1 (a). And so, applying successive evolution gates on the MPS as well as singular value decompositions to restore the MPS original tensor-site dependent form as shown in Fig. B.1 (b) will eventually lead to a time-t evolved state. This whole procedure is known as the time-evolution block decimation (TEBD) algorithm [266].

The main limitation about time-evolution is the linear growth of entanglement entropy with time [111] while evolving the state. This implies to keep larger and larger number of states D in the MPS if one wants to be accurate, strongly limiting numerical simulations in practice. Thus, fixing a maximum number of kept states D limits simulations to a finite time t_{max} (typically of the order of few tens of the inverse energy scale of the system). Although its use did not prove to be systematically reliable in our case, I would like to mention the possibility to use so-called linear prediction technique [267], coming from data analysis, which aims at predicting "longer time" behavior from the knowledge of dynamical correlations at "intermediate time".

[3] In practice, we actually use a Trotter decomposition of the fourth order with an error scaling as $\mathcal{O}(\tau^5)$ and which reads $e^{-i\mathcal{H}\tau} = U(\tau_1)U(\tau_1)U(\tau_2)U(\tau_1)U(\tau_1)$ where $U(\tau_i) = e^{-i\mathcal{H}_{\text{odd}}\tau_i/2} e^{-i\mathcal{H}_{\text{even}}\tau_i} e^{-i\mathcal{H}_{\text{odd}}\tau_i/2}$ with $\tau_1 = (4 - 4^{\frac{1}{3}})^{-1}\tau$ and $\tau_2 = \tau - 4\tau_1$ [263–265].

b. Finite temperature

To address the challenge of mixed states, several MPS-based methods have been proposed, developed and compared [268], e.g., the finite-temperature Lanczos method [269], the purification scheme of a pure state in an enlarged Hilbert space [270], and, more recently, the minimally-entangled typical thermal states approach [271,272]. In all my works, I have used the purification scheme which introduces an auxiliary Hilbert space Q acting as a thermal bath [45]. It can be taken as a copy of the physical Hilbert space P, thus enlarging it to $\mathrm{P}\otimes\mathrm{Q}$ or, equivalently, doubling the system size to $2N$ with N physical and N auxiliary degrees of freedom. The overall idea is to represent the density matrix of the physical system,

$$\rho_\beta = \mathrm{e}^{-\beta\mathcal{H}}/\mathcal{Z}(\beta), \quad \text{with } \mathcal{Z}(\beta) = \mathrm{Tr}\,\mathrm{e}^{-\beta\mathcal{H}}, \tag{B.14}$$

at temperature $\beta = 1/T$ in an artificially enlarged Hilbert space as a pure state,

$$|\Psi_\beta\rangle = \sum_n a_n |\phi_n\rangle_\mathrm{P} |\phi_n\rangle_\mathrm{Q}, \text{ where } \rho_\beta = \mathrm{Tr}_\mathrm{Q}|\Psi_\beta\rangle\langle\Psi_\beta|, \tag{B.15}$$

where Tr_Q is the partial trace over auxiliary degrees of freedom $\{|\phi_n\rangle_\mathrm{Q}\}$. To get how this scheme works, we first rewrite the density matrix as,

$$\rho_\beta = \mathcal{Z}^{-1}(\beta)\mathrm{e}^{-\beta\mathcal{H}/2}\, I\, \mathrm{e}^{-\beta\mathcal{H}/2}, \tag{B.16}$$

with I the identity operator which is nothing but $\mathcal{Z}(0)\rho_0$ according to Eq. (B.14). Assuming that we know what is the MPS representing the wavefunction $|\Psi_{\beta=0}\rangle$ such that if we trace over its auxiliary degrees of freedom, Eq. (B.15) is fulfilled and give us the right density matrix ρ_0 of the physical system then it follows that[4],

$$\rho_\beta = \frac{\mathcal{Z}(0)}{\mathcal{Z}(\beta)}\mathrm{e}^{-\beta\mathcal{H}/2}\,\mathrm{Tr}_\mathrm{Q}\Big[|\Psi_{\beta=0}\rangle\langle\Psi_{\beta=0}|\Big]\mathrm{e}^{-\beta\mathcal{H}/2}. \tag{B.17}$$

Since the Hamiltonian in the exponential does not act on the auxiliary space Q, the partial trace can be pulled out as

$$\rho_\beta = \frac{\mathcal{Z}(0)}{\mathcal{Z}(\beta)}\mathrm{Tr}_\mathrm{Q}\Big[\mathrm{e}^{-\beta\mathcal{H}/2}|\Psi_{\beta=0}\rangle\langle\Psi_{\beta=0}|\mathrm{e}^{-\beta\mathcal{H}/2}\Big]. \tag{B.18}$$

At the end, an imaginary time evolution has to be performed over the infinite temperature MPS ($\beta = 0$) in order to get the finite temperature MPS,

$$|\Psi_\beta\rangle = \mathrm{e}^{-\beta\mathcal{H}/2}|\Psi_{\beta=0}\rangle, \tag{B.19}$$

which can be performed using the TEBD algorithm described in the previous section except that now $it \to \beta/2$. In this formulation, the computation of physical observables is straightforward,

$$\langle\mathcal{O}\rangle_\beta = \mathrm{Tr}_\mathrm{P}\Big[\mathcal{O}\rho_\beta\Big] = \frac{\mathcal{Z}(0)}{\mathcal{Z}(\beta)}\mathrm{Tr}_\mathrm{P}\Big[\mathcal{O}\,\mathrm{Tr}_\mathrm{Q}|\Psi_\beta\rangle\langle\Psi_\beta|\Big] = \frac{\mathcal{Z}(0)}{\mathcal{Z}(\beta)}\langle\Psi_\beta|\mathcal{O}|\Psi_\beta\rangle, \tag{B.20}$$

where we have used Eq. (B.18) for the expression of the density matrix ρ_β in the last equality. Plus, since the resulting overlap $\langle\Psi_\beta|\mathcal{O}|\Psi_\beta\rangle$ is a number, the partial traces

[4] We will show that the infinite temperature MPS representing $|\Psi_{\beta=0}\rangle$ can hopefuly be constructed exactly at the end, but we do not need to worry about that for now.

can be safely dropped. The ratio of the two partition functions trivially follows from the expectation value of the identity operator,

$$\langle I\rangle_\beta = 1 = \mathrm{Tr}_\mathrm{P}\Big[I\rho_\beta\Big] = \frac{\mathcal{Z}(0)}{\mathcal{Z}(\beta)}\mathrm{Tr}_\mathrm{P}\mathrm{Tr}_\mathrm{Q}|\Psi_\beta\rangle\langle\Psi_\beta| = \frac{\mathcal{Z}(0)}{\mathcal{Z}(\beta)}\mathrm{Tr}_\mathrm{P}\mathrm{Tr}_\mathrm{Q}\langle\Psi_\beta|\Psi_\beta\rangle. \quad \text{(B.21)}$$

Finally, we get that the thermal average value of an observable $\mathcal{O}$ is given by,

$$\langle\mathcal{O}\rangle_\beta = \frac{\langle\Psi_\beta|\mathcal{O}|\Psi_\beta\rangle}{\langle\Psi_\beta|\Psi_\beta\rangle}, \quad \text{(B.22)}$$

which is easy to compute. At this point we still do not know what the infinite temperature MPS is and this is what we shall focus on now. The $\beta = 0$ density matrix of the physical system is given by,

$$\rho_0 = \frac{1}{d^N}I = \left(\frac{1}{d}I\right)^{\otimes N}, \quad \text{(B.23)}$$

which factorizes over each of the N degrees of freedom and where d^N corresponds to the Hilbert space size. Hopefully, the MPS representing $|\Psi_{\beta=0}\rangle$ can be factorized in pairs of physical and auxiliary degrees of freedom $|\Psi_{\beta=0}\rangle = |\psi_1\rangle|\psi_2\rangle\ldots|\psi_N\rangle$. Noting that

$$\begin{aligned}\frac{1}{d}I_n &= \frac{1}{d}\sum_{\{\sigma_n\}}|\sigma_n\rangle_\mathrm{P}\langle\sigma_n|_\mathrm{P} \\ &= \mathrm{Tr}_\mathrm{Q}\left[\left(\frac{1}{\sqrt{d}}\sum_{\{\sigma_n\}}|\sigma_n\rangle_\mathrm{P}|\sigma_n\rangle_\mathrm{Q}\right)\left(\frac{1}{\sqrt{d}}\sum_{\{\sigma_n\}}\langle\sigma_n|_\mathrm{P}\langle\sigma_n|_\mathrm{Q}\right)\right], \quad \text{(B.24)}\end{aligned}$$

where the sum runs over the $\{\sigma_n\}$ states of the local Hilbert space of the nth degree of freedom. It follows that the local state $|\psi_n\rangle$ corresponds to a maximally entangled state,

$$|\psi_n\rangle = \frac{1}{\sqrt{d}}\sum_{\{\sigma_n\}}|\sigma_n\rangle_\mathrm{P}|\sigma_n\rangle_\mathrm{Q}. \quad \text{(B.25)}$$

which is trivial enough to be built exactly within the MPS formalism as shown in Fig. B.2. Indeed, the MPS in this enlarged Hilbert space can be pictured as a ladder with one leg corresponding the physical degrees of freedom P and the other to the auxiliary ones Q. At infinite temperature, the rungs are independently maximally entangled but not entangled to each other. For instance, the rungs for a spin-1/2 system read $|\psi_n\rangle = (|\uparrow_{\mathrm{P},n}\uparrow_{\mathrm{Q},n}\rangle + |\downarrow_{\mathrm{P},n}\downarrow_{\mathrm{Q},n}\rangle)/\sqrt{2}$[5].

It becomes increasingly difficult to reach low temperatures with this method. This might seem a bit surprising at first since I have just explained in the introductory section on MPS in the previous chapter that there is no better way we know of to represent a one-dimensional ground state (an exactly zero temperature state!) thanks to the area law. Unfortunately, because of the auxiliary sites which are used

[5]One can actually carry out local unitary transformations on a rung on both physical P and auxiliary Q degrees of freedom separately and keep the maximally entangled structure. In practice, to have a system $\mathrm{P}\otimes\mathrm{Q}$ with conserved quantities, we will use $|\psi_n\rangle = (|\uparrow_{\mathrm{P},n}\downarrow_{\mathrm{Q},n}\rangle + |\downarrow_{\mathrm{P},n}\uparrow_{\mathrm{Q},n}\rangle)/\sqrt{2}$ such that $S^z_\mathrm{tot}(\mathrm{P}) + S^z_\mathrm{tot}(\mathrm{Q}) = 0$ is a conserved quantity. Note that $S^z_\mathrm{tot}(\mathrm{P})$ and $S^z_\mathrm{tot}(\mathrm{Q})$ are not conserved quantities separately.

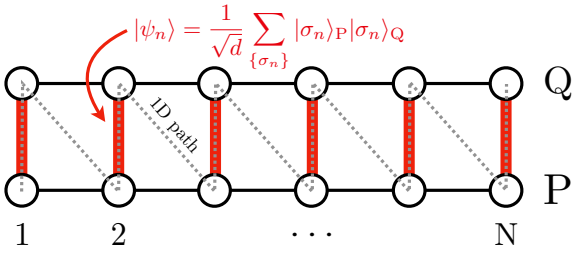

Figure B.2: Representation of the MPS $|\Psi_\beta\rangle$ in an enlarged Hilbert space $\mathrm{P} \otimes \mathrm{Q}$, where the lwer leg represents the physical degrees of freedom P and the upper one the auxiliary ones Q, hence artificially doubling the system size $N \to 2N$. As an MPS can only represent one-dimensional system, a 1D path is chosen between the vertices of the lattice, at the price of long-range interactions (up to second neighbors f, see the dotted line). The infinite temperature MPS corresponds to a product state of maximally entangled states between pairs of physical and auxiliary degrees of freedom (in red here). This makes the choice of the ladder lattice very convenient to actually encode exactly the maximally entangled states on the rung of the ladder.

to represent the thermal state, one expects a volume-law entanglement entropy (i.e. linear with the system size N). As a consequence, the size of the virtual dimension D needed to describe accurately the system will grow exponentially as the temperature T decreases. We are basically able to reach $\beta_{\max} J \sim 10$ with J the energy scale of the system. When using real-time evolution on a mixed state, one can make use of the auxiliary degrees of freedom by time-evolving them with $-\mathcal{H}$, which is mathematically without effect regarding the physical properties of the system, but has been shown to improve substantially the accessible time range [273]. By construction, this trick only applies to finite-temperature simulations. More recently, a more general approach has been proposed to find an approximately-optimal way to represent auxiliary degrees of freedom by sequentially applying local disentangling operations, whose real time evolution by $-\mathcal{H}$ is just one possibility [274].

c. Chebyshev expansion of the spectral function

The finite temperature spectral function $S^{\mu\upsilon}_{\mathbf{q}}(\omega)$ defined in Eq. (10) can also be expressed through the Källén-Lehmann spectral representation,

$$S^{\mu\upsilon}_{\mathbf{q}}(\omega) = \frac{\pi}{\mathcal{Z}(\beta)} \sum_{m,n} \mathrm{e}^{-\beta E_m} |\langle n|S^{\mu}_{\mathbf{q}}|m\rangle|^2 \delta\Big[\omega - (E_n - E_m)\Big] \delta_{\mu\upsilon}, \tag{B.26}$$

where $(S^{\mu}_{\mathbf{q}})^\dagger = S^{\upsilon}_{-\mathbf{q}}$ has been assumed. The sum is performed over the eigenstates $|m\rangle$ of energy E_m of the Hamiltonian describing the system. The result is a collection of delta peaks which eventually forms a continuum in the thermodynamic limit. In the current MPS framework, the spectral function in the form (B.26) can be rewritten as,

$$S^{\mu\upsilon}_{\mathbf{q}}(\omega) = \langle \Psi_\beta | \left(S^{\mu}_{\mathbf{q}} \otimes \mathcal{I}_Q\right) \delta\left(\omega - \mathcal{L}\right) \left(S^{\upsilon}_{-\mathbf{q}} \otimes \mathcal{I}_Q\right) |\Psi_\beta\rangle / \langle \Psi_\beta | \Psi_\beta \rangle, \tag{B.27}$$

with $\mathcal{L} = \mathcal{H}_P \oplus (-\mathcal{H}_Q) = \mathcal{H}_P \otimes \mathcal{I}_Q - \mathcal{I}_P \otimes \mathcal{H}_Q$ the Liouville operator where $\mathcal{H}_{P,Q}$ is the Hamiltonian acting either on the physical or the auxiliary space. The eigenvalues

of $\mathcal{L}$ are all the differences of the eigenenergies of the Hamiltonian, which makes the relation with the original representation more obvious. A way to compute this quantity is to represent it as a Chebyshev polynomials expansion of the first kind [275–280] that we will briefly explain. First of all, the Chebyshev polynomials $T_n(x)$ are defined by the recurrence relation,

$$\begin{aligned} T_0(x) &= 1, \\ T_1(x) &= x, \\ T_n(x) &= 2xT_{n-1}(x) - T_{n-2}(x), \end{aligned} \tag{B.28}$$

where $T_n(x) = \cos[n \arccos(x)]$ are the only polynomials satisfying the above relation. They form a sequence of orthonormal functions on the interval $x \in [-1, 1]$,

$$\int_{-1}^{1} \frac{\mathrm{d}x}{\pi\sqrt{1-x^2}} T_n(x)T_m(x) = \begin{cases} 0 & n \neq m \\ 1 & n = m = 0 \\ \frac{1}{2} & n = m \neq 0 \end{cases}, \tag{B.29}$$

so that a function $f(x)$ defined on the interval $x \in [-1, 1]$ can be expressed via the expansion $f(x) = \sum_{n=0}^{\infty} a_n T_n(x)$, which eventually converges to $f(x)$ as long as the function has all nice properties one can expect: it needs to be smooth and continuous mostly. The coefficients a_n can be computed recursively because the Chebyshev polynomials form an orthogonal basis, with

$$\int_{-1}^{1} \frac{\mathrm{d}x}{\pi\sqrt{1-x^2}} T_0(x)f(x) = \sum_{n=0}^{\infty} a_n \int_{-1}^{1} \frac{\mathrm{d}x}{\pi\sqrt{1-x^2}} T_0(x)T_n(x), \tag{B.30}$$

equals to (B.29). Here, $T_0(x)$ has been chosen for convenience as a reference. At the end,

$$f(x) = \frac{1}{\pi\sqrt{1-x^2}} \left[\mu_0 + 2\sum_{n=1}^{\infty} \mu_n T_n(x)\right], \quad \mu_n = \int_{-1}^{1} \mathrm{d}x\, f(x)T_n(x) \tag{B.31}$$

where the coefficients μ_n are known as the Chebyshev moments. Now the idea is to express the spectral function $S^{\mu\nu}_{\mathbf{q}}(\omega)$ (B.27) as a Chebyshev expansion by computing its moments μ_n recursively[6]. For the Chebyshev expansion to be well-defined and convergent, a first step is to rescale the frequency ω of the spectral function such that it is bounded by $[-1, 1]$. This is done by mapping the bandwidth W of the Liouvillian, corresponding to the difference between its largest and smallest eigenvalues, to $[-1, 1]$. They can be obtained using standard DMRG with the Liouvillian $\mathcal{L}$ as an input directly rather than the Hamiltonian as one would usually do[7]. Ultimately, the Liouvillian operator is rescaled as,

$$\mathcal{L} \to \mathcal{L}' = \frac{1}{a}\left(\mathcal{L} + \frac{W}{2}\right) - W', \quad \text{and} \quad \omega \to \omega' = \frac{1}{a}\left(\omega + \frac{W}{2}\right) - W', \tag{B.32}$$

[6]The Chebyshev expansion is favored compared to any other such as a Legendre expansion because of its "better numerical properties" such as convergence and goodness of fit. I took the example of Legendre polynomials because they are defined in the same interval $x \in [-1, 1]$ with similar orthogonality properties.

[7]The largest eigenvalue of $\mathcal{L}$ can be obtained using $-\mathcal{L}$ as an input. However, its largest eigenvalue is equal to the opposite of the minimal one, i.e. $E_{\min} = -E_{\max}$. This is because the eigenvalues of $\mathcal{L}$ correspond to all the possible eigenvalue differences of the Hamiltonian $\mathcal{H}$.

with $W' = 1 - \varepsilon/2$, where $\varepsilon = 0.025$ is a numerical safeguard to ensure that $\omega' \in [-1, 1]$ and $a = W/2W'$. The Chebyshev vectors $|t_n\rangle$ are constructed through the recursion relation,

$$|t_n\rangle = 2\mathcal{L}'|t_{n-1}\rangle - |t_{n-2}\rangle, \tag{B.33}$$

with $|t_0\rangle = (S^{\upsilon}_{-\mathbf{q}} \otimes \mathcal{I}_Q)|\Psi_\beta\rangle$ and $|t_1\rangle = \mathcal{L}'|t_0\rangle$ as starting point, similarly to Eq. (B.28). The expansion of the spectral function (B.27) reads,

$$S^{\mu\upsilon}_{\mathbf{q}}(\omega) = \frac{1}{a\sqrt{1-\omega'^2}}\left[\langle t_0|t_0\rangle + 2\sum_{n=1}^{\infty}\langle t_0|t_n\rangle T_n(\omega')\right] \Big/ \langle\Psi_\beta|\Psi_\beta\rangle, \tag{B.34}$$

where the overlaps $\langle t_0|t_n\rangle$ are the Chebyshev moments μ_n we need to compute. Although all the operations to carry might seem straightforward here, like applying an MPO to an MPS or computing the overlap between two MPS, there is one, the addition of two MPS $|\Psi\rangle + |\Phi\rangle$ as in the above recursion relation, that is actually a bit tricky, in the sense that it is not simply the element-wise sum of the tensors elements [45]. Indeed, consider,

$$|\Psi\rangle = \sum_{\sigma_1}\sum_{\sigma_2}\cdots\sum_{\sigma_N} A^{\sigma_1}_{a_1} A^{\sigma_2}_{a_1 a_2}\cdots A^{\sigma_N}_{a_{N-1}}|\sigma_1\sigma_2\cdots\sigma_N\rangle, \tag{B.35}$$

and

$$|\Phi\rangle = \sum_{\sigma_1}\sum_{\sigma_2}\cdots\sum_{\sigma_N} B^{\sigma_1}_{b_1} B^{\sigma_2}_{b_1 b_2}\cdots B^{\sigma_N}_{b_{N-1}}|\sigma_1\sigma_2\cdots\sigma_N\rangle. \tag{B.36}$$

The resulting MPS from the addition reads,

$$|\Psi\rangle + |\Phi\rangle = \sum_{\sigma_1}\sum_{\sigma_2}\cdots\sum_{\sigma_N} C^{\sigma_1}_{c_1} C^{\sigma_2}_{c_1 c_2}\cdots C^{\sigma_N}_{c_{N-1}}|\sigma_1\sigma_2\cdots\sigma_N\rangle, \tag{B.37}$$

where $C^{\sigma_n}_{c_{n-1}c_n} = A^{\sigma_n}_{a_{n-1}a_n} \oplus B^{\sigma_n}_{b_{n-1}b_n}$, except for the first and last tensors, made of two indices only; what we have to do here is to form respectively a row vector $C^{\sigma_1}_{c_1} = [A^{\sigma_1}_{a_1}\ B^{\sigma_1}_{b_1}]$ and a column vector $C^{\sigma_N}_{c_{N-1}} = [A^{\sigma_N}_{a_{N-1}}\ B^{\sigma_N}_{b_{N-1}}]^{\mathrm{T}}$. Surprisingly, the addition of two MPS of respective virtual dimensions D_Ψ and D_Φ leads to a new MPS of virtual dimension $D_\Psi + D_\Phi$. Of course, the new MPS representation of the state resulting from the addition might be uneconomical, e.g., performing $|\Psi\rangle + |\Psi\rangle = 2|\Psi\rangle$ should not lead to a growth of the virtual dimension but just to a rescaling of the tensor elements by a factor 2. Hence, following the addition of two MPS, it is advisable to perform a singular value decomposition in order to compress it to a lower virtual dimension D if possible, without loosing too much information.

What is computationally difficult with this method is to accurately compute the MPS $|t_n\rangle$ or equivalently the Chebyshev moments μ_n to reconstruct the spectral function (B.34) in a second step. The recursive way to compute Chebyshev vectors by successive multiplication and additions makes the virtual dimension of $|t_n\rangle$ grow and require some control and truncation. This limits the maximum order n reliably accessible in the Chebyshev expansion. Due to the finite $n \leq N_{\mathrm{cheb}}$ truncation which introduces artificial oscillations of period $\sim 1/N_{\mathrm{cheb}}$, we attach a damping factor to the moments $\mu_n \to g_n\mu_n$. There are multiple choices for g_n, and we employ in our case a Jackson damping [276] given by,

$$g_n = \frac{(N_{\mathrm{cheb}} - n - 1)\cos\frac{\pi n}{N_{\mathrm{cheb}}+1} + \sin\frac{\pi n}{N_{\mathrm{cheb}}+1}\cot\frac{\pi n}{N_{\mathrm{cheb}}+1}}{N_{\mathrm{cheb}}+1}. \tag{B.38}$$

2. Quantum Monte Carlo

Because of the "sign problem" ("phase problem"), real-time dynamics is not accessible in quantum Monte Carlo simulations. Instead, one can compute imaginary-time ($\tau = -it$) correlations and then, a posteriori, analytically continue from the imaginary axis to the real axis. This procedure is difficult due to the limited information contained in the correlation functions in the presence of statistical sampling errors, resulting in a wide range of possible solutions when transforming to real time. I will first explain how to compute $\langle S^{\mu}_{\mathbf{r}}(\tau) S^{\upsilon}_{\mathbf{r}'}(0)\rangle$ within the Stochastic Series Expansion formulation based on Ref. 281, and the analytic continuation will be discussed in the next section.

Measuring diagonal correlation functions We will distinguish two kinds of correlation functions in the following, diagonal (related to the operator S^z) and off-diagonal ones (related to the operators $S^{\pm}$) because they are computed differently within the algorithm. Starting easy, static (equal time) diagonal correlations are straightforwardly computed since a configuration is expressed in the S^z basis. Using the notations introduced in the previous chapter, the static diagonal correlation reads,

$$\langle S^z_{\mathbf{r}} S^z_{\mathbf{r}'}\rangle = \left\langle \frac{1}{M+1}\sum_{p=0}^{M}\Big[\langle\sigma(p)|S^z_{\mathbf{r}}|\sigma(p)\rangle\langle\sigma(p)|S^z_{\mathbf{r}'}|\sigma(p)\rangle\Big]\right\rangle, \tag{B.39}$$

where the outermost average is performed over different Monte Carlo configurations. The sum runs over the M slices p[8]. Also, $|\sigma(p)\rangle$ is obtained after the action of the first p operators of the string on the initial configuration $|\sigma(0)\rangle$. The prefactor $1/(M+1)$ is the normalization of the sum. In the end, all the information required to compute the static diagonal correlation (B.39) is already accessible within the algorithm without much effort. The next question asks if there are equally efficient estimators for time-dependent diagonal correlations? The imaginary-time does not explicitly appear in a Monte Carlo configuration of the stochastic series expansion algorithm, as it would in a standard path integral approach, but one can show [49, 50] that it is related to the propagation index p. Precisely, an imaginary-time separation τ corresponds to a binomial distribution of propagation distances $\Delta p = p' - p \in [0, M]$[9],

$$w(\tau, \Delta p) = \binom{M}{\Delta p}\left(\frac{\tau}{\beta}\right)^{\Delta p}\left(1-\frac{\tau}{\beta}\right)^{M-\Delta p}, \tag{B.40}$$

where $w(\tau, \Delta p)$ is known as the weight factor and $\tau \in [0, \beta]$. Therefore, the diagonal time-dependent correlation function is related to the correlator

$$C^{zz}(\mathbf{r}, \mathbf{r}', \Delta p) = \frac{1}{M+1}\sum_{p=0}^{M}\Big[\langle\sigma(p+\Delta p)|S^z_{\mathbf{r}}|\sigma(p+\Delta p)\rangle\langle\sigma(p)|S^z_{\mathbf{r}'}|\sigma(p)\rangle\Big], \tag{B.41}$$

[8] As already discussed, the $(M-n)$ identity operators in a given operator string are uniformly distributed over all the possible Monte Carlo configurations to sample and do not influence the mapping from index p to imaginary time τ. All calculations here can be performed by only considering the nonidentity operators in the operator string of a given configuration, i.e. one can make the substitution $M \to n$. I find it more convenient to consider a fixed string size M for computational reasons I will explain in the following, but the two approaches can be found in the literature.

[9] One can ensure that Δp is positive thanks to the periodicity $|\sigma(0)\rangle = |\sigma(M)\rangle$ resulting from the cyclic property of the trace in the partition function.

via,

$$\langle S^z_{\mathbf{r}}(\tau) S^z_{\mathbf{r}'}(0)\rangle = \left\langle \sum_{\Delta p=0}^{M} w(\tau, \Delta p) C^{zz}(\mathbf{r}, \mathbf{r}', \Delta p) \right\rangle, \tag{B.42}$$

where the average is performed over different Monte Carlo configurations. Within the algorithm, the computation of $C^{zz}(\mathbf{r}, \mathbf{r}', \Delta p)$ is similar to $C^{zz}(\mathbf{r}, \mathbf{r}', 0)$, with no additional difficulty.

Measuring off-diagonal correlation functions The computation of the off-diagonal time-dependent correlation function $\langle S^{\mp}_{\mathbf{r}}(\tau) S^{\pm}_{\mathbf{r}'}(0)\rangle$ is more involved, since the off-diagonal operators introduce highly non-local changes to a configuration. An analogous problem occurred when trying to define an efficient update scheme satisfying detailed balance for the off-diagonal operators in the first chapter, and led to the development of the directed loop update algorithm. The proposed strategy is to compute on the fly, directly during the loop update process, the correlator $C^{\pm\mp}(\mathbf{r}, \mathbf{r}', \Delta p)$ such that

$$\langle S^{\pm}_{\mathbf{r}}(\tau) S^{\mp}_{\mathbf{r}'}(0)\rangle = \left\langle \sum_{\Delta p=0}^{M} w(\tau, \Delta p) C^{\pm\mp}(\mathbf{r}, \mathbf{r}', \Delta p) \right\rangle. \tag{B.43}$$

The (directed) loop update algorithm can be pictured as a worm moving in the configuration space making a closed loop at the end. The loop consists of I successive intervals or segments between the exit leg of an off-diagonal vertex and the entrance leg of the next off-diagonal vertex encountered in the loop. The interval edges consist of one operator $S^{\pm}$ acting at positon $\mathbf{r}$ in space and p along the propagation axis. The worm has a fixed tail, corresponding to the starting point or first interval edge. During the loop update, its head will pop out and slip from one edge to the other until it bites its own tail, marking the end of the off-diagonal update. Rather than positioning the off-diagonal operators on the edges of the intervals, they can be put on the worm's head: every time the worm enter a new interval, a new operator is attached to it. In its path, the worm modify a state $|\sigma(p)\rangle$ of the configuration space to $|\tilde{\sigma}(p)\rangle$. The off-diagonal correlators can be measured between the operator positioned at the tail and the moving head of the worm, both separated by Δp propagation indices. If during the update process the head and tail are at the same propagation index $\Delta p = 0$ (they can be at different positions $\mathbf{r}$ in space), the off-diagonal correlator reads,

$$C^{\pm\mp}(\mathbf{r}, \mathbf{r}', \Delta p = 0) = \langle \tilde{\sigma}(p) | S^{\pm}_{\mathbf{r}} S^{\mp}_{\mathbf{r}'} | \sigma(p)\rangle, \tag{B.44}$$

and for $\Delta p \neq 0$,

$$C^{\pm\mp}(\mathbf{r}, \mathbf{r}', \Delta p) = \langle \tilde{\sigma}(p) | S^{\pm}_{\mathbf{r}} | \sigma(p)\rangle \langle \tilde{\sigma}(p + \Delta p) | S^{\mp}_{\mathbf{r}'} | \sigma(p + \Delta p)\rangle, \tag{B.45}$$

where $S^{\mp}_{\mathbf{r}}$, $S^{\mp}_{\mathbf{r}'}$ are the operator located at the tail and at head of the worm respectively.

In practice, recording all the measured correlators will drastically reduce the efficiency of the loop update algorithm. Plus, the storage table of all the correlators $(\mathbf{r}, \mathbf{r}', \Delta p)$ is huge and intractable in practice for memory related issues since every time the worm's head slip from one propagation index p to $p + 1$ a new correlator has to be measured. Workarounds need to be found. Regarding memory, a finite set of $\{\tau\}$ points is defined beforehand. With a fixed number M of operators in

the string, the weight factors $w(\tau, \Delta p)$ can be computed after the thermalization process once and for all. The size of storage table now scales as $\mathcal{O}(N^2 \text{size}\{\tau\})$ rather than $\mathcal{O}(N^2 M)$ with N the total number of degrees of freedom. Using translation invariance or going in momentum space $|\mathbf{r} - \mathbf{r}'| \to \mathbf{q}$, the scaling factor N^2 can be reduced to N. Regarding the slowing down of the loop update by the measurements, one can realize that within a given interval, the correlator remains constant, and the contribution of an entire interval to $\langle S^{\pm}_{\mathbf{r}}(\tau) S^{\mp}_{\mathbf{r}'}(0)\rangle$ in one step,

$$\langle S^{\pm}_{\mathbf{r}}(\tau) S^{\mp}_{\mathbf{r}'}(0)\rangle = \left\langle \sum_{i=1}^{I} C^{\pm\mp}(\mathbf{r}, \mathbf{r}', i) \Big[W(\tau, p_{i,2}) - W(\tau, p_{i,1}) \Big] \right\rangle, \tag{B.46}$$

where $C^{\pm\mp}(\mathbf{r}, \mathbf{r}', i)$ is the constant correlator value on an entire interval $i \in]p_{i,1}, p_{i,2}]$ of the propagation axis and $W(\tau, \Delta p) = \sum_{n=0}^{\Delta p} w(\tau, n)$ is called the integrated weight function.

3. Stochastic Analytic Continuation

The analytic continuation from imaginary-time τ to real-time t (or frequencies ω) of the correlation functions is done by inverting the Laplace transform $\mathfrak{L}$,

$$S(\tau) = \mathfrak{L}\Big[S(\omega)\Big](\tau) = \frac{1}{\pi} \int_{-\infty}^{+\infty} \mathrm{d}\omega \; \mathrm{e}^{-\tau\omega} \; S(\omega), \tag{B.47}$$

where I have purposely omitted the various indices usually attached to the spectral function for readability. The inverse Laplace transform is not readily done numerically: $\mathfrak{L}[S(\omega)](\tau)$ will uniquely determine $S(\tau)$ but the inverse operation, namely recovering $S(\omega)$ from $S(\tau)$ will not. In other words, arbitrarily small changes in $S(\tau)$ can produce arbitrarily large changes in the value of $S(\omega)$. Due to the numerical precision or more specifically the Monte Carlo sampling errors, the operation to carry is an *ill-conditioned* (unstable) problem since the errors in the measurement data may lead to indefinitely large errors in the solutions [282], hence an infinite number of possible solutions. Fortunately in physics, the functions $S(\omega)$ we are looking for have specific features or some that can be excluded, i.e. there is usually no high-frequency components, especially at low-temperature and, as a matter of fact, these functions are actually quite smooth[10]. This may help in choosing among possible solutions the most probable ones.

Many methods have been developed to overcome this issue, but all are far from solving it reliably in all cases and with a perfect control the problem, which is mathematically ill-posed anyway. To illustrate the wide range of methods, I will cite the singular value decomposition method [283, 284], the non-negative least-squares method [285], the method of consistent constraints [286] and the Padé approximants which consists of parametrizing the numerical function by means of a ratio of two polynomials, or equivalently by a terminating continued fraction and then analytically continuing the Padé expression to real frequencies [287–289]. Most commonly used (or known) in the condensed matter theory community is the "Maximum Entropy" method [259, 290–294] of which we will briefly recall the main ideas before moving to the stochastic analytic continuation (SAC) method that I used in my work, following Ref. 262.

[10] Except for possible singular $\delta(\omega)$ peak contributions.

General definitions As discussed in the previous section, quantum Monte Carlo simulations provide the imaginary time correlation $S(\tau)$ for a finite set of τ_i points with $i = 1, 2, \ldots, N_\tau$. The data are correlated in two ways: first, successive measurements result from close configurations and several Monte Carlo updates are required before fully decorrelating consecutive measurements. Then at a given measurement step in the Monte Carlo algorithm the data at different τ points are also correlated because they result from exactly the same configuration. Unless working with a different simulation for each of the τ points, this second source of correlations is *inevitable*. A simple standard deviation to evaluate the error bars is not enough and their full characterization requires the covariance matrix, which can be evaluated with the Monte Carlo data divided up into a large number of bins N_b,

$$C_{ij} = \frac{1}{N_b(N_b-1)} \sum_{b=1}^{N_b} \Big[S_b(\tau_i) - S(\tau_j)\Big] \Big[S_b(\tau_j) - S(\tau_i)\Big] \tag{B.48}$$

where the average of the Monte Carlo data of a bin b is noted $S_b(\tau_i)$ and the global average by $S(\tau_i) = \sum_b^{N_b} S_b(\tau_i)$. In our case, a bin is comprised of a thousand successive measurements such that data in different bins are uncorrelated. The diagonal elements of the covariance matrix C_{ij} are the squares of the standard statistical errors, i.e. $\sigma_i^2 = C_{ii}$, and all other elements $i \neq j$ would be zero only if the data at different τ points were strictly independent. The numerical analytic continuation performed by the maximum entropy or stochastic analytic continuation methods is based on the parametrization of the spectral function such as a large number of δ functions with adjustable positions and amplitudes in the frequency domain. These parameters are adjusted such that the Laplace transform (B.47) of the proposed spectrum provides imaginary-time data $\tilde{S}(\tau)$ close to the real ones obtained by QMC in the sense of the "goodness of fit",

$$\chi^2\Big[S(\omega)\Big] = \sum_{i,j=1}^{N_\tau} \Big[S(\tau_i) - \tilde{S}(\tau_j)\Big] C_{ij}^{-1} \Big[S(\tau_j) - \tilde{S}(\tau_i)\Big]. \tag{B.49}$$

However, minimizing χ^2 does not produce useful results since the best solution consists of a typically small number of sharp peaks [295, 296], not counting the many other very different solutions with almost the same χ^2 value, reflecting the ill-conditionned nature of the inverse of the Laplace transform. The maximum entropy or stochastic analytic continuation methods provide some regularization mechanism to overcome this. In the first one, the entropy E (as in information theory) of the spectrum with respect to a default model $D(\omega)$ is defined as $E[S(\omega)] = -\int_{-\infty}^{\infty} \mathrm{d}\omega\, S(\omega) \ln[S(\omega)/D(\omega)]$ [259, 290–294]. The default model is a smooth function that serves as the zero (maximum) entropy configuration and which can hard code any features of the true spectral function if known in advance. The maximum entropy method solution is the function that minimizes $Q[S(\omega)] = \chi^2 - \alpha E$ with α a parameter that controls the degree of regularization. One can show that the likelihood of any spectral function $S(\omega)$ to be the true spectral function is equal to $P[S(\omega)] \propto \mathrm{e}^{-Q[S(\omega)]}$. The minimization of Q can be performed using Newton's method for instance, and numerous ways of defining α exist in literature: a compromise between over-fitting ($\alpha = 0$) and over-smoothing by $D(\omega)$ ($\alpha \to \infty$).

The Stochastic Analytic Continuation In the stochastic analytic continuation (SAC), the entropy is not imposed explicitly but is generated implicitly by a Monte Carlo sampling procedure of a suitably parametrized spectrum [296–299]. In the SAC method, a spectrum $S(\omega)$ is sampled according to the probability distribution,

$$P\Big[S(\omega)\Big] \propto \exp\left(-\frac{\chi^2}{2\Theta}\right), \tag{B.50}$$

with χ^2 the goodness of the fit defined in Eq. (B.49) and Θ a fictitious temperature (this is a parameter) playing a regularization role similar to the paramater α in the Maximum Entropy method [297]. Indeed, making the connection with a statistical-mechanics problem, $\chi^2/2$ plays the role of an energy and Θ of the temperature. At low temperature, the Monte Carlo will lead to low-energy configurations (spectrums with a small $\chi^2/2$) whereas in the limit $\Theta \to +\infty$, all configurations (all spectra, independently of their χ^2) have the same probability (B.50). Hence, the value of Θ is very important and needs to be carefully set. I will discuss a scheme of fixing the temperature in the following and first discuss a parametrization for the spectrum as well as the Monte Carlo method engineered in the SAC. For convenience, we redefine the Laplace transform (B.47) such that it now reads,

$$S(\tau) = \int_0^{+\infty} \mathrm{d}\omega\; K(\tau,\omega)\; \tilde{S}(\omega), \quad \text{with } K(\tau,\omega) = \frac{\mathrm{e}^{-\tau\omega} + \mathrm{e}^{-(\beta-\tau)\omega}}{1+\mathrm{e}^{-\beta\omega}}, \tag{B.51}$$

where $\tilde{S}(\omega) = S(\omega)(1+\mathrm{e}^{-\beta\omega})$. We have used the fact that $S(-\omega) = \mathrm{e}^{-\beta\omega}S(\omega)$ and that $\tau_{\max} = \beta$ with the symmetry property $S(\tau \geq \beta/2) = S(\beta-\tau)$. Basically, it means that the computation of the dynamical correlation functions can be reduced to $\tau \leq \beta/2$ and the parametrization of the spectral function $\tilde{S}(\omega)$ to positive frequencies. It is parametrized as the sum of a large number N_δ of δ functions,

$$\tilde{S}(\omega) = \sum_{n=1}^{N_\delta} a_n \delta(\omega - \omega_n), \quad \text{with } \sum_{n=1}^{N_\delta} a_n = S(\tau=0), \tag{B.52}$$

where the normalization constraint on the δ functions amplitude ensures the right sum rules for the spectral function[11]. In practice, we have used $N_\delta = 500$, all of fixed different amplitudes $a_n = n$, but with a position ω_n in frequency space that will be optimized by the Monte Carlo. We restrict the frequency space to the interval $\omega_n \in [0, \omega_{\max}]$ where $\omega_{\max}$ needs to be sufficiently large such that the spectral function should have a negligible weight above this threshold, e.g. we have used $\omega_{\max} = 10$ in our works. Because every Monte Carlo movement will require the computation of χ^2 to know if it is accepted or rejected, it is useful to use a discrete frequency space rather than working in the continuum, e.g. a small frequency step $\Delta_\omega = 0.05$ was used in practice. This way, the Kernel $K(\tau,\omega)$ can be computed once and for all at the beginning and the computation of the Laplace transform (B.47) reads $\tilde{S}(\tau) = \sum_n a_n K(\tau,\omega_n)$. Moreover, it is also useful to work in the eigenbasis of the covariance matrix (B.48), which lightens numerical operations for the computation of χ^2.

[11] We have the sum rule corresponding to the zero time and zero space correlation function, $S^{\mu\upsilon}_{\mathbf{r}=\mathbf{0}}(t=0) = S^{\mu\upsilon}_{\mathbf{r}=\mathbf{0}}(\tau=0) = \langle S^\mu_{\mathbf{r}} S^\upsilon_{\mathbf{r}}\rangle$ where the last term is usually very easily computed exactly for $S^\mu_{\mathbf{r}} = (S^\upsilon_{\mathbf{r}})^\dagger$.

We have used two different Monte Carlo updates to move the δ functions in the frequency space. The first one randomly picks a δ function amongst the N_δ available and randomly suggest a new position $\omega_n \to \omega_n + d$ with d chosen at random within a window centered at $d = 0$. The width of the window is adjusted during the Metropolis algorithm to give an acceptance rate close to 0.5. Similarly, the second update randomly picks two δ functions at a time and try to move them independently in the frequency space. After thermalization, the spectrums are collected and averaged over sufficiently many update steps to obtain smooth results.

The temperature Θ needs to be set in the first place before performing the Metropolis algorithm. As already mentioned, it should not be too small (overfitting), nor too large (then any spectrum would be possible). Hopefully, there exists a range of Θ over which the average $\overline{\chi^2}$ value is small but the fluctuations are significant, and cause an acceptable smoothing of the spectrum. There is no agreement on exactly how the temperature should be chosen, but in general the different schemes proposed in the literature produce very similar results. In our work, the adopted strategy is to perform a simulated annealing by adjusting successively the value of the temperature, as in Refs. 261 and 262. We start with a large value $\Theta_{\text{init}} = 100$ and perform Monte Carlo updates as describe above. The average $\overline{\chi^2}$ along with the variance $\sigma_{\chi^2} = \overline{(\chi^2)^2} - \overline{\chi^2}^2$ is computed over a sufficient number of spectrums and saved along with the value of Θ. In the next step the temperature is reduced, e.g. $\Theta_{\text{step}} = \Theta_{\text{prev. step}}/1.1$, and the measurement of $\overline{\chi^2}$ and σ_{χ^2} is repeated. It has been found that a "good value" is given by,

$$\overline{\chi^2}\Big(\Theta_{\text{good}}\Big) \approx \min\left[\overline{\chi^2}\Big(\Theta\Big)\right] + a\sigma_{\chi^2}, \tag{B.53}$$

with a a constant of order one. There is a simple hand-waving argument in favor of this choice for the temperature. The idea is to add one standard deviation to the minimum average $\overline{\chi^2}$. Indeed, if one sees N_τ as the number of degrees of freedom as in a simple fitting procedure in the computation of χ^2 (B.49), then one standard deviation corresponds roughly to the removal of distortions due to "fitting to the statistical errors". This choice has proven to to provide excellent results [261, 262].

III. One-dimensional spin systems

Adapted from the work Phys. Rev. B **94**, 144409 (2016)

Maxime Dupont, Sylvain Capponi, and Nicolas Laflorencie

I will present results of numerical simulations performed on one-dimensional spin chains in order to extract the so-called spin-lattice relaxation rate $1/T_1$ accessible through NMR experiments [250]. Building on numerical tensor network methods using the Matrix Product States formalism, we can follow the non-trivial crossover occurring in critical chains between the high-temperature diffusive classical regime and the low-temperature response described by the Tomonaga-Luttinger liquid (TLL)

theory, for which analytical expressions are known. In order to compare analytics and numerics, we focus on a generic spin-1/2 XXZ chain which is a paradigm of gapless TLL, as well as a more realistic spin-1 anisotropic chain, modeling the DTN material discussed in the previous chapter and which can be either in a trivial gapped phase or in a TLL regime induced by an external magnetic field. Thus, by monitoring the finite temperature crossover, we provide quantitative limits on the range of validity of TLL theory, that will be useful when interpreting experiments on quasi-one-dimensional compounds.

The NMR $1/T_1$ spin-lattice relaxation rate contains lots of information on the dynamical properties of the system since it is directly related to dynamical spin-spin correlations. Moreover, being a local quantity, a crucial property of NMR technique, we will argue that reliable data can be obtained even though we will simulate finite spin chains. Being of fundamental interest, the low temperature behavior of the NMR relaxation rate has been investigated for several one-dimensional or quasi-one-dimensional quantum magnets. Spin-gapped compounds, such as two-leg ladders $SrCu_2O_3$ [300], $BiCu_2PO_6$ [301], $Sr_{14-x}Ca_xCu_{24}O_{41}$ [302], weakly coupled Haldane chains Y_2BaNiO_5 [303], or dimerized spin chains $AgVOAsO_4$ [304], exhibit an activated relaxation at low temperature. For gapless Heisenberg chain systems, the low-energy critical behavior has been studied [305–308] for Sr_2CuO_3 which is an almost ideal realization with a large one-dimensional exchange interaction $J \sim 2000$ K and much smaller three-dimensional couplings so that the ordering temperature is pushed down to $T_c \simeq 5$ K. For such an SU(2) symmetric compound[12], a careful comparison of experimental and numerical NMR data has shown the prominent role of logarithmic corrections [309]. Another route to TLL behavior is to apply an external magnetic field on gapped materials such as spin-1 Haldane gap compound [310] $(CH_3)_4NNi(NO_2)_3$ or dimerized spin-1/2 chains [311]. For such systems, a theoretical analysis of the $1/T_1$ behavior has been performed in Refs. 312 and 166. A useful experimental review on NMR properties of several spin chains can be found in Ref. 313. Note also that $1/T_1$ measurements have also been used to characterize one-dimensional metallic phase in carbon nanotube [314] or quasi-one-dimensional superconductor [315].

More recently, interesting quasi-one-dimensional spin-gapped materials have also been investigated using NMR [316]: an anisotropic spin-1 system $NiCl_2$-$4SC(NH_2)_2$ (DTN) and a spin-ladder one $(C_5H_{12}N)_2CuBr_4$ (BPCB). In both cases, $1/T_1$ measurements could be interpreted either as coming from magnon (respectively spinon) excitations in the gapped (respectively gapless) one-dimensional phase, and the quantum critical regime was also argued to be universal. Most importantly, the whole temperature range, including one-dimensional as well as three-dimensional regimes, was discussed. Experimentally, when decreasing temperature, the NMR relaxation rate $1/T_1$ has been found to diverge in the TLL regime, with power-law governed by a characteristic exponent. Such an analysis is used in experiments to determine the corresponding TLL exponent K [317, 318]. For example, it was a smoking-gun signature of attractive TLL in $(C_7H_{10}N)_2CuBr_4$ (DIMPY) compound [173, 319]. However, given that we are generically dealing with quasi-one-dimensional materials, critical fluctuations and three-dimensional ordering will limit the low-energy one-dimensional

[12]Since the NMR technique requires an external magnetic field, the SU(2) symmetry (which is experimentally never exact anyway) is theoretically broken. However, the energy coupling J being immensely large in this compound, the applied magnetic field is negligible.

regime, and a genuine TLL critical behavior is observable only within some finite window in temperature.

1. Models and predictions

Studied models Although both models that we studied in this work have already been introduced in the previous chapter, I will briefly recall them here for consistency. We first considered one of the simplest paradigmatic example of TLL liquid, namely the spin-1/2 XXZ chain Hamiltonian:

$$\mathcal{H}_{\mathrm{XXZ}} = J \sum_{j=1}^{N-1} \left[\frac{1}{2} \left(S_j^+ S_{j+1}^- + S_j^- S_{j+1}^+ \right) + \Delta S_j^z S_{j+1}^z \right] - H \sum_{j=1}^{N} S_j^z \tag{B.54}$$

where $\Delta \in (-1, 1]$ denotes the Ising anisotropy, J the coupling strength and H is an applied magnetic field along the same direction as the anisotropy. The Hamiltonian is defined with open boundary conditions here, as will be used in our numerical simulations. In the range $\Delta \in (-1, 1]$ the XXZ model can be described by a TLL as long as its spectrum remains gapless [37]. As a function of magnetic field, the gapless regimes extends up to a critical field $H_c = J(\Delta + 1)$, and the system becomes gapped for $H > H_c$. In the latter regime, the gap increases linearly with the applied magnetic field, $\Delta_g = H - H_c$.

We also discuss the quasi-one-dimensional magnetic insulator compound "DTN", whose relevant three-dimensional structure consists of weakly coupled $S = 1$ chains in the two other transverse (with respect to the chain axis) directions. Although there is three-dimensional magnetic order observed below $T_c \sim 1.2$ K [230] due to weak interchain couplings along the two transverse directions, $J_\perp/J \simeq 0.08$, one expects one-dimensional physics and a TLL regime at higher T. The effective Hamiltonian to describe this situation reads

$$\mathcal{H}_{\mathrm{DTN-1D}} = J \sum_{j=1}^{N-1} \mathbf{S}_j \cdot \mathbf{S}_{j+1} + \sum_{j=1}^{N} \left[D \left(S_j^z \right)^2 - g\mu_B H S_j^z \right], \tag{B.55}$$

where $\mathbf{S}_j = (S_j^x, S_j^y, S_j^z)$ are spin-1 operators and $J = 2.2$ K is the one-dimensional antiferromagnetic coupling and $D = 8.9$ K is the single-ion anisotropy. The magnetic field H is given in Tesla with $g = 2.31$. In the absence of magnetic field, due to the large on-site anisotropy D, the system is in the so-called large-D phase [235]. This is a trivial phase, adiabatically connected to the product state $|00\cdots0\rangle$ where each spin is in a non-magnetic $S^z = 0$ state. Clearly, this phase has a finite spin-gap, which corresponds to the first critical field H_{c1} needed to magnetize the system. Its value is known to be, at first order in $J/D \ll 1$ [237]: $H_{c1}/g\mu_B = D - 2J + \mathcal{O}(J^2/D) \simeq 3$ T. At finite magnetic field there is a gapless TLL regime for $H \in [H_{c1}, H_{c2}]$, with $H_{c2}/g\mu_B = D + 4J = 11.4$ T. Above this critical saturation field, the system becomes gapped again, entering a fully polarized phase. In the TLL phase and close to the upper critical field H_{c2}, the DTN Hamiltonian can be mapped toward an effective XXZ model of spins $S = 1/2$. Using perturbation theory, effective parameters [316, 320] are given by $J \to 2J$ and $\Delta = 0.5$. This result can be refined using contractor renormalization method [321, 322] leading to the same value of J but a slightly reduced $\Delta = 0.36$. Both mappings lead to a value of the effective magnetic field $H \to H - J - D$.

Tomonaga-Luttinger Liquid prediction for the NMR relaxation rate Let us first recall that the retarded dynamical spin susceptibility within the linear response theory is given by the Kubo formula as,

$$\chi^{\mu\nu}_{\mathbf{q}}(\omega) = i\sum_{\mathbf{r}}\int_{-\infty}^{+\infty} \mathrm{d}t\, \mathrm{e}^{i(\omega t - \mathbf{q}\cdot\mathbf{r})}\Theta(t)\left\langle\left[S^{\mu}_{\mathbf{r}}(t), S^{\nu}_{\mathbf{0}}(0)\right]\right\rangle, \tag{B.56}$$

where $\Theta(t)$ is the Heaviside function ensuring causality. Precisely, the susceptibility corresponds to the linear response of the observable $S^{\mu}_{\mathbf{r}}(t)$ to an external time and space-dependent perturbation $H_{\mathbf{r}'}(t)$ such as magnetic field of the type $H^{\nu}_{\mathbf{r}'}(t)S^{\nu}_{\mathbf{r}'}$. The susceptibility can be related to the spectral function by [21],

$$\mathrm{Im}\left[\chi^{\mu\nu}_{\mathbf{q}}(\omega)\right] = \frac{1-e^{-\beta\omega}}{2} S^{\mu\nu}_{\mathbf{q}}(\omega). \tag{B.57}$$

In the one-dimensional Tomonaga-Luttinger Liquid framework, the dynamical susceptibility $\chi^{\mu\nu}_{q}(\omega)$ can be computed exactly for the longitudinal (zz) and transverse components ($\pm\mp$) [37, 323]. In the limit $\beta\omega \ll 1$, the exponential in Eq. (B.57) is expanded to first order $\mathrm{e}^{-\beta\omega} \simeq 1-\beta\omega$ and the temperature dependence of the spectral function in the limit $\omega \to 0$, corresponding to the NMR frequency, can be extracted [166, 210, 323],

$$\frac{1}{T_1^{\perp}} = \frac{A_0 \cos\left(\frac{\pi}{4K}\right)}{u}\left(\frac{2\pi T}{u}\right)^{\frac{1}{2K}-1} B\left(\frac{1}{4K}, 1-\frac{1}{2K}\right), \tag{B.58}$$

and

$$\frac{1}{T_1^{\parallel}} = \frac{A_1 \cos(\pi K)}{2u}\left(\frac{2\pi T}{u}\right)^{2K-1} B(K, 1-2K) + \frac{KT}{4\pi u^2}, \tag{B.59}$$

with $B(x,y)$ the Euler Beta function, u and K the usual TLL parameters and $A_{0,1}$ prefactors of the static correlation functions. Generically $1/T_1^{\perp}$ diverges as we approach zero temperature as a K-dependent power-law, and dominates over $1/T_1^{\parallel}$. Note that for finite magnetic field, additional subleading corrections are expected [324].

2. Spin-1/2 XXZ chain

Case study of the non-interacting point As a benchmark, we will first be interested in the XXZ Hamiltonian (B.54) at $\Delta = H = 0$ that can be mapped onto a model of non-interacting spinless fermions at half-filling using a Jordan-Wigner transformation, as already discussed in the first chapter. It can easily be diagonalized in Fourier space and one can make use of the fermionic nature of the operators through Wick's theorem to compute analytical expressions of the dynamical correlation functions $\langle S^{\mu}_{r}(t) S^{\nu}_{r}(0)\rangle$ required to obtain the NMR relaxation rate $1/T_1$ [325, 326]. Unlike the TLL expressions (B.58) and (B.59) which are only valid in the low-energy limit, the results presented in this section will be valid for all regimes. We show the "bare" results in Fig. B.3. Ideally, one is interested in the thermodynamic limit but we see that, at finite temperature (hence finite correlation length), working on finite length chains with only a moderate number of sites N allows to get reliable

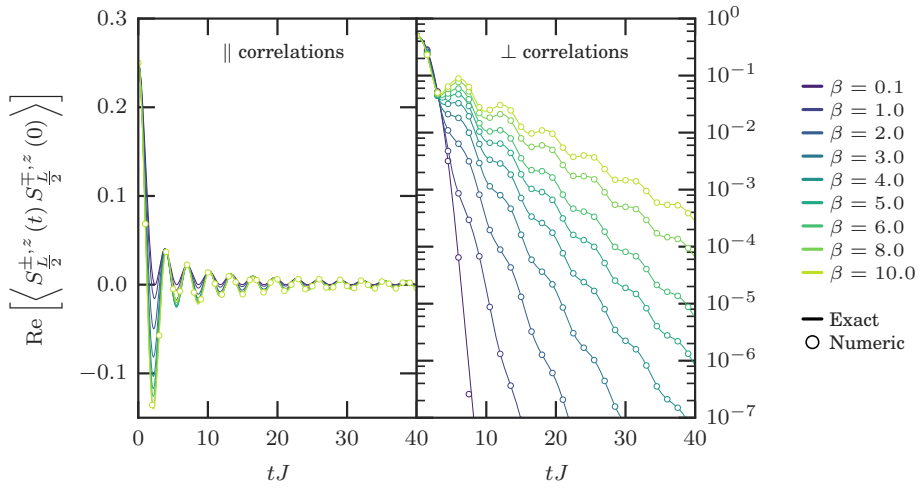

Figure B.3: We compare numerical results (circles) used to determine the $1/T_1$ with analytical results (straight lines) for the XX model. For the transverse ($\perp$) case, exact results are computed on a chain of size $N = 64$. As for the longitudinal ($\parallel$) case, the chain size is $N = 1000$. Numerics on their side are performed on a chain of $N = 64$ sites. The left panel shows the real value of the dynamical correlations. For readability, we only display numerical results for the lowest temperature for the longitudinal correlations. Indeed, this is a priori the hardest to compute and thus the most subject to errors.

data. Indeed, the MPS estimates agree perfectly with the exact expressions. First of all, we consider the local dynamical correlation of the site in the middle of the chain reducing de facto boundary effects. Then, as finite size effects are known to be caused by the reflection of the propagating excitations at TLL velocity u on the boundary of the system, one can estimate a time below which the dynamical correlations can be considered as free of finite size effects , basically $ut \sim N$. We first discuss the transverse correlations, see Fig. B.3. For all temperatures, they decay rather quickly to zero, so that we can safely truncate data to a maximum time $t_{\max}$ and get reliable values of $1/T_1^{\perp}$ by integrating over time. Moreover, we have also checked that finite size effects are extremely small since we are computing a local correlation. The same cannot be said for the longitudinal correlations. They continue to oscillate even for high temperatures and long times, and their amplitude gets (very) slowly smaller with time. This implies severe limitations to get data in the thermodynamic limit. For instance, exact computations were done on $N = 1000$ and still displayed oscillations of amplitude around 10^{-4} at $tJ = 1000$. This makes the value of $1/T_1^{\parallel}$ very difficult to estimate. This well-known behavior is related to spin diffusion-like behavior [327, 328] which causes a logarithmic divergence at small frequency ω. However, we have to remember that the NMR frequency ω_0 eventually provides a natural cutoff.

Extending to the whole XXZ regime Building on the perfect agreement observed previously between MPS estimates and the exact analytical solution of the XX model, we are now confident to extend our study to the more generic XXZ case $-1 < \Delta \leq 1$, described by a TLL, and compute the relaxation rates. Results are plotted in Fig. B.4 for various values of the anisotropy. The simulations were performed on systems of size $N = 64$ with a cutoff of $\varepsilon = 10^{-10}$ in the singular values. We kept a maximal

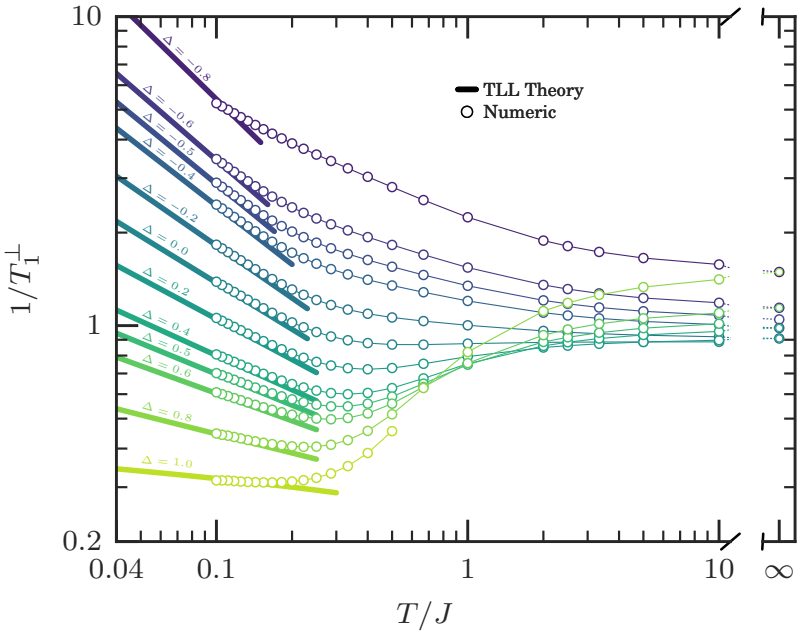

Figure B.4: Transverse relaxation rate $1/T_1^\perp$ versus reduced temperature T/J for the spin-1/2 XXZ chain at various Δ and $H = 0$ obtained numerically using MPS techniques (circles, from top to bottom: $\Delta = -0.8, -0.6, -0.5, -0.4, -0.2, 0.0, 0.2, 0.4, 0.5, 0.6, 0.8, 1$). Numerics are compared to TLL theory Eq. (B.58) at low temperature (thick lines) for $|\Delta| < 1$, and with Eq. (B.60) for the SU(2) Heisenberg point $\Delta = 1$. The thin lines between the circles are guides to the eyes.

number of $D = 500$ states. A fourth order Trotter decomposition was used with a Trotter step of $\tau = 0.1$.

First, in the gapless regime we do observe an excellent quantitative agreement between numerical estimates and the TLL prediction Eq. (B.58) at low enough temperature. This asymptotic regime with a power-law behavior $\sim T^{1/2K-1}$ occurs only below $T/J \sim 0.1 - 0.2$ (depending on the anisotropy Δ). Here we stress that there are no free parameters in the analytic expressions, the TLL parameters being known exactly. The isotropic limit $\Delta = 1$ is a special point where logarithmic corrections appear in several quantities [58, 72, 75], leading to a very slow divergence of the isotropic NMR relaxation rate [308, 329],

$$\frac{1}{T_1} \simeq \frac{1}{\sqrt{2\pi^3}} \sqrt{\ln \frac{\Lambda}{T} + \frac{1}{2} \ln \left(\ln \frac{\Lambda}{T} \right)}, \tag{B.60}$$

where $\Lambda \simeq 24.27J$. MPS estimates compare well with this parameter-free expression, as visible in Fig. B.4. Interestingly, we notice the non-monotonic behavior of $1/T_1^\perp$ with temperature only when $\Delta \gtrsim 0$ (which corresponds to repulsive or vanishing interactions in the fermionic language). As a last comment, we have observed that for infinite temperature ($\beta = 0$), the value of $1/T_1^\perp$ does not depend on the sign of Δ, which is expected since the many-body spectrum of $\mathcal{H}(\Delta)$ is an odd function of Δ. Its value is minimum for $\Delta = 0$ with $1/T_1^\perp = \sqrt{\pi}/2J$ [330] and increases with $|\Delta|$. At the isotropic point $|\Delta| = 1$ we expect the relaxation rate to diverge due to the diffusion-like behavior [327, 328] of the dynamical correlation function. Our

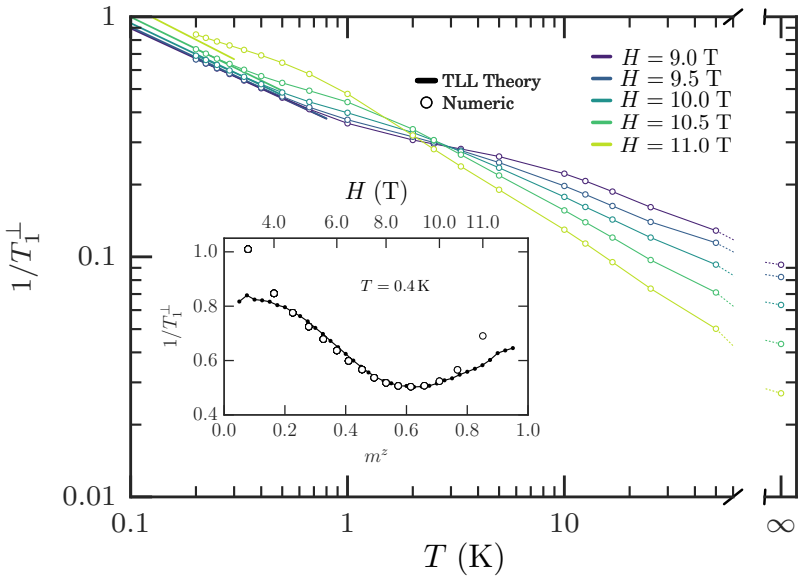

Figure B.5: Transverse relaxation rate $1/T_1^\perp$ plotted versus temperature T for the spin-1 DTN chain obtained numerically using MPS techniques (circles). The low temperature behavior is compared to TLL prediction (straight lines). The magnetic field H is given in Tesla. The inset compares TLL prediction (straight dotted line) and numerical results for $T = 0.4$ K (circles) and covers the whole TLL phase from H_{c1} ($m^z = 0$) to H_{c2} ($m^z = 1$).

results at infinite-T go beyond Baker-Campbell-Hausdorff expansion developed up to $\mathcal{O}(t^2)$ in Ref. 331 to compute $\langle S_j^\pm(t) S_j^\mp(0)\rangle$ at short times, which would suggest $1/T_1^\perp \sim 1/J\sqrt{1+\Delta^2}$. This prediction is in contrast to what we found, namely the transverse relaxation rate increasing with $|\Delta|$. Indeed, while such an expansion finds the correct gaussian behavior for $\Delta = 0$, higher-order terms have to be taken into account for $|\Delta| > 0$ where the transverse dynamical correlation function at longer times gets larger when increasing $|\Delta|$.

3. One-dimensional S=1 DTN compound

We now move to the DTN compound in its one-dimensional limit described by Eq. (B.55). We compute the relaxation rates for various values of the magnetic field H, mainly close to H_{c2} which is relevant for NMR experiments [316]. It is a more challenging system to simulate than the XXZ model as it is made of spins $S = 1$ (enlarged local Hilbert space). The simulations were performed on open chains of size $N = 64$ with a cutoff of $\varepsilon = 10^{-10}$ in the singular values. We kept a maximal number of $D = 150$ states. A fourth order Trotter decomposition was used with a Trotter step of $\tau = 0.02$.

Numerical results, shown in Fig. B.5, compare extremely well with TLL prediction at low temperature. Interestingly, the TLL power-law behavior starts at slightly higher temperature, as compared to the XXZ model, $T \simeq 0.5$ K ($T/J \sim 0.2$), especially as we approach the middle of the TLL phase, away from the critical field H_{c2}. We point out that there are again no adjustable coefficients, the TLL parameters versus the magnetic field of the $S = 1$ DTN chain being known from independent

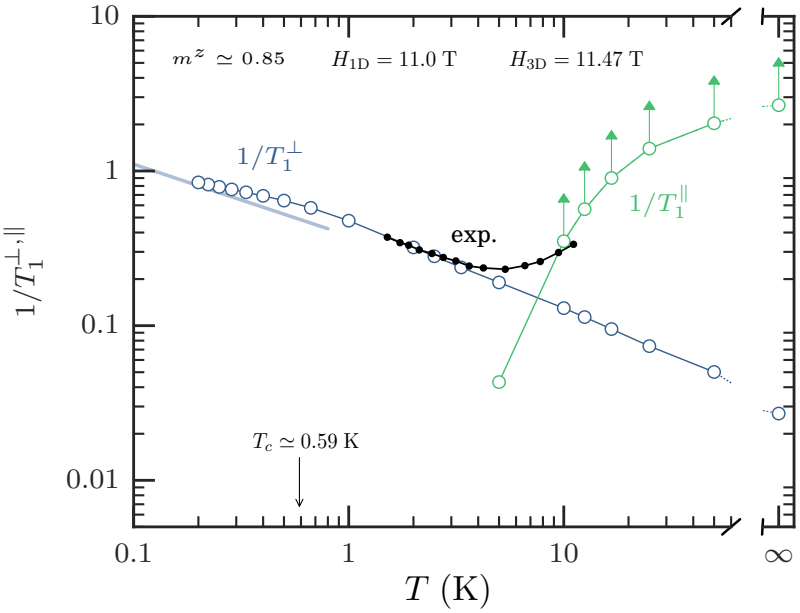

Figure B.6: Longitudinal $1/T_1^{\parallel}$ and transverse $1/T_1^{\perp}$ relaxation rates for the DTN spin-1 chain at $H = 11.0$ T, corresponding to $m^z \simeq 0.85$. As $1/T_1^{\parallel}$ cannot be estimated for sure, we only provide a lower bound. The non-monotonic behavior observed experimentally at high T in Ref. 316 apparently comes from the large contribution of $1/T_1^{\parallel}$ at high temperature. Experimental data for DTN taken from Ref. 316 at the same magnetization are shown for comparison, after a proper rescaling in order to match the low-T regime. The three-dimensional XY transition temperature $T_c(m^z \simeq 0.85) \simeq 0.59$ K is also shown (taken from Ref. 174).

calculations (as discussed in the previous chapter). The tiny difference that appears at low temperature between numerical data and TLL is due to the limited number of states D kept when performing calculations. Though this does not dispute the TLL prediction, it reveals the challenge in such time-dependent simulations. The inset in Fig. B.5 shows the transverse relaxation rate at $T = 0.4$ K for various values of the magnetic field covering the whole range from H_{c1} to H_{c2}. Once more, there is a very good agreement between numerics and TLL theory except when one gets close to the critical fields: for $H = 11.0$ T, the power law is not met yet for the lowest temperature we could reach $T = 0.2$ K. The non-monotonic behavior of $1/T_1^{\perp}$ observed in the XXZ model is absent for the DTN and may seem odd at first place since it can be mapped effectively onto a $S = 1/2$ XXZ chain with $\Delta = 0.5$ or 0.36 and could thus be compared with Fig. B.4. However this non-monotonic variation is observed at high temperature while this mapping is only justified in the low-energy limit.

One can also try to compare the relaxation rates of Fig. B.5 with the NMR data for the DTN compound given in Ref. 316. What draws our attention is the non-monotonic regime of $1/T_1^{\perp}$ observed at high temperature experimentally, which, as we have just discussed, is not theoretically predicted for a single DTN chain. Yet it cannot be attributed to three-dimensional effects as $J_{\perp} = 0.18$ K is very small compared to the temperature T. We then observed that experiments are performed by proton ^{1}H NMR which probes both $1/T_1^{\perp}$ and $1/T_1^{\parallel}$. We therefore interpret this effect

as due to the longitudinal contribution of the relaxation rate. We show in Fig. B.6 both the transverse and longitudinal $1/T_1^{\perp,\parallel}$ as a function of temperature. We cannot precisely estimate the value of $1/T_1^{\parallel}$ due to its dependence on ω_0 (and therefore on our maximum time in numerical simulations) so that we give a lower bound. Its high temperature contribution to the total relaxation rate clearly dominates over the transverse part and explains well the experimental non-monotonic regime at high T. Perhaps more importantly, as displayed in Fig. B.6, the three-dimensional XY ordering observed in DTN [174, 230] for $m^z \simeq 0.85$ at $T_c \simeq 0.59$ K occurs above the asymptotic regime where the genuine TLL power-law behavior is expected. It is therefore impossible to directly extract TLL exponents in DTN, because of interchain effects that eventually lead to an ordering of the coupled TLLs. Ideally we would expect for quasi-one-dimensional systems the TLL description of the NMR relaxation to be valid in the temperature regime $J \gg T \gg J_\perp$ that will be discussed in greater details in the next section, especially regarding the effect of $J_\perp$. Concerning the difficulty to obtain reliable data at high temperature for the longitudinal $1/T_1^{\parallel}$, it is well known that this is due to spin diffusion-like behavior [327, 328]. Therefore, measurements should in principle depend explicitly on the NMR frequency ω_0.

4. Summary and discussions

Performing time-dependent numerical simulations at finite temperature on one-dimensional systems to compute the NMR relaxation rate $1/T_1$, we have discussed the temperature range validity of analytical predictions for two models (i) the paradigmatic example for Tomonaga-Luttinger liquids: the spin-1/2 XXZ chain for various Ising anisotropies, and (ii) a more realistic $S = 1$ Hamiltonian, relevant for experiments on the DTN compound as a function of an external magnetic field. Both models present in some regime a gapless phase that can be described by *low-energy* TLL theory, with a relaxation rate dominated by its transverse component $1/T_1^{\perp} \sim T^{1/2K-1}$ algebraically diverging at low temperature, where K is the dimensionless TLL exponent. We observed that the expected power-law behavior occurs only below $T/J \sim 0.1 - 0.2$, thus defining the low-energy limit of validity of TLL theory an order of magnitude below the energy scale J of the system. It is important to be able to define this limit as TLL predictions are often used experimentally on quasi-one-dimensional compounds to extract the value of K. As a consequence, we believe that it remains experimentally challenging [311], and often impossible, to explore a genuine critical one-dimensional regime in quasi-one-dimensional compounds when J is small and three-dimensional ordering prevents a wide TLL regime. For instance, we have shown that for DTN, the XY ordering temperature is larger than the crossover temperature towards TLL behavior.

We have also studied the transverse relaxation rates of these two models in other regimes than TLL theory: we considered high temperatures, with a peculiar non-monotonic behavior in the $S = 1/2$ XXZ model in the repulsive regime at high T, which does not exist for the one-dimensional $S = 1$ model of DTN. However, such a non-monotonic dependence with temperature at high T is experimentally observed in DTN. We showed that this effect comes from the longitudinal contribution of the relaxation rate $1/T_1^{\parallel}$ dominating at high temperature over the transverse part. We want to emphasize again the role of three-dimensional ordering at finite temperature,

preventing the observation of a one-dimensional TLL regime. As discussed for the particular case of DTN, one needs a hierarchy of energy scale $J \gg T \gg J_\perp$ to be able to directly extract the TLL exponent K from the divergence of $1/T_1$ with T. While completing this work, a related numerical study by Coira *et al.* has appeared [332]. Our results are perfectly compatible with each other when comparison can be made, such as the transverse $1/T_1$ data for a single spin-1/2 XXZ chain with $\Delta \geq 0$.

IV. Weakly coupled spin chains

Adapted from the work arXiv:1806.04913 (2018)

Maxime Dupont[13], Sylvain Capponi, Nicolas Laflorencie, and Edmond Orignac

Extending our previous work on purely one-dimensional systems, we now theoretically address the question of the dynamical response in quantum antiferromagnets for weakly coupled spin chains. Indeed, residual couplings are always present in nature, thus inevitably escaping the theoretical one-dimensional world. In particular, we present a comprehensive theoretical study based on both analytical calculations (bosonization + random phase and self-consistent harmonic approximations) and numerical simulations (quantum Monte Carlo + stochastic analytic continuation) which allows us to describe the full temperature crossover for the NMR relaxation rate $1/T_1$, from one-dimensional Tomonaga-Luttinger liquid physics to the three-dimensional ordered regime, as a function of inter-chain couplings. The dynamical structure factor, directly probing the INS intensity, is also computed for the different regimes.

As widely discussed, a three-dimensional array of weakly coupled spin chains with a coupling J along the chains and $J_\perp \ll J$ in the transverse directions is expected to display three dimensional behavior for $T \lesssim J_\perp$, developing true long-range order. However, at higher temperature this system should exhibit signatures of one-dimensional physics, approximately in the range $J_\perp \ll T \ll J$. This regime has already been identified for several compounds through thermodynamic quantities. For example the specific heat in the quasi-one-dimensional spin-1/2 chain antiferromagnet $BaCo_2V_2O_8$ material [79] and in the metal-organic $S = 1/2$ two-legs ladder system $(C_5H_{12}N)_2CuBr_4$ [80] shows a one-dimensional linear behavior $\propto T$. Another interesting case concerns the (purely one-dimensional) logarithmic corrections predicted by Eggert *et al.* [75] for the magnetic susceptibility of a $S = 1/2$ Heisenberg chain, which has been observed for the quasi-one-dimensional cuprate Sr_2CuO_3 [76–78]. For weakly coupled two-dimensional planes, I presented a work in the first chapter where we studied how smoothly the ordering process of the three-dimensional system is affected. We showed that the AF order parameter $m^{\mathrm{AF}}(T)$ curve is modified with a non-trivial change of convexity when reducing the interplane coupling as observed in the spin$-1/2$ Heisenberg antiferromagnetic ladder compound $(C_7H_{10}N)_2CuBr_4$ (DIMPY) [204]. Similar theoretical works have also been dedicated to the dimensional modulation of the spin stiffness [217, 333].

[13] In this theoretical collaboration, I carried out all the numerical simulations.

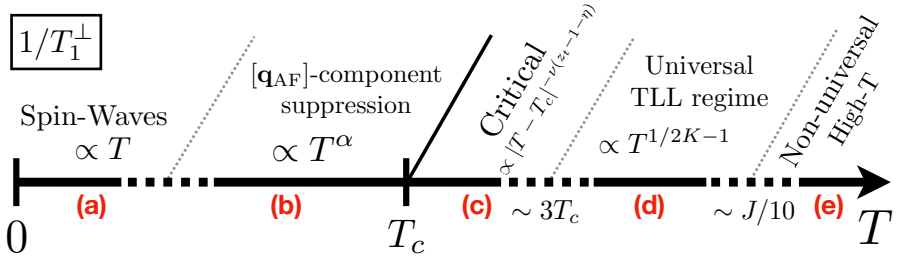

Figure B.7: Different temperature regimes and crossovers for the transverse component of the NMR relaxation rate $1/T_1^\perp$, as defined in Eq. (13) for an anisotropic three-dimensional antiferromagnet made of weakly coupled chains with an ordering temperature T_c. The coupling strengths are J along the chain direction and $J_\perp$ in the transverse direction, see Eq. (B.61). (a) Deep in the ordered phase, the NMR relaxation rate increases linearly $\propto T$ from the absolute zero temperature due to spin-waves contributions. (b) Right below the critical temperature T_c, the NMR relaxation rate goes through a strong algebraic suppression $\propto T^\alpha$ ($\alpha \simeq 4-5$) due to its "$[\mathbf{q}_{\rm AF}]$-component suppression". The change of behavior from (b) to (a) sets a first crossover temperature. (c) When approaching the transition from above the critical temperature, the NMR relaxation rate diverges with critical exponents ν, η and z_t characterizing the universality class of the transition, i.e. $\propto |T-T_c|^{-\nu(z_t-1-\eta)}$. The divergence associated to the transition is observed up to approximately $\simeq 3T_c$. (d) For $J_\perp/J \ll 1$ we can expect a crossover towards one-dimensional physics with a diverging NMR relaxation rate $\propto T^{1/2K-1}$ where K is the Tomonaga-Luttinger liquid parameter. (e) At high temperature, larger than $\sim J/10$, the $1/T_1^\perp$ behavior is non-universal. Note that if $3T_c \gtrsim J/10$, the region (d) of the diagram is squashed, and no universal TLL physics is present in the system, at least regarding the NMR relaxation rate.

A key question we wish to address is about the signatures of a genuine one-dimensional physics above T_c, and in particular the temperature range where a universal TLL regime is expected. As seen in the ladder system $(C_5H_{12}N)_2CuBr_4$ [80] the TLL crossover regime based on measurements of the magnetocaloric effect is not sharply defined. Thus, one might ask how such a crossover shows up in dynamical quantities such as the dynamical spin structure factor $S_{\mathbf{q}}(\omega)$ measured by inelastic neutron scattering experiments or the nuclear magnetic resonance spin-lattice relaxation rate $1/T_1$. This is of great experimental interest, in particular to estimate the TLL parameter K. For instance, the NMR relaxation rate of a TLL diverges algebraically at low temperature as $1/T_1 \propto T^{1/2K-1}$ [166, 210]. We found in our previous work that for a strictly one-dimensional system, the predicted universal power-law dependence can indeed be asymptotically observed, but only at quite low temperature: $T \lesssim J/10$. As for static quantities, a finite three-dimensional coupling $J_\perp$ will ultimately change the dynamical response when approaching T_c. When getting close to T_c, we will see that the NMR relaxation rate diverge with a power-law $1/T_1 \propto |T-T_c|^{-\nu(z_t-1-\eta)}$ with an exponent $\nu(z_t-1-\eta) > 0$ characteristic of the phase transition. These different regimes for $T > T_c$ summarized in Fig. B.7 (c–e) are studied in great details in this work based on analytical and numerical calculations.

The TLL prediction is often used to fit the experimentally measured NMR

relaxation rate versus T and obtain the dimensionless TLL parameter K, but a proper definition of the temperature window inside which the genuine one-dimensional properties can be observed is missing. For instance, we showed that for the quasi-one-dimensional $S = 1$ chain $NiCl_2$-$4SC(NH_2)_2$ (DTN) material [316], the critical temperature is larger than the crossover temperature towards the 1D regime, thus preventing the observation of TLL behavior. In other words, the region Fig. B.7 (d) is squashed to zero for DTN, although it has proven to display other one-dimensional fingerprints (see our work presented in the first chapter). Another promising material with a smaller three-dimensional coupling (hence a smaller T_c) is DIMPY [171, 173] where the $1/T_1$ has been fitted to obtain K versus the external magnetic field H, but has shown some discrepancy with the expected value $K(H)$ computed numerically. Our present work reveals that the experimental fitting temperature range $2T_c < T < 3T_c$ is probably too close to the critical temperature to be reliable. This will be discussed in greater details in the following.

In NMR experiments, one way to map the boundary between the disordered and ordered phases is to determine the temperature T_c at which the hyperfine splitting of "the NMR line" in the spectrum of the targeted nucleus vanishes [166, 174, 204]. Another way is to look at the relaxation rate $1/T_1$ as a function of T, expected to diverge at the transition, and resulting in practice in a strong enhancement [173, 204, 317, 318]. Below T_c, experimental observations of the NMR relaxation rate show that it is greatly suppressed with temperature, empirically fitting an algebraic dependence, $1/T_1 \propto T^\alpha$ with $\alpha \simeq 4 - 5$ as observed in the two-leg spin-1/2 ladder $Cu_2(C_5H_{12}N_2)_2Cl_4$ compound [334], DTN [335] and DIMPY [204]. This behavior, reported as "$[\mathbf{q}_{\mathrm{AF}}]$-component suppression" in Fig. B.7 (b) will be discussed and compared with our numerical results, providing some insights and explanations. Finally, although it remains very challenging to observe, both experimentally and numerically since it should happen at very low temperature, deep in the ordered phase the NMR relaxation rate is expected to grow linearly with T due to spin-waves contribution from the absolute zero, as shown in Fig. B.7 (a).

1. Models and definitions

We study coupled quantum spin-1/2 chains in three dimensions, ultimately forming a tetragonal lattice as shown in Fig. B.8 (a). The system is generically described by the following Hamiltonian,

$$\mathcal{H} = \mathcal{H}^{\mathrm{1D}} + J_\perp \sum_{\mathbf{r}} \sum_{\mathbf{u}=\mathbf{b},\mathbf{c}} \mathbf{S}_{\mathbf{r}} \cdot \mathbf{S}_{\mathbf{r}+\mathbf{u}}, \tag{B.61}$$

where the second term couples nearest-neighbor spins along the transverse directions $\mathbf{b}$ and $\mathbf{c}$ with a Heisenberg interaction of strength $J_\perp$. The first term of Eq. (B.61) describes a single XXZ spin chain,

$$\mathcal{H}^{\mathrm{1D}} = J \sum_{\mathbf{r}} \left(S^x_{\mathbf{r}} S^x_{\mathbf{r}+\mathbf{a}} + S^y_{\mathbf{r}} S^y_{\mathbf{r}+\mathbf{a}} + \Delta S^z_{\mathbf{r}} S^z_{\mathbf{r}+\mathbf{a}} \right), \tag{B.62}$$

with J the nearest-neighbor antiferromagnetic exchange along the chain direction $\mathbf{a}$ and Δ the Ising anisotropy along the z spin component. Although we focused in this

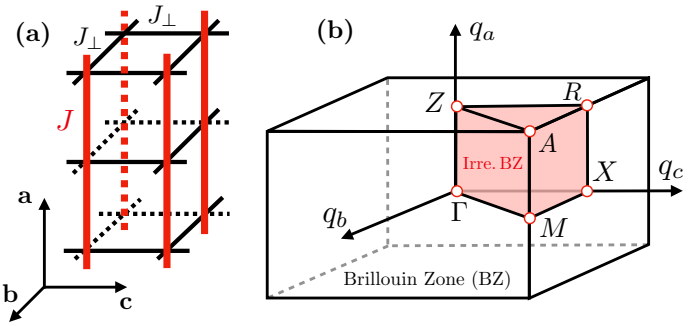

Figure B.8: **(a)** Three-dimensional tetragonal lattice with the spatial **a** direction non equivalent to **b** and **c**. The spin$-1/2$ degrees of freedom live on the vertices. The Brillouin zone and irreducible Brillouin zone (red region) are shown in panels **(b)** with wave vectors $\mathbf{q} = (q_a, q_b, q_c)$. The vertices $Z = (\pi, 0, 0)$, $R = (\pi, 0, \pi)$, $A \equiv \mathbf{q}_{\rm AF} = (\pi, \pi, \pi)$, $\Gamma = (0, 0, 0)$, $X = (0, 0, \pi)$ and $M = (0, \pi, \pi)$ are high-symmetry points of the Brillouin zone.

work on this specific model, it should apply for any system describing coupled one-dimensional Tomonaga-Luttinger liquids [37]. The periodicity and spatial symmetries of the system define the Brillouin zone (BZ) and irreducible Brillouin zone as shown in Fig. B.8 (b). One can define momentum space spin operators through a Fourier transformation, $S^\mu_{\mathbf{q}} = \sum_{\mathbf{r}} \mathrm{e}^{-i\mathbf{q}\cdot\mathbf{r}} S^\mu_{\mathbf{r}}/\sqrt{N}$. N is the total number of spins in the system, $\mathbf{q} = (q_a, q_b, q_c)$ the wave vector with $q_{a,b,c} \in]-\pi, \pi]$ its components along the **a**, **b**, **c** spatial directions and $\mu \in [x, y, z]$ the spin component respectively.

Bosonized Hamiltonian In the presence of a weak interchain coupling, the quasi-long range order of the chains will turn into a long range order for sufficiently low temperature. For $\Delta < 1$ ordering in the XY plane is favored. To describe such long-range ordering within bosonization, either the random phase approximation (RPA) [147, 212] or the self-consistent Hartree approximation [336–339] can be used (see below what the two approximations are about). The former is more convenient to address the fluctuations above the transition, while the latter gives a simpler picture of the low temperature phase. The low energy, long wavelength physics of the Hamiltonian (B.62) for an Ising anisotropy $|\Delta| < 1$ can be captured by the bosonization formalism [34, 71, 340],

$$\mathcal{H} = \sum_{\mathbf{r}_\perp} \int \frac{\mathrm{d}x}{2\pi} \left\{ uK \Big[\pi \Pi_{\mathbf{r}_\perp}(x)\Big]^2 + \frac{u}{K} \Big[\partial_x \phi_{\mathbf{r}_\perp}(x)\Big]^2 \right\}, \tag{B.63}$$

where $\mathbf{r}_\perp = n_b \mathbf{b} + n_c \mathbf{c}$, x is the position along the direction **a**, and bosonic fields obey the commutation relation $[\phi_{\mathbf{r}_\perp}(x), \Pi_{\mathbf{r}'_\perp}(x')] = i\delta_{\mathbf{r}_\perp, \mathbf{r}'_\perp} \delta(x - x')$.

Random phase approximation In the same spirit as what we did in the first chapter for the static AF order parameter, the random phase approximation [147, 212] can also apply for time-dependent quantities. One assumes that a spin chain responds to an effective field that is the sum of the applied space-time dependent external field $H^\mu_{\mathbf{q}}(\omega)$ and an internal field generated by the sum of responses of the other chains. Above the critical temperature, the linear response of a single chain is given by,

$$S^\mu_{\mathbf{q}}(\omega) = \chi^{\mu\mu}_{\rm 1D}(q_a, \omega) \Big\{ H^\mu_{\mathbf{q}}(\omega) - 2J_\perp \Big[\cos(\mathbf{q}\cdot\mathbf{b}) + \cos(\mathbf{q}\cdot\mathbf{c})\Big] S^\mu_{\mathbf{q}}(\omega) \Big\}, \tag{B.64}$$

where $\chi^{\mu\mu}_{\rm 1D}(q_a,\omega)$ is the susceptibility of a single chain along the $\mathbf{a}$ direction with $\mu\in[x,y,z]$ the spin component. Defining likewise $S^\mu_{\mathbf{q}}(\omega)=\chi^{\mu\mu}_{\mathbf{q}}(\omega)H^\mu_{\mathbf{q}}(\omega)$, where $\chi^{\mu\mu}$ is now the susceptibility of the full three-dimensional system, one gets the expression

$$\chi^{\mu\mu}_{\mathbf{q}}(\omega)=\frac{\chi^{\mu\mu}_{\rm 1D}(q_a,\omega)}{1+2J_\perp\Big[\cos(\mathbf{q}\cdot\mathbf{b})+\cos(\mathbf{q}\cdot\mathbf{c})\Big]\chi^{\mu\mu}_{\rm 1D}(q_a,\omega)}, \tag{B.65}$$

from which the dynamical spin structure factor $S^{\mu\mu}_{\mathbf{q}}=\coth(\beta\omega){\rm Im}\chi^{\mu\mu}_{\mathbf{q}}(\omega)$ is obtained using the fluctuation-dissipation theorem. We recover that the static response function, $\chi^{\mu\mu}_{\mathbf{q}_{\rm AF}}(\omega=0)$ is divergent at a temperature such that $1-4J_\perp\chi^{\mu\mu}_{\rm 1D}(q_a=\pi,\omega=0)=0$, which defines the critical temperature T_c. It can be shown that the divergence occurs at a higher temperature T_c for $\mu=x,y$ than $\mu=z$ [147]. In three dimensions, below T_c, easy-plane antiferromagnetic order sets in, and Eq. (B.65) is not applicable anymore. Indeed, in the ordered phase, each chain is subject to a staggered magnetic field $H^x_{\mathbf{r}}=H^x_{\rm MF}e^{i\mathbf{q}_{\rm AF}\cdot\mathbf{r}}$ — this is what we used in the two works presented in the first chapter, one can refer to them for greater details. As a result, rotation symmetry U(1) is reduced to a $\mathbb{Z}_2$ rotation around the x axis, and translation symmetry to even multiples of $\mathbf{a}$. Besides the normal response functions, $\chi^{\mu\mu}_{\rm 1D,normal}$, an umklapp response $\chi^{yz}_{\rm 1D,umklapp}$ is present. The expressions of RPA susceptibility are modified [212], and poles associated with Goldstone modes appear. Such modes are expected to yield a contribution linear in temperature to the NMR relaxation rate $1/T_1$. However, in order to do precise calculations of response functions within bosonization, since the bosonized Hamiltonian in the ordered phase is a quantum sine-Gordon model [37, 166], one has to resort to form factor expansion techniques [341] generalized to positive temperature [342]. Such calculations quickly become very involved, and a more elementary approach is provided by the self-consistent harmonic approximation.

Self-consistent harmonic approximation In the low temperature phase, we have to consider the full Hamiltonian,

$$\mathcal{H}=\mathcal{H}^{\rm 1D}+J_\perp A_0\sum_{\mathbf{r}_\perp}\int{\rm d}x\Big[\cos(\theta_{\mathbf{r}_\perp}-\theta_{\mathbf{r}_\perp+\mathbf{b}})+\cos(\theta_{\mathbf{r}_\perp}-\theta_{\mathbf{r}_\perp+\mathbf{c}})\Big], \tag{B.66}$$

with A_0 the prefactor of the transverse static correlations of a single chain. In the self-consistent harmonic approximation [336], one makes the approximation for the cosine terms,

$$\cos(\theta_{\mathbf{r}_\perp}-\theta_{\mathbf{r}_\perp+\mathbf{b}})\simeq\Big\langle\cos(\theta_{\mathbf{r}_\perp}-\theta_{\mathbf{r}_\perp+\mathbf{b}})\Big\rangle\left[1-\frac{1}{2}(\theta_{\mathbf{r}_\perp}-\theta_{\mathbf{r}_\perp+\mathbf{b}})^2+\frac{1}{2}\Big\langle(\theta_{\mathbf{r}_\perp}-\theta_{\mathbf{r}_\perp+\mathbf{b}})^2\Big\rangle\right], \tag{B.67}$$

turning (B.66) into a quadratic Hamiltonian whose interchain coupling $J_\perp A_0\langle\cos(\theta_{\mathbf{r}'_\perp}-\cos\theta_{\mathbf{r}_\perp})\rangle$ have to be determined self-consistently [337–339]. The self-consistent Hartree approximation allows to calculate the expectation value of the order parameter [337] and also predicts the dispersion of Goldstone modes [338].

2. Tomonaga-Luttinger regime at high temperature

Dynamical structure factor Before addressing the NMR relaxation rate, let us first discuss the dynamical structure factor in the paramagnetic regime above the

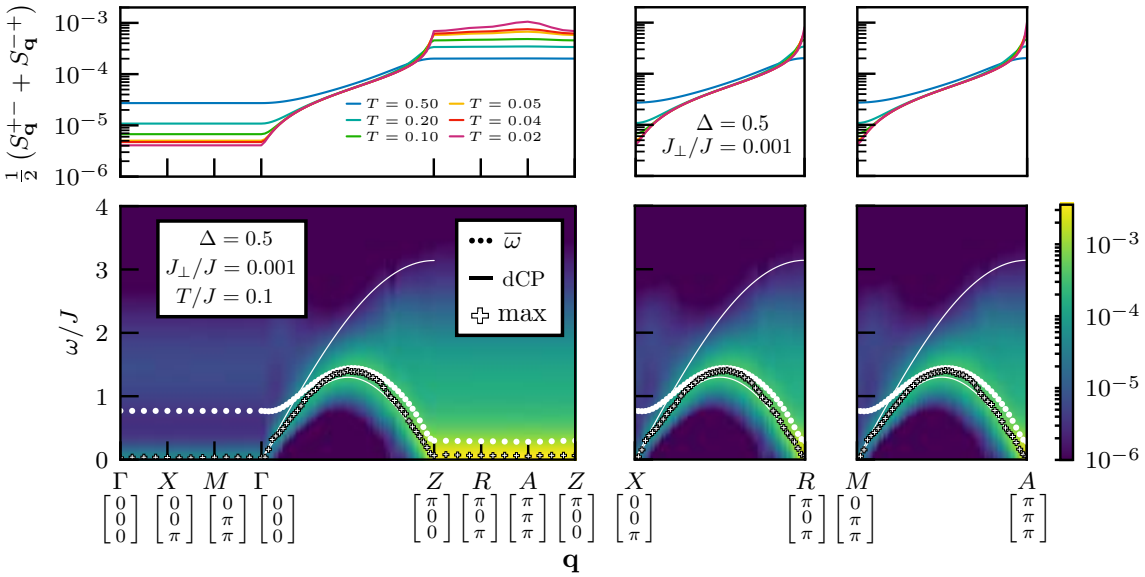

Figure B.9: The lower panels show the transverse inelastic neutron scattering intensity $I^{\perp}$ for weakly coupled spin chains in three dimensions with $J_\perp/J = 0.001$ and an Ising anisotropy $\Delta = 0.5$ along the spatial $\mathbf{a}$ direction. The $\mathbf{q}$ points follow the high symmetry lines of the BZ of Fig. B.8 (b). The temperature of the system is $T = 0.1J$, such that we are in the universal one-dimensional regime with $3T_c \lesssim T \lesssim 0.1J$, making the BZ lines ΓZ, XR and MA equivalent and corresponding all to the single chain spectrum. The white dot symbols show the first moment of the spectrum and the plus symbols the position of the maximum of intensity at a given $\mathbf{q}$ point. We also show the two sine branches of the des Cloizeaux-Pearson dispersion relations in Eq. (B.68) where the prefactor of the lower one corresponds to the TLL velocity $u \simeq 1.299J$ of a single chain with $\Delta = 0.5$. Note that the critical temperature for this system is $T_c/J \simeq 0.007$ (evaluated by the RPA estimate with a rescaled transverse coupling $J_\perp \to 0.69J_\perp$). The upper panels correspond to the static structure factor. The data are from quantum Monte Carlo simulations on the largest available system of size $N = 96 \times 8 \times 8 = 6\,144$ spins.

transition. To do so we have simulated very weakly coupled XXZ chains $J_\perp/J = 10^{-3}$ in Eq. (B.61) and $\Delta = 0.5$ in Eq. (B.62). Such a very anisotropic system orders below $T_c \simeq 0.007J$. In Fig. B.9 we show the transverse scattering intensity along the high symmetry lines of the BZ, computed in quantum Monte Carlo supplemented by stochastic analytic continuation. The spectrum along the chains direction $\mathbf{a}$, corresponding to the lines ΓZ, XR and MA are indistinguishable compared to the single chain spectrum. This is expected for such weakly coupled chains in a temperature range fulfilling $T_c \ll T \ll J$. For comparison, the better-known isotropic SU(2) Heisenberg chain, where Bethe ansatz calculations are available at zero temperature, has its dominant contribution (i.e. 98% of the spectral weight) coming from a two and four spinons continuum [343–346] bounded from below and above by des Cloizeaux-Pearson (dCP) dispersion relation [57, 347],

$$\varepsilon_{\text{lower}}(q) = \frac{J\pi}{2}|\sin q|, \quad \varepsilon_{\text{upper}}(q) = J\pi\left|\sin\frac{q}{2}\right|. \tag{B.68}$$

For the XXZ case, predictions are mostly available for the longitudinal dynamical

spin structure factor at small q [348, 349], e.g. $S^{zz}_{q\to 0} = Kq$ with K the dimensionless TLL parameter. Similarities are nonetheless visible: excitations are bounded from above by $\varepsilon_{\text{upper}}(q)$ and from below by a sine branch with a prefactor corresponding to the TLL velocity for a single chain at $\Delta = 0.5$, $u \simeq 1.299J$, a bit smaller than the velocity at the isotropic point, $u = J\pi/2$. The bounds are broadened due to finite temperature effects. Low-energy ($\omega \to 0$) excitations are restricted here to the usual commensurate modes $q \sim 0$ and $q \sim \pi$, while it is known that in presence of any additional magnetic field along the the same direction as the Ising anisotropy (hence at finite magnetization density m^z), the XY correlations of the system would develop incommensurate modes at $q = 2\pi m^z$ and $q = 2\pi(1 - m^z)$ in addition to the commensurate ones [37, 155].

NMR relaxation rate We now turn our attention to the transverse component of the NMR relaxation rate for $T > T_c$. From its definition, it follows that in the low-energy limit $\omega/T \ll 1$, it is related to the following integral,

$$\frac{1}{T_1^\perp} = \lim_{\omega\to 0} \frac{T}{\omega} \int_{\text{BZ}} \frac{\mathrm{d}^3\mathbf{q}}{(2\pi)^3} \mathrm{Im}\Big[\chi^{\pm\mp}_{\mathbf{q}}(\omega)\Big]. \tag{B.69}$$

Within the random phase approximation, the dominant contribution to the NMR relaxation rate is given by

$$\begin{aligned}\frac{1}{T_1^\perp} = \int \frac{\mathrm{d}q_b \mathrm{d}q_c}{(2\pi)^2} \int_{-\Lambda}^{\Lambda} \frac{\mathrm{d}q_a}{2\pi} \left\{ \lim_{\omega\to 0} \frac{T}{\omega} \mathrm{Im}\Big[\chi^{\pm\mp}_{\text{1D}}(\pi + q_a, \omega)\Big] \right\} \\ \times \left\{ 1 + 2J_\perp \Big[\cos(q_b) + \cos(q_c)\Big] \mathrm{Re}\chi^{\pm\mp}_{\text{1D}}(\pi + q_a, \omega = 0) \right\}^{-2}, \end{aligned} \tag{B.70}$$

where $\Lambda \ll \pi$ is a momentum cutoff. Its computation provides the following analytical expression,

$$\begin{aligned}\frac{1}{T_1^\perp} = \frac{A_0}{2u\Gamma^2\left(\frac{1}{4K}\right)} \left(\frac{2\pi T}{u}\right)^{\frac{1}{2K}-1} \int_{-\infty}^{+\infty} \frac{\mathrm{d}\xi}{\sin^2\left(\frac{\pi}{8K}\right) + \sinh^2(\pi\xi)} \left| \frac{\Gamma\left(\frac{1}{8K} + i\xi\right)}{\Gamma\left(1 - \frac{1}{8K} + i\xi\right)} \right|^2 \\ \times \frac{\mathrm{E}\left[\left(\frac{T_c}{T}\right)^{4-1/K} \left| \frac{\Gamma\left(1 - \frac{1}{8K}\right)\Gamma\left(\frac{1}{8K} + i\xi\right)}{\Gamma\left(\frac{1}{8K}\right)\Gamma\left(1 - \frac{1}{8K} + i\xi\right)} \right|^4 \right]}{1 - \left(\frac{T_c}{T}\right)^{4-1/K} \left| \frac{\Gamma\left(1 - \frac{1}{8K}\right)\Gamma\left(\frac{1}{8K} + i\xi\right)}{\Gamma\left(\frac{1}{8K}\right)\Gamma\left(1 - \frac{1}{8K} + i\xi\right)} \right|^4} \end{aligned} \tag{B.71}$$

where the integration over q_a and q_b has been performed exactly in terms of elliptic integrals [350]: $\mathrm{E}(x)$ is a complete elliptic integral of the second kind. $\Gamma(x)$ and $B(x, y)$ are respectively the Euler Gamma and beta functions. The above expression can rewritten as,

$$\frac{1}{T_1^\perp} = \left(\frac{1}{T_1^\perp}\right)_{\text{1D}} \times \Phi\left(\frac{T_c}{T}, K\right). \tag{B.72}$$

The enhancement factor Φ depends only on T_c/T and the Tomonaga-Luttinger exponent K. In the limit $T_c/T \to 0$, we recover the NMR relaxation rate of a single chain since $\Phi(0, K) = 1$ in Eq. (B.71).

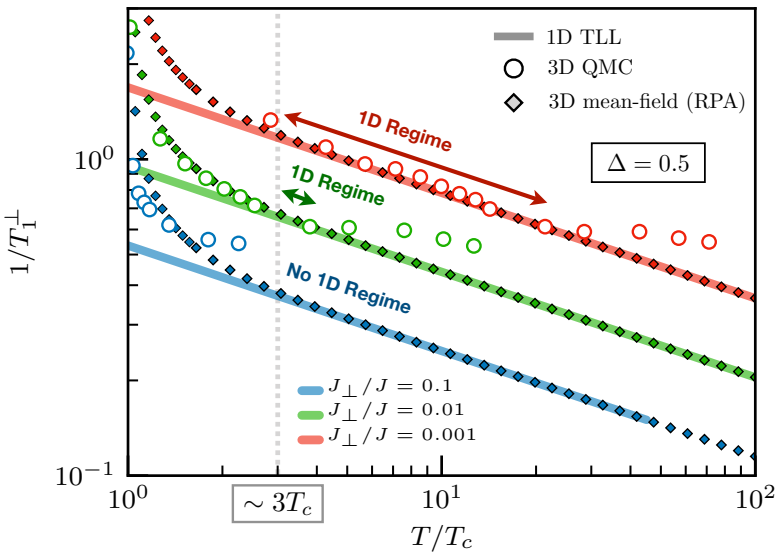

Figure B.10: Transverse component of the NMR relaxation rate $1/T_1^\perp$ defined for weakly coupled chains in three dimensions with an Ising anisotropy $\Delta = 0.5$ along the spatial direction **a**, for various transverse couplings between the chains $J_\perp/J = 0.1$ (blue), 0.01 (green) and 0.001 (red). The temperature axis has been rescaled by the critical temperature T_c of each model, respectively $T_c/J \simeq 0.224$, 0.04 and 0.007. The bold straight lines correspond to the purely one-dimensional TLL prediction, the small diamonds to the three-dimensional mean-field (RPA) calculations (B.71) and the circles to quantum Monte Carlo simulations. It shows that if any, the universal one-dimensional regime of the NMR relaxation rate is visible for $T \gtrsim 3T_c$. We stress that there are no free parameters to adjust the different estimates here.

Numerically, the $1/T_1^\perp$ is directly computed from the spectral function in the limit $\omega \to 0$. Quantum Monte Carlo simulations have been performed for weakly coupled XXZ chains $J_\perp/J = 10^{-1}$, 10^{-2} and 10^{-3} with an Ising anisotropy $\Delta = 0.5$ along the chain direction **a**. These systems respectively develop long-range AF order below $T_c/J \simeq 0.224$, 0.04 and 0.007. Numerical simulations results as well as the RPA calculation of Eq. (B.71) and the purely one-dimensional result are plotted together in Fig. B.10. In the high temperature limit, the RPA calculation gives back the purely one-dimensional prediction $\propto T^{1/2K-1}$, which becomes valid at low enough temperature $T \lesssim J/10$ [332, 351]. For coupled chains with $J_\perp/J = 0.1$, the system gets ordered above this crossover temperature preventing any one-dimensional regime. As the three-dimensional coupling is lowered, the critical temperature decreases and a one-dimensional regime sets up above T_c. Yet, the temperature should be such that $T \gg T_c$ to ensure that the transition does not spoil the universal 1D behavior. Indeed, as we approach the transition (critical regime), the NMR relaxation rate deviates from the power-law dependence, which will be discussed thoroughly in the next section. For $J_\perp/J = 10^{-2}$ and 10^{-3}, we find that for $T \gtrsim 3T_c$ we are far enough from the transition and able to observe the 1D regime. More precisely, we find that for $\Delta = 0.5$, systems with a three-dimensional coupling $J_\perp/J < 10^{-2}$ display a nonzero temperature window $T \in [3T_c, J/10]$ (assuming that $3T_c < J/10$) inside which the observation of the genuine $\propto T^{1/2K-1}$ behavior for the NMR relaxation

rate is possible. We stress that in Fig. B.10, there are no free parameters to adjust the different estimates.

3. Critical regime

As we approach the transition, the NMR relaxation rate is strongly enhanced, as observed in Fig. B.10 for $T \lesssim 3T_c$ and numerous experiments [173,204,317,318]. This can be understood within a scaling hypothesis since $1/T_1$ is related to a correlation function. Specifically, at the transition, we expect a divergence of both the correlation length ξ and the correlation time τ, linked through the relation $\tau \sim \xi^{z_t}$ with z_t the dynamical exponent in the sense of real-time dynamics[14] [352,353]. Within a scaling hypothesis, the local ($\mathbf{r} = \mathbf{0}$) time-dependent correlation function takes the form,

$$S^{\pm\mp}_{\mathbf{r}=\mathbf{0}}(t) = \xi^{2-D-\eta}\,\tilde{\mathcal{G}}\left(\xi^{1/\nu}|T-T_c|, t/\xi^{z_t}\right), \tag{B.73}$$

where $\tilde{\mathcal{G}}$ is a universal scaling function, D the dimensionality of the system, η the anomalous exponent and ν the correlation length exponent. Its Fourier transform to frequency space in the limit $\omega_0 \to 0$ is the transverse component of the NMR relaxation rate (12) and simplifies to,

$$\frac{1}{T_1^{\perp}} = \xi^{2-D-\eta+z_t}\mathcal{G}\left(\xi^{1/\nu}|T-T_c|\right) \tag{B.74}$$

where $\xi^{z_t}\mathcal{G}$ is the integral of $\tilde{\mathcal{G}}$ with $\mathcal{G}$ a universal scaling function as well. Setting $D = 3$ and using the scaling form of the correlation length $\xi \sim |T-T_c|^{-\nu}$ in Eq. (B.74), one obtains the behavior of the NMR relaxation rate when approaching the transition, $T \to T_c$,

$$\frac{1}{T_1^{\perp}} \propto |T-T_c|^{-\nu(z_t-1-\eta)}, \tag{B.75}$$

which diverges as long as $\eta < z_t - 1$ since $\nu > 0$.

In the classical limit, our model becomes the three-dimensional XY model, the critical dynamics of which is described by Model E of Refs. 353 and 354. In model E, the non-conserved order parameter and the conserved magnetization have different dynamical exponents, respectively $z_{\phi,t}$ and $z_{m,t}$, satisfying $z_{\phi,t} + z_{m,t} = 3$. In Eq. (B.75), we have $z_t \equiv z_{\phi,t}$ since the relaxation rate is obtained from a correlation function related to the order parameter. Two possible fixed points exist for model E dynamics [354], $z_{m,t} = z_{\phi,t} = 3/2$ and $z_{m,t} < z_{\phi,t}$. Using the values of exponents obtained from numerical simulations in Ref. 355, $\eta = 0.035$, $\nu = 0.6693$ and $z_{\phi,t} = 1.62$, we find a behavior $1/T_1^{\perp} \sim |T-T_c|^{-0.3915}$, that should hold in the classical critical region of the transition. Alternatively, with a purely relaxational dynamics (the so-called model A) [356], a classical dynamical exponent $z_t = 2$ would be obtained, leading to $1/T_1^{\perp} \sim |T-T_c|^{-0.64}$. We expect that in systems where magnetization is non-conserved as a result of Dzyaloshinskii-Moriya or dipolar interactions, this model A exponent will apply. Outside this classical critical region, the mean-field exponents are recovered. In the vicinity of the antiferromagnetic

[14] This exponent is not to be mistaken with "z", the dynamic critical exponent appearing in the context of quantum phase transitions [21].

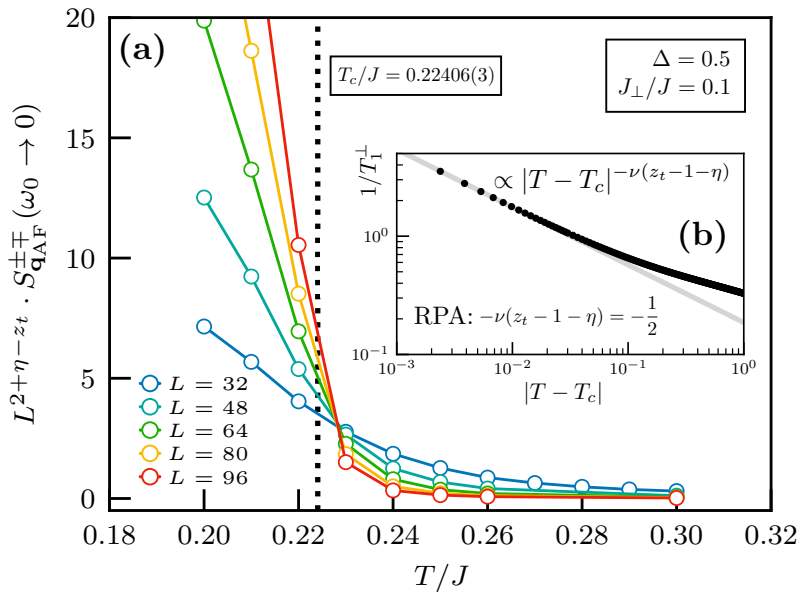

Figure B.11: (a) Rescaled transverse dynamical spin structure factor at the AF wave vector in the limit $\omega \to 0$ for different system sizes $N = L^3/8^2$ made of weakly coupled chains with $J_\perp/J = 0.1$ and an Ising anisotropy $\Delta = 0.5$ along the spatial direction **a**. The transverse dynamical spin structure factor has been rescaled according to the scaling law (B.76). The anomalous critical exponent takes the value of the 3D XY universality class $\eta = 0.0381$ [175], and $z_t = 1.62$ [355] was considered. The crossing point for the different sizes using these exponents is compatible with the expected critical temperature $T_c/J \simeq 0.224$ for this system. **(b)** Transverse component of the NMR relaxation of Eq. (B.71) from RPA calculations versus $|T - T_c|$ with $T > T_c$. A divergence with the mean-field exponents $\nu = 0.5$ and $\eta = 0$ as well as $z_t = 2$ is observed as $T \to T_c$ according to Eq. (B.75).

ordering, $T \to T_c$, we can expand the denominator in the integral of the Φ function in Eq. (B.72), and recover the mean-field behavior $1/T_1^\perp \propto |T - T_c|^{-1/2}$ [147], compatible with the mean-field exponents $\eta = 0$ and $\nu = 1/2$ if $z_t = 2$ [353]. This is visible in Fig. B.11 (b) for weakly coupled chains with $J_\perp/J = 0.1$ and an Ising anisotropy $\Delta = 0.5$ along the spatial direction **a**.

A similar scaling to the transverse NMR relaxation rate of Eq. (B.74) can be obtained for the transverse dynamical spin structure factor at the AF wave vector in the limit $\omega \to 0$,

$$S^{\pm\mp}_{\mathbf{q}_{\rm AF}}(\omega_0 \to 0) = \xi^{1-D-\eta+z_t}\, \mathcal{F}\Big(\xi^{1/\nu}|T - T_c|\Big), \tag{B.76}$$

with $\mathcal{F}$ a universal scaling function. At criticality, ξ diverges and one can make the substitution $\xi \to L$ for a finite-size system of linear size L. The above scaling implies scale invariance at the critical temperature for $S^{\pm\mp}_{\mathbf{q}_{\rm AF}}(\omega_0 \to 0)/L^{1-D-\eta+z_t}$. We plot in Fig. B.11 (a) setting $D = 3$ and $z_t = 1.62$ (see previous discussion) and using the 3D XY universality class value of the exponent $\eta = 0.0381$ [175]: it is noteworthy that the different curves show a crossing point close to the critical temperature $T_c/J \simeq 0.224$ of the system made of weakly coupled chains with $J_\perp/J = 0.1$ and

an Ising anisotropy $\Delta = 0.5$ along the spatial direction **a**. However, the crossing is not extremely accurate, which could be related either to the numerical value of z_t or more probably to the analytic continuation procedure. Similarly, we are unable to get the universal scaling function as a rescaling of the x axis by $T \to (T - T_c)L^{1/\nu}$ with $\nu = 0.6717$ [175, 241, 242] (the 3D XY universality class value of the correlation length exponent) does not provide a satisfactory collapse of our data. The inability to properly estimate error bars of analytically continued data is partially to blame, but more importantly the diverging value of $S_{\mathbf{q}_{\rm AF}}(\omega_0 \to 0)$ below the critical temperature is not accurately evaluated. It is known that analytic continuation has troubles to capture sharp peaks such as δ or quasi-δ contributions in spectral functions like the one present in $S_{\mathbf{q}_{\rm AF}}(\omega)$ as $\omega \to 0$ below the critical temperature.

4. Ordered phase

As discussed in the previous section, the strong enhancement when approaching T_c is understood within a scaling hypothesis, provided $z_t + 2 - D - \eta > 0$. In the ordered phase, a linear dependence of the $1/T_1$ with the temperature is predicted [147] due to spin-waves contribution but has never been observed experimentally so far. Instead, a stronger suppression of the NMR relaxation rate is reported $\propto T^\alpha$ with $\alpha \simeq 4 - 5$, as in the two-leg spin-1/2 ladder $Cu_2(C_5H_{12}N_2)_2Cl_4$ compound [334], DTN [335] and DIMPY [204]. We show in this section that the linear spin-waves contribution should manifest only at low temperature and discuss the meaning of the strongly suppressed $1/T_1$ close to T_c by looking at its different momenta components.

Close to the transition From the definition (B.8), the NMR relaxation rate can be expressed as a sum over all momenta $\mathbf{q}$ of the dynamical spin structure factor $S_{\mathbf{q}}(\omega_0)$ at the NMR frequency. We show in Fig. B.12 (b) the relative weight versus temperature of the AF momentum $\mathbf{q}_{\rm AF}$ compared to all the others by defining,

$$W_{\mathbf{q}_{\rm AF}} = \frac{S_{\mathbf{q}_{\rm AF}}(\omega_0)}{\sum_{\mathbf{q}} S_{\mathbf{q}}(\omega_0)}. \tag{B.77}$$

The AF wavevector clearly dominates below the critical temperature as hinted by Fig. B.11 (a) showing its diverging behavior below T_c (the exponent $2+\eta-z_t$ is close to zero and the multiplicative factor $L^{2+\eta-z_t}$ on the y axis roughly of order one). As mentioned a couple of times, there is experimentally no divergence of the $1/T_1$ below T_c but a strong suppression. This can only mean that the sharp AF contribution at low frequency $\omega \to 0$ is not captured in the ordered phase, which can be explained by the finiteness of the NMR frequency ω_0. To avoid a specific dependence on the NMR frequency of the relaxation rate, we make a new definition removing the $\mathbf{q}_{\rm AF}$ contribution,

$$\frac{1}{T_1^\perp} = \sum_{\mathbf{q} \neq \mathbf{q}_{\rm AF}} S^{\pm\mp}_{\mathbf{q}}(\omega_0 \to 0). \tag{B.78}$$

The regular contribution, if any, at low frequency of the AF component is also dismissed in this definition but should not contribute more than any other wavevector and only induce an error of order $1/N$, with N the number of spins (or equivalently the number of terms in the sum).

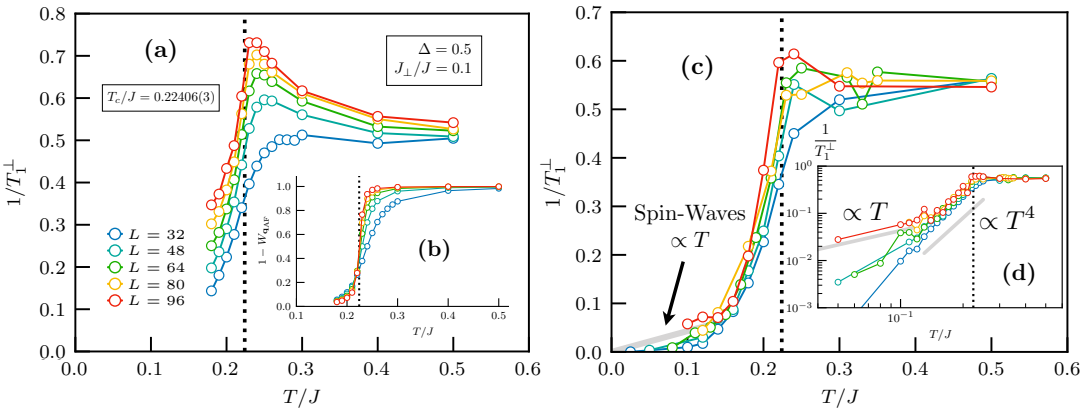

Figure B.12: Transverse component of the NMR relaxation rate $1/T_1^\perp$ Eq. (B.78) where the $\mathbf{q}_{\mathrm{AF}}$ component has been removed (see discussions in main text) for weakly coupled chains in three dimensions with an Ising anisotropy $\Delta = 0.5$ along the spatial direction $\mathbf{a}$. It has been computed numerically using QMC+SAC on different system sizes $N = L^3/8^2$ with an interchain coupling $J_\perp/J = 0.1$, leading to a critical temperature $T_c/J \simeq 0.224$ (vertical dotted line). In panel **(a)** and its inset **(b)**, the stochastic analytic continuation has been performed independently on all $\mathbf{q}$ components of $S_{\mathbf{q}}(\omega_0)$ and summed thereafter to obtain the NMR relaxation rate. In panels **(c)** and **(d)**, the sum over $\mathbf{q}$ of the imaginary time QMC data is performed before doing the analytic continuation. The inset **(b)** shows the relative weight of the $\mathbf{q} \neq \mathbf{q}_{\mathrm{AF}}$ components in the $1/T_1$ as a function of the temperature with $W_{\mathbf{q}_{\mathrm{AF}}}$ defined in Eq. (B.77). The inset **(d)** is the same as **(c)** in log-log scale where the power-law compatible with $\propto T^4$ can be observed. At lower temperature, the spin-waves contribution of the $1/T_1 \propto T$ is plotted with the prefactor computed by the self-consistent Hartree approximation in Eq. (B.83) (with no free parameter).

Focusing on weakly coupled chains $J_\perp/J = 0.1$ with Ising anisotropy $\Delta = 0.5$ along the spatial direction $\mathbf{a}$, we plot in Fig. B.12 (a) the NMR relaxation rate from the definition (B.78) with no AF contribution. The stochastic analytic continuation has been performed independently on the $N - 1$ dynamical spin structure factors in momentum space and summed thereafter[15]. The $1/T_1$ is very little affected in the disordered phase from the $\mathbf{q}_{\mathrm{AF}}$ component removal. It still displays a diverging behavior when approaching the critical temperature (the maximum value increases with system size) and the position of the maximum gets closer and closer to the actual value of T_c as the system size is increased. In the ordered phase, the NMR relaxation rate is suppressed for each one of the sizes but still growing with system size N. This is undoubtedly a technical artifact of the stochastic analytic continuation: it is not able to resolve accurately the very small contributions of the different $\mathbf{q}$ points which are all added up at the end. This can be seen as the sum of positive-definite (because a spectral function is positive-definite) "numerical noise"; note the hundreds to thousands contributions added up.

In an attempt to overcome this issue, we first perform the sum of the imaginary

[15]Here we exploit the tetragonal structure of the studied Hamiltonian (B.61) to only perform analytic continuation on $\mathbf{q}$ points of the irreducible BZ, see Fig. B.8. In the thermodynamic limit, this reduces the computational cost by a non-negligible factor ~ 16 (from 5 to 10 for the finite lattices studied in the present work).

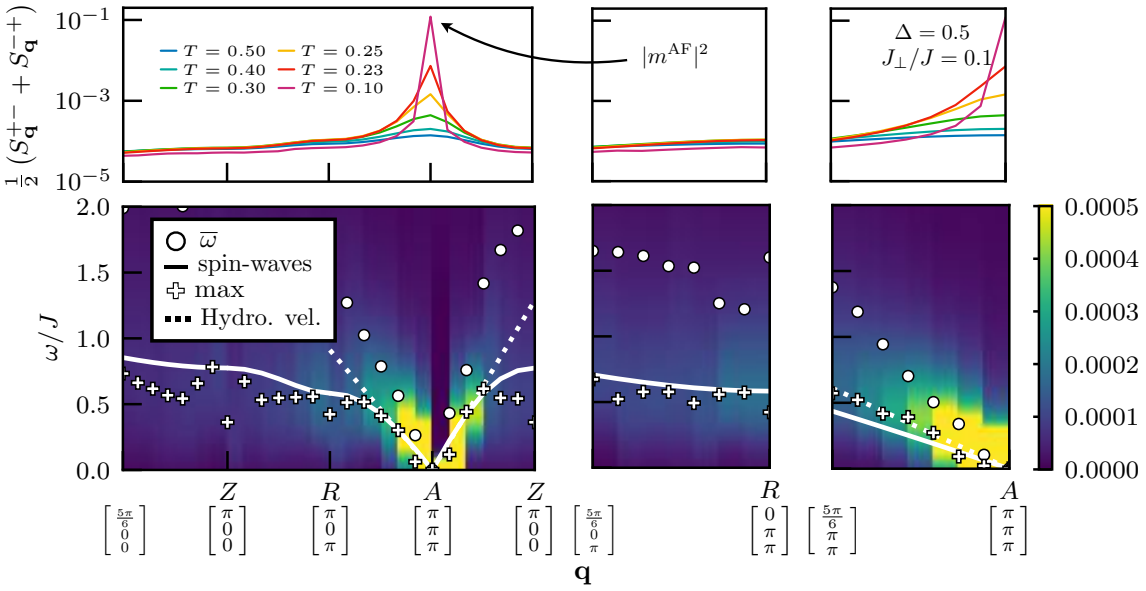

Figure B.13: Lower panels: transverse inelastic neutron scattering intensity $I^\perp$ for weakly coupled spin chains in three dimensions with $J_\perp/J = 0.1$ and an Ising anisotropy $\Delta = 0.5$ along the spatial $\mathbf{a}$ direction. The $\mathbf{q}$ points follow the high symmetry lines of the BZ of Fig. B.8 (b), focusing on regions where the spectral weight is the more significant. The temperature of the system is $T = 0.1J$, below the critical temperature $T_c/J \simeq 0.224$, explaining why all the spectral weight is located at the AF wave vector. The white dot symbols show the first moment of the spectrum. The straight white line is the spin-waves dispersion relation $\varepsilon_{\mathrm{sw}}(\mathbf{q})$ with a gapless mode at the AF wave vector. The plus symbols correspond to the maximum of intensity in the spectrum at a given $\mathbf{q}$ point. The dotted white lines around the AF wavevector show the linear dispersion relation around $\mathbf{q}_{\mathrm{AF}}$ of the SW spectrum but with corrected (hydrodynamic) velocities, compared to the bare spin-waves ones, see text. For visibility, the color intensity has been saturated to 0.0005. The upper panels correspond to the static structure factor whose value at $A \equiv \mathbf{q}_{\mathrm{AF}}$ is the modulus square of the order parameter which clearly develops for $T < T_c$ (a careful finite-size scaling analysis would need to be performed in order to obtain the order parameter value in the thermodynamic limit $N \to \infty$). The data are from quantum Monte Carlo simulations on the largest available system of size $N = 96 \times 12 \times 12 = 13\,824$ spins.

time data resulting from the quantum Monte Carlo simulations, except for $\mathbf{q}_{\mathrm{AF}}$ component, and then run a single analytic continuation. The result is shown in Fig. B.12 (c) for the same system as panel (a), and is visually not as smooth as the first panel. The high-temperature regime is not as well-captured as before with no precise maximum defined at the transition. On the contrary, in the ordered regime, the NMR relaxation rate seems more or less independent of the system size, a good indicator since it is a local probe. The same data are shown in Fig. B.12 (d) in log-log scale. It becomes increasingly difficult at low temperature to collect an accurate estimate of the NMR relaxation rate which becomes exceedingly small. Nonetheless, we are able to observe a strong suppression below T_c, compatible with a power-law dependence $1/T_1^\perp \propto T^4$ as experimentally measured.

Spin-waves contribution at low temperature Deep in the ordered phase at zero temperature, the spin-waves (SW) dispersion relation can be obtained by treating semi-classically the Hamiltonian (B.61). The idea is to first make a rotation of the spin operators in order to align the quantization axis with the classical order along the x direction [224]. Then, the Dyson-Maleev representation of the $S = 1/2$ operators is introduced and only quadratic terms are kept. In this representation, the truncated Hamiltonian is diagonalized through a Bogoliubov transformation with the SW excitation spectrum given by $\varepsilon_{\text{sw}}(\mathbf{q}) = \sqrt{A_{\mathbf{q}}^2 - B_{\mathbf{q}}^2}$, where

$$A_{\mathbf{q}} = 2J_\perp + J + \left(\frac{\Delta - 1}{2}\right)\cos\left(\pi - q_a\right), \tag{B.79}$$

and,

$$B_{\mathbf{q}} = J\left(\frac{\Delta + 1}{2}\right)\cos\left(\pi - q_a\right) + J_\perp\Big[\cos\left(\pi - q_b\right) + \cos\left(\pi - q_c\right)\Big], \tag{B.80}$$

with a zero mode at the AF wavevector (π, π, π). Expanding the cosines close to the antiferromagnetic wave vector, we obtain a linear dispersion relation $\varepsilon_{\text{sw}}(\mathbf{q} \to \mathbf{q}_{\text{AF}}) \sim v_{\text{sw}}^\nu |\mathbf{q} - \mathbf{q}_{\text{AF}}|$ with v_{sw}^ν the SW velocity, which depends on the direction $\nu \in [a, b, c]$ of the Brillouin zone for an anisotropic system,

$$v_{\text{sw}}^\nu = \sqrt{J_\nu\left[J\left(\frac{\Delta + 1}{2}\right) + 2J_\perp\right]}, \text{ with } J_a \equiv J \text{ and } J_{b,c} \equiv J_\perp. \tag{B.81}$$

We plot in Fig. B.13 the spectral function in the ordered phase of weakly coupled chains with $J_\perp/J = 0.1$ and an Ising anisotropy $\Delta = 0.5$ along the spatial $\mathbf{a}$ direction. As expected in the ordered phase, the maximum of intensity is located at $\mathbf{q}_{\text{AF}}$ with a zero mode. We also compute the first moment of the spectral function (white dots) and display the position of the maximum of intensity (plus symbols). We only focus on regions of the BZ close to the AF wavevector, where the spectral weight is the more significant to be reliable (note that the color intensity has been saturated for visibility). The spin-waves dispersion relation $\varepsilon_{\text{sw}}(\mathbf{q})$ derived above is also shown (straight line) and overlaps pretty well with the maximum of intensity, which seems more relevant than the first moment here. The linear dispersion above the ground state around the antiferromagnetic wave vector is overall well-captured, with the linear slope given by the SW velocity of Eq. (B.81). This is especially true in the transverse RA and AZ directions but the maximum of intensity deviates from the SW dispersion relation along the chain direction as observed in the right panel. This is certainly due to the linear spin-wave approximation restricted to $\mathcal{O}(1/S)$ corrections. To go further, a well-known way to extract the velocity in an antiferromagnet is to use the analog of a hydrodynamic relationship relating the velocity to the spin stiffness and the susceptibility [357, 358],

$$v_{\text{hydro}}^\nu = \sqrt{\frac{\rho_s^\nu}{\chi}}, \quad v_{\text{hydro}}^a = 1.334(6) \text{ and } v_{\text{hydro}}^{b,c} = 0.29(1) \tag{B.82}$$

where χ is the magnetic susceptibility and ρ_s^ν the spin stiffness in the $\nu \in [a, b, c]$ spatial direction. We computed both quantities for the system studied here, performing a careful finite-size scaling analysis ($N \to \infty$) and making sure that we were probing the ground state by being at sufficiently low temperature. Our final estimates are

displayed in Eq. (B.82) and plotted as dotted lines in Fig. (B.13). The correction is almost invisible in the transverse directions but provides a better overlap to the maximum of intensity along the chain direction.

Through the self-consistent Hartree approximation, one can compute deep in the ordered phase, i.e. close to absolute zero temperature, the form of the NMR relaxation rate. It displays a linear behavior with temperature resulting from the spin-waves contribution,

$$\frac{1}{T_1^{\perp}} = T \left(\frac{m^{\mathrm{AF}}(T)}{v_{\mathrm{sw}}^{b,c}\sqrt{4K}} \right)^2 , \tag{B.83}$$

where $m^{\mathrm{AF}}(T)$ is the expectation value of the order parameter, K the dimensionless TLL parameter and $v_{\mathrm{sw}}^{b,c}$ the SW velocity transverse to the chain direction $\mathbf{a}$. Since the order parameter rapidly saturates to its zero temperature value — this is already the case at $T \simeq T_c/2$ — it is justified to make the substitution $m^{\mathrm{AF}}(T) \to m^{\mathrm{AF}}(0)$ in Eq. (B.83). This prediction is shown in Fig. B.10 (c,d) using the zero temperature estimate of the order parameter, $m^{\mathrm{AF}}(0) = 0.35(1)$ and $K = 0.75$ for spin chains with an Ising anisotropy $\Delta = 0.5$. We hardly capture this linear behavior at low temperature numerically, for reasons discussed earlier. However, we remain confident that the parameter free expression in Eq. (B.83) makes it possible to experimentally provide a quantitative estimate of the crossover temperature between the two regimes below T_c, where lower temperatures are more reliably accessible than numerically. Although the linear behavior has never been experimentally observed so far to our knowledge, Eq. (B.83) should provide some guidance.

5. Summary and outlook

In this work, we described the full temperature crossover for the nuclear magnetic resonance spin-lattice relaxation rate $1/T_1$, from one-dimensional Tomonaga-Luttinger liquid physics to the three-dimensional ordered regime, as a function of inter-chain couplings. We properly defined the temperature window inside which the observation of the universal one-dimensional behavior is possible $T \in [3T_c, J/10]$, assuming that $3T_c < J/10$. Furthermore, we provided some insights regarding experimental observations of the NMR relaxation rate below the critical temperature, strongly suppressed and empirically fitting $1/T_1 \propto T^{\alpha}$ with $\alpha \simeq 4-5$. Also in the ordered phase, the transverse inelastic neutron scattering intensity was discussed and compared to spin-waves dispersion relation which overlaps with the maximum of intensity of the spectral function.

It would be interesting to investigate the fully SU(2) symmetric case, which transition is in a different universality class. This case is more difficult to tackle analytically since the real-space response functions of the single chain present logarithmic corrections and no explicit expression of their Fourier transform is known. This prevents the application of RPA methods to obtain the behavior of the response functions above the transition, unless logarithmic corrections are neglected. In the low temperature phase, the situation is worse since applying the self-consistent harmonic approximation would violate the SU(2) symmetry, yielding incorrect results, in particular for the Goldstone modes. More sophisticated analytical approaches, that can fully preserve the symmetry will have to be developed.

As a last remark, it would be also interesting to consider the case of coupled chains in two-dimensions [359]. However, the situation in this case is even less favorable for an analytical approach. Indeed, the Mermin-Wagner theorem prohibits the existence of long-range ordering at any positive temperature [17–20]. For chains forming a rectangular lattice, the low temperature phase has only quasi-long range order [213–215] until the Berezinskii-Kosterlitz-Thouless (BKT) transition [213–215] where short range order sets in. In such situation, mean field theory breaks down since the gaussian fluctuations around the saddle-point cannot be controlled [360]. However, SCHA [339] correctly reproduces the quasi-long range ordered phase, and can be used to predict the BKT transition [213–215] temperature. But it incorrectly predicts a first order transition [337], indicating its breakdown at temperatures of the order of the BKT transition temperature. The SCHA might thus be applicable, as in the 3D case, to the calculation of the NMR relaxation rate near zero temperature.

V. Haldane S=1 spin chain

Manuscript under preparation

Sylvain Capponi, **Maxime Dupont**[16], Anders W. Sandvik, and Pinaki Sengupta

As discussed in the first chapter, the $S = 1$ Heisenberg chain in one-dimension is a paradigmatic example of a gapped system as conjectured by Haldane [81, 82] and verified numerically [88, 361, 362] or experimentally [89–92]. Its Hamiltonian is given by,

$$\mathcal{H} = J \sum_i \mathbf{S}_i \cdot \mathbf{S}_{i+1} \tag{B.84}$$

where J is the antiferromagnetic nearest-neighbor exchange and the numerical value of the spin gap is $\Delta_g/J \simeq 0.41$ [88, 361, 362]. Because of the SU(2) symmetry of the Hamiltonian (B.84), all spin components are equivalent and we consider the total (as the sum of all spin components) NMR relaxation rate, and total spin structure factor without distinction between longitudinal and transverse contributions in the following. For very low-temperature, the spectral function $S_q(\omega)$ is dominated by a single magnon branch. At intermediate temperatures, relative to the gap Δ_g, the competition between quantum and thermal fluctuations makes the problem quite difficult, and recent numerical work has shown that intra-band magnon scattering can lead to additional features in the spectral function [363, 364]. The NMR relaxation rate being related to a local and dynamical spin correlation function, it is natural to expect a simple activated law $1/T_1 \propto \exp(-\Delta_g/T)$ at low temperature in a $S = 1$ chain. There are some predictions based on the low-energy effective field-theory, namely the nonlinear sigma model. In the large-N approximation, the simple activated law above was found [252]. In a refined similar calculation, J. Sagi and I. Affleck confirmed this result up to $\log(T/\omega_0)$ corrections (ω_0 being the NMR

[16] In this theoretical collaboration, I carried out the numerical simulations based on Matrix Product States methods.

frequency), and also extended the result to finite magnetic field and other anisotropic cases [365]. Using a semiclassical approach to the O(3) nonlinear sigma model (although being integrable, finite temperature correlations are hard to compute), S. Sachdev and K. Damle have improved over the previous result, by taking into account spin diffusion which occurs at long time [253]. Their result is $1/T_1 \propto \exp(-3\Delta_g/2T)$, with a factor 3/2 in the activated law.

Thanks to progress that has been done to compute dynamical properties for integrable models (mostly at $T = 0$ usually though), R. M. Konik has claimed to obtain "exact low-temperature expansions of correlation functions" for Haldane chains [366]. He was able to improve over J. Sagi and I. Affleck results [365] by including higher order terms, but he still recovers purely ballistic transport, i.e. $1/T_1 \propto \exp(-\Delta_g/T)$. Now, there are some subtleties in all approaches when taking the long time limit [367] and it could well be that integrability or not of the model might change results qualitatively [257]. So it seems that an unbiased numerical study of the full quantum one-dimensional model is called for and we shall provide results in the following. More broadly, the issue of ballistic versus diffusive transport in single $S = 1$ chain appears to be still controversial.

1. Spin diffusion at large temperature

A simple emergence of the spin diffusion phenomenon lies within the diverging behavior of the one-dimensional spin$-1/2$ diffusion constant D in the anisotropic $S = 1/2$ XXZ model, connected to the spin dc-conductivity $\sigma_{\rm dc}$ via the associated static susceptibility χ through the Einstein relation, $D = \sigma_{\rm dc}/\chi$. From linear response theory, the spin diffusion constant reads $D = \lim_{t\to\infty} \int_0^t {\rm d}t' C(t')/N\chi$ with $C(t) = \langle J(t)J(0)\rangle$ and $J(t)$ the time-dependent spin current operator [368, 369]. If the operator J is a conserved quantity, i.e. $[\mathcal{H}, J] = 0$ as in the non-interacting case, it is clear that the above integral diverges since this leads to a time-independent current-current correlation function in the integral $C(t) \propto t^{-\alpha}$ with $\alpha = 0$. Moving away from what looks like a limiting pathological case, what happens at a non-zero Ising anisotropy for the diffusion constant is at the center of the Drude weight issue [257, 369, 370]. More generally, a system is said to display spin diffusion if the long-time decay form of some spin correlation function is algebraic,

$$\lim_{t\to\infty} \left| \langle S^a_r(t) S^b_0(0)\rangle \right| \propto t^{-\alpha_r}, \quad \alpha_r \geq 0. \tag{B.85}$$

where a priori the exponent α_r could depend on the distance r [328]. This behavior was first predicted in a phenomenological theory describing the time-dependence spin correlation function by a classical diffusion equation [257, 371]. This description is a priori all the more valid at high temperature where quantum effects are not prevailing and implies a conserved quantity (such as the total spin $\mathbf{S}_{\rm tot}$ or the total magnetization $S^z_{\rm tot}$ along the quantization axis) due the associated continuity equation. Especially, a purely diffusive exponent $\alpha = D/2$ with D the dimensionality is found. The next question asks whether or not an exact treatment of the microscopic model is consistent with this prediction. In particular, the paradigmatic anisotropic XXZ spin-1/2 chain has been intensively studied in this respect [307, 327, 328, 330, 372–374]: at infinite temperature, the diffusion exponent α of the local correlation function $\langle S^z_0(t) S^z_0(0)\rangle$ along the quantization axis z is exactly equal to one at the non-interacting (XX) point

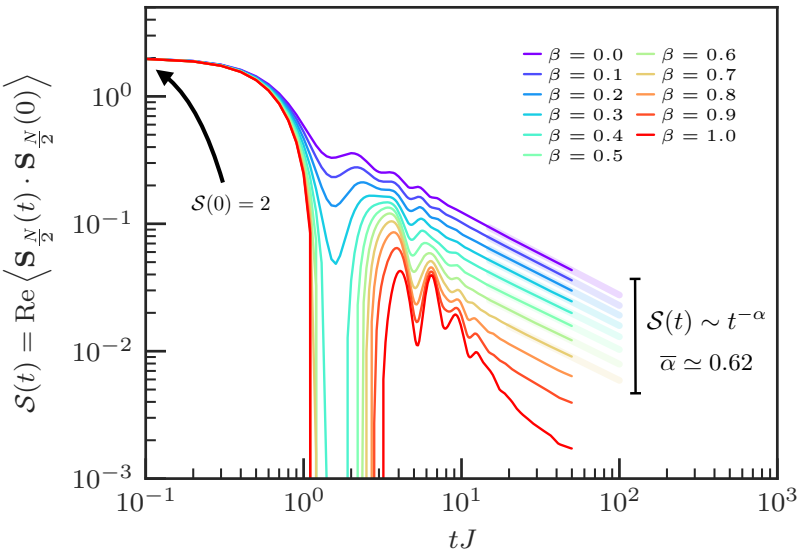

Figure B.14: Real part of the local correlation function $\langle \mathbf{S}_{L/2}(t) \cdot \mathbf{S}_{L/2}(0) \rangle$ versus time for various inverse temperatures $0 \geq \beta J \geq 1$, computed using matrix product states on $N = 64$ spin chains. For $\beta J \lesssim 0.8$, a spin diffusion like behavior is found with an exponent $\overline{\alpha} \simeq 0.62$ independent of temperature. Specifically, the bold translucid straight lines (in the log-log scale) correspond to the power-law fit $\propto t^{-\alpha}$ considered. A maximum bond dimension of size $D = 1000$ was used in the simulation as well as a fourth order Trotter decomposition for both the imaginary and real time evolutions with a time step of 0.1.

and found to vary continuously with the Ising anisotropy. This result is qualitatively similar with the expected power-law decay although it differs quantitatively from the expected $\alpha = 0.5$ exponent. On the other hand, the transverse (compared to the quantization axis) correlation $\langle S^{\pm}_{r=0}(t) S^{\mp}_{r=0}(0) \rangle$ does not display any diffusive behavior at long time. This is because S^z_{tot} commutes with the Hamiltonian and naturally appears in the momentum space formulation of the longitudinal correlation function $\langle S^z_{r=0}(t) S^z_{r=0}(0) \rangle = \sum_q \langle S^z_{-q}(t) S^z_q(0) \rangle / N$ at the $q = 0$ point; while it does not in the transverse case. Spin diffusion rises questions regarding the NMR relaxation $1/T_1$ which as a result of spin diffusion explicitly depends on the NMR frequency, playing the role of a cutoff, as $1/T_1 \sim \omega_0^{\alpha-1}$. Ultimately, a dominant contribution from $q \sim 0$ modes, especially over $q \sim \pi$ modes which one naively expects to dominates in antiferromagnets, is a signature of spin diffusion. For instance, this has been observed in the one-dimensional $S = 1/2$ Sr_2CuO_3 [255] and $Cu(C_4H_4N_2)(NO_3)_2$ [375] compounds, as well as in a $S = 1$ compound $AgVP_2S_6$ [376].

Using matrix product states, we are able to compute the time-dependent local spin-spin correlation function of the $S = 1$ chain as shown in Fig. B.14. At high temperature $\beta J \lesssim 0.8$, an algebraic form is observed at long time t, in qualitative agreement with the phenomenological spin diffusion theory. The diffusion exponent obtained by fitting the long-time decay by a simple power-law is found to be independent of temperature and in average equal to $\overline{\alpha} \simeq 0.62$. Its value is slightly smaller than in the $S = 1/2$ case where $\alpha \simeq 0.68$ was obtained in Ref. 328, and compatible with the classical limit $S \to \infty$ where $\alpha = 0.5$ is expected to be recovered.

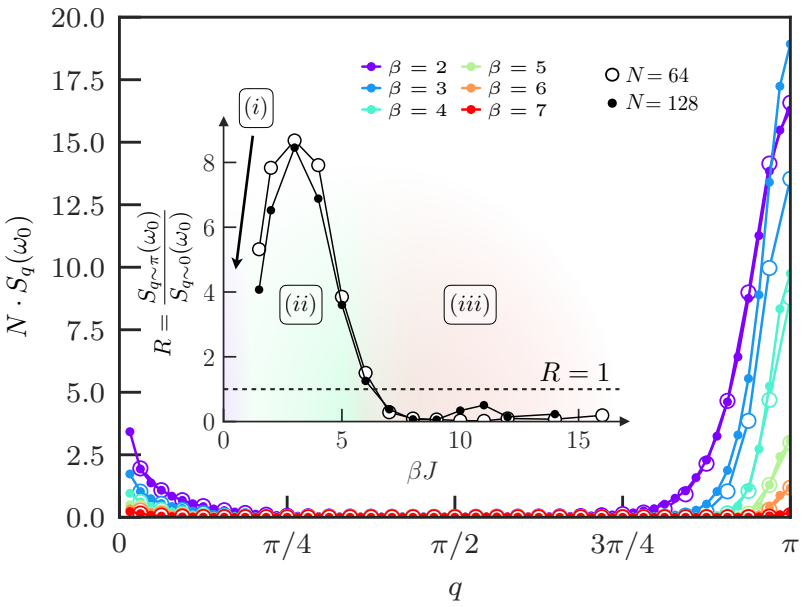

Figure B.15: Momentum contribution $S_q(\omega_0 \to 0)$ to the $1/T_1$ obtained from QMC simulations on chains of length $N = 64$ and $N = 128$ for various inverse temperatures $\beta J = 2, 3, 4, 5, 6$ and 7. The y axis has been multiplied by N so that we can compare systems with different lengths N. The inset shows the ratio R of the contributions close to $q \sim \pi$ versus $q \sim 0$, as defined in Eq. (B.86). Three different regions are observed: *(i)* corresponds to spin diffusion at high temperature, dominated by $q \sim 0$ modes with an explicit dependence of the $1/T_1$ value with the NMR frequency ω_0. In region *(ii)*, at inverse temperatures around the inverse spin gap, i.e. $\beta \sim 1/\Delta_g = 2.44$, the spin-lattice relaxation rate is dominated by $q \sim \pi$ contribution as one might expect from an antiferromagnet. However, as the temperature is lowered, a crossover is observed where $q \sim 0$ contributions start to dominate again in region *(iii)*, see discussions in text.

2. Contributions of antiferromagnetic modes

Although we are ultimately interested in the local dynamical spectral function, we focus now on small ω for the entire $S_q(\omega)$ at finite temperature, in order to investigate which momenta contribute significantly to $1/T_1$. Indeed, the spin-lattice relaxation rate can be given as a sum over momenta q of $S_q(\omega_0)$. We plot in Fig. B.15 these contributions to $1/T_1$ as a function of momentum q. In order to check the finite-size effect, we multiply by N so that $1/T_1$ is proportional to the integral under the curves and we can compare systems with different lengths N. As expected, since this is a local dynamical quantity, it does not depend much on N at fixed β. Regarding the temperature dependence, we propose to quantify the relative importance of momenta close to 0 and π by defining a ratio,

$$R = \frac{\sum_{\frac{\pi}{2} \leq |q| \leq \pi} S_q(\omega_0)}{\sum_{0 \leq |q| \leq \frac{\pi}{2}} S_q(\omega_0)}. \tag{B.86}$$

As seen in Fig. B.15, there is a rather sharp crossover around $\beta J \simeq 6$ below (respectively above) which low-energy spectral weight is mostly at $q \sim \pi$ (respectively

$q \sim 0$). It can be expected that, due to antiferromagnetic interaction, excitations with momentum $q \sim \pi$ should be important, and thus $R > 1$. However, as is known from a long time [252, 365], relaxation is in fact dominated by two-magnon processes at very low-temperature (due to energy conservation), hence we do expect $q \sim 0$ to dominate at low enough temperature (much lower than the gap), which is illustrated when $R < 1$ at large β. We can also observe a divergence at small q for any finite temperature T, which would correspond to spin diffusion. Indeed, our QMC data can be well fitted as $\propto q^{-1}$ for small q (data not shown), so that we formally get a divergence as $\ln N$ which would correspond to spin diffusion: namely, the $1/T_1$ relaxation rate does depend explicitly on a cutoff, which is experimentally the NMR frequency ω_0. We seem to observe the same behavior for any temperature, with an exponent $\alpha = 1$ quite different from our MPS results for which we found $\alpha \simeq 0.62$. However, it is known that at high-temperature, the small range of imaginary-time data $\tau \in [0, \beta/2]$ limits the accuracy of the stochastic analytic continuation, and we do not trust quantitatively the SAC results at small β.

3. Temperature dependence of the NMR relaxation rate

Combining our numerical results, we can obtain the full behavior of $1/T_1$ versus inverse temperature β, see Fig. B.16. At high temperature, we are more confident in MPS results since imaginary-time simulation are limited to small time $\tau = \beta/2$ and cannot produce very reliable results, but anyhow for temperature above the Haldane gap ($\beta \lesssim 1/\Delta_g$), there is a spin diffusion regime where the $1/T_1$ explicitly depends on the cutoff procedure, see above.

For intermediate and low temperature, we can only rely on QMC simulations since real-time data obtained from MPS are limited to time $tJ \sim 50$ and strong oscillations prevent a reliable estimate of the Fourier transform (note that $1/T_1$ becomes exponentially suppressed). As already seen in Fig. B.15, there is another crossover between a regime with dominant $q \sim \pi$ contributions ($1/\Delta_g \lesssim \beta J \lesssim 6$) where the $1/T_1$ decreases very fast, approximately as $\exp(-3\beta\Delta_g)$, which should not be trusted too much since this is valid in a rather small temperature interval. At lower temperature, the signal becomes extremely small and in order to have some intuition on the quality of our data, we have performed a bootstrap analysis of our QMC data using ten bootstrap samples followed by SAC. We extract some tentative error bars from this analysis as visible in Fig. B.16. In this low-temperature regime $\beta J \gtrsim 6$, we observe that $q \sim 0$ contributions are dominant.

4. Summary of results and conclusion

Our numerical study relies on different numerical techniques: MPS, expected to be valid at high-tempeature and SAC on top of QMC simulations which we trust for low-temperature studies. We can summarize our key findings in different temperature regimes:

– High-temperature ($T > \Delta_g$): we have observed a spin diffusion regime which prevents any universal prediction since by definition, $1/T_1$ explicitly depends

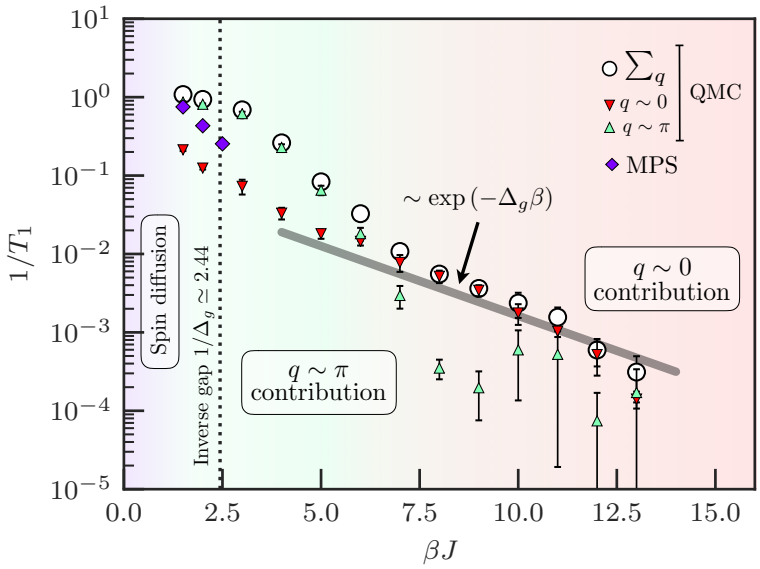

Figure B.16: NMR spin-lattice relaxation rate $1/T_1$ versus inverse temperature β obtained from QMC simulations on a $N = 128$ spins chain (white circles), and from MPS calculations on a $N = 64$ spins chain. In the latter case, we only show data where $S_{r=0}(\omega_0)$ could be precisely determined, i.e. with a "relatively fast" decay of the correlation $\langle S^z_{N/2}(t) S^z_{N/2}(0)\rangle$ to perform a proper Fourier transform despite the maximum time t we could reach in practice. We also plot separately the contributions coming from $q \sim 0$ (lower red triangles) and $q \sim \pi$ (upper green triangles) of the QMC data. The dark bold line corresponds to a naive activated law $\propto \exp(-\beta\Delta_g)$, expected to be valid when β is much larger compared to the inverse spin gap $1/\Delta_g \simeq 2.44$. Spin diffusion data at high temperatures have been discarded since they explicitly depend on the NMR frequency ω_0 and have been discussed earlier on their own.

on some numerical cutoff or experimental parameters. More precisely, our MPS data suggest an exponent in real time correlation data which is not really one half, as expected classically, but rather $\alpha \simeq 0.62$. Since a similar, but larger exponent, $\alpha \simeq 0.68$ has been computed for the spin-1/2 chain case [328], it would be interesting to investigate whether the classical result is recovered in the classical limit, i.e. $1/S \to 0$.

– Intermediate regime ($1/\Delta_g < \beta J \lesssim 6$): we have shown that the dominant contributions to $1/T_1$ come from momenta $q \sim \pi$, that can be simply interpreted since we have a large Lorentzian peak at the antiferromagnetic wavevector π and single magnon excitation can be thermally excited in this temperature range.

– Low-temperature regime ($\beta J \gtrsim 6$): due to energy conservation, dominant contribution to $1/T_1$ is due to two-magnon processes [252, 365] and occurs at $q \sim 0$. This regime is compatible with a simple activated law $1/T_1 \propto \exp(-\beta\Delta_g)$, as shown in Fig. B.16.

From an experimental point of view, one has to remember that a precise comparison of $1/T_1$ depends on which nucleus is probed and what are the hyperfine

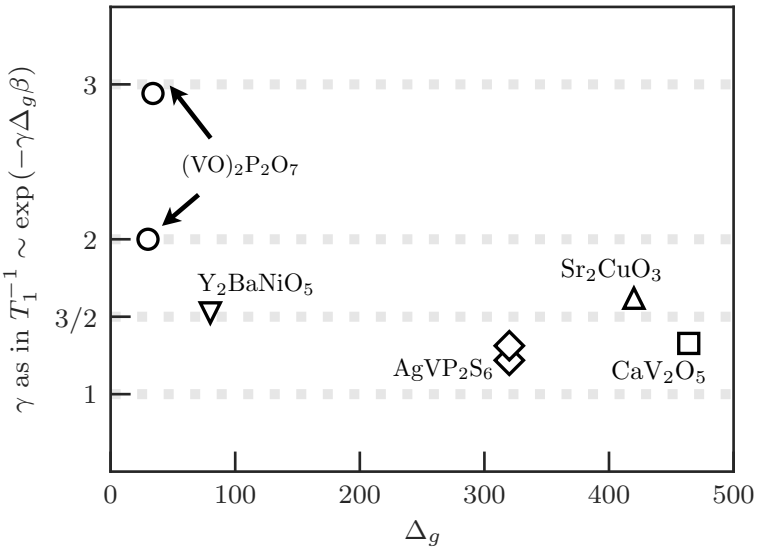

Figure B.17: In the same spirit as Ref. 377, we report in this figure the prefactor $\gamma \geq 1$ to the spin gap Δ_g observed in the activated law of the NMR relaxation rate $1/T_1 \propto \exp(-\beta\gamma\Delta_g)$ in various gapped one-dimensional compounds, investigated experimentally. $AgVP_2S_6$ [376,378] and Y_2BaNiO_5 [303] are one-dimensional $S = 1$ Haldane systems while $SrCu_2O_3$ [300,379], CaV_2O_5 [380] and $(VO)_2P_2O_7$ [381,382] are two-leg spin-1/2 ladder systems which also display a finite spin gap Δ_g.

couplings to the electronic spins. Indeed, for instance, if the NMR nucleus is coupled symmetrically to two $S = 1$ magnetic ions, then the $q \sim \pi$ contributions will be filtered out due to the form factors. We have shown that there is a nontrivial crossover when comparing the $q \sim \pi$ versus $q \sim 0$ component contributions as shown in Fig. B.16. As a result, we do expect that depending on the NMR details (such as nucleus probed and hyperfine couplings), the temperature behavior could be non-universal in a temperature range of the order of the spin gap. This could explain the various results obtained when comparing the activation energy from $1/T_1$ and the spin gap — which can also be extracted from NMR signal through the Knight shift for instance —, see Fig. B.17. Also, it could hinder any attempt to fit the $1/T_1$ behavior in this intermediate regime.

Some puzzles remain though, as for instance $AgVP_2S_6$ where the activation gap seems larger than the spin gap, independent of the NMR nucleus [376]. As pointed out by R. M. Konik in Ref. 366, one cannot exclude that easy axis spin anisotropy, weak interchain interaction or spin-phonon couplings could change qualitatively the temperature behavior. In particular, these additional ingredients are already known to modify strongly spin diffusion [383]. In some other related systems, such as an explicit dimerized $S = 1/2$ chain, which is also a one-dimensional gapped system, it has been shown for instance that a simple activated law $1/T_1 \propto \exp(-\beta\Delta_g)$ holds [332] for the NMR relaxation rate. It will be interesting to investigate other simple, yet non trivial, gapped one-dimensional systems such as spin-1/2 ladder or other dimerized chains where a simple activated law is often measured [380,381,384].

— Chapter C —

Interplay between interactions and disorder in quantum antiferromagnets

Understanding the subtle effect of disorder in quantum interacting systems is one of the major challenges of modern condensed matter physics. The presence of random impurities or defects in regular crystalline materials breaks the symmetry of translation, and may lead to novel physical phenomena, in particular at a very low temperature where quantum effects are dominant. A very famous example is the Anderson localization [385–388] in the absence of interaction, where quantum interference of electronic waves due to multiple scattering processes induced by the impurities can completely block the transport, thus driving a metal-to-insulator phase transition. Extending this prediction towards realistic condensed matter systems, where inter-particle interactions cannot be ignored, is a highly non-trivial issue which is hard to track experimentally, with only a few examples: metal-insulator transition in two-dimensional silicon MOSFETs [389], localization of ultra-cold atoms in quasi-periodic potentials [390–392], Cooper pair localization in disordered superconducting thin films [393]. Interestingly, there is a set of condensed matter quantum systems for which the interplay between disorder and interactions can be investigated in details: antiferromagnetic Mott insulators. In such systems, the amount of disorder can be controlled by chemical doping, in contrast with other types of materials where intrinsic disorder is unavoidably present but more difficult to quantify and control.

Section I I will first review the physical properties of two different phases of matter induced by disorder in quantum antiferromagnets, namely the *random singlet glass* phase and the *Bose-glass* phase. As already mentioned, disorder can be experimentally induced by chemical doping in magnetic compounds. This results on the theoretical side in couplings or more generally Hamiltonian parameters drawn from some random distribution. Regarding the random singlet phase, we shall see that a renormalization group analysis leads to a very simple, yet accurate and asymptotically exact picture of this quantum phase. On the other hand, the Bose-glass phase is more difficult to apprehend with no simple microscopic picture to which to relate. Nevertheless, its physical properties are relatively well-established and unambiguously characterize this phase.

Section II This section mixes dynamics and disorder to study the dynamical properties of Heisenberg spin chains with random antiferromagnetic exchange cou-

plings, which realize the random singlet phase in the low-energy limit [394–396]. The investigations were carried using numerical tools presented in the previous chapter. First concerned with the dynamical structure factor, we find a continuous narrow band of low-energy excitations extending throughout the Brillouin zone, instead of being restricted to $q \sim 0, \pi$ as found in the clean system. Regarding the NMR spin-lattice relaxation rate $1/T_1$, we show that it is broadly distributed. Its mean value first decreases with the temperature, but below a crossover temperature it starts to increase and likely diverges in the zero temperature limit. We show that this divergence is due to rare events in the disordered chains and is concealed in experiments, where the typical value is actually accessed.

Section III The last section combines a series of works on the chemically doped "DTN" compound at high magnetic fields, whose clean version was introduced in the first chapter of this manuscript. It has been proposed in prior publications as the first experimental realization of the Bose-glass phase in a quantum magnet [397–399]. The starting point of our works was to experimentally study the putative high magnetic fields Bose-glass phase by nuclear magnetic resonance. Unexpected observations hinted that something else than a Bose-glass was at play. We theoretically show that the disorder itself is actually getting ordered, forming a Bose-Einstein condensation through an order-by-disorder mechanism that I will discuss. Moreover, we provide a complete picture of the phase diagram "magnetic fields *vs.* doping concentrations *vs.* temperatures". At low doping there is still room for a Bose-glass phase and we study the critical properties of the Bose-Einstein condensation to Bose-glass transition. The theoretically predicted disorder-induced revival of Bose-Einstein condensation in "DTN" was afterwards experimentally observed by nuclear magnetic resonance.

I. The physics of the random singlet glass and Bose-glass quantum phases

1. The random singlet glass phase

In order to make the following discussion, it is convenient to introduce a model in which the random singlet phase emerges: the spin-1/2 Heisenberg chain with random exchange couplings,

$$\mathcal{H} = \sum_i J_i \mathbf{S}_i \cdot \mathbf{S}_{i+1}, \tag{C.1}$$

where $J_i > 0$ is drawn from some distribution[1]. This model is very close in the writing to the "clean" spin-1/2 Heisenberg chain, thoroughly discussed in the first chapter, and realizing in the low-energy limit a Tomonaga-Luttinger liquid phase. However, the presence of any amount of disorder in the exchange couplings brings

[1] The exact form of the distribution (bimodal, gaussian, uniform...) does not really matter since in all cases, the random singlet phase will emerge at low-energy in the thermodynamic limit.

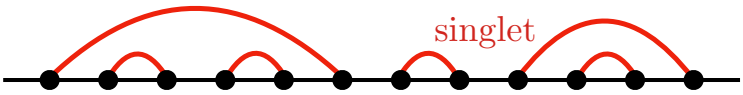

Figure C.1: Effective cartoon of the random singlet ground state in a one-dimensional spin chain. Dots correspond to spin degrees of freedom and red bonds to singlets (C.2) formed between a pair of spins.

the system into a completely different, "random singlet" phase[2] [394–396].

Strong-disorder Renormalization Group This disorder-induced quantum state of matter can be studied by means of the strong-disorder renormalization group scheme, and lead to an accurate microscopic picture of the actual exact ground-state. I will only briefly discuss the renormalization procedure but one can refer to Ref. 396 for a complete review. At the first step, the two neighboring spins with the strongest energy coupling J_i are set into a singlet,

$$|\text{singlet}\rangle = \frac{1}{\sqrt{2}}\Big[|\uparrow_i\downarrow_{i+1}\rangle - |\downarrow_i\uparrow_{i+1}\rangle\Big]. \tag{C.2}$$

which locally minimizes the energy $E_{\text{singlet}} = -3J_i/4$ of the two spins independently of the rest. These two spins are now frozen, as is the singlet they form. A new effective coupling is computed using perturbation theory between the two (right $i-1$ and left $i+2$) spins next to the singlet,

$$\tilde{J}_{i-1,i+2} = \frac{J_{i-1}J_{i+2}}{2J_i}. \tag{C.3}$$

The generated new coupling is always smaller than the decimated bond. The procedure is repeated until all spins have been paired into singlets. Noting Ω the relevant energy-scale of the system at a given step, i.e. the energy of the decimated bond, it gradually decreases during the renormalization process. The resulting asymptotic state can be nicely pictured as a collection of spin paired up into singlets spanning arbitrary distances, as shown in Fig. C.1. The technical part of the renormalization procedure, that I am skipping here, tells us that the asymptotic distribution of the couplings J generated by the decimation is given by,

$$P(J,\Omega) = \frac{-1}{\Omega \ln \Omega}\left(\frac{\Omega}{J}\right)^{1+1/\ln\Omega}\Theta(\Omega - J), \tag{C.4}$$

where $\Theta(x)$ is the Heaviside step function and the initial energy scale Ω_0 of the decimation procedure has been set to unity, i.e. $\Omega \to \Omega/\Omega_0$. In an infinitely large system, at the fixed point, the energy scale Ω vanishes and the coupling distribution becomes singular, $P(J) \sim 1/J$. Approaching the fixed point, one can show that the fraction of free spins is given by renormalization group by $n_{\text{free}} \sim \ln^{-2}(\Omega)$. Hence, a typical distance between remaining spins is $L_{\text{free}} \sim 1/n_{\text{free}} = \ln^2(\Omega)$. While the energy scale is concretely defined in the context of a running decimation procedure, it also has direct physical interpretations as an energy cutoff in various situations: for instance, finite temperature can roughly be captured by setting the scale at

[2] It is worthwhile to point out that the random singlet phase has never been observed in systems of dimension $D > 1$. Moreover, introducing an Ising anisotropy $-1 < \Delta \leq 1$ in the system (C.1) preserves the nature of random singlet phase.

$\Omega = T$. The radical change in the ground state due to disorder naturally affects the low-energy properties of the system. At low temperatures one can expect that excitations of the weak singlets — those that have been decimated at the latter stages in the renormalization procedure — will give rise to low-energy excitations not present in the uniform system. Especially, at temperature $T \sim \Omega \ll 1$, one expects spins that have not been decimated yet to behave as free spins that should essentially contribute to the magnetic susceptibility as a Curie law $\sim 1/T$. Following this argument, at $\Omega = T$, a density n_{free} of spins contributes to the susceptibility, which leads to

$$\chi \sim \frac{n_{\text{free}}}{T} = \frac{1}{T \ln^2(T)}. \tag{C.5}$$

In comparison, the susceptibility takes a finite value as $T \to 0$ in the clean chain, up to logarithmic corrections [75].

Observation of the random singlet phase Experimentally, spin chains with random antiferromagnetic exchange couplings were first proposed and investigated extensively in the context of a class of quasi-one-dimensional Bechgaard salts [400–407]. In these systems, a power-law divergent magnetic susceptibility was observed, $\chi \sim 1/T^\alpha$ with α typically around $0.7-0.8$, i.e., smaller than $\alpha = 1$ predicted by the strong disorder renormalization group theory [395], though the log correction in the (later derived) theoretical result (C.5), may at least be partially to blame for the discrepancy. Another scenario is that the random Hubbard model, from which the random Heisenberg model for the materials was derived [400], has a different form of the divergence [408]. In a more recent study of a different material, $BaCu_2(Si_{0.5}Ge_{0.5})_2O_7$ [409, 410], the predicted random singlet behavior is rather well reproduced. Note that these systems should not have any ferromagnetic couplings, in which case the random singlet phase is not realized, due to the formation of arbitrarily large effective magnetic moments [411], as observed in $Sr_3CuPt_{1-x}Ir_xO_6$ [412].

Many works [413–416] have been devoted to unbiased numerical studies of this model, with various numerical methods, including quantum Monte Carlo simulations and the DMRG technique, to test the many predictions based on the renormalization group scheme. For instance, the average correlation function between two spins at distance r follows an algebraic decay $\overline{C(r)} \sim (-1)^r/r^2$, where the exponent 2 found is to be compared with the exponent 1 of the clean chain. These numerical works have confirmed the various behaviors associated with the random singlet phase, but also have made it clear that non-asymptotic corrections can partially mask the random singlet physics when considering system sizes and temperatures that can be reached in practice. In addition, multiplicative logarithmic corrections have also been found [416].

2. The Bose-glass phase

Unlike the random singlet phase, there is no simple microscopic picture of the Bose-glass phase. The set of properties defining it is however well-established: it is a quantum phase (zero temperature), it has a finite susceptibility, its low-energy spectrum is gapless, spin-spin correlations are short-ranged (exponentially decaying), and there is no phase coherence, i.e. no spontaneous symmetry breaking. In short,

it is a many-body localized ground-state, physically really different from a critical random singlet state with algebraically decaying correlations. The first appearance in literature of this elusive phase of matter traces back to the work of D. S. Fisher and M. P. A. Fisher in 1988 [157, 417]. Around the same time, although the name "Bose-glass" was not explicitly mentioned, this disordered phase was studied in one-dimensional quantum systems by T. Giamarchi and H. J. Schulz [418, 419]. A prototype model displaying a Bose-glass phase, especially well-suited for numerical studies, corresponds to spin-1/2 degrees of freedom on a regular lattice with no frustration. The spins are coupled through a standard antiferromagnetic Heisenberg or XXZ interaction and are in addition subject to a magnetic field with a random component such as $\propto -\sum_i (H + H_i) S_i^z$, with H the static field and H_i drawn from some random distribution. The width of the distribution, such as its variance, quantifies the disorder strength δH in the system and is a relevant parameter of the model in order to study the phase diagram of the system against disorder. Regarding the prototype $S = 1/2$ model at zero temperature, it is well-known to display superfluidity (in any dimension) or Bose-Einstein condensation (in dimensions greater or equal to two). The question is whether or not disorder can destroy the global phase coherence and if yes, is there a critical disorder strength δH_c. In this respect, the dimensionality of the system is of great importance: in one dimension ($D = 1$) any infinitesimal disorder strength is a relevant perturbation in most of the cases [37, 420–422], while in $D = 2$ a finite disorder strength is required [423, 424] to destroy the zero-temperature superfluid condensate, leading to the Bose-glass state. For $D = 3$ one needs stronger randomness to eventually induce many-body localization in the ground state ($T = 0$) [425].

Qualitative picture of the Bose-glass phase Assuming a nonzero critical disorder strength δH_c, the "theorem of inclusions" [426] states that there will always exist in one phase, arbitrarily large, though exponentially rare, regions of the competing phase. This allows to derive some properties of the Bose-glass phase and at the same time initiate a microscopic picture, though not as satisfying as the random singlet one. Put in other words, the theorem reports that in a Bose-glass phase there will always be near-uniform regions that mimic the properties of the clean system and which can be pictured as superfluid — Bose-Einstein condensate — droplets. Though spatially isolated, the known properties of these droplets allow one, for example, to prove that the energy spectrum in the Bose-glass phase is gapless since superfluid excitations are gapless as well. Moreover, the disconnected superfluid clusters confer to the Bose-glass phase its finite susceptibility (or compressible nature in bosons language) since they are compressible themselves. The absence of long-range order in the Bose-glass phase is a result of the lack of phase coherence between the different superfluid droplets in the system and explains its insulating properties.

Within this picture, the Bose-glass to superfluid (or Bose-Einstein condensate) transition is often described as a percolation transition [427], with coherent droplets of increasing sizes which will merge at some points to develop a global phase coherence over the whole system. This description has been used in both theoretical [425, 428–431] and experimental [432–434] studies of the transition which found that the critical point δH_c corresponds exactly to the percolation threshold δH_{perc}. On the other hand, some works [435–438] found that there is a discrepancy between the location of the two points and put forward a "quantum percolation scenario": even when there is no percolating superfluid cluster in the system, quantum tunneling between

separated clusters lead to an effective global phase coherence with $\delta H_c > \delta H_{\text{perc}}$.

Observation of the Bose-glass phase The main motivation to introduce and study the disordered Bose-Hubbard model in the first place [157, 417] was to explain experimental observations of ^{4}He in porous media. In such experiments, ^{4}He is adsorbed on Vycor glass [439, 440] or on aerogel glass [441–444] that one can picture as random three-dimensional networks of interconnected pores of varying size. The onset of superfluidity appears at a finite critical density n_c of Helium deposited on the inside walls of the pores. For $n < n_c$, ^{4}He atoms are localized due to repulsive interactions and the random medium, but upon increasing their density n, the substrate potential is smoothed by the adsorbed bosons in the pores which form layers. Once a critical coverage at n_c is reached, a delocalized state appear with superfluidity emerging following a power-law $\rho_s \sim (n - n_c)^\zeta$, as experimentally observed in 1983 [441]. The theory of M. P. A. Fisher *et al.*, a few years later [157], provided the scaling relation $\zeta = \nu(D + z - 2)$ with D the dimensionality, z the dynamical exponent and ν the correlation length exponent. The bounds and estimate values of the critical exponents derived in the same work for superfluid to Bose-glass transition were in agreement with the experiment, indicating that Helium in porous media realizes a disorder-induced quantum phase transition belonging to a new universality class.

A few other experiments in various systems also display this transition. For instance, a transition from a superconducting to insulator phase has been observed in amorphous (disordered) indium oxide films InO [393, 445, 446] as a result of localization of Copper pairs due to disorder. The main concern is to make sure that the Copper pairs survive as such at the transition and are not destroyed to conserve their bosonic nature otherwise the nature of the transition would be different [447, 448]. It has also been observed in an array of quasi-one-dimensional samples of ^{39}K cold atoms, subject to a quasiperiodic optical lattice, the depth of which fixes the disorder strength [390]. The interaction energy between atoms can be varied thanks to a Feshbach resonance. Studying the phase diagram of the system in the plane "interaction strength *vs.* disorder strength", the first indication on the nature of the system comes from measurements of root-mean-square width of the momentum distribution, which characterizes the coherence of the system. Further evidences on the nature of the different phases are obtained by transport measurements and Bragg spectroscopy.

Another type of systems in which the Bose-glass phase has been investigated are antiferromagnetic Mott insulators [449–452]. It has been reported in the weakly coupled strong rung spin-1/2 ladder compound $(CH_3)_2CHNH_3Cu(Cl_xBr_{1-x})_3$ [453] by means of neutron diffraction, and in the $Tl_{1-x}K_xCuCl_3$ material [454] studied by specific heat and electron spin resonance measurements. Measurements consistent with the thermodynamic scaling of the specific heat established for a Bose-glass phase were also observed in the randomly diluted quantum spin-1/2 chains $(Yb_{1-x}Lu_x)_4As_3$ [455], a realization of the linear Heisenberg antiferromagnet partitioned into finite-size segments by the diamagnetic dopants Lu^{3+}, creating site-diluted chains with missing adjacent bonds. The Br doped spin-1 system $Ni(Cl_{1-x}Br_x)_2$-4SC$(NH_2)_2$ "DTNX" compound, whose clean version was introduced in the first chapter of this manuscript, has also been reported to host Bose-glass phase at low and high magnetic fields with both numerical (quantum Monte Carlo simulations) and experimental (specific heat, susceptibility, and neutron diffraction measurements) evidences [231, 397–399, 456].

We will revisit thoroughly in the last section of this chapter the high-magnetic field phase diagram of this material, which actually hosts much more than a Bose-glass phase.

II. Dynamical properties of random S=1/2 Heisenberg chains

Adapted from the work Phys. Rev. B **97**, 104424 (2018)

Yu-Rong Shu, **Maxime Dupont**[3], Dao-Xin Yao, Sylvain Capponi, and Anders W. Sandvik

We study in this work the dynamical properties at finite temperature of Heisenberg spin chains with random antiferrormagnetic exchange couplings, which realize the random singlet phase in the low-energy limit. We use complementary numerical methods: the Chebyshev expansion within the matrix product state (MPS) formalism and the stochastic analytic continuation of quantum Monte Carlo (QMC) results in imaginary time. Specifically, we investigate the dynamic spin structure factor $S_q(\omega)$ and its $\omega \to 0$ limit, which are closely related to inelastic neutron scattering and nuclear magnetic resonance experiments through the spin-lattice relaxation rate $1/T_1$. Our study reveals a continuous narrow band of low-energy excitations in $S_q(\omega)$, extending throughout the q-space, instead of being restricted to $q \sim 0$ and $q \sim \pi$ as found in the uniform system. Close to $q = \pi$, the scaling properties of these excitations are well captured by the random-singlet theory [457, 458], but disagreements also exist with some aspects of the predicted q-dependence further away from $q = \pi$. Furthermore we also find spin diffusion effects close to $q = 0$ that are not contained within the random-singlet theory but give non-negligible contributions to the mean $1/T_1$. To compare with NMR experiments, we consider the distribution of the local relaxation rates $1/T_1$. We show that the local $1/T_1$ values are broadly distributed, approximately according to a stretched exponential. The mean $1/T_1$ first decreases with T, but below a crossover temperature it starts to increase and likely diverges in the limit of a small nuclear resonance frequency ω_0. Although a similar divergent behavior has been predicted [395] and experimentally observed for the static uniform susceptibility, as in the $BaCu_2(Si_{0.5}Ge_{0.5})_2O_7$ compound for instance [409, 410], this divergent behavior of the mean $1/T_1$ has never been experimentally observed. We find distinction between the mean and typical values of the distribution, which discloses the discrepancy between the divergence of $1/T_1$ as $T \to 0$ in our results and vanishing behavior found previously [459, 460].

[3] In this theoretical collaboration, I carried out all the numerical simulations based on Matrix Product States methods.

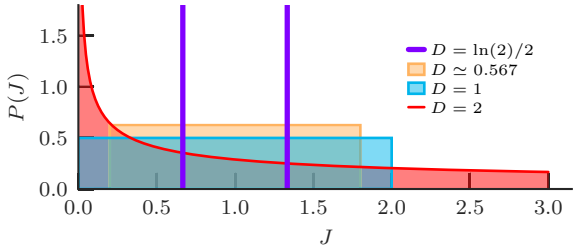

Figure C.2: Sketch of the four different disorder distributions of the random exchange couplings considered in this work. They are defined by Eq. (C.7) (except the bimodal distribution) and referred to by the disorder strength $D^2 = \overline{(\ln J)^2} - \overline{\ln J}^2$.

1. Model and definitions

We consider the SU(2) symmetric $S = 1/2$ Heisenberg chain with random nearest-neighbor couplings, described by the Hamiltonian,

$$\mathcal{H}_{\text{random singlet}} = \sum_{i=1}^{N} J_i \mathbf{S}_i \cdot \mathbf{S}_{i+1}. \tag{C.6}$$

Both open and periodic boundary conditions are considered, depending on the numerical method (periodic for QMC and open for MPS). The exchange couplings J_i are drawn from one out of several distributions defined by,

$$P(J) = \frac{A}{d} J^{-1+1/d}, \quad \text{with} \quad A = \frac{1}{J_{\text{max}}^{1/d} - J_{\text{min}}^{1/d}} \quad \text{and} \quad J_{\text{min}} < J < J_{\text{max}}, \tag{C.7}$$

in which d is a convenient parameter controlling the shape of the distribution. We quantify the disorder strength D by the variance of the distribution of the logarithm of the couplings, i.e. $D^2 = \overline{(\ln J)^2} - \overline{\ln J}^2$ [396]. For $d = 1$, the exchange couplings are uniformly drawn from the box $[J_{\text{min}}, J_{\text{max}}]$, while when $d > 1$ the distribution has a power law form. In the limit of $d \to \infty$ and $J_{\text{min}} = 0$, it corresponds to the singular distribution at the random singlet fixed-point. Both the cases $d = 1$ and $d = 2$ with $J_{\text{min}} = 0$ are studied in the present work. One would expect that the asymptotic random singlet behavior is better manifested (with less non-universal contributions) if d is large, but numerically, with the relatively small system sizes accessible in practice, it is easier to compute proper disorder averages if d is smaller. The values chosen here reflect a practical compromise in this regard. We also consider the case $J_{\text{min}} = 0.2$ and $d = 1$, to compare with previous results for the dynamic structure factor obtained with this distribution [460]. The values of J_{max} are chosen by imposing that the average of all random couplings $\bar{J}$ equals to 1, to ensure that the overall energy scale of the hamiltonian (C.6) equals unity in all cases. We finally also consider the bimodal distribution where J_i takes the values 2/3 and 4/3 with equal probability, in order to compare with experiments where this distribution has been proposed for the Heisenberg spin-1/2 chain compound $BaCu_2(Si_{1-x}Ge_x)_2O_7$ compound at $x = 0.5$ [459]. All the different disorder distributions considered in this work are summarized in Fig. C.2.

Regular and singular contributions to the spectral function For the isotropic random Heisenberg chain we considered, the finite temperature dynamic structure factor is defined as follow, through the Källén-Lehmann spectral representation,

$$S_q(\omega) = \frac{3\pi}{\mathcal{Z}(\beta)} \sum_{m,n} e^{-\beta E_m} |\langle n|S_q^z|m\rangle|^2 \delta\Big[\omega - (E_n - E_m)\Big], \tag{C.8}$$

where the sum is performed over the eigenstates of the Hamiltonian[4]. While for a finite system a spectral function is strictly speaking a sum of δ functions, the density of these increases rapidly with increasing system size and a smooth continuous distribution forms when some small broadening is imposed. However, in some cases isolated δ functions with non-zero weight can remain even in the thermodynamic limit. Generically, in Eq. (C.8) one can separate a δ function at $\omega = 0$, which we will refer to as the *singular* contribution, and *regular* parts forming a continuum: $S_q(\omega) = S_q^{\text{sing}}(\omega) + S_q^{\text{reg}}(\omega)$. It is clear that this singular part arises from degenerate energy eigenstates $E_m = E_n$,

$$S_q^{\text{sing}}(\omega) = \frac{3\pi}{\mathcal{Z}(\beta)} \sum_{m,n}^{E_m=E_n} \mathrm{e}^{-\beta E_m} |\langle n|S_q^z|m\rangle|^2 \delta(\omega) = a_q(\beta)\, \delta(\omega)\,, \tag{C.9}$$

with $a_q(\beta)$ the weight of the δ-function at $\omega = 0$. It follows that the regular part can be easily computed by constraining $E_n \neq E_m$ in Eq. (C.8), which forms a continuous distribution when some small broadening is imposed or by collecting the spectral weight in a histogram with finite bin width. In fact the contributions to the weight $a_q(\beta)$ of the possible singular part only can originate from eigenstates for which $S^z_{\text{tot}} \neq 0$ (assuming that the total number of spins is even). In the presence of disorder, there is normally no degeneracy in the energy spectrum — apart from that related to the SU(2) symmetry, which does not play any role with the operators S_q^z considered here (since these operators change the total spin by one unit). Accidental degeneracies can occur in principle, but would just contribute to the smooth (in the thermodynamic limit) continuum of the spectral function when $\omega \to 0$. Disregarding these possible accidental degeneracies, the condition $E_m = E_n$ implies $|m\rangle \equiv |n\rangle$. In the sector with zero total magnetization, we can use the spin-inversion symmetry operator Π, which flips all spins: $S_i^z \to -S_i^z$. It has the eigenvalues $p_n = \pm 1$ depending on whether the state $|n\rangle$ has odd (+) or even (−) total spin. It is easy to show that diagonal matrix elements vanish in this sector,

$$\langle n|S_q^z|n\rangle = \langle n|\Pi^2 S_q^z \Pi^2|n\rangle = -p_n^2 \langle n|S_q^z|n\rangle = -\langle n|S_q^z|n\rangle, \tag{C.10}$$

since $\Pi S_q^z \Pi = -S_q^z$. Hence, there is no δ-peak contribution from the sector of $S^z_{\text{tot}} = 0$. The singular contribution at $\omega = 0$ could be probed using inelastic neutron scattering experiments but is not relevant for NMR experiments performed at small but nonzero resonance frequency and therefore should be excluded in the $1/T_1$. It is thus advantageous to perform thermodynamic calculations in the $S^z_{\text{tot}} = 0$ subspace and we will refer to this as the canonical (C) ensemble — contrary to

[4]Because of the SU(2) symmetry of the Hamiltonian considered, the spin components x, y, z are equivalent. For convenience, we only consider the z spin component, with a factor three in the dynamical spin structure factor to account for each component contribution.

the grand canonical (GC) ensemble, which includes all magnetization sectors[5]. At zero temperature, the C and GC ensembles are the same for most Hamiltonians since the ground state has $S^z_{\text{tot}} = 0$ (and also is a total-spin singlet), and at finite temperature the two ensembles yield the same mean values for most observables in the thermodynamic limit. This last statement on the equivalence between C and GC ensembles however does not, a priori, account for singular contributions or specific observables. For instance, evaluating the static uniform susceptibility $\chi(T) = \langle (S^z_{\text{tot}})^2 \rangle / NT$, vanishes identically in the C ensemble while in the random singlet phase it diverging as $1/T$ when $T \to 0$ in the GC ensemble [394, 395, 461].

Numerically work in the canonical ensemble In the following, what is referred as $S(\omega)$ corresponds in fact to its computation in the C ensemble. Quantum Monte Carlo simulations were performed using the β-doubling trick [462] but measurements were only carried on configurations respecting the $S^z_{\text{tot}} = 0$ condition. The idea behind the β-doubling trick is to speed up the thermalization process and simulate efficiently disordered systems where averaging over many disorder samples need to be done on top of usual simulations. One usually starts from an inverse temperature $\beta = 1$ with N_{e} Monte Carlo updates, followed by N_{m} measurements, at the end of which we have a sequence of operators S_M and a basis state $|\sigma\rangle$. The next step consists in doubling the inverse temperature $\beta \to 2\beta$ and use the previous $|\sigma\rangle$ state along with the doubled operator string as the initial configuration. Indeed, if $\{|\sigma\rangle, S_M\}$ was a typical configuration at inverse temperature β, $S_M \to S_M + (S_M)^{-1}$, with $(S_M)^{-1}$ the reverse operator string (the two operator strings are connected tail-to-tail), might be a good starting guess to represent a typical configuration at 2β. The process is repeated until $\beta = 2^p$ with $p \in \mathbb{N}$ reaches the desired value. In practice, we use $N_{\text{e}} = 1000$ and $N_{\text{m}} = 2N_{\text{e}}$. These rather short simulations are optimal for disorder averaging when the statistical errors are dominated by the fluctuations between different disorder samples, rather than the intrinsic Monte Carlo statistical error.

Concerning the method presented to simulate finite-temperature with matrix product states in the previous chapter, the initial state at $\beta = 0$ before performing the imaginary time evolution corresponds to the GC ensemble in the sense that the quantum number $S^z_{\text{tot}}(\text{P} + \text{Q})$ is conserved but not $S^z_{\text{tot}}(\text{P})$ and $S^z_{\text{tot}}(\text{Q})$ separately. To build a state fulfilling that condition, one has to project the initial maximally entangled state onto the fixed $S^z_{\text{tot}}(\text{P}) = 0$ sector exclusively,

$$|\Psi^{\text{C}}_{\beta=0}\rangle = \mathcal{P}_{S^z_{\text{tot}}(\text{P})=0} |\Psi^{\text{GC}}_{\beta=0}\rangle, \tag{C.11}$$

with $\mathcal{P}_{S^z_{\text{tot}}(\text{P})=0}$ the projector operator such that the total magnetization along the z axis is fixed to zero. This operator is hard to build in a Matrix Product Operator (MPO) representation, but recent works [463, 464] suggest two alternative ways to build a canonical initial state, which we adopt here,

$$|\Psi^{\text{C}}_{\beta=0}\rangle \propto \left(\sum_{n=1}^{N} S^+_n(\text{P}) \otimes S^+_n(\text{Q}) \right)^{\frac{N}{2}} \prod_{n=1}^{N} |{\downarrow}_n\rangle_{\text{P}} |{\downarrow}_n\rangle_{\text{Q}}. \tag{C.12}$$

This state fulfills both the condition of a maximal entanglement between pairs of physical and auxiliary sites and fixed $S^z_{\text{tot}}(\text{P})$. The normalization constant is fixed by the value of the partition function at infinite temperature in the C ensemble.

[5] Using a standard Matsubara–Matsuda transformation [146], we can map the model onto a hardcore bosonic one, where canonical and grand-canonical are performed at fixed number of particles or chemical potential respectively.

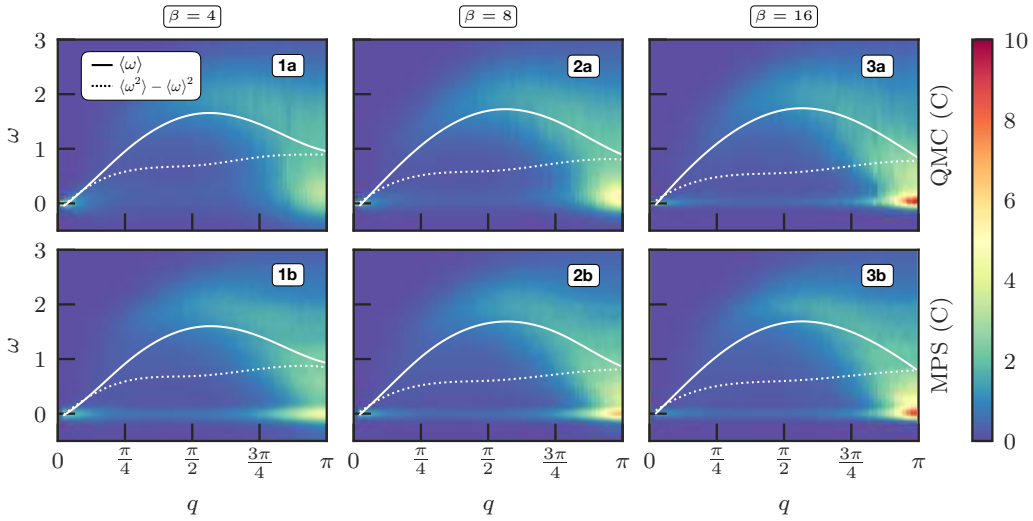

Figure C.3: Comparison of QMC (upper panels) and MPS (lower panels) results for $S_q(\omega)$ at inverse temperatures $\beta = 4, 8$ and 16 computed in the C ensemble ($S^z_{\rm tot} = 0$). The QMC calculations were carried out on $N = 128$ periodic systems and the MPS calculations on $N = 64$ open systems, in both cases with the $D = 1$ box distribution of couplings. The white curves show the first two cumulants, $\langle\omega\rangle$ (solid curves) and $\langle\omega^2\rangle - \langle\omega\rangle^2$ (dashed curves) computed directly from the spectra. We show cuts through the $\beta = 16$ data set at fixed frequencies and momenta in Fig. C.4.

2. Dynamic structure factor

In Fig. C.3 we compare MPS and QMC results for $S_q(\omega)$ for the full range of q values at three different inverse temperatures, $\beta = 4$, 8 and 16 for $D = 1$. In the current case, the results obtained by both methods agree very well at $\beta \simeq 16$. We make both vertical and horizontal cuts (at fixed q and ω, respectively) through $S_q(\omega)$ at $\beta = 16$, as shown in Fig. C.4 to show the details. Only a small discrepancy can be seen in the low q modes in panel (d), which simply originates from the different boundary conditions. At high temperatures, the low-energy structures are slightly broadened in the QMC results, and as β increases, the imaginary-time information becomes adequate for the stochastic analytic continuation (SAC) to generate high quality spectra. While the MPS results are clearly more reliable at high T, we have concluded that the QMC+SAC method is advantageous in the low-T regime, where we cannot reach sufficiently large system sizes with the MPS method. Therefore, we regard the two methods as complementary in different temperature regimes.

Comparing with the Heisenberg chain without disorder [307], we find out that the main shape of the spectra are similar, as also found experimentally [465] (see discussion below). However, in the disordered chains there is also a prominent band at very low energies, with spectral weight extending throughout the Brillouin zone but with a strong maximum around $q = \pi$ at low temperatures (and a weaker maximum around $q = 0$). This feature is a clear sign of excitations related to the high density of low-energy states in the random singlet state. For $D \simeq 0.567$, the work in Ref. 460 found similar structures of $S_q(\omega)$, except that the low energy peaks are claimed to be singular δ peaks, which is different from what we observe here as we have explicitly eliminated this singular contribution by working in the C ensemble.

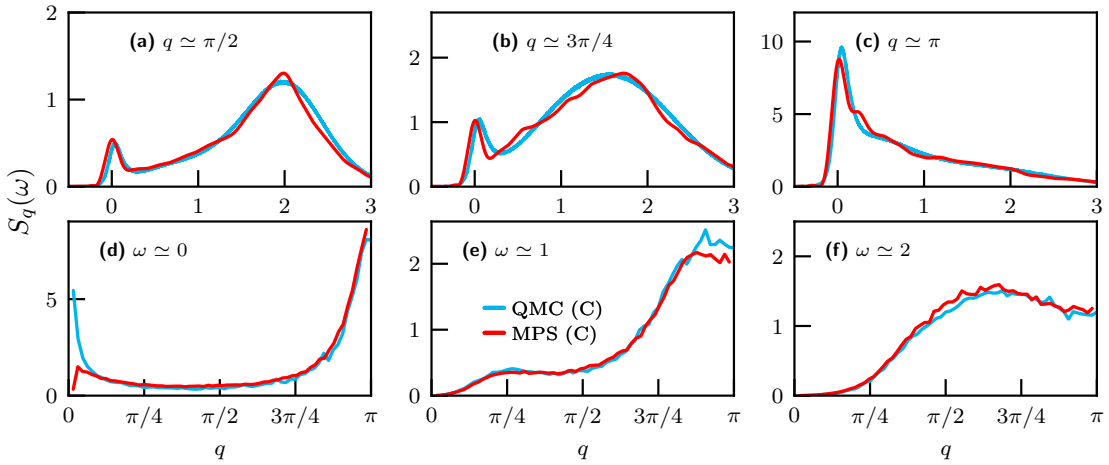

Figure C.4: Cuts at fixed momentum (upper row) and fixed frequency (lower row) of the dynamic structure factor $S_q(\omega)$ at $\beta = 16$, from the same calculations as Fig. C.3 at three different q and ω values. MPS and QMC results are shown as blue and red curves, respectively. The slightly horizontal shift of the data at fixed momentum in panels **(a)**, **(b)** and **(c)** between the two methods is due to the different definitions of q for PBC (QMC case) and OBC (MPS case). At fixed low energy ($\omega \simeq 0$) in panel **(d)**, the difference at small q between MPS and QMC is due to the different boundary conditions used.

Thus, $S_q(\omega)$ in Fig. C.3 excludes any delta peak at $\omega = 0$ and only represents the regular contributions which still show a (regular) very sharp low-frequency peak. Apart from the discrepancy regarding the claimed singular peak, the results for $S_q(\omega)$ shown in Fig. S5 of Ref. 460 also appear to show a sharp structure around $q = \pi$ rather far above zero energy, whereas our results, for the same disorder strength and similar system size, show a more continuously evolving spectral weight with maximal intensity at significantly lower frequency. The reason for the different forms is not clear to us, but the consistent results from both MPS and QMC+SAC calculations in our work (such as the near perfect agreement at $\beta = 16$ in Fig. C.3) makes us confident that these results are correct.

Comparison with "Strong Disorder Renormalization Group" predictions Next we discuss scaling behaviors of $S_q(\omega)$ at low T. According to the strong disorder renormalization group (SDRG) theory, at low energies, when q is close to π, at the random singlet fixed point $S_q(\omega)$ obeys the scaling form [457, 458],

$$S_q(\omega) = A\left\{ l_v \omega \ln^3(\Omega_0/\omega) \Phi\left[\sqrt{|(q-\pi)l_v|}\ln(\Omega_0/\omega)\right]\right\}^{-1}, \tag{C.13}$$

where A and l_v are non-universal constants and Ω_0 is a cutoff energy scale. The universal scaling function $\Phi(x)$ is given by

$$\Phi(x) = 1 + x\frac{\cos(x)\sinh(x) + \sin(x)\cosh(x)}{\cos^2(x)\sinh^2(x) + \sin^2(x)\cosh^2(x)}. \tag{C.14}$$

To test this form, in Fig. C.5 (a) we plot QMC results for $S_q(\omega)$ at a fixed low frequency $\omega \simeq 0$ for $N = 64$, $D = 2$ at three low temperatures $\beta = 64, 128$, and

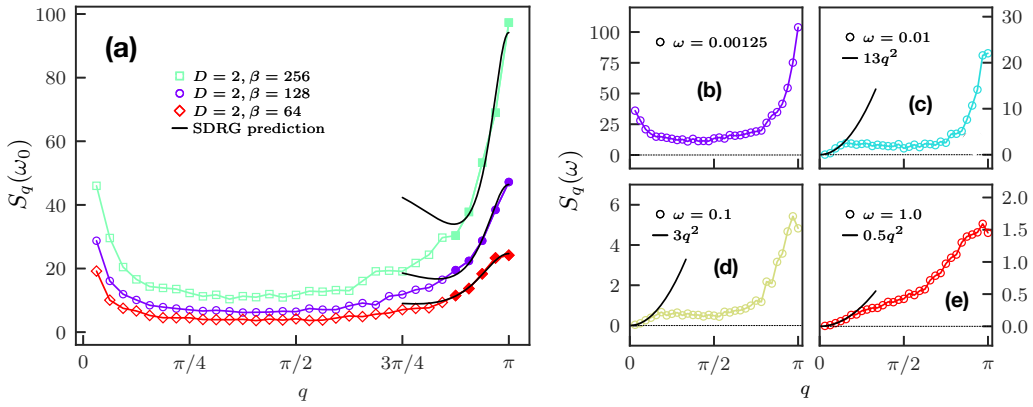

Figure C.5: **(a)** QMC result of $S_q(\omega)$ at fixed frequency $\omega = 0.00025$ for the $D = 2$ disorder distribution at three different temperatures; $\beta = 64$, 128 and 256. The solid curves are fits to the SDRG scaling form $a\Phi(b\sqrt{|q-\pi|})$ of Eq. (C.13) at fixed ω close to $q = \pi$. The estimated constants from these fits are $(a, b) = (12.3, 15.9)$, $(23.2, 20.8)$, and $(47.1, 27.0)$, for $\beta = 64$, 128 and 256 respectively. **(b,c,d,e)** QMC results of $S_q(\omega)$ at different cut-off frequency ω for systems with $D = 2$, $\beta = 128$. Panel (b) shows that for small ω, the contribution close to $q = 0$ is divergent, while panels (c,d,e) indicate that when the horizontal cut in Fig. C.2 is made above the narrow band at low energy, the quadratic vanishing behavior predicted by the random singlet theory is approximately recovered.

256[6]. In the SDRG scheme the cutoff-scale Ω_0 in Eq. (C.13) can be interpreted as the temperature [394, 395]. We have chosen a very small frequency $\omega = 0.00025$, so that we are in the low-frequency regime $\omega \ll \Omega_0$, as required for the scaling form to be valid at the temperatures considered [457, 458]. We have fitted the data to the form (C.13) individually for the three cases, but we can see that the trend for increasing β ($\sim 1/\Omega_0$) is roughly as expected based on the factor $\ln^{-3}(\Omega_0/\omega)$ which directly controls the value at $q = \pi$. We should also note here that there may still be some finite-size effects left for the system size considered here, and in order to test the predicted form in greater detail one would have to systematically study the convergence with increasing N at fixed β values. Nevertheless, in Fig. C.5 (a) we observe a peak at $q = \pi$ consistent with the predicted scaling form, reflecting the predominantly antiferromagnetic character of the low-energy fluctuations [457, 458], but moving away from $q = \pi$ we do not observe the minimum present in the theoretical form. Instead we see a broader minimum at smaller q (away from the region of wavenumber where the theoretical form can be expected to apply) and a maximum as $q \to 0$ that is not predicted by the SDRG theory.

In addition to the peak structure at $q = \pi$, Ref. 458 also predicts a quadratically vanishing behavior for small q, i.e. $S_{q\to 0}(\omega) \propto q^2$ for small ω, which is clearly different from our results. As the temperature is lowered, we observe a peak that increases sharply instead. Similar behavior can be seen in Fig. C.4 (d), even though the temperature there is higher. However, as shown in Fig. C.5 (b,c,d,e), when the frequency ω of the cut is fixed at larger values, e.g., at $\omega \simeq 0.1$, a q^2 behavior is roughly reproduced. This indicates that the origin of the low-q peak at very low

[6] We do not consider MPS calculations here because the temperatures are too low for this method to work well.

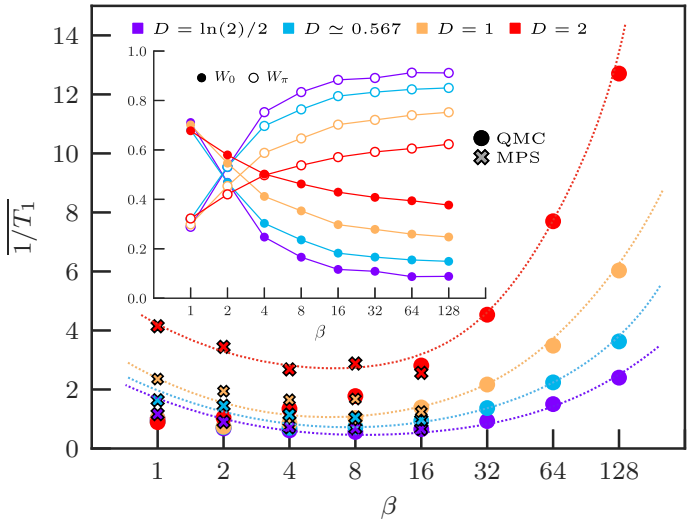

Figure C.6: Temperature dependance of the mean NMR relaxation rate $\overline{1/T_1}$ for different disorder distributions. MPS data (shown with x symbols) are available only up to $\beta = 16$ due to size limitations ($N = 64$), while the QMC results (circles) are shown also at lower temperatures based on $N = 128$ systems. The inset shows the relative contributions from wavevectors close to 0 and π. Dotted lines are guides to the eye. MPS data are expected to be more reliable than QMC ones (because of the SAC) at high temperatures, hence the slight disagreement observed in the figure

frequencies (likely the whole band of low-energy excitations significantly away from $q = \pi$) in Fig. C.3 is beyond the SDRG description, but the SDRG behavior for small q can still be seen approximately once one moves away from these very low frequencies. The low-energy behavior of $S_{q\simeq 0}(\omega \sim 0)$ is likely instead related to anomalous spin diffusion and will be important for the NMR relaxation rate $1/T_1$, which we will discuss further below.

3. NMR relaxation rate

We have extracted the NMR spin-lattice relaxation rate $1/T_1$ for different temperatures and disorder distributions. The results from QMC and MPS calculations are summarized in Fig. C.6. In the MPS calculations we directly averaged the local spectral function $S_{r=0}(\omega)$ obtained for each individual disorder realization over several hundred realizations, while in the QMC calculations we performed the stochastic analytic continuation on the disorder averaged imaginary-time correlations data.

Spin diffusion regime Due to the conservation of S^z_{tot}, low-energy contributions are expected for small momenta q in $S_q(\omega)$. This is known as spin diffusion and is only significant at high temperature in most systems [178, 306]. In this regime, the relaxation rate will explicitly depends on the cutoff (length scale, NMR frequency not being exactly zero, etc.). In order to quantify contributions of the low q and the $q \sim \pi$ modes, we separate the contributions from small q and q close to π. In practice, this can be accomplished by separating the q space into two equal parts [306], defining a relative weight $W_0 = \sum_{|q|\leq \pi/2} S_q(\omega = 0) / \sum_q S_q(\omega = 0)$, which will typically be

dominated by the $q \sim 0$ contributions. Similarly, we define $W_\pi = 1 - W_0$ to capture the $q \sim \pi$ contributions. The temperature dependence of W_0 and W_π are plotted in the inset of Fig. C.6 for different disorder distributions. At high temperatures, W_0 dominates $1/T_1$ and there exists a crossover temperature where W_π overwhelms W_0. Even at the lowest temperature accessed, W_0 is still non-negligible and grows as the disorder gets stronger, implying that spin diffusion tends to play an important role in the random singlet phase. This aspect of the dynamics appears to be beyond the prediction made within the SDRG approach — recalling that SDRG suggests a vanishing W_0 at low T [458]. It is helpful to notice that, since W_0 is normalized and evidently decays much slower than $1/T_1$ is growing, the un-normalized partial spectral weight $\sum_{|q|\leq\pi/2} S_q(\omega = 0)$ increases as $T \to 0$.

Low-temperature regime At low-temperature, we expect a more universal behavior when the spin-diffusive contributions are not important, as found, for instance, in the uniform chain [332, 351]. Down to the lowest temperature accessible in the MPS calculations, $\beta \simeq 16$, no tendency of increasing $1/T_1$ with β is observed for any of the disorder distributions studied. The QMC results, however, exhibit a crossover feature from the spin diffusion regime to the low T regime, with a disorder-dependent crossover scale. As seen clearly in Fig. C.6, for $\beta \geq 16$, $1/T_1$ increases dramatically as $T \to 0$, mainly due to the large contributions from q close to π, which is similar to the uniform Heisenberg chain [178, 306]. It is noteworthy that the contribution to $1/T_1$ from $q \sim 0$ is not always negligible even at low temperature, especially for strong disorder D, which will be relevant for our discussion of experiments in the next section. However, here we have a sharp discrepancy with both experiments and previous numerical results [459, 460], in which $1/T_1$ was found to be decreasing as T decreases. We believe such discrepancies arise from the difference between the typical and mean values of a very broad distribution of $1/T_1$ values, as we will explain next.

Distribution of NMR relaxation rate Here we consider the distribution of $1/T_1$. In a homogeneous system, the locally defined relaxation rate is also homogeneous, taking single value, while in a disorder system one expects a distribution of relaxation rates, associated with the measurement of the local dynamical correlation on each (inequivalent) site of the system. In such a disordered system, the *global* nuclear spin component along the applied magnetic field M_z is the average over each nucleus (sites i) and relaxes as,

$$1 - M_z(t) \propto \frac{1}{N} \sum_{i=1}^{N} \mathrm{e}^{-t/T_{1,i}}. \tag{C.15}$$

In an experimental setup, one has only access to $M_z(t)$, which can be phenomenologically modeled by a stretched exponential to take into account disorder effects,

$$1 - M_z(t) \simeq \mathrm{e}^{-(t/\tau_0)^\gamma} \tag{C.16}$$

with τ_0 and γ fit parameters characterizing the stretched exponential distribution of $1/T_1$ [466, 467]. It is evident that the uniform case should be recovered with $\gamma = 1$ and $1/\tau_0 = 1/T_1$ at any temperature. For the disordered chains, Fig. C.7 (a–d) shows the cumulative integrated probability distribution of $1/T_1$ computed using MPS. The distribution spreads over a few orders of magnitude and broadens as the temperature

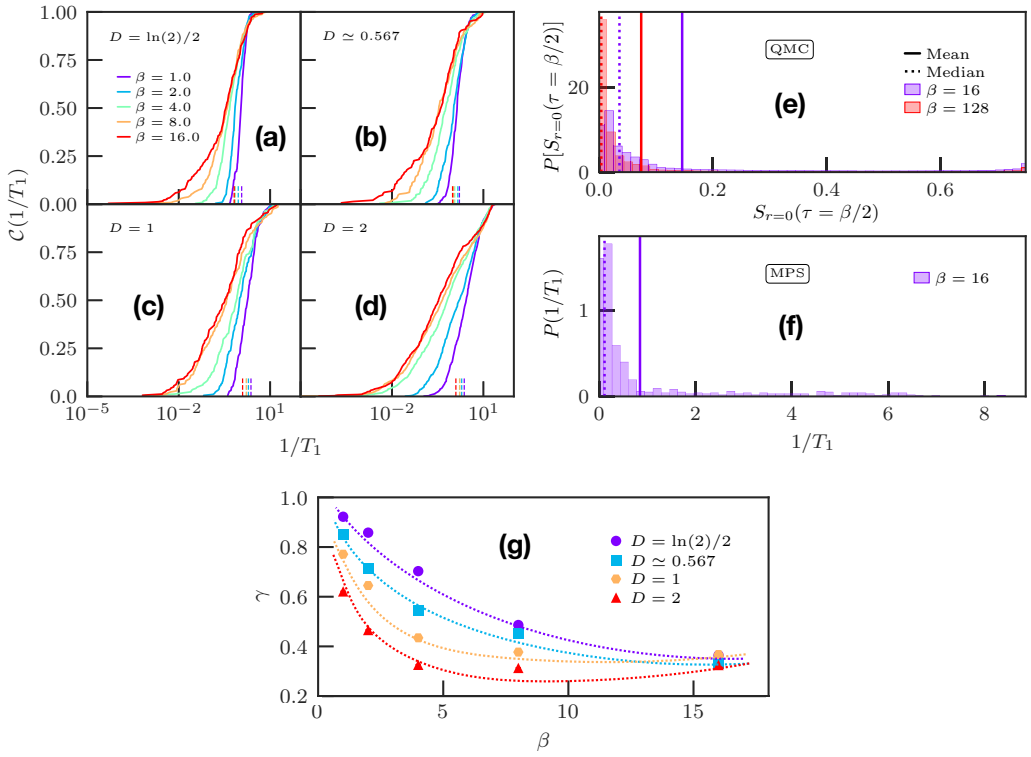

Figure C.7: (a,b,c,d) Cumulative probability distribution of the NMR relaxation rate $1/T_1$ obtained from MPS simulations for the different coupling distributions at $\beta = 1$, 2, 4, 8 and 16. Note that the x axis is shown on a logarithmic scale. The vertical marks indicate the corresponding mean values graphed in Fig. C.6. **(e,f)** Distributions of $1/T_1$ in $D = 2$ systems from MPS calculations and $S_{r=0}(\tau = \beta/2)$ approximation from QMC calculations. The mean and median values are indicated by the vertical solid and dotted lines, respectively. The distributions are so broad that the mean value is dominated by the "rare events" contribution, while the median value corresponds to typical events. **(g)** Temperature dependence of the stretched exponential exponent γ as in Eq. (C.16) for the different coupling distributions considered. Dotted lines are guide to the eye.

decreases. Also, the larger the disorder strength D is, the broader the distribution is at fixed temperature.

From the distribution, the response function $M_z(t)$ can be constructed and fitted to a stretched exponential as in Eq. (C.16), thus determining the parameters τ_0 and γ. The cumulative distribution in Fig. C.7 (a–d) implies a pronounced tail in $P(1/T_1)$, and further, the existence of a γ that is much smaller than one [460], which we verify in Fig. C.7 (g) where we plot the temperature dependence of the exponent γ. Its value decreases with the temperature and the disorder distribution strength D, which reflects the broadening of the distribution. Yet, at low temperature, the exponent seems to converge to a given value independently of the disorder strength, showing the limits of the stretched exponential fitting of the data. We also plot the temperature dependence of $1/\tau_0$ (interpreted as the NMR relaxation rate in experiments) for $D = 2$ in Fig. C.8, and these results agree well with previous investigations [459, 460]. However, the stretched exponential is only an approximation, since it neglects rare events, which can be indeed seen as some anomalously large $1/T_1$ values in Fig. C.7 (f).

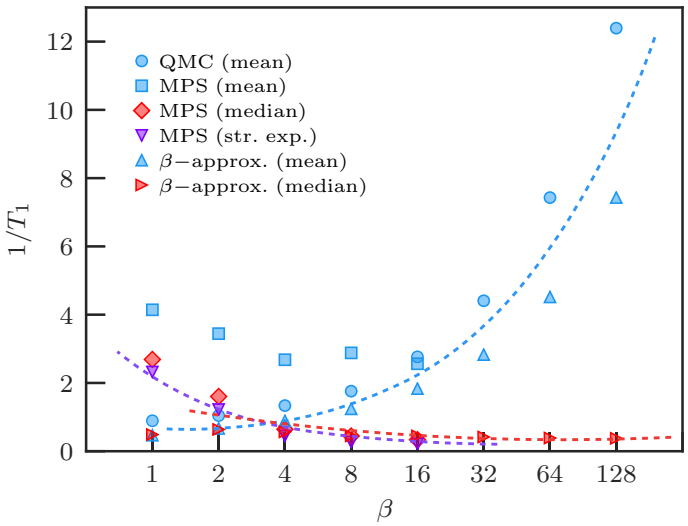

Figure C.8: Mean and median values of $1/T_1$ obtained using different methods: MPS, QMC+SAC and QMC with β-approximation according to Eq. (C.17). We also show the stretched exponential fit parameter $1/\tau_0$ defined in Eq. (C.16) obtained from the $1/T_1$ distribution of the MPS data. Symbols are the computed data point and the lines are only guides to the eye. While the mean NMR relaxation rate value is increasing with the inverse temperature β (dashed blue line), the median value and the stretched exponential distributions are both decreasing (dashed red and purple lines).

These large values are very unlikely within the stretched exponential distribution, and, thus, the resulting $1/\tau_0$ value only gives an estimate of a *typical* $1/T_1$. Here and below we use the median value of $1/T_1$, which is relatively insensitive to the rare events, to represent a typical measurement.

In QMC calculations we do not perform the SAC procedures for individual disorder realization but always work with the disorder averaged $S(\tau)$ in order to have sufficient statistical precision, so that we do not have access to the distribution of $1/T_1$ in this case. To study the $1/T_1$ distribution we instead use a long-standing approximation (which we will refer here to as the "β-approximation") where the $1/T_1$ value can be be obtained directly from imaginary-time data without full analytic continuation [468]. We here provide an alternative derivation of the β-approximation based on $1/T_1$ expressed using $S_{r=0}(\omega)$ instead of the related dynamic susceptibility $\chi_q(\omega)$ considered previously. The general idea underlying the approximation is that the low-frequency behavior is most strongly reflected at the longest imaginary-time value $\tau = \beta/2$. At this τ point, by replacing $S_{r=0}(\omega)$ by its Taylor expansion around $\omega = 0$ and keeping only the leading term, we obtain,

$$S_{r=0}(\tau = \beta/2) = \frac{2}{\pi}\int_0^{+\infty} \mathrm{d}\omega\, \mathrm{e}^{-\beta\omega/2}\Big[S_{r=0}(\omega=0) + \omega\partial_\omega S_{r=0}(\omega=0) + \ldots\Big]$$
$$\simeq \frac{4}{\pi\beta} S_{r=0}(\omega=0) = \frac{1}{T_1}\frac{4}{\pi\beta}. \qquad \text{(C.17)}$$

For the above approximation to be good, $S_{r=0}(\omega)$ should not show a strong ω dependence in the window $[0, \Delta\omega]$, where $\Delta\omega$ scales as $2/\beta$. However, in the case considered here, $S_{r=0}(\omega)$ appears to have a very high but narrow peak, with a width

smaller than $2/\beta$, in the vicinity of $\omega = 0$ and a much lower, broader peak at higher energies, especially for strong disorder at low T. Therefore, it is reasonable for the β-approximation to deviate from the exact results, as we indeed find. In any case, we expect the distribution of approximants to reflect the distribution of $1/T_1$. According to Eq. (C.17), at fixed temperature, $1/T_1$ is proportional to $S_{r=0}(\tau = \beta/2)$ so that the $1/T_1$ distribution can be readily read off from the distribution of $\mathrm{S}_{r=0}(\tau = \beta/2)$, which we graph in Fig. C.7 (e). We also plot MPS results for $P(1/T_1)$ at $\beta = 16$, $D = 2$, for comparison in Fig. C.7 (f). The distribution $P[S_{r=0}(\tau = \beta/2)]$ is bounded by the equal-time value $S_{r=0}(\tau = 0) = 3/4$ and has a long tail that becomes more evident as the temperature decreases. The tail contributes large rare-event values to the mean $1/T_1$, which originate from a small number of sites with almost free spins in some disorder realizations [458]. These rare events dominate the mean value of $P[S_{r=0}(\tau = \beta/2)]$, and this value may not be suitable to describe the experimental NMR measurements analyzed with the assumed stretched-exponential distribution [459]. Alternatively, we use the typical value of the distribution to represent a local probe more properly [458].

We present the temperature dependence of $1/T_1$ for $D = 2$ in Fig. C.8, using the different methods discussed above. The mean values obtained using QMC+SAC and MPS are computed in the momentum space, as also already shown Fig. C.6, while the other calculations were performed in real space. Even though the β-approximation cannot fully reproduce the QMC+SAC result, it indeed impressively catches the expected low-T diverging trend [458]. In addition, in the low-T regime we observe good agreements between Refs. 459 and 460 and the median $1/T_1$ extracted from the MPS results using the stretched exponential fitting.

4. Summary and discussions

Summary of the results In this work, we carried out the Chebyshev expansion method using matrix product states and quantum Monte Carlo (supplemented by the SAC method) calculations to study the dynamical properties of the random $S = 1/2$ Heisenberg chain. We are able to ascertain that, in the random singlet phase, the finite-temperature dynamic structure factor $S_q(\omega)$ preserves high-energy features (at ω of the order of the mean exchange constant) similar to those of the clean chain but broadened by the disorder, while new features appear at low energy. Most prominently, the large density of low-energy excitations, expected at low T in the random singlet phase, gives rise to a dispersionless narrow band of spectral weight at $\omega \sim 0$. These low-energy excitations should be localized due to the disorder. For q close to π, $S_q(\omega)$ largely obeys the scaling form predicted by the SDRG approach [457, 458], however, the SDRG expectation that $S_{q\simeq 0}(\omega) \propto q^2$ [458] is not fulfilled in the limit of $\omega \to 0$. Instead, we find that $S_{q\simeq 0}(\omega \sim 0)$ is large and increase as T is lowered, suggesting that, in the presence of disorder, spin diffusion plays an important role even at very low temperatures. This diffusive feature is beyond the realm of the SDRG method [458].

We extracted the NMR spin-lattice relaxation rate $1/T_1$ from the low-energy behavior of $S_q(\omega)$ and also studied the corresponding distribution. In the QMC+SAC approach we compute only the mean value of $1/T_1$ over the disorder, while in an experiment one can expect to probe typical values instead. To study the distribution

of $1/T_1$, we use MPS calculations as well as an approximate method [468] to extract the values from the imaginary-time QMC correlation functions that does not require full analytic continuation. These calculations reveal a broad distribution of $1/T_1$ values, which can be fitted using stretched exponentials, in agreement with previous investigations [460, 469], except for rare very large values. The stretched exponential fitting is not sensitive to such rare contributions in the tail, thus giving the typical value of the distribution instead of the true mean $1/T_1$. The typical $1/T_1$ exhibits a slowly decaying behavior as T decreases [460, 469]. Furthermore, we find that rare events are responsible for the divergence of the mean $1/T_1$ as $T \to 0$. This behavior is also in agreement with analytical predictions of the excitations in the random singlet phase [458].

Relevance to experiments The perhaps most extensive NMR studies of the random singlet state were carried on $BaCu_2SiGeO_7$ [469], which can be modeled as weakly coupled spin-1/2 Heisenberg chains with bimodal distribution of the couplings, with in-chain random couplings $J_a = 24$ meV and $J_b = 50$ meV [469], though it is also known that neglected small three-dimensional interchain couplings are ultimately responsible for antiferromagnetic ordering at very low temperature ($T_c = 0.7$ K) [465]. In the experiments, $1/T_1$ was found to decrease slowly as T is lowered [459, 469], as also seen in our results for the typical relaxation rate.

It should be stressed that comparisons between model calculations and experiments, especially for dynamical quantities, still have to be viewed with some caution and further work will be needed to clarify the effects of various perturbations normally not included in the models. In fact, even for clean materials, e.g., $BaCu_2Si_2O_7$ (with $J = 24.1$ meV $\simeq 280$ K), no increase was observed in the $1/T_1$ at low-temperature in disagreement with recent numerical studies [332, 351] and Tomonaga Luttinger liquid theory, where a logarithmic increase in predicted [308, 329]. We believe that these discrepancies can have several explanations. First, the small three-dimensional coupling J_{3D} which is responsible for the three-dimensional ordering in the clean ($T_c = 9.2$ K) and disordered ($T_c = 0.7$ K) compounds is not that small, and our work in the previous chapter showed that the NMR relaxation can be affected already at temperature of order $3T_c$. As for the disordered system $BaCu_2SiGeO_7$, the NMR experiments were performed using the ^{29}Si nucleus [469], which is coupled almost symmetrically to two Cu ions (on J_a bonds only), hence resulting in filtering-out of the antisymmetric component $q \sim \pi$ by the hyperfine form factor. As a result, such NMR data would correspond to measurements primarily of the $q \sim 0$ modes, which are responsible for a relatively small fraction of the total $1/T_1$ computed here under the assumption of a strictly on-site hyperfine coupling.

It would be interesting to perform NMR studies also on a different nucleus. We have not studied distributions of the low-frequency structure factor beyond the completely local on-site correlations, and it is therefore not possible at this point to make more detailed comparisons with the experiments with a realistic hyperfine form-factor involving also nearest-neighbor correlations. The role of mean versus typical relaxation rates in the experiments is also not fully settled, as one cannot completely rule out that rare events also play some role. It is also clear that further work is needed to understand the role of three-dimensional couplings on the random singlet phase and on its dynamical properties.

III. Doped S=1 antiferromagnet DTN*X* compound at high magnetic fields

Adapted from the works Phys. Rev. Lett. **118**, 067203 (2017)

Anna Orlova, Rémi Blinder, Edwin Kermarrec, **Maxime Dupont**[7], Nicolas Laflorencie, Sylvain Capponi, Hadrien Mayaffre, Claude Berthier, Armando Paduan-Filho, and Mladen Horvatić

and Phys. Rev. Lett. **118**, 067204 (2017)

Maxime Dupont, Nicolas Laflorencie, and Sylvain Capponi

and Phys. Rev. B **96**, 024442 (2017)

Maxime Dupont, Sylvain Capponi, Mladen Horvatić, and Nicolas Laflorencie

and arXiv:1801.01445 (2018)

Anna Orlova, Hadrien Mayaffre, Steffen Krämer, **Maxime Dupont**, Nicolas Laflorencie, Sylvain Capponi, Armando Paduan-Filho, and Mladen Horvatić

In this series of works, we study the interplay between disorder and interactions for emergent bosonic degrees of freedom induced by an external magnetic field in the disordered quasi-one-dimensional $S = 1$ antiferromagnetic compound $Ni(Cl_{1-x}Br_x)_2$-$4SC(NH_2)_2$ (DTNX), introduced in the first chapter for the disorder-free case. When doping with Br impurities, DTNX displays fascinating properties [398]: it was reported as an exceptionally convenient archetype material presenting a Bose-glass (BG) phase [397–399]. Both the Bose-Einstein condensation (BEC) and the trivial ferromagnetic (FM) phase of the clean case are robust to disorder and subsist in the doped DTNX compound, although their associated critical fields H_{c1} and H'_{c2} are shifted. In addition, new BG regimes are predicted to (i) substitute the gapped large-D regime at low field and (ii) to intervene between the BEC and the polarized phase between H_{c2} and H'_{c2} (see Fig. C.9 for a comparative picture between $x = 0$ and $x \neq 0$). The BG phase in DTNX can be pictured and defined as follows: coexisting with a gapped background, localized magnetic states occur in the vicinity of impurities and display a finite local susceptibility. These localized degrees of freedom are spatially separated with exponentially decaying correlations which prevent any long-range ordering. Prior to our works, it was proposed in Ref. 398 that the BG phase at high magnetic field is uninterrupted between the BEC and FM regimes, from H_{c2} to H'_{c2}, as shown in Fig. C.9 for $x \neq 0$. Instead, it turns out that the impurity degrees of freedom display a striking "many-body delocalization" with a resurgence of a global phase coherence, leading to disorder-induced long-range order [449, 450]. Building on nuclear magnetic resonance experiments, we first describe the localization of isolated impurity states, providing a realistic theoretical modeling for DTNX. Going beyond single impurity localization we use quantum Monte Carlo simulations to explore many-body effects from which pairwise effective interactions lead to a impurity-induced Bose-Einstein condensation (BEC) revival

[7] In all these experimental/theoretical collaborations, I performed the theoretical work and analysis.

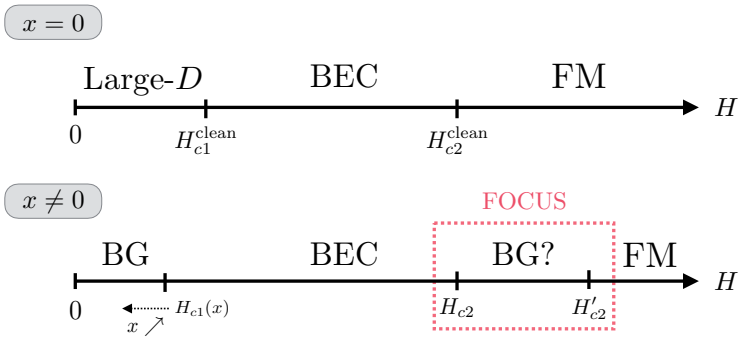

Figure C.9: Zero temperature phase diagram of DTN ($x = 0$) and DTNX ($x \neq 0$) as a function of the magnetic field H. In the clean case, the intermediate long-range ordered phase (BEC) is bounded by two critical fields $H_{\text{c1}}^{\text{clean}}$ and $H_{\text{c2}}^{\text{clean}}$. Below $H_{\text{c1}}^{\text{clean}}$, DTN is in a large-$D$ phase due to strong single-ion anisotropy, and above $H_{\text{c2}}^{\text{clean}}$, the material is a fully polarized ferromagnet (FM). The disorder $x \neq 0$ expands the DTNX phase diagram with new BG phases. However, we find that the high magnetic field BG phase is actually undermined by long-range ordering induced by the disorder and focus on this putative BG at high magnetic field (red square). Note also that the first critical field H_{c1} is renormalized downwards by the doping.

at $H \geq 12.3$ T. Moreover we address the question of the existence of a many-body localized Bose-glass (BG) phase in DTNX, which is found to compete with a series of a new kind of BEC regimes made out of the multi-impurity states. The global magnetic field–temperature phase diagram of DTNX reveals a very rich structure for low impurity concentration, with consecutive disorder-induced BEC mini-domes separated by intervening many-body localized BG regimes. Upon increasing the impurity level, multiple mini-BEC phases start to overlap, while intermediate BG regions vanish. Finally, further nuclear magnetic resonance experiments critically address the stability of the Bose-glass phase in doped DTN ($x = 13 \pm 1\%$), and find that, as we predict it, it indeed hosts a novel disorder-induced *ordered* state of matter, where many-body physics leads to a resurgence of quantum coherence emerging from localized states[8].

1. Microscopic modeling

The DTN material is a three-dimensional antiferromagnet consisting of weakly coupled chains of $S = 1$ spins, borne by Ni^{2+} ions, subject to a strong single-ion anisotropy. The potential interest of this system, presenting at low temperature a magnetic-field-induced, 3D-ordered, canted phase, was already realized in 1981 [51],

[8]Actually, the experiments probed the NMR relaxation rate $1/T_1$. This is a *local* quantity that cannot directly detect long-range order. However, interpreting the temperature position of the maximum of $T_1^{-1}(T, H)$ as the critical temperature between an ordered and disordered phase provided a phase boundary compatible with the one obtained by quantum Monte Carlo simulations. Moreover, inside the new ordered phase, the power-law behavior of $T_1^{-1}(T)$ is identical to the one observed inside the main BEC phase at lower fields, $H \in [H_{\text{c1}}, H_{\text{c2}}]$.

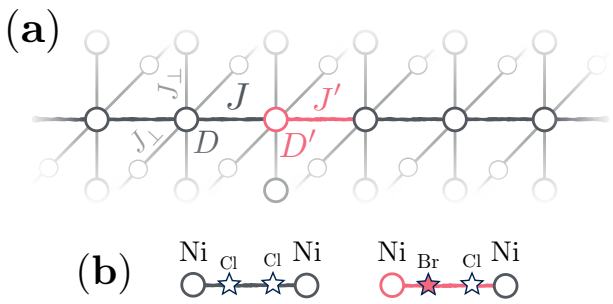

Figure C.10: **(a)** Sketch representation of the relevant three-dimensional structure for DTNX model. On the chains, the clean sites (single ion anisotropy D) with nearest-neighbor interaction (J) are in grey. The doped ones (single ion anisotropy D') are in pink with the modified interaction (J') in pink as well. The three dimensional coupling between the chains $J_\perp$ is not affected by the doping. For readability, only one thick line representing a single chain is displayed. **(b)** Two types of $S = 1$ dimers: clean Cl−Cl (left hand side) and doped Br−Cl (right hand side), with Br preferentially positioned on the "left" (see supplementary material of Ref. 398).

but DTN became a topical system only after this type of phase was recognized to be a convenient representative of the BEC [143,147], and the upper critical field of the BEC phase in DTN is found to be experimentally well accessible, $H_{c2}^{\text{clean}} = 12.3$ T [470]. Since then, it became one of the most studied archetypal materials for the BEC-type spin systems [44]. To describe pure and doped DTN we use the following model for $S = 1$ spins on a tetragonal lattice:

$$\mathcal{H}_{\text{DTN}X} = \sum_i \Bigg\{ \sum_m \Big[J_{i,m} \mathbf{S}_{i,m} \cdot \mathbf{S}_{i+1,m} + D_{i,m} \left(S^z_{i,m}\right)^2 - g\mu_B H S^z_{i,m} \Big] + \sum_{\langle m,n \rangle} J_\perp \mathbf{S}_{i,m} \cdot \mathbf{S}_{i,n} \Bigg\}, \tag{C.18}$$

where for pure DTN the AF exchange along the chain direction is $J_{i,n} = J = 2.2$ K, the single-ion anisotropy is $D_{i,n} = D = 8.9$ K, and the chains are coupled by the interchain coupling between the nearest-neighbor sites (denoted by $\langle m, n \rangle$) $J_\perp = 0.18$ K. H is an external magnetic field applied along the single-ion anisotropy axis z, preserving the U(1) symmetry. We use $g = 2.31$ for the gyromagnetic factor, such that in the absence of chemical disorder, the clean upper critical field $H_{c2}^{\text{clean}} = (D + 4J + 8J_\perp)/g\mu_B = 12.3$ T, as pictured in Fig. C.9 ($x = 0$).

In the doped DNTX compound, as shown in Fig. C.10 (b), one of the two Cl^- ions in the intrachain J coupling bond may be substituted by the doped Br^- impurity, introducing thereby disorder in the system. Based on the macroscopic experimental data (magnetization, susceptibility and specific heat) and global modeling of the system by quantum Monte Carlo simulation, DTNX was proposed to be a model system for the investigation of the Bose-glass phase [397, 398]. It is assumed that doping introduces only local perturbations: each Br impurity modifies only the exchange coupling value of the affected bond to $J' = 2.42J$ and the single-ion anisotropy of the closest Ni ion to $D' = 0.36D$, without affecting any other bond or

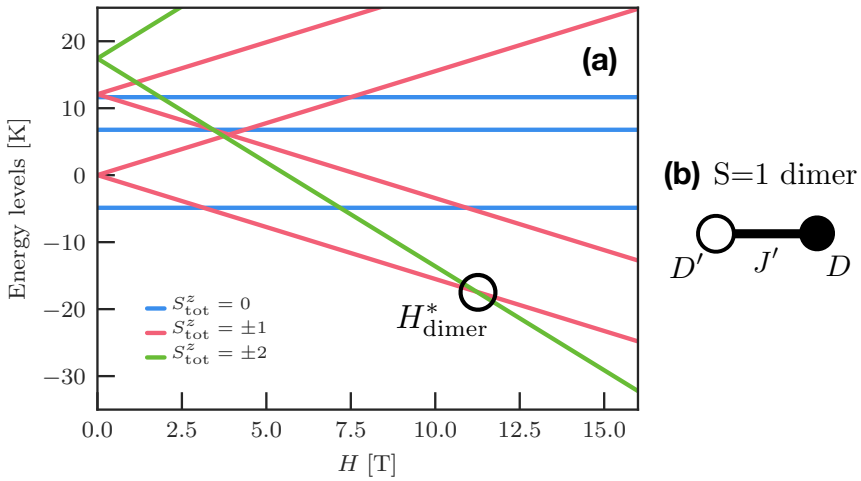

Figure C.11: **(a)** Energy levels of an isolated doped $S = 1$ dimer, shown in panel **(b)**, plotted against the external magnetic field. A level crossing between $S^z_{\rm tot} = 2$ and $S^z_{\rm tot} = 1$ states occurs at $H^*_{\rm dimer} \simeq 11.2$ T using realistic microscopic parameters J', D' and D (see text).

anisotropy value (see Fig. C.10 (b)). In comparison to the initially proposed J' and D' values [398], the values given here are refined by combining NMR measurements and theoretical work, which is explained in the following.

As regards other experimental investigations of the DTNX compound, the doping dependence of the critical behavior near the first critical field H_{c1} was studied by neutrons [456] and compared to the situation in the nominally pure compound DTN [231]. In contrast to the initially proposed evidence for the theoretically expected change of criticality from the BEC-type to BG-type [398], the situation appears inconclusive: the experimentally observed critical behavior is always affected by the distribution of the critical field values and the effects of elasticity, and is probably not representative of the theoretically expected physics. We further mention the detailed neutron study of the 6% doped DTNX compound in Ref. 471 in which a non-dispersive (local) mode is detected above the top of the magnon band. From NMR results this mode is explicitly attributed to the doped impurities.

a. Single impurity physics

Single doped S=1 dimer A first step into understanding Br-doping effects is to consider a single Br impurity in a isolated $S = 1$ dimer, see Fig. C.10 (b). The resulting Hamiltonian is a 9×9 block-diagonal matrix, which can be *analytically* diagonalized within $S^z_{\rm tot} = 0$, ± 1 and ± 2 symmetry sectors. In the following we use $J' = 5.32$ K and $D' = 3.2$ K which are the microscopic parameters determined from a direct comparison between NMR data and theory. This comparison will be discussed below. The eigenenergy levels are shown in Fig. C.11 against the external magnetic field H. The crossing between the two lowest $S^z_{\rm tot} = 2$ and $S^z_{\rm tot} = 1$ levels occurs at

$$H^*_{\rm dimer} = \left[J' + \frac{D' + D}{2} + \frac{1}{2}\sqrt{(D - D')^2 + (2J')^2} \right] / g\mu_B \simeq 11.2 \text{ T}. \qquad \text{(C.19)}$$

At high magnetic field, one can restrict the problem in the vicinity of $H^*_{\rm dimer}$ to the

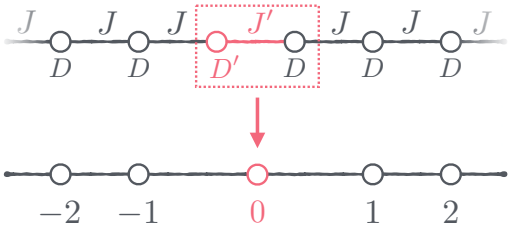

Figure C.12: Effective one-dimensional model for the dynamics of a single impurity dimer described at high magnetic field as a two-level system $\{|\Phi_1\rangle, |\Phi_2\rangle\}$.

two lowest-lying levels. One of them is the ground state in the $S^z_{\rm tot} = 1$ sector with eigenvector

$$|\Phi_1\rangle = \sqrt{\ell}|\uparrow 0\rangle + \mathrm{e}^{i\theta}\sqrt{1-\ell}|0\uparrow\rangle, \tag{C.20}$$

where

$$1/\ell = 1 + \left[\frac{D-D'}{2J'} - \sqrt{1+\left(\frac{D-D'}{2J'}\right)^2}\right]^2, \tag{C.21}$$

and θ is a phase factor. The other is the ground state in the $S^z_{\rm tot} = 2$ sector, trivially given by $|\Phi_2\rangle = |\uparrow\uparrow\rangle$. The imbalance between local anisotropies, $D' \neq D$, leads to a spin imbalance between the left and right sites of the perturbed dimer. Their respective local magnetization in the $|\Phi_1\rangle$ state is simply equal to

$$m_z^{\rm left} = \ell \quad \text{and} \quad m_z^{\rm right} = 1-\ell. \tag{C.22}$$

Although it provides some insight to the local magnetization imbalance, this single dimer model is clearly oversimplified, as the clean environment is totally neglected. In particular, it yields a crossover field $H^*_{\rm dimer} \simeq 11.2$ T *below* $H^{\rm clean}_{\rm c2} = 12.3$ T. One can easily refine this picture by adding the mean-field contribution of the surrounding spins of the clean background, assumed to be fully polarized, which leads to

$$H^*_{\rm Mean-Field} = H^*_{\rm dimer} + (J + 4J_\perp)/g\mu_B \simeq 13 \text{ T} > H^{\rm clean}_{\rm c2}. \tag{C.23}$$

This is self-consistent with our assumption and confirms that the clean background polarizes before the impurities in DTNX when increasing H.

One impurity on a single chain Going beyond the above mean-field scenario, we now deal with the dynamics of a single spin flipped state $|\ldots\uparrow\uparrow 0\uparrow\uparrow\ldots\rangle$ in a fully polarized background, in the presence of a central perturbed dimer. We first start this analysis on a single chain of N sites and work in the $S^z_{\rm tot} = N-1$ symmetry sector. Using the two-level system representation $\{|\Phi_1\rangle, |\Phi_2\rangle\}$, the central dimer is replaced by a single site (at position 0) as pictured in Fig. C.12, which can accommodate one of the two states. Our new basis is made of the following states labeled by the position j of the flipped spin,

$$\begin{aligned} |0\rangle &\equiv |\ldots\uparrow\uparrow\uparrow\rangle|\Phi_1\rangle|\uparrow\uparrow\uparrow\ldots\rangle, \\ |1\rangle &\equiv |\ldots\uparrow\uparrow\uparrow\rangle|\Phi_2\rangle|0\uparrow\uparrow\ldots\rangle, \\ |-2\rangle &\equiv |\ldots\uparrow 0\uparrow\rangle|\Phi_2\rangle|\uparrow\uparrow\uparrow\ldots\rangle, \quad \text{etc.} \end{aligned} \tag{C.24}$$

In order to get a symmetric tight-binding structure for the low-energy dynamics, one has to define for $j > 0$ a new set of states,

$$|\bar{j}\rangle = \sqrt{\ell}|j\rangle + \mathrm{e}^{i\theta}\sqrt{1-\ell}|-j\rangle. \tag{C.25}$$

For an initial $S = 1$ chain of N sites and open boundary conditions, the dynamics in the new basis is governed by the following effective tight-binding model with $\tilde{N} = N/2 - 1$,

$$\mathcal{H}_{\mathrm{tight-binding}} = J\sum_{j=0}^{\tilde{N}-1}\left(|\bar{j}\rangle\langle\overline{j+1}| + |\overline{j+1}\rangle\langle\bar{j}|\right) - \Delta|0\rangle\langle 0| + C\sum_{j=0}^{\tilde{N}}|\bar{j}\rangle\langle\bar{j}|, \tag{C.26}$$

where the constant C and the impurity energy shift Δ located at the ($\bar{j} = 0$) boundary are respectively

$$\begin{aligned} C &= 2N(D + J - H) - 2J + D' + J' - H, \\ \Delta &= J' - J + \left(D' - D + \sqrt{(D'-D)^2 + (2J')^2}\right)/2 \simeq 6.3 \text{ K}. \end{aligned} \tag{C.27}$$

Note that this description, based on the localization of the spin flip excitation on the perturbed dimer is only valid for $J' > J$. The tight-binding Hamiltonian given by Eq. (C.26), having a localized boundary (impurity) potential Δ, admits a localized ground state $|\Psi_0\rangle = \sum_{j=0}^{\tilde{N}} c_j|\bar{j}\rangle$, where $c_j \propto \exp(-j/\lambda)$ for $\Delta > J$. Inserting this form into Eq. (C.26) gives

$$|\Psi_0\rangle = \sum_{j=0}^{\tilde{N}} c_0(-1)^j \exp\left[-j\ln\left(\frac{\Delta}{J}\right)\right]|\bar{j}\rangle. \tag{C.28}$$

In the limit $\tilde{N} \gg \lambda = 1/\ln(\Delta/J)$, the occupation of the central (impurity) site is $|c_0|^2 = 1 - \exp(-1/\xi_\parallel)$, where the localization length governing the decay of the spin density is given by

$$\xi_\parallel = \frac{1}{2\ln(\Delta/J)} = 0.47. \tag{C.29}$$

The energy of this localized bound-state can also be obtained analytically, and the energy difference with the fully polarized state leads to the crossover field value

$$\begin{aligned} H^*_{1\mathrm{D}} &= \left\{D + 2J\left[1 + \cosh\left(\frac{1}{2\xi_\parallel}\right)\right]\right\}/g\mu_B \\ &= H^*_{\mathrm{dimer}} + J/g\mu_B + J^2/(g\mu_B\Delta) \simeq 13.1 \text{ T}. \end{aligned} \tag{C.30}$$

As compared to the isolated dimer picture discussed above, the first correction term corresponds to the mean-field contribution of the fully polarized one-dimensional environment, $J/g\mu_B = 1.4$ T. The delocalization of the flipped spin over its neighboring sites does not extend over large scales, but it is nevertheless gains some kinetic energy, pushing the crossover field further up by $J^2/(g\mu_B\Delta) = 0.5$ T.

One impurity in the three-dimensional lattice The previous single impurity analysis can be extended to a three-dimensional lattice with a similar Hamiltonian to Eq. (C.26). The exponential ansatz solution now includes two different localization lengths along and perpendicular to the chain direction $\xi_{\parallel,\perp}$, with $\xi_\parallel$ given by Eq. (C.29) and

$$\xi_\perp = \frac{1}{2\,\mathrm{arcsinh}\,(\Delta/2J_\perp)} = 0.14, \tag{C.31}$$

expressed in units of lattice spacings. As a result, the final crossover magnetic field is

$$H^* = \left[H^*_{\mathrm{mean-field}} + J\mathrm{e}^{-1/2\xi_\parallel} + 4J_\perp \mathrm{e}^{-1/2\xi_\perp}\right]/g\mu_B \simeq 13.6\ \mathrm{T}, \tag{C.32}$$

where the very short transverse correlation length makes the last correction term negligible (0.01 T). The magnetization profiles of the original physical (magnetic) sites at $T = 0$ and for $H < H^*$ can be computed in the vicinity of the impurity. On the perturbed left and right dimer sites,

$$\begin{aligned} m_z^{\mathrm{left}} &= 1 - (1-\ell)\left[1 - \mathrm{e}^{-1/\xi_\parallel}\right]\left[1 - \mathrm{e}^{-1/\xi_\perp}\right]^2, \\ m_z^{\mathrm{right}} &= 1 - \ell\left[1 - \mathrm{e}^{-1/\xi_\parallel}\right]\left[1 - \mathrm{e}^{-1/\xi_\perp}\right]^2, \end{aligned} \tag{C.33}$$

where ℓ is defined in Eq. (C.21). A similar expression can be obtained for the magnetization of the other (clean) sites of the three-dimensional system.

Exact diagonalization Besides the analytical approach presented above for the one-dimensional chain and the realistic three-dimensional system, we also performed exact diagonalization calculations. Working in a fixed $S^z_{\mathrm{tot}} = N - 1$ symmetry sector allows us to diagonalize large systems without much effort, the Hamiltonian matrix being of $N \times N$ size. We verified that the exponentially localized state ansatz is valid in the limit $J_\perp \ll J$, and is thus exact in the one-dimensional case. In Fig. C.13 we compare the analytical results for the local magnetization with the ones computed by exact diagonalization on a system of size $N = 40 \times 20 \times 20$ spins with one dimer located in the middle. The two results agree very well, even though in the semi-log scale one can see a small difference between the two methods, especially in the transverse direction. We also determined the correlation lengths $\xi_\parallel = 0.476$ and $\xi_\perp = 0.169$ by fitting exact diagonalization results to exponential decays.

b. NMR versus theory

The above described level crossing is clearly evidenced in the recent NMR results presented in Fig. C.14 (b). Before discussing these, we first recall the archetypal signature of a level crossing as observed in molecular crystals consisting of antiferromagnetic spin rings: the molecular level crossing is there observed as a sharp, "tanh-shaped" step in the magnetization that is concomitant with a peak of the T_1^{-1} NMR relaxation rate, whose magnetic field dependence at low temperature directly reflects the corresponding linear opening of the gap between the two levels [473, 474]. In DTNX the NMR data also show a peak in T_1^{-1} at the same field value, $H^* = 13.63$ T, where a step was previously observed in the bulk magnetization data [398]. The position (H^*) of this T_1^{-1} peak is found to be nearly doping

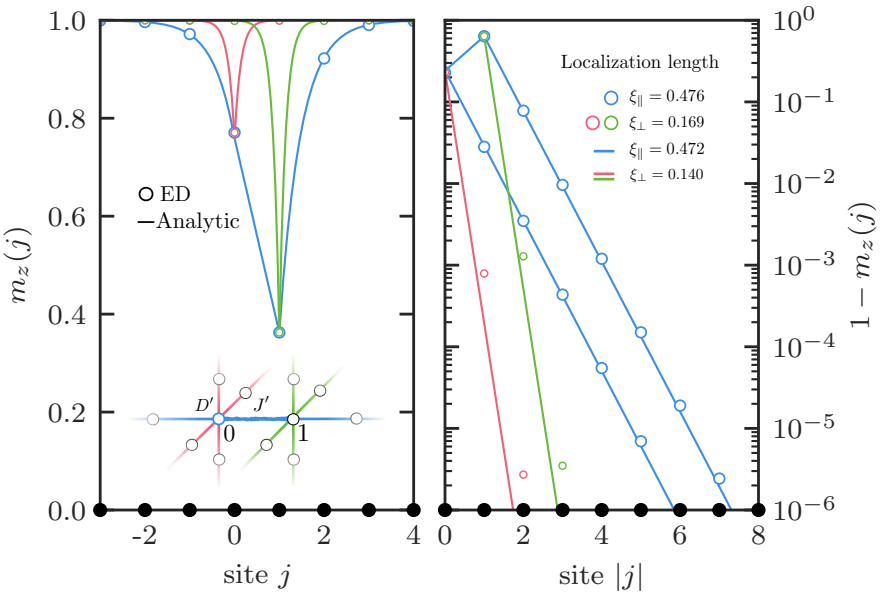

Figure C.13: Local magnetization profile in the $S^z_{\text{tot}} = N-1$ symmetry sector (single spin flip) close to a doped bond, comparing the exact diagonalization results (symbols) with the analytical ones (lines). The inset defines the color code: the blue curve is along the spin chain direction and the pink/green ones are perpendicular to it. The right panel in semi-log scale shows the exponential localization of the depolarization around the impurity with very short localization lengths: $\xi_\parallel = 0.476$ and $\xi_\perp = 0.169$ is obtained by exact diagonalization.

independent, which means that it should be associated to a single-impurity effect. Furthermore, the field dependence of the T_1^{-1} peak reveals the linear gap opening above H^*, thereby confirming the level crossing scenario[9].

The NMR spectra provided the second key-information to describe the impurity levels: the precise value of the local polarization of the spin at the right-hand-side of the dimer, as sketched in Fig. C.10 (b) and labeled as "site 1" in Fig. C.13. Below H^* and at low temperature this site is depolarized to $m_z^{\text{right}} = 0.365$ (see Fig. C.14 (a) for experimental data), which provides the second independent information on the impurity states. Together with the $H^* = 13.63$ T value determined from the position of the T_1^{-1} peak at low temperature, using equations (C.32) and (C.33), or, equivalently, the exact diagonalization results shown in Fig. C.15 (a,b), we can precisely determine the two local impurity values D' and J',

$$J' = 2.42J \quad \text{and} \quad D' = 0.36D. \tag{C.34}$$

These values are in agreement with the ones proposed previously ($J' = 2.35J$ and $D' = 0.5D$) [398] from the global fits, where the determination was mostly relying on the H^* value only (as plotted in Fig. C.15 (a)), so that the D' value was in fact not precisely known. Finally, the NMR results (see complete discussion in Ref. 472) provide also clear evidence of effects going beyond the single-impurity description:

[9] We cannot use the dependence observed below H^* because it is affected by the critical behavior related to the nearby quantum phase transition at H_{c2}.

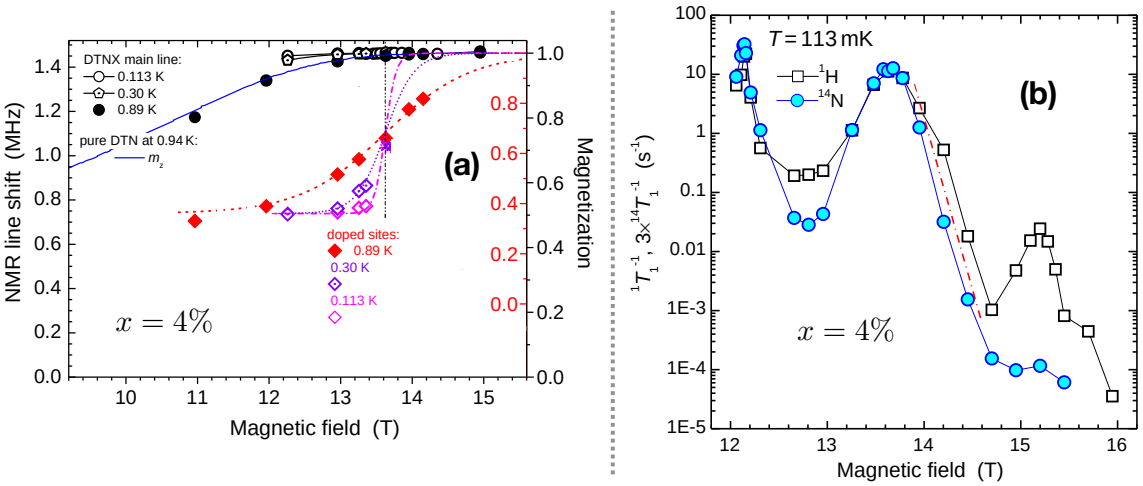

Figure C.14: **(a)** Magnetic field dependence of the local magnetization (right scales) measured in 4% doped DTNX by the NMR line position (left scale) of the high frequency ^{14}N regular line (circles and pentagons, outer right scale) and impurity line (other symbols, inner right scale for diamonds) at 0.89, 0.30, and 0.113. Blue solid line is the 0.94 K magnetization of pure DTN from Ref. 470. Vertical dash-dot-dot line denotes the level-crossing value $H^* = 13.6$ T. **(b)** Magnetic field dependence of $1/T_1$ measured by ^{1}H and ^{14}N NMR in 4% doped DTNX at 113 mK. Adapted from Ref. 472.

the temperature dependence of the level-crossing gap above H^* reveals that the gap value is (inhomogeneously) distributed, and the local polarization m_z^{right} above H^* is found to present an unexpected field dependence at low temperature. Furthermore, a weak secondary peak of T_1^{-1} was found above H^* at $H^{**} = 15.2$ T. This brings us to the following section that treats the many-body effects.

2. Many-body effects beyond single impurity

a. Effective theory from pairwise interactions

Mutual effect of two impurities The above given analysis of a single Br-doped bond provides us with a precise picture of DTNX above H_{c2}: the clean background is fully polarized and only the sites in the direct vicinity of Br-impurities remain not yet fully polarized, whereas this depolarization is exponentially localized. The localization lengths in both longitudinal and transverse directions are shorter than one lattice spacing unit. In realistic DTNX samples with low doping concentration, $2x \ll 1$, isolated impurities (of "length" $l = 1$) are the most common objects. However, there are also other objects, zones or clusters consisting of more than one isolated impurity ($l > 1$). As long as $2x < 31.2\%$ — the site percolation threshold on a cubic lattice [475] — there cannot be an infinite-size Br-doped cluster in the sample. Below this limit, plethora of impurity clusters of various sizes and spatial configurations may exist, but the bigger ones are more rare. Moreover, the bigger they are, the larger the magnetic field value has to be to polarize them, giving rise to Lifshitz tails [476, 477] in the magnetization curve, up to $H'_{c2} = (D' + 4J' + 8J_\perp)/g\mu_B \simeq 16.7$ T, which is

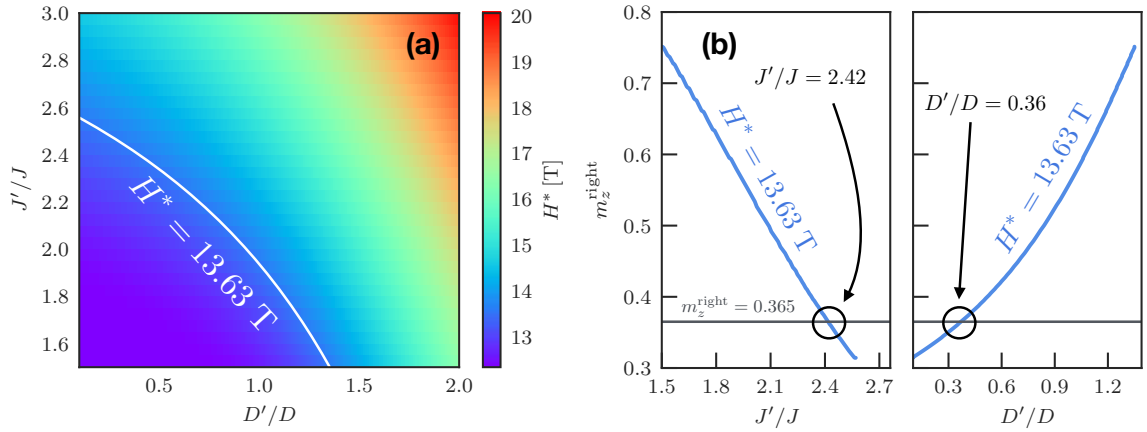

Figure C.15: **(a)** Color map of the crossover field H^* plotted in the anisotropy–coupling plane using exact diagonalization. All the pairs of parameters $(D'/D, J'/J)$ along the white line correspond to the same value of the crossover field $H^* = 13.63$ T. **(b)** Zero temperature magnetization of the right-hand-side site of the doped dimer below H^*, calculated using exact diagonalization, plotted against one of the adjustable parameters J' and D', while the other parameter is adjusted to maintain the crossover field at $H^* = 13.63$ T (see the white line in panel a). The bottom grey line shows the experimental value of $m_z^{\text{right}} = 0.365$.

the second critical field for the hypothetical homogeneously and fully doped sample, $2x = 1$. Above H'_{c2} all the impurity cluster sizes, and thus the whole sample, are necessarily totally polarized. In the following, we will first consider the mutual effect of *two* impurities depending on their relative distance $r_{\parallel,\perp}$.

To this end we performed exact diagonalization computations in the high magnetization sectors $S^z_{\text{tot}} = N, N-1, N-2$ of the three-dimensional system described by Eq. (14) containing $N = 16 \times 8 \times 8$ spins and two impurities located at varying distances $r_{\parallel,\perp}$. The magnetization process of the two impurities is shown in Fig. C.16 for increasing distances $r_{\parallel,\perp}$. For short relative separation between two impurities, a magnetization plateau at $S^z_{\text{tot}} = N - 1$ is clearly visible. However, its width gets rapidly reduced when the two dopants are moved apart. When $r_{\parallel,\perp}$ is large enough, the plateau width shrinks to zero, and one recovers the already discussed single impurity limit: a single level crossing at $H^* = 13.63$ T between the ground state energy of the $S^z_{\text{tot}} = N$ and $S^z_{\text{tot}} = N - 2$ symmetry sectors.

The presence of such plateaus at short distances is a signature of the mutual effect of the two impurities. In the inset of Fig. C.16 an exponential decay for the size of these plateaus is reported as a function of the relative distance between impurities for both parallel and perpendicular directions. The length scales controlling such decay reflect the localization lengths $\lambda_\parallel \simeq 0.92 \sim 2\xi_\parallel$ and $\lambda_\perp \simeq 0.32 \sim 2\xi_\perp$. We further study this exponential decay of the effective coupling between impurity states in the next subsection.

Effective bosonic description Having realized that close-by impurities do not behave as isolated, it becomes clear that many-body physics should play a role in DTNX, and that one has to consider the pairwise effects. We therefore propose an effective hard-core bosons model description for DTNX at high magnetic field

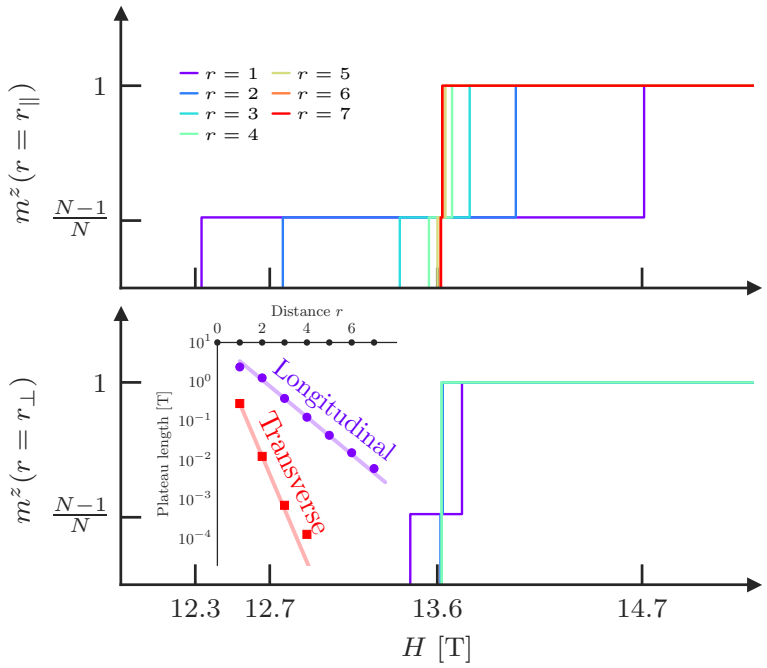

Figure C.16: Exact diagonalization results for the magnetization steps in a $N = 16 \times 8 \times 8$ system with two impurities. Top: impurities in the same chain at distance $r = r_\parallel$. Bottom: impurities in different chains at distance $r = r_\perp$ ($r_\parallel = 0$). In both cases, as a function of inter-impurities distance d, a magnetization plateau develops at $m^z = (N-1)/N$ when impurities get closer. Inset: Behavior of the plateau *length* as a function of the distance r (symbols). An exponential decay $\sim \exp(-r_{\parallel,\perp}/\lambda_{\parallel,\perp})$ (lines) is observed, where $\lambda_\parallel \simeq 0.92$ and $\lambda_\perp \simeq 0.32$.

($H > H_{c2}$), based on exact diagonalization and which reveals an effective AF pairwise interaction between the impurities around H^*. Again, what is called an impurity corresponds to a Br-doped bond as pictured in Fig. C.10 (b), which exponentially localizes the depolarization.

The picture of the effective model is as follows: the fully polarized state is the vacuum and decreasing the field will lead to more and more depolarized impurities, which we take for the effective particles. The initial model of DTNX is mapped to a hard-core bosons model where the number of particles is controlled by the chemical potential (magnetic field). The size of the local Hilbert space, labeled by $|1\rangle$ and $|0\rangle$, is therefore reduced to the presence or not of a particle, or, in the initial language, to a depolarized or polarized impurity. A generic hard-core bosons hamiltonian limited to a two-body interaction is

$$\mathcal{H}_{\mathrm{tV}} = \sum_{i,j} \left[t_{ij} \left(b_i^\dagger b_j + \mathrm{h.c.} \right) + V_{ij} n_i n_j \right] - \sum_i \mu_i n_i + C, \tag{C.35}$$

where t_{ij} is the hopping strength, V_{ij} is the interaction potential and μ_i is the chemical potential. C is a constant shift of the whole energy spectrum. The operators $b_i^\dagger$ and b_i are respectively the creation and annihilation operators of hard-core bosons ($\langle n_i \rangle = \langle b_i^\dagger b_i \rangle \leq 1$) on site i. They obey bosonic commutation relations $[b_i, b_j^\dagger] = 0$ on

different sites $i \neq j$ and fermionic ones on the same site $\{b_i, b_i^\dagger\} = 1$. The summation is over all possible sites $i \neq j$ containing an impurity in the initial model. The idea is to determine the Hamiltonian parameters that will reproduce the most faithfully the way impurities (de)polarize, taking into account the many-body effects.

To obtain the effective model parameters, we project the wave-functions of the low-energy spectrum of the real DTNX model Eq. (14) onto the effective model. Since we have a pairwise interaction between the particles, we perform these calculations with two impurities at positions i and j in the initial spin $S = 1$ model varying the distance between them in the longitudinal ($r_\parallel$) and the transverse ($r_\perp$) directions. We use exact diagonalization on the initial model in $S^z_{\text{tot}} = N$, $N-1$ and $N-2$ symmetry sectors and make the following correspondence between the states of initial model and the effective one. First, the vacuum is associated to the fully polarized state $|\varphi_N\rangle$ of energy E_N and defines the energy shift C,

$$E_N|\varphi_N\rangle \longrightarrow C|0_i 0_j\rangle. \tag{C.36}$$

Then, we associate the state with two particles in the effective model with the $S^z_{\text{tot}} = N-2$ symmetry sector ground state $|\varphi_{N-2}\rangle$ of energy E_{N-2},

$$E_{N-2}|\varphi_{N-2}\rangle \longrightarrow (V_{ij} - \mu_i - \mu_j + C)|1_i 1_j\rangle. \tag{C.37}$$

The correspondence in the $S^z_{\text{tot}} = N-1$ symmetry sector is a bit more sophisticated as we have two possible different states $|0_i 1_j\rangle$ and $|1_i 0_j\rangle$ in the effective model. Considering the dimer states $|\Phi_1\rangle$ and $|\Phi_2\rangle$ defined earlier, we build the following two states in the initial spin language,

$$\begin{array}{rcl} |\phi_1\rangle & = & |\uparrow\uparrow\uparrow\cdots\rangle|\Phi_2\rangle|\uparrow\uparrow\uparrow\cdots\rangle|\Phi_1\rangle|\uparrow\uparrow\uparrow\cdots\rangle, \\ |\phi_2\rangle & = & |\uparrow\uparrow\uparrow\cdots\rangle|\Phi_1\rangle|\uparrow\uparrow\uparrow\cdots\rangle|\Phi_2\rangle|\uparrow\uparrow\uparrow\cdots\rangle, \end{array} \tag{C.38}$$

where $|\Phi_1\rangle$, $|\Phi_2\rangle$ are at the positions i and j of the two impurities. We assume that linear combinations of $|\phi_1\rangle$ and $|\phi_2\rangle$ will be good approximations of the exact states $|\varphi_{N-1}\rangle$ (ground state of energy E_{N-1}) and $|\varphi'_{N-1}\rangle$ (first excited state of energy E'_{N-1}) of the $S^z_{\text{tot}} = N-1$ symmetry sector. These exact states are projected onto the trial ones,

$$\begin{array}{rcl} |\psi_1\rangle & = & |\phi_1\rangle\langle\phi_1|\varphi_{N-1}\rangle + |\phi_2\rangle\langle\phi_2|\varphi_{N-1}\rangle, \\ |\psi_2\rangle & = & |\phi_1\rangle\langle\phi_1|\varphi'_{N-1}\rangle + |\phi_2\rangle\langle\phi_2|\varphi'_{N-1}\rangle, \end{array} \tag{C.39}$$

which are orthogonalized using standard Gram-Schmidt procedure and normalized to form a new eigenbasis with respective energies E_{N-1} and E'_{N-1}. We then make the correspondence between the effective Hamiltonian matrix in the basis $\{|1_i 0_j\rangle, |0_i 1_j\rangle\}$ and the initial model,

$$E_{N-1}|\psi_1\rangle\langle\psi_1| + E'_{N-1}|\psi_2\rangle\langle\psi_2| \longrightarrow \begin{pmatrix} C - \mu_i & t_{ij} \\ t_{ij} & C - \mu_j \end{pmatrix}. \tag{C.40}$$

When the two impurities are spatially well separated with no overlap of the exponentially localized depolarization clouds, the ground state is twice degenerated as expected, with $E_{N-1} = E'_{N-1}$ when $r_{\parallel,\perp} \gg 1$.

The above procedure fully determines the parameters of the effective Hamiltonian. They are computed varying the distance between the two impurities along the main chain ($r_\parallel$) and the perpendicular direction ($r_\perp$) and plotted in Fig. C.17. Exact

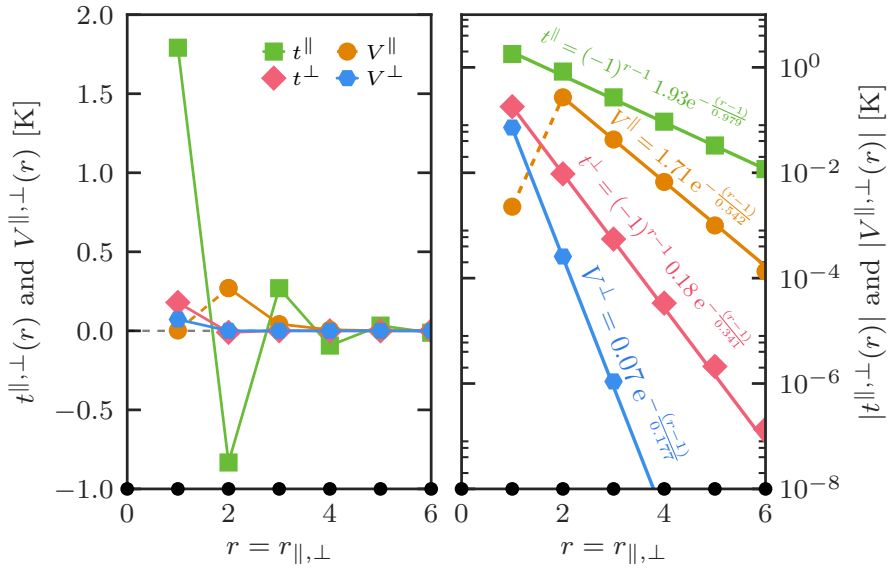

Figure C.17: Effective coupling parameters defined by Eq. (C.35) and determined using exact diagonalization, plotted as a function of the distance $r_{\parallel,\perp}$ between the impurities. The results are given in both linear (left panel) and logarithmic scale (right panel). The hopping term t displays the AF character of the underlying microscopic model in both the longitudinal (green squares) and transverse (pink diamonds) directions. The interaction potential, although non-staggered, decays more rapidly with distance than the hopping terms (yellow circles in the longitudinal direction and blue hexagons in the transverse one).

diagonalization calculation is performed on a system of $N = 16 \times 8 \times 8$ spins with periodic boundary conditions. The hopping term t and the interaction potential V are both exponentially decaying: $t, V \propto \exp(-|\mathbf{r}|/\lambda)$ with $\lambda_{\parallel,\perp} \simeq 2\xi_{\parallel,\perp}$ for t and $\lambda_{\parallel,\perp} \simeq \xi_{\parallel,\perp}$ for V, where ξ is the localization length of the wave-function around the impurity introduced in Eqs. (C.29) and (C.31). The hopping parameter is non-frustrated and preserves the AF character of the underlying microscopic model. The interaction potential is frustrated but decays more quickly than the hopping term, making it typically one or more orders of magnitude smaller. We thus assume this frustrated term to be irrelevant and therefore neglect it in the following. The chemical potential value is site-independent, with $\mu_i = g\mu_B(H - H^*) = \mu$ which controls the density of particles. Shifting the Hamiltonian (C.35) by $-C$, we finally get

$$\mathcal{H}_{\text{eff}} = \sum_{i,j} t_{ij} \left(b_i^\dagger b_j + \text{h.c.} \right) - \mu \sum_i n_i. \tag{C.41}$$

This effective hard-core bosons model gives a quite simple two-level system description for the localized states living in the vicinity of Br-impurities. One should emphasize that,

(i) This effective Hamiltonian (C.41) is defined on a sparse three-dimensional network of $2xN$ active sites;

(ii) These sites are coupled through *non-frustrated* hopping terms which decay exponentially with their relative separation, yielding a random hopping problem due to the random location of the impurities in the original three-dimensional cubic lattice;

(iii) The hard-core bosons density is controlled by a non-random chemical potential $\mu \propto (H - H^*)$.

Although the hopping term in Eq. (C.41) is exponentially suppressed with $|\mathbf{r}|$, it couples impurities at all distances. In order to mimic in a more simple way the random distribution of distances between impurities and its implications on the couplings distribution, we developed a phenomenological toy model of hard-core bosons. We first limit ourselves to the one-dimensional case following Ref. 478 and Ref. 479. The normalized probability to have two impurities at distance $r = r_{\parallel} = r_{\perp}$ is given by $p(r) = 2x\,(1-2x)^{r-1}$, which can be used to compute the couplings distribution

$$p(t) = \sum_{r=1}^{+\infty} p(r)\delta\left[t - t(r)\right]. \tag{C.42}$$

Going in the continuum limit with the a hopping parameter of the form $t(r) \propto (-1)^{r-1}\exp\left(-r/\lambda\right)$, one gets in the dilute limit $2x \ll 1$,

$$p(t) \propto t^{-1-\lambda\ln(1-2x)} \simeq t^{-1+2\lambda x}. \tag{C.43}$$

In three dimensions, we simply replace in a heuristic way the characteristic length scale λ by a characteristic volume v_λ and introduce $\delta^{-1} = 2v_\lambda x$, a phenomenological parameter in the toy model controlling the disorder. Finally, we introduce the toy Hamiltonian

$$\mathcal{H}_{\text{toy}} = \sum_{\langle ij\rangle} t_{ij}\left(b_i^\dagger b_j + \text{h.c.}\right) - \mu\sum_i n_i, \tag{C.44}$$

where the hopping is possible between nearest neighbors only and its strength is generated from a broad distribution $p(t) \sim t^{-1+1/\delta}$, with $t \leq J$ along the chains and $t \leq J_\perp$ in the transverse directions. The toy model is more practical for quantum Monte Carlo simulations than the effective model since interactions are limited to nearest neighbors.

The interplay between disorder and interactions for bosonic systems has mostly been investigated for diagonal disorder, i.e. random potentials. Here the disorder is of off-diagonal nature, i.e. with random hopping t_{ij}, a problem which has been less studied. At the single-particle level, it is known that randomness of the hopping terms modifies the Anderson localization at the center of the band where a delocalized state exists [480, 481]. Moreover, for the so-called Lifshitz model [482], describing three-dimensional diluted semiconductors with isotropic hopping terms $\sim \exp(-r/\xi)$, it was shown that extended states exist if the impurity density is above the critical one, $\rho > \rho_c$, where $\rho_c \simeq (3\xi)^{-3}$ [483]. In the presence of interactions, a few existing studies of random exchange quantum antiferromagnets have shown that long-range order remains in the presence of disorder [484, 485], a phenomenon corroborated by order-from-disorder mechanisms observed in quantum spin gapped materials doped with impurities [486, 487]. In view of these results, one can reasonably expect a

similar effect for the effective Hamiltonian (C.41), at least in the vicinity of half-filling, when $H \sim H^*$. More precisely, the effective bosonic degrees of freedom, hopping on a diluted three-dimensional lattice, should display low temperature long-range order, i.e. BEC, meaning transverse magnetic order for the original DTNX material. This general expectation has been unambiguously confirmed by realistic simulations discussed below. However, this description is limited to strong dilution $2x \ll 1$, where many-body physics is faithfully captured by the above pairwise coupling approach. Below, we go beyond and address the question of multi-impurity effects which may modify this simple picture.

b. Multi-impurity effects

Magnetization curve The zero-temperature high magnetic field magnetization profile of DTNX, obtained using QMC simulations, is shown in Fig. C.18 (b) where step-like features are clearly visible. To understand this dependence, we focus on objects made of two impurities ($l = 2$) close to each others at distances $r_\parallel = 1, 2$ along the chain direction, and which happen with respective probabilities $\propto (2x)^2$ and $\propto (1-2x)(2x)^2$. Longer distances rapidly approach the isolated impurity case ($r_\parallel \gg 1$), as shown in Fig. C.16. Furthermore, the case of impurities next to each others in the transverse directions can be considered as practically isolated impurities due to the extremely short localization length $\xi_\perp$. Finally, considering objects consisting of more than two impurities ($l \geq 3$) is equivalent to deal with rare events due to the very small probability of existence, $\propto x^l$.

First of all, as pictured in Figure C.18 (a), the $r_\parallel = 1$ case has a first level crossing around $H = 12.3$ T, close to H_{c2}, the critical field which ends the BEC phase. This provides a very simple explanation for the measured magnetization both experimentally by Yu *et al.* [398] and in numerical simulations presented in Fig. C.18 (b) where m_z is found to be larger than $\simeq (1-2x)$, the value expected if only clean sites were fully polarized. Instead, at H_{c2} impurities in this particular $r_\parallel = 1$ configuration are (half-)polarized which leads to a total magnetization $m_z \simeq (1-2x) + (2x)^2$, in excellent agreement with both experimental results [398] and our numerical simulation shown in Fig. C.18 (b). Also, instead of sharp, square steps sketched in Fig C.18 (a), in a realistic sample one expects smooth, rounded steps at the edge of the plateaus, due to the bandwidth of the levels crossing, resulting from the effective interaction between impurities. Moreover, something like true plateaus cannot exist, because there is a multitude of level crossings corresponding to all the different impurity cluster configurations. We are therefore left with a compressible (non-zero magnetic susceptibility) phase up to H'_{c2}. Although this phase is compressible, level crossings at $H = 12.7$ T, 13.6 T and 14.7 T stand out because (i) they are well isolated from the others and (ii) concern a relatively large number of objects, which explains the strong step-like feature visible at these specific magnetic fields in the magnetization curve [Fig. C.18 (b)] or in its first derivative, the magnetic susceptibility curve [Fig. C.18 (c)]. In other words, at each of these levels crossing, there is a qualitative change in the sample as a macroscopic number of the studied "impurity objects" are getting polarized at the same time. As already mentioned for the $r_\parallel = \infty$ case, the simultaneous closing of the local gap $\Delta(r_\parallel = 1, 2, \infty)$ of these objects, together with an effective pairwise AF interaction between them, opens the

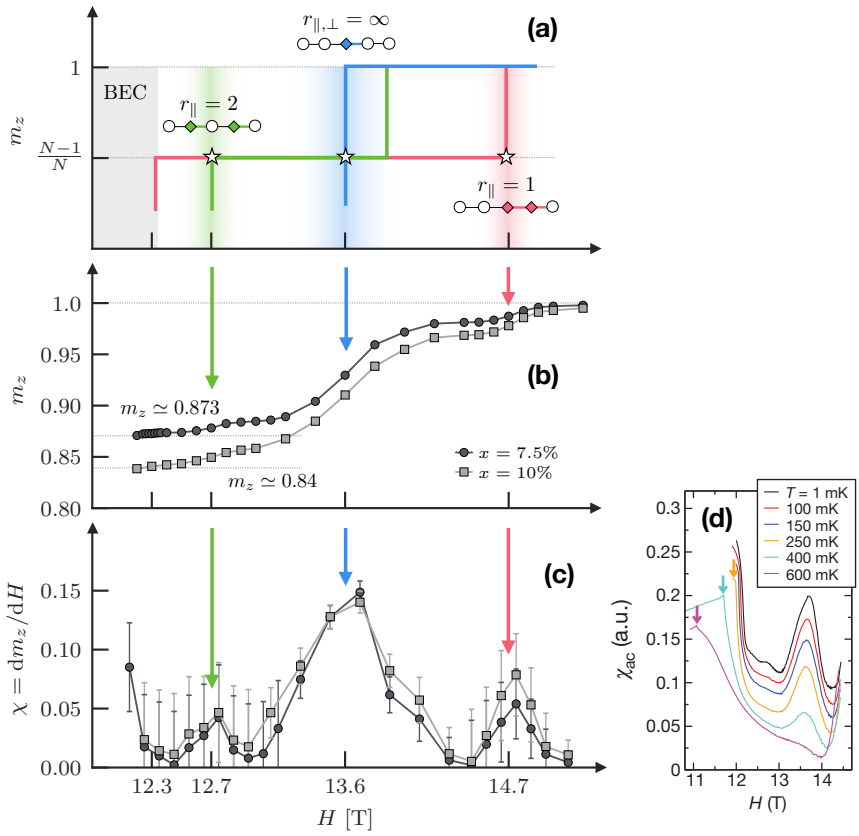

Figure C.18: The top **(a)** panel is a simplified version of Fig. C.16, focusing on the clearly separated level crossings for two impurities at distance $r = 1, 2$ and ∞. The central panel **(b)** displays the zero temperature magnetization curve at doping concentration $x = 7.5\%$ (circle) and $x = 10\%$ (square) from numerical simulations of the Hamiltonian (14) using QMC and the β-doubling scheme. The results are from samples containing $N = 40 \times 8 \times 8$ spins and each point is averaged over 200 disorder configurations. The bottom panel **(c)** shows the first numerical derivative of the magnetization curve (corresponding to the magnetic susceptibility χ). The highlighted levels crossing in the first panel are clearly identified in realistic numerical simulations, as denoted by vertical arrows. **(d)** a.c. susceptibility of $x = 8\%$ DTNX close to the lower and upper critical fields. The curves have been vertically shifted with respect to one another for readability purposes. Panel (d) is adapted from Ref. 398.

door to a global phase coherence of these new objects, in sharp contrast with the BG regime predicted in Ref. 398. This scenario is indeed verified (see discussions below) around $H^* = 13.6$ T where a BEC* of the single impurities was numerically observed. Based on similar mechanisms, we claim that there should also exist long-range order at the two other levels crossing, $H = 12.7$ T and $H = 14.7$ T, with possible intermediate BG regions at low doping concentrations. Before presenting numerical evidence for such a scenario, we address now the experimental facts concerning multi-impurity physics in DTNX.

Experimental evidences The first experimental evidence for the level crossing at 12.7 T can be found in the ac-susceptibility data presented in Fig. C.18 (d), adapted from Ref. 398: at this field value there is a barely visible peak in the magnetic field

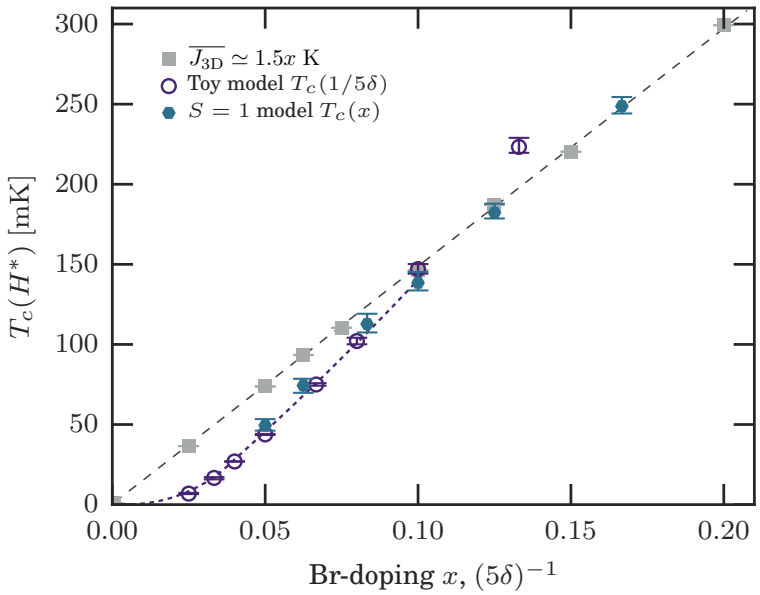

Figure C.19: Critical ordering temperature T_c for the impurity-induced long-range order at $H^* = 13.6$ T plotted against the impurity concentration x for the $S = 1$ model Eq. (14) (hexagons) and for the effective hard core bosons toy-model Eq. (C.44) at half-filling (circles) plotted against $(5\delta)^{-1}$, suggesting long-range order for all finite x values. The average effective pairwise coupling between impurities in the transverse direction is also shown (square symbols) for comparison. Lines are guides to the eyes.

dependence, present only in the lowest temperature, 1 mK data. The NMR data of Fig. C.14 (b) provide a clear direct experimental evidence for the level crossing at 14.7 T: the low temperature (113 mK) data for the T_1^{-1} relaxation rate of protons present a clear peak at slightly higher field value $H^{**} = 15.2$ T. The small difference between the predicted and the observed H^{**} value can be accounted for by improving the above given simplest model that describes DTNX by the first trivial correction: the impurity modifying the J coupling into J' value corresponds only to the most probable configuration where the doped bond is between one affected spin, having the anisotropy D', and one unaffected spin, having the "normal" anisotropy D. When two neighboring bonds are doped, the bond between the two affected spins, both having D' anisotropy, is in fact expected to have somewhat different exchange coupling J''. Indeed, a slight modification, $J'' = 1.12J'$, is enough to match the theoretically predicted value with the experimentally observed H^{**}. We have thus clearly explained the observed peak of $1/T_1$ and quantified the first obvious correction to the model. This correction being small, for simplicity, we have neglected it in numerical simulations.

3. Impurity-induced long-range order at finite temperature

We use QMC through the stochastic series expansion algorithm to simulate the $S = 1$ DTNX Hamiltonian (14) and the toy model of hard-core bosons (C.44) that we derived. Simulations are performed on three-dimensional systems of $N = L \times L/R \times$

L/R sites from $L = 24$ up to $L = 120$, where $R > 1$ is an anisotropic aspect ratio[10], numerically favorable when dealing with weakly coupled chains ($J_\perp/J \simeq 0.08$) [195]. For various system sizes, temperatures and Br-doping concentrations $x = 10\%$, 12.5% and 16.67%, we compute two different thermodynamic quantities: the spin stiffness ρ_s [194, 240] and the transverse AF order parameter $|m^{\rm AF}|^2 \equiv \sum_{i,j} e^{i\mathbf{q}\cdot\mathbf{r}_{ij}} \langle S_i^+ S_j^- \rangle / N^2$ at the AF wave-vector $\mathbf{q}_{\rm AF} = (\pi, \pi, \pi)$, which both reveal a finite temperature transition using a standard finite-size scaling analysis [180],

$$\begin{array}{rcl} \rho_s(L) & = & L^{2-D}\, \mathcal{G}_{\rho_s}\left[L^{1/\nu}\,(T - T_c)\right] \\ m^{\rm AF}(L) & = & L^{-\beta/\nu}\, \mathcal{G}_{m^{\rm AF}}\left[L^{1/\nu}\,(T - T_c)\right], \end{array} \quad \text{and} \tag{C.45}$$

where $D = 3$ is the dimensionality. The 3D-XY critical exponents [175, 241, 242] $\nu = 0.6717$ (the correlation length exponent) and $\beta = 0.3486$ (the order parameter exponent) are used to extract the critical temperature T_c, after a Bayesian scaling analysis [243, 244]. One can also include corrections to scaling of the form $\mathcal{G}\left[L^{1/\nu}\,(T - T_c)\,(1 + cL^{-\omega})\right]$, where ω is a subleading exponent accounting for a finite-size drift, which gives similar values within the error bars. Our final T_c estimates (Fig. C.20) are averages of the individual T_c from ρ_s and $m^{\rm AF}$ crossings, with and without irrelevant corrections, while the given error bars reflect uncertainty between various estimates[11].

The critical temperature at the crossover H^* field grows with the doping x, as shown in Fig. C.19 for $5\% \leq x \leq 16.67\%$ where we observe long-range order at finite temperature for all doping levels. The ordering temperature grows linearly with x. This is qualitatively expected from a naive mean-field reasoning, as the average coupling between the chains (setting the 3D energy scale for a finite critical temperature) is $\overline{J_{\rm 3D}} \sim J_\perp x$. More precisely, exact diagonalization calculations of the effective pairwise coupling between impurities in DTNX, discussed earlier, yield an average energy coupling in the transverse direction $\overline{J_{\rm 3D}} \simeq 1.5x$ (K), which compares well with QMC estimates, at least for large enough dopings $x \geq 8\%$. For small x, accurate estimates for T_c are very hard to obtain because simulations get slower with inverse temperature, and finite size effects become more serious when the number of impurities decreases. Nevertheless, we can observe at low doping that the ordering temperature starts to deviate form a simple linear scaling and displays a faster decay. While it is impossible to exclude the existence of a critical concentration $x_c < 5\%$ where T_c vanishes, it is reasonable to expect that $T_c(x, H^*)$ will vanish only when $x \to 0$, presumably with a convex form different from the mean-field-like shape observed for $x > 8\%$.

Fig. C.20 shows the global magnetic field–temperature H–T phase diagram obtained from extensive QMC simulations of the DTNX model Eq. (14) for various Br-impurity concentrations x. As previously discussed, besides the clean BEC type order below $H_{c2} = 12.3$ T, doping with Br leads to a new type of disorder-induced

[10] For the $S = 1$ model, we used $(x, R) = (16.67\%, 6)$, $(12.5\%, 8)$, $(10\%, 10)$, $(8.33\%, 6)$,$(6.25\%, 8)$, $(5\%, 10)$ for data obtained through "standard QMC" and $(x, R) = (10\%, 5)$, $(7.5\%, 5)$ for data obtained through the QMC β-doubling scheme, with an average over 300 disorder realizations. For the toy model, simulations are carried out with $R = 5$ and $L = 20, 30, 40, 50$, and averaged over a large number ≥ 500 of samples.

[11] The critical temperature data for $x = 10\%$ from $H = 12.5$ T to $H = 13.0$ T (Fig. C.20), are estimated using the β-doubling procedure, which strongly limits the temperature grid taken to perform the finite-size scaling analysis (C.45): $1/T = 2^p$ with $p \in \mathbb{N}$. Therefore, the error bars in this case reflect the closest available (min/max) temperatures to the estimated T_c value.

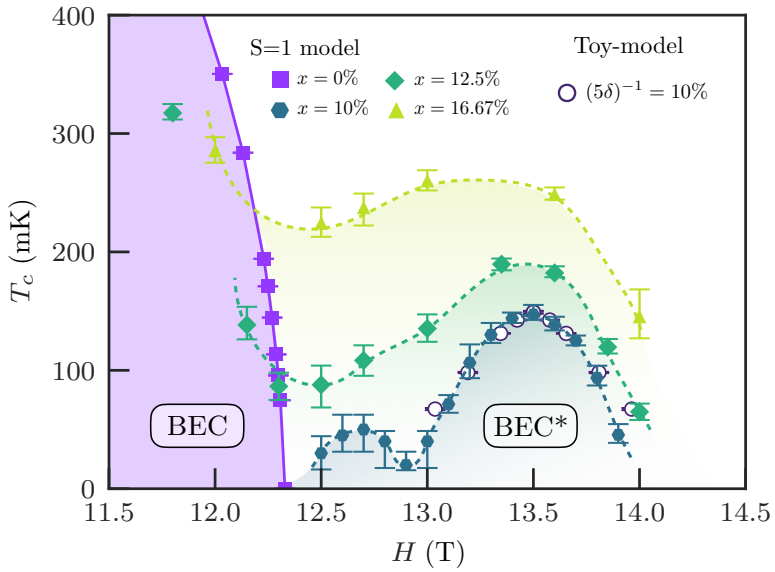

Figure C.20: Finite temperature phase diagram at high magnetic field for various Br doping concentrations, obtained by QMC simulations of DTNX (14) for $x = 0$ (square), $x = 10\%$ (hexagon), $x = 12.5\%$ (diamond), $x = 16.67\%$ (triangle) and the hard-core bosons toy model of Eq. (C.44) (circle) with $\delta = 2$ (we found that $\delta = 1/5x$ yields a remarkably good agreement with the $S = 1$). Besides the clean BEC dome at $x = 0$, a new impurity-induced ordered regime BEC* develops at higher magnetic field. The hard-core bosons BEC* dome is centered around $H = 13.5$ T. While at large doping $x = 12.5\%$ and $x = 16.67\%$, BEC and BEC* overlap, for $x = 10\%$ one clearly sees two resurgent distinct BEC* mini-domes (see text).

ordered phase, which we call BEC*, appearing as a mini-dome centered around the single-impurity crossover field $H^* \simeq 13.6$ T. This regime is quite extended and overlap with the clean BEC dome for $x > 10\%$. Interestingly, for $x = 10\%$ a second mini-dome appears, centered around 12.7 T and separated from the main BEC* phase made of single impurity states around H^*. This observation clearly confirms the expectation that objects made of two neighbouring impurities at distance $r_{\parallel} = 2$, whose crossover field is precisely at 12.7 T, should experience an effective interactions also leading to the long-range order. The natural question opened by the observation of a second, "satellite" BEC* phase concerns the general trend when the impurity concentration gets more reduced: one can wonder whether more satellites may appear, and if intervening localized BG regimes could eventually be stabilized between these ordered phases. In order to address this fundamental issue, especially important to properly define the real extent of the high-field BG state proposed by Yu *et al.* [398], we now turn to ground state physics at lower impurity concentration.

4. Zero-temperature phase diagram and Bose-Glass physics

To study the $T = 0$ phase diagram of DTNX at high magnetic fields, we use the QMC techniques again, but this time associated with the β-doubling scheme [462]

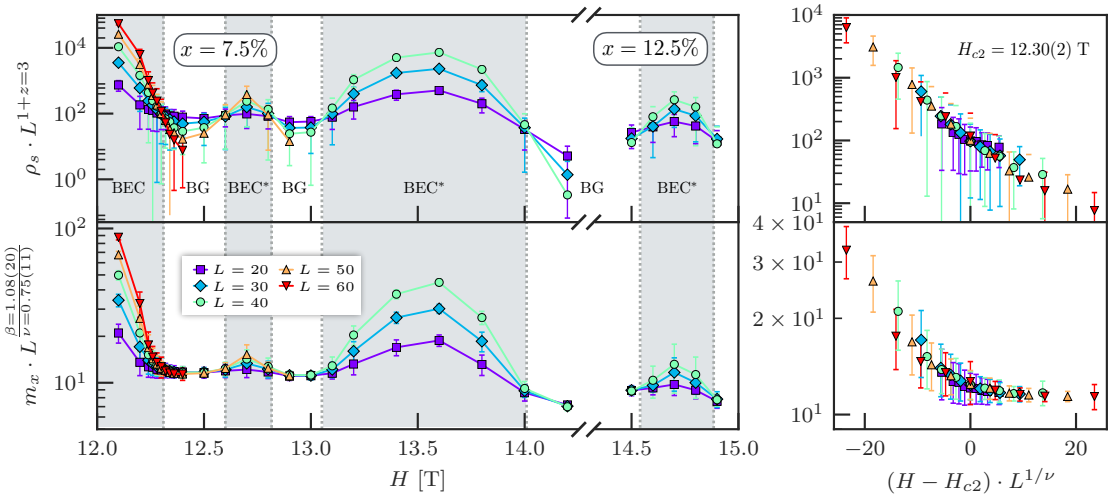

Figure C.21: Left: finite size scaling analysis ($L = 20, \ldots, 60$ with an aspect ratio $R = 5$) for the spin stiffness ρ_s and the AF order parameter m^{AF} at zero temperature, from QMC simulations with the β-doubling scheme, for $x = 7.5\%$ Br doping. For points above 14.3 T, the Br doping is taken to be $x = 12.5\%$ to reduce numerical difficulties in computing ρ_s and m^{AF} at high magnetization. Each point is averaged over 200 independent disordered samples. The dynamical exponent value was set exactly to $z = D = 3$. The first quantum critical point position $H_{c2} = 12.30(2)$ T and exponent $\nu = 0.75(11)$ were estimated from the ρ_s data. Setting thus H_{c2} and ν, the order parameter exponent $\beta = 1.08(20)$ was then determined from the m^{AF} data. Right: scaling functions Eq. (C.46) for the data around H_{c2}, which gives quite good collapse, thus supporting that $z = D = 3$.

to reach low temperatures much faster than in standard schemes, in order to probe the ground state properties. We remark that this method leads to large Monte Carlo errors, due to the purposely small number of performed thermalization and measurement steps, and may occasionally lead to systems out of the ground state for some samples. Nevertheless, the estimate of the observables over different disorder realizations is reliable, as it gives larger statistical errors (sample-to-sample fluctuations) than the ones generated by the method. We compute the spin stiffness ρ_s and the transverse order parameter m^{AF}, averaged over 200 different samples for each of the points presented in Figure C.21. The finite size scaling analysis close to the BEC–BG transition follows

$$\begin{aligned} \rho_s(L) &= L^{2-D-z}\, \mathcal{G}_{\rho_s}\left(L^{1/\nu}\,|H - H_{\mathrm{c}}|\right) \qquad \text{and} \\ m^{\mathrm{AF}}(L) &= L^{-\beta/\nu}\, \mathcal{G}_{m^{\mathrm{AF}}}\left(L^{1/\nu}\,|H - H_{\mathrm{c}}|\right), \end{aligned} \tag{C.46}$$

where H_{c} is the critical field, $D = 3$ is the dimensionality and z is the dynamical exponent. The zero-temperature phase diagram of DTNX at high magnetic field is shown in Fig. C.21 for the Br doping concentration $x = 7.5\%$. Both the main BEC* phase and its left "satellite" centered around 12.7 T get reduced as compared to their $x = 10\%$ extension, and two intervening localized BG phases are stabilized in between. Above 14 T, a third BG regime is also observed. Interestingly, ordered phase appears at each of the noticeable levels crossings $H = 12.7$ T, $H = 13.6$ T and $H = 14.7$ T. For the highest field value, this feature is also reported, but for a

higher doping concentration ($x = 12.5\%$), because of numerical difficulties to capture ground state properties close to saturation (which corresponds to very small density of particles).

The BEC-BG phase transition The quantum phase transition between BEC and BG phases remains controversial in various aspects, such as the precise value of some critical exponents [423–425, 488–490]. While it is now well established that the correlation length exponent ν satisfies the Harris-Chayes bound $\nu \geq 2/D$ [491, 492], there are still some debates regarding the dynamical exponent equality $z = D$ [423, 424, 488–490], as well as for the exponent ϕ governing the critical temperature $T_c \sim |H - H_c|^{\phi}$, for which some recent results [398, 399] are inconsistent with the theoretical bound $\phi \geq 2$ [157], verified in a more recent numerical study [493]. Besides these theoretical discussions, only a few experimental realizations of dirty bosons are available to test such predictions, and in particular for condensed matter systems. In $Tl_xK_{1-x}CuCl_3$ [454] and $(C_4H_{12}N_2)Cu_2(Cl_{1-x}Br_x)_6$ [494], as well as in DTNX [398], the measured exponent of the critical boundary was found to be $\phi \sim 1$, which lies clearly below the $\phi = 2$ bound.

In the following we address some critical properties of the $T = 0$ BEC-BG transition close to H_{c2}, the critical field ending the ordered phase of the clean degrees of freedom, for a doping level $x = 7.5\%$, as shown in Fig. C.21. We start with the finite size scaling analysis of the spin stiffness ρ_s, setting the dynamical exponent to exactly $z = 3$. This leads to a very nice single-point crossing for the different system sizes $L = 20, 30, 40, 50$ and 60, meaning that there is a quantum phase transition happening at the crossing point, $H_{c2} = 12.30(2)$ T. This value for the quantum critical point is identical to the value of H_{c2}^{clean} in pure DTN, suggesting that the degrees of freedom defining the end of this first ordered phase are the "clean" spins. By optimizing the collapse of the data sets obtained for different L values on a single (scaling) curve, one can estimate the correlation length exponent $\nu = 0.75(11) > 2/3$, compatible with the Harris-Chayes criterion. Using these estimates of H_{c2} and ν, we perform a similar finite size scaling analysis for the AF order parameter m^{AF}, and get the exponent $\beta = 1.08(20)$, in agreement with the previous work [399]. The scaling collapse of m^{AF} data is also very good, confirming the value of ν obtained from ρ_s data. Through the hyperscaling relation, the anomalous exponent η is found to be

$$\eta = 2\beta/\nu - D - z + 2 = -1.12(10), \tag{C.47}$$

which verifies the inequality $\eta \leq 2 - D = -1$ [157]. Overall, the dynamical exponent value $z = D = 3$ is fully compatible with our results, confirming previous studies [399, 493, 495]. Note also that good crossings are obtained at the other BG-BEC* transitions, as visible in Fig. C.21. We have not directly addressed the so-called "ϕ-crisis" raised by conflicting numerics [493, 496]. It is clearly a very difficult numerical task to safely probe the quantum critical regime using finite temperature data. Moreover, we believe that the very peculiar situation at play in DTNX, with successive narrow BEC* and BG regimes, is not favorable to disentangle a genuine quantum critical regime from crossover effects due to competing phases.

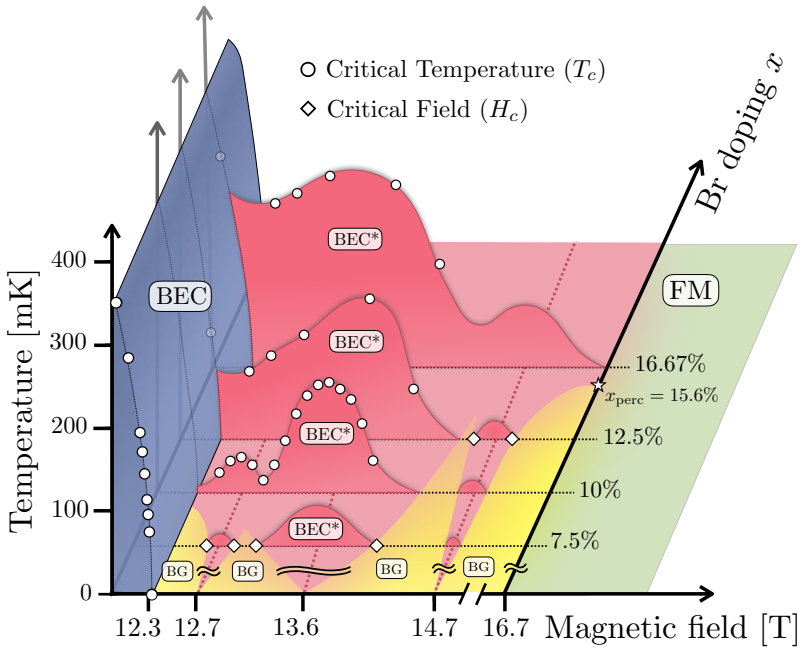

Figure C.22: Global Magnetic field – temperature phase diagram for DTNX based on numerical (QMC) results (circles and diamonds), displayed for varying Br doping x. For small finite doping x, above the clean BEC phase (blue dome) at $H > 12.3$ T, a succession of impurity-induced BEC* phases (pink domes) is stabilized together with intervening localized Bose-glass (BG) regimes (yellow regions), before getting into the fully polarized ferromagnet (FM, green region). Such a localization-delocalization series is expected to disappear for increasing doping x, to eventually form a unique impurity induced BEC* regime, overlapping with the principal BEC dome. Above the three-dimensional percolation threshold $x_{\mathrm{perc}} = 15.6\%$, the system is expected to be ordered at all field values up to the full polarization.

5. Summary of results and experimental observation

In a first step, based on NMR experiments at high magnetic field we have fully determined the microscopic model of the DTNX compound. Indeed, the experimental results can be interpreted and understood via single impurity physics, which makes it possible to perform analytical as well as exact diagonalization calculations on large systems from which a unique set of coupling parameters (J', D') can be determined for the impurity degrees of freedom. Moreover, this simple description provides fruitful insights on the picture of DTNX at high magnetic field, such as the strong localization of isolated impurity states and the fact that the clean background polarizes for a smaller magnetic field than the impurities. Thus, a simple picture of DTNX at high magnetic field consists in a frozen (clean) background with a collection of impurities spatially randomly distributed, yet to be polarized upon increasing the magnetic field. A natural extension was then to study the mutual effect of two impurities. By means of exact diagonalization, we reveal that, despite the strong localization of the impurity states, there exists an effective unfrustrated pairwise interaction between impurity degrees of freedom. In order to capture the relevant low-energy physics we have built an effective model of bosons in a diluted lattice with

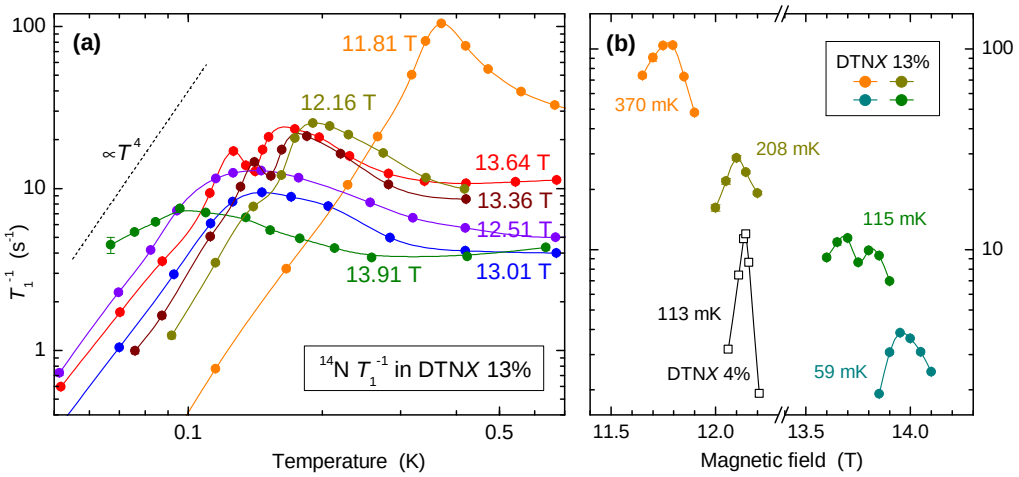

Figure C.23: **(a)** Temperature dependence of the NMR $1/T_1$ relaxation rate in 13% doped DTNX at selected field values. The strong decrease of $1/T_1 \propto T^4$ at low temperature is a signature of the ordered BEC phase, while the relatively broad maximum corresponds to the critical spin fluctuations at the phase transition into this phase. The error bars are less than the symbol size, except for one point. **(b)** Magnetic field dependence of $1/T_1$ in the vicinity of the phase transition into the ordered phase. Several positions of the 13% doped DTNX phase diagram (solid dots) are compared to the case of much less, 4% doped DTNX (open squares), to show how strongly is the $1/T_1$ peak broadened by increasing the doping-induced disorder.

an exponentially decaying coupling with the distance between bosons. This model suggests that the bosonic degrees of freedom can order at low-enough temperature, which is confirmed by quantum Monte Carlo simulations of the full microscopic model. This paves the way to a resurgence of global phase coherence in DTNX, in sharp contrast with the uninterrupted many-body localized Bose-glass phase reported in Ref. 398. We have extended the finite-temperature study of the realistic DTNX Hamiltonian with state-of-the-art quantum Monte Carlo simulations at lower temperature, for a Br concentration $x = 10\%$, in order to compute the extension of the disorder-induced BEC* revival and of the Bose-glass regime. We have first shown that, for this concentration, the BEC* is connected to the large BEC phase of the clean sites without any intervening BG. Furthermore, we reveal that the critical temperature boundary of the BEC* actually presents not one, but two distinct domes: the expected one centered at $H^* \sim 13.6$ T, which corresponds to the condensation of single impurity degrees of freedom, and a new one centered around $H \sim 12.7$ T. The new dome can be understood as the ordering of multi-impurity objects. This considerably extends the current picture of the phase diagram of DTNX at high magnetic field: at low enough doping concentration, the consecutive disorder-induced BEC* mini-domes are separated by intervening many-body localized Bose-glass regimes. A summary of our results is shown in Fig. C.22, which displays a complete three-dimensional representation of the high magnetic field phase diagram of DTNX, "magnetic field *vs.* temperature *vs.* Br concentration". However, decreasing the doping concentration makes it very hard to reliably obtain the critical temperature in numerical simulations. Consequently, we rather turned our attention to $T = 0$ physics for $x = 7.5\%$, focusing on the still controversial quantum phase transition

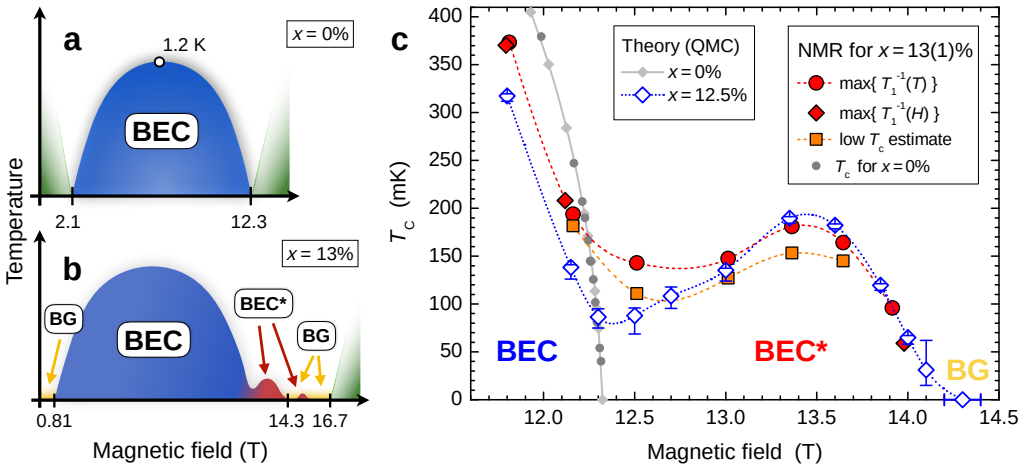

Figure C.24: Sketch of the global phase diagram of **(a)** pure DTN, and **(b)** 13% doped DTNX, where colors denote the BEC (blue) and BEC* (red) phases, and the Bose-glass (BG, yellow) and gapped (green) regimes. **(c)** Focus on the main BEC* phase. The T_c determined from QMC simulations for 12.5% doping (blue open diamonds) is compared to T_c estimates from the T_1^{-1} NMR data in a (13 ± 1)% doped sample: solid red dots and diamonds denote respectively the maximum of $T_1^{-1}(T)$ and $T_1^{-1}(H)$ dependence, reflecting the maximum of the critical spin fluctuations, while orange squares provide the lowest estimate for the T_c, taken to be the point where the $T_1^{-1}(T)$ dependence switches into the power-law regime of the ordered phase. The grey small dots and diamonds are respectively the experimental points and the QMC simulation of the BEC phase boundary in the pure DTN, as reported in Ref. 174.

between the BEC and Bose-glass phases, in order to determine the critical exponents.

On the experimental side, the former NMR experiments that brought a basis for the microscopic description of the doped sites, have been carried out (for technical convenience) on relatively lightly 4% doped sample, where the transition into the BEC* phase is theoretically predicted to be well below 40 mK, and could not be experimentally reached. As by stronger doping the predicted phase diagram is pushed up into the experimentally accessible range of temperature, the (13±1)% doped DTNX was investigated in order to check for the existence of the disorder-induced BEC* phase and establish its experimental phase diagram. In general, a second order phase transition into an antiferromagnetically ordered phase can be detected by NMR using either static or dynamic observables. In the former case, we directly observe the growth of the order parameter, here the transverse spin polarization, through the splitting or broadening of NMR lines. While this is nicely visible in pure DTN [174], in strongly doped DTNX sample this method could not be employed, because the NMR lines are much broader and the relevant signal much weaker. The point is that the order of the BEC* phase is established only for the minority sites, those affected by doping. Fortunately, the ordering temperature T_c can also be determined from the corresponding peak of critical spin fluctuations, measured through the nuclear spin-lattice relaxation rate $1/T_1$. Indeed, in a pure or weakly disordered system, a sharp peak in the observed T or H dependence of $T_1^{-1}(T, H)$ data precisely defines the T_c, as shown in Fig. C.23. However, this peak is broadened by disorder, and in the 13% doped DTNX data, only a very broad maximum of

T_1^{-1} is separating the high temperature regime above the BEC* phase, where the relaxation is essentially constant, from the rapid power-law decrease, $T_1^{-1} \propto T^4$, observed inside this phase. While this low temperature behavior of $T_1^{-1}(T)$ is clearly a fingerprint of the ordered phase, the exact experimental determination of T_c is not evident and different estimates are plotted in Fig. C.24.

Remarkably, the experimental estimates of the 13% doped DTNX phase boundary are qualitatively identical and quantitatively quite close to the theoretical quantum Monte Carlo predictions, in particular regarding the maximum T_c value of the BEC* phase and its upper field boundary. The observed differences are minor: in the theoretical prediction, the BEC part of the ordered phase is pushed by 0.1 T towards lower field and the minimum of T_c between the BEC and the BEC* part is (therefore) significantly deeper. The NMR data thus provide the final proof for the existence of the new disorder-induced phase, whose microscopic nature is revealed by the corresponding, precisely defined theoretical description discussed in this section. In particular, theory tells us that the BEC* phase, in contrast to a Bose-glass, is indeed fully three-dimensional coherent. NMR, being a *local* microscopic technique, cannot directly provide this information, but the BEC* phase is accessible to neutron experiments, which can provide further insights on how the coherence is established in this highly inhomogeneous system.

Several fundamental aspects remain to be understood, for instance, how the *inhomogeneity* of the order parameter in the BEC* phase develops when approaching the transition to the many-body localized Bose glass. Furthermore, as the doping dependence of the T–H phase diagram of DTNX is now well understood, we can focus on the narrow windows in which Bose-glass phase does exist, to study its not yet well understood finite-temperature properties or excitations. One appealing issue concerns the possible existence of a finite-temperature glass transition above the Bose-glass regime, where, despite the absence of a coherent response, the transverse susceptibility is expected to diverge [157] with an unknown critical exponent.

Conclusion

Quantum magnets have proven to be ideal systems regarding the study and emergence of new phases of matter. Especially, the apparent simplicity of "spin models" provide an ideal testing ground for theories, experiments, and numerical simulations in quantum magnetism. This allows for a better understanding of the physics at play and of the microscopic mechanisms responsible for the enthralling properties in these novel quantum systems. Interestingly, the theoretical work presented in this manuscript is substantially connected with experiments, which made a direct and fruitful comparison possible.

I. Summary

I started with a short introduction on the microscopic origin of the so-called Mott insulators systems, whose relevant degrees of freedom are the electronic spins holding the magnetic properties. Then, I briefly reminded the key ideas of the phase transition phenomenon, that is a complete change in the physical properties of a system by tuning an external parameter such as temperature, pressure or an external magnetic field. I finished this introduction by giving a few examples of different numerical methods and algorithms that one can develop and engineer in an attempt to solve many-body problems. This mostly served as the building blocks of more advanced numerical tools presented in the following chapters.

Chapter A The first chapter of this manuscript was a natural, though more specialized, follow-up of the introduction. Its first section was dedicated to one-dimensional antiferromagnets. I reviewed their general properties and emphasized the fact that one-dimensional quantum systems are very peculiar and require a specific theoretical treatment owing to the strong quantum fluctuations they exhibit. For instance, they cannot develop long-range order by spontaneously breaking a continuous symmetry, even at zero temperature where they are limited to quasi-long-range order with algebraically decaying correlation functions. As discussed, this is well-captured, as well as their other low-temperature properties, by the universal Tomonaga-Luttinger liquid field theory, fully characterized by two parameters u and K that one can hopefully relate to the underlying microscopic model.

The next section moved to three-dimensional quantum antiferromagnets, and more precisely to a specific class that displays antiferromagnetic ordering in the XY plane while the "z spin component" is subject to some anisotropy through

the interactions or induced by an external magnetic field along a specific direction. One key message was to make the connection between this kind of order and the Bose-Einstein condensation phenomenon, better known in cold atom experiments, where a macroscopic fraction of the degrees of freedom occupy the lowest energy level in the system. I have made the connection clear and eventually built up a dictionary from bosons to spins language. I also provided experimental examples of such magnetic systems where Bose-Einstein condensation fingerprints have been unambiguously observed.

The following section was more technical and introduced numerical methods to investigate the quantum systems discussed previously. Specifically, I first presented the Matrix Product States formalism along with the variational Density-Matrix Renormalization Group method to obtain, in the most efficient way up to date, zero temperature properties of one-dimensional interacting quantum systems. I then introduced Quantum Monte Carlo in its Stochastic Series Expansion formulation, cleverly defining a configuration space in which to sample the partition function of a quantum system with efficient movements from one configuration to another, fulfilling both ergodicity and detailed balance as required for any stochastic method.

The first work that followed this introductory part was concerned with the dimensional modulation of the antiferromagnetic order parameter m^{AF} in weakly coupled antiferromagnetic planes. We closely investigated how smoothly the ordering process of the three-dimensional system is modulated into that of the two-dimensional one with reduction of dimensionality in the limit of a zero interplane coupling. In particular, it is well-known that in a fully three-dimensional system, the order parameter exhibits a concave temperature dependence. On the other hand, it exhibits spontaneous long-range order only at zero temperature in the two-dimensional limit. We showed using a series of complementary theoretical and numerical methods that the $m^{\mathrm{AF}}(T)$ curve is modified with a non trivial change of convexity when reducing the interplane coupling. This dictates the existence of a quasi-two-dimensional ordered phase where the system behaves two-dimensionally except for the suppressed but nonzero $m^{\mathrm{AF}}(T)$ breaking a continuous symmetry. This work was strongly motivated by the weakly coupled spin-1/2 ladder compound $(C_7H_{10}N)_2CuBr_4$, also known as "DIMPY". In this material, the ladders are coupled in a two-dimensional fashion making planes and also in a three-dimensional way where the interplane coupling is the smallest energy scale in the system. The order parameter, experimentally measured by nuclear magnetic resonance showed for instance such a crossover towards a quasi-two-dimensional limit.

Finally, I focused on a realistic antiferromagnetic quantum $S = 1$ spin compound, $NiCl_2$-$4SC(NH_2)_2$ known as "DTN" for short, with an interesting double hatting. On one side, it is three-dimensional and displays a Bose-Einstein condensation upon applying a sufficiently large magnetic field at low temperature. On the other side, its weak three-dimensional couplings make possible experimental investigations for universal Tomonaga-Luttinger liquid properties at intermediate temperature. Specifically, the high-field properties of the antiferromagnetic ordered phase such as its order parameter and its critical temperature were studied by nuclear magnetic resonance and directly compared to several theoretical approaches. Quantum Monte Carlo simulations provided excellent fit to the data, and we used them as a reference to discuss the applicability of approximate techniques and their sensitivity to the strength of the three-dimensional coupling. We found that analytical predictions

based on the one-dimensional Tomonaga-Luttinger liquid framework were very good for the critical temperature as long as a renormalization of the three-dimensional coupling is performed beforehand, but deviated too much for the order parameter m^{AF}. Our conclusion was that the DTN compound is actually "not sufficiently one-dimensional" to be described by such approaches.

Chapter B Overall, I was interested in this second chapter in the dynamical — time-dependent — properties of quantum antiferromagnets at finite temperature. I first introduced the quantities of interest, namely the dynamical spin structure factor obtained through inelastic neutron scattering experiments and the the nuclear magnetic resonance (NMR) spin-lattice relaxation rate, the so-called $1/T_1$. I briefly explained the underlying physics of these experimental probes and related what is experimentally measured to what actually needs to be computed to have a direct comparison.

Precisely, I discussed in the second section the general numerical methods to capture time-dependent phenomena in quantum systems. First, based on the Matrix Product States formalism, I discussed the time-evolution block decimation algorithm, which is a natural and elegant way to apply the time evolution operator $\exp(-i\mathcal{H}t)$ on a one-dimensional quantum system. I also introduced the "ancilla trick" to simulate mixed (finite temperature) states with Matrix Product States while it is originally designed to deal with pure (zero temperature) states. I then presented how to compute dynamical correlation functions in the stochastic series expansion formulation of quantum Monte Carlo. However, this has the major caveat that dynamical data are obtained in imaginary time so that analytic continuation is needed a posteriori. This is an ill-posed problem due to the intrinsic sampling statistical error of the measured observables, resulting in an infinite number of solutions from imaginary time to real time. To overcome this issue I presented the stochastic analytic continuation method, which performs stochastic samplings of all possible results and average those that fit the quantum Monte Carlo data equally well, with very promising results.

The first work that I presented regarding dynamics intensively used Matrix Product States to compute the nuclear magnetic resonance spin-lattice relaxation rate in paradigmatic one-dimensional spin chains realizing Tomonaga-Luttinger liquids in the low-energy limit. Analytical predictions tell us that this quantity is expected to behave versus temperature with a power-law dependence, whose exponent is a function of the dimensionless Tomonaga-Luttinger parameter K, i.e. $1/T_1 \propto T^{1/2K-1}$. The main goal of this work was to properly define the crossover "low-temperature limit" between a non-universal high temperature regime and the universal one-dimensional properties at low-temperature in quantum spin chains. We found that quite independently of the underlying model, this crossover temperature is about $\sim J/10$ with J the characteristic energy scale of the system, i.e. the antiferromagnetic exchange coupling. It was important to be able to define this limit as Tomonaga-Luttinger liquid predictions are often used experimentally on quasi-one-dimensional compounds to extract the value of K. As a consequence, we believe that it remains experimentally challenging to explore the genuine critical one-dimensional regime in quasi-one-dimensional compounds when J is small and three-dimensional ordering prevents a wide Tomonaga-Luttinger liquid regime. For instance, we have shown that for the quasi-one-dimensional $S = 1$ compound "DTN", the antiferromagnetic ordering temperature is larger than the crossover temperature

towards one-dimensional behavior.

The next work that I discussed was the natural continuation of the previous one by introducing a three-dimensional coupling $J_\perp$ between the antiferromagnetic spin chains. I presented a comprehensive theoretical study based on both analytical calculations (bosonization plus random phase and self-consistent harmonic approximations) and numerical simulations (quantum Monte Carlo supplemented by stochastic analytic continuation). This allows us to describe the full temperature crossover for the nuclear magnetic resonance spin-lattice relaxation rate $1/T_1$, from one-dimensional Tomonaga-Luttinger liquid physics to the three-dimensional ordered regime, as a function of inter-chain couplings. We previously found that in strictly one-dimensional systems, one can asymptotically observe the predicted power-law dependence $1/T_1 \propto T^{1/2K-1}$, but only at quite low temperature $T \lesssim J/10$. A finite three-dimensional coupling $J_\perp$ will ultimately change the dynamical response when approaching the critical temperature. The Tomonaga-Luttinger liquid prediction is often used to fit the experimentally measured relaxation rate versus T and obtain the dimensionless parameter K, but a proper definition of the temperature window inside which the genuine one-dimensional properties can be observed was missing. In particular, when getting close to the critical temperature, we showed that the NMR relaxation rate diverges with a power-law $1/T_1 \propto |T - T_c|^{-\nu(z_t-1-\eta)}$ with an exponent $\nu(z_t - 1 - \eta) > 0$ characteristic of the phase transition. We properly defined a crossover temperature between the critical and one-dimensional regimes with $T \gtrsim 3T_c$ and found that systems with a three-dimensional coupling $J_\perp/J < 10^{-2}$ display a nonzero temperature window $T \in [3T_c, J/10]$, assuming that $3T_c < J/10$, inside which the observation of the universal one-dimensional behavior is possible. For example, considering experiments on "DIMPY", the $1/T_1$ has been fitted to obtain K versus the external magnetic field H, but has shown some discrepancy with the expected value $K(H)$ computed numerically. Our quantitative work reveals that the experimental fitting temperature range $2T_c < T < 3T_c$ was probably too close to the critical temperature to be reliable. In the ordered phase, we identified two regimes. Close to the transition, the NMR relaxation rate is first strongly suppressed with temperature, empirically $1/T_1 \propto T^\alpha$ with $\alpha \simeq 4 - 5$ as experimentally observed in some compounds. At lower temperature deep in the ordered phase, the NMR relaxation rate increases linearly with T due to spin-waves contribution from the absolute zero. We also discussed the dynamical structure factor that we computed for the different regimes and which is directly probing the inelastic neutron scattering intensity.

The last section was again focused on a purely one-dimensional system, the $S = 1$ Heisenberg chain, with a finite Haldane spin gap $\Delta_g/J \simeq 0.41$. A simple activated law is expected for the nuclear magnetic resonance spin-lattice relaxation rate $\propto \exp(-\gamma\Delta_g/T)$, but conflicting works based on field theory of the nonlinear O(3) sigma model predict $\gamma = 1$ or $\gamma = 3/2$. On the experimental side, everything within this range (and beyond) has been observed. An unbiased numerical study of the full quantum one-dimensional model was necessary in order to reconcile and settle the different analytical predictions as well as the experimental observations. At high temperature, $T > \Delta_g$, we have observed a spin diffusion regime, with an exponent that is not really one half, as expected classically, but a bit larger. At intermediate temperatures, $J/6 \lesssim T < \Delta_g$: we have shown that the dominant contributions to $1/T_1$ come from momenta $q \sim \pi$ that can be simply interpreted since we have a large

Lorentzian peak at the antiferromagnetic wavevector π and single magnon excitation can be thermally excited in this temperature range. At lower temperatures, $T \lesssim J/6$ due to energy conservation, dominant contribution to $1/T_1$ is due to two-magnon processes and occurs at $q \sim 0$ and our best fit in this regime is compatible with a simple activated law, $\gamma = 1$. Our results were discussed in regards of experiments and different scenarios were proposed to explain the discrepancies.

Chapter C In the last chapter, I got interested in the interplay between interactions and disorder in quantum antiferromagnets. In these systems, the disorder can be induced by chemical doping by randomly substituting one atom by another and drive the "clean system" towards new quantum phases of matter. On the theoretical side, the doping results in couplings or more generally Hamiltonian parameters drawn from some random distribution. I introduced in the first section two specific phases in this respect, the random singlet glass phase and the Bose-glass phase. I provided a microscopic picture of the former, realized by the one-dimensional Heisenberg model with random antiferromagnetic exchange couplings using strong disorder renormalization group. Singlets are successively formed between the two spins with the strongest exchange coupling at each stage, thereby decimating this spin pair from the system but yielding a new effective interaction between the spins previously coupled to it. The resulting asymptotic state can be nicely pictured as a collection of spin paired up into singlets spanning arbitrary distances. From the renormalization group analysis, the physical properties can be derived (correlations, susceptibility...) and I discussed the comparison between these predictions and numerical studies of the model as well as some experimental realizations. I then moved to the Bose-glass phase, more difficult to apprehend with no simple microscopic picture to which to relate. Nevertheless, the "theorem of inclusions" provides some insights and defines the phase as a collection of spatially isolated and disconnected superfluid droplets of various sizes. The fact that these clusters do not interact with each others is responsible for the lack of global phase coherence in this phase resulting in exponentially decaying correlation functions. I also presented various experiments in different systems, including Mott insulators in which the Bose-glass phase has been observed.

The first work combined disorder and dynamics by focusing on the dynamical properties of the random singlet phase in random one-dimensional Heisenberg spin chains. The investigations were carried out using state-of-the-art numerical tools such as Matrix Product States and quantum Monte Carlo supplemented by stochastic analytic continuation. First concerned with the dynamical structure factor, we found a continuous narrow band of low-energy excitations extending throughout the Brillouin zone, instead of being restricted to momenta $q \sim 0$ and $q \sim \pi$ as found in the clean system. Regarding the nuclear magnetic resonance spin-lattice relaxation rate, we show that the local $1/T_1$ values are broadly distributed. More precisely, its mean value first decreases with the temperature, but below a crossover temperature it starts to increase and likely diverges in the zero temperature limit. We show that this divergence is due to rare events in the disordered chains and is concealed in experiments, where the typical value is actually accessed, as in the spin-1/2 random Heisenberg chain material $BaCu_2(Si_{1-x}Ge_x)O_7$.

In the last section, I thoroughly summarized a series of works on the chemically doped $Ni(Cl_{1-x}Br_x)_2$-4SC$(NH_2)_2$ "DTNX" compound at high magnetic fields, which has been proposed in prior publications, as the first experimental realization of the

Bose-glass phase in a quantum magnet. We have first fully determined the microscopic model of the DTNX compound based on nuclear magnetic resonance experiments which can be interpreted and understood via single impurity physics. This made it possible to perform analytical as well as exact diagonalization calculations on large systems from which a unique set of coupling parameters could be determined for the impurity degrees of freedom. This simple description provided fruitful insights on the microscopic picture of DTNX at high magnetic field with a strong localization of isolated impurity states and the fact that the clean background polarizes at a smaller magnetic field than the impurities. Thus, a simple picture of DTNX at high magnetic field consists in a frozen (clean) background with a collection of impurities spatially randomly distributed, yet to be polarized upon increasing the magnetic field. By studying the mutual effect of two impurities we revealed that, despite the strong localization of the impurity states, there exists an effective unfrustrated pairwise interaction between impurity degrees of freedom. This paved the way to a resurgence of global phase coherence in DTNX, in sharp contrast with the many-body localized Bose-glass phase reported previously. Indeed, using large scale quantum Monte Carlo simulations, we showed that the disorder itself is actually getting ordered, forming a Bose-Einstein condensation through a novel order-by-disorder mechanism. Moreover, we determined a complete picture of the phase diagram "high magnetic fields *vs.* doping concentrations *vs.* temperatures". At low doping there is still room for a Bose-glass phase and we studied the critical properties of the Bose-Einstein condensation to Bose-glass transition. We found critical exponents compatible with previous studies confirming the universal character of the transition, although we could not be conclusive regarding the "ϕ-crisis" raised by conflicting numerics. The theoretically predicted disorder-induced revival of Bose-Einstein condensation in "DTN" was afterwards experimentally observed and verified by nuclear magnetic resonance that I briefly discussed to conclude this series of works.

II. Open questions and perspectives

It clearly emerges from the work presented within this manuscript that one can make a strong connection between theory and experiments in strongly correlated systems with state-of-the-art numerical techniques. Especially, advances in the computation of dynamical quantities open new routes in understanding new phases of matter, connecting with nuclear magnetic resonance and inelastic neutron scattering experiments for magnetic materials or equivalently Bragg spectroscopy for cold atom setups. More generally, the developed tools can also be used for the study of out-of-equilibrium quantum systems which has attracted a considerable amount of attention over the last years in condensed matter theory and quantum gases communities on both the theoretical and experimental sides. This gives access to quantum dynamics governed by unitary evolution in order to study quantum dynamical phenomena: many-body localization [391, 392, 497, 498], discrete time crystals [499, 500] and dynamical quantum phase transitions [501–503] to cite but a few.

Localization is a key mechanism in the breaking of ergodicity in disordered quantum systems, and in this respect, it is likely that the physics of classical spin glasses [504], observed in the Edward-Anderson model (i.e. a classical Ising model with random coupling strengths) and in the directed polymers problem [505, 506] for instance, will also emerge in their quantum counterparts. A crucial point is the extreme fragility of spin glasses; a small change in a parameter such as a small disorder perturbation of the disorder configuration induces a complete reorganization of the equilibrium configurations. In the context of spin-glass physics, this property has been coined "chaos". The glassy properties of disordered quantum systems like the random singlet phase and the Bose-glass phase have never been looked at although one calls the Bose-glass phase *glass* for example. One could also look at dynamical properties of the Bose-glass phase, which have been relatively little explored [507], and probably get some more insights on the microscopic picture, e.g. what are the excitations?

Still regarding the Bose-glass phase, it is a many-body localized *ground* state in one-dimension of the spin-1/2 Heisenberg model subject to a random field in the $S^z_{\text{tot}} = 0$ sector, i.e. $\mathcal{H} = \sum_i \mathbf{S}_i \cdot \mathbf{S}_{i+1} - \sum_i H_i S^z_i$. This is also the paradigmatic model to study what is known as "the many-body localization phenomenon" [508]. In a nutshell, an eigenstate of this Hamiltonian belongs to one of the two phases called thermal or many-body localized and is labelled by two numbers: the disorder strength H which is related to the width of the box for a uniform disorder with $H_i \in [-H, +H]$, and its normalized position in the spectrum $\varepsilon \in [0, 1]$, $\varepsilon = 0$ corresponding to the ground state of $\mathcal{H}$. A thermal state satisfies the eigenstate thermalization hypothesis (ETH) [509, 510], meaning in one word that statistical mechanics works: the reduced density matrix ρ_A of a subsystem A (with respect to the rest of the system) of an eigenstate $|n\rangle$ will take a thermal form $\rho_A(|n\rangle) \propto \exp(-\mathcal{H}/T_n)$ with the temperature T_n matching the one of the canonical ensemble reproducing the eigenstate energy, $\langle \mathcal{H} \rangle_{T_n} = \langle n|\mathcal{H}|n\rangle$ (see Ref. 511 for a more detailed introduction). On the other hand, a many-body localized (MBL) state is not thermal and a statistical mechanics description in terms of a canonical ensemble does not work. Interestingly, high-energy MBL states behave roughly as ground states, especially regarding the entanglement entropy fulfilling the area law. The Bose-glass phase corresponds to the ground state ($H \neq 0, \varepsilon = 0$) and one can wonder if high-energy MBL eigenstates are connected somehow to many-body localized ground states, i.e. is a high-energy MBL eigenstate the ground state of the same Hamiltonian but with a different disorder configuration?

Finally, machine learning has found its way to condensed matter problems. For instance, it has been successfully used so far to detect nontrivial [512] or topological phase transitions [513] and find effective Monte Carlo movements [514] to significantly reduce the computational complexity of simulations. Tensor network methods have also found their way to the machine learning community to represent neural networks. What is promising is the possibility to use the efficient optimization algorithms that have been developed for tensor networks (like the density matrix renormalization group algorithm) for machine learning problems [515–520].

Bibliography

[1] L. D. Landau, "*The Theory of a Fermi Liquid*," Sov. Phys. JETP **3** (1957).

[2] L. D. Landau, "*Oscillations in a Fermi Liquid*," Sov. Phys. JETP **5** (1957).

[3] L. D. Landau, "*On the Theory of Fermi Liquid*," Sov. Phys. JETP **35** (1959).

[4] P. Nozières, "*Theory of Interacting Fermi systems*" (W. A. Benjamin, New York, 1961).

[5] N. Ashcroft and N. D. Mermin, "*Solid State Physics*" (Saunders College, Philadelphia, 1976).

[6] N. F. Mott and R. Peierls, "*Discussion of the paper by de Boer and Verwey*," Proc. Phys. Soc. **49**, 72 (1937).

[7] J. Hubbard, "*Electron correlations in narrow energy bands*," Proc. R. Soc. A **276**, 238 (1963).

[8] C. L. Cleveland and R. Medina, "*Obtaining a Heisenberg Hamiltonian from the Hubbard model*," American Journal of Physics **44**, 44 (1976).

[9] L. Landau and E. Lifshitz, "*Quantum Mechanics: Non-Relativistic Theory*", Course of Theoretical Physics (Elsevier Science, 1981).

[10] H. E. Stanley, "*Introduction to Phase Transitions and Critical Phenomena*," American Journal of Physics **40**, 927 (1972).

[11] S.-K. Ma, "*Modern theory of critical phenomena*" (WA Benjamin, Inc., Reading, MA, 1976).

[12] N. Goldenfeld, "*Lectures on phase transitions and the renormalization group*", Frontiers in physics No. 85 (1992).

[13] L. D. Landau, "*On the theory of phase transitions*," Zh. eksp. teor. Fiz **7** (1937).

[14] K. G. Wilson, "*Renormalization Group and Critical Phenomena. I. Renormalization Group and the Kadanoff Scaling Picture*," Phys. Rev. B **4**, 3174 (1971).

[15] K. G. Wilson, "*Renormalization Group and Critical Phenomena. II. Phase-Space Cell Analysis of Critical Behavior*," Phys. Rev. B **4**, 3184 (1971).

[16] K. G. Wilson, "*The renormalization group and critical phenomena*," Rev. Mod. Phys. **55**, 583 (1983).

[17] N. D. Mermin and H. Wagner, "*Absence of Ferromagnetism or Antiferromagnetism in One- or Two-Dimensional Isotropic Heisenberg Models*," Phys. Rev. Lett. **17**, 1133 (1966).

[18] P. C. Hohenberg, "*Existence of Long-Range Order in One and Two Dimensions*," Phys. Rev. **158**, 383 (1967).

[19] A. Auerbach, "*Interacting Electrons and Quantum Magnetism*" (Springer-Verlag, 1994).

[20] T. Momoi, "*Quantum fluctuations in quantum lattice systems with continuous symmetry*," J. Stat. Phys. **85**, 193 (1996).

[21] S. Sachdev, "*Quantum Phase Transitions*" (Cambridge University Press, Cambridge, UK, 2001).

[22] M. Vojta, "*Thermal and Quantum Phase transitions*," Lectures at the Les Houches Doctoral Training School in Statistical Physics (2015).

[23] A. Lüscher and A. M. Läuchli, "*Exact diagonalization study of the antiferromagnetic spin-$\frac{1}{2}$ Heisenberg model on the square lattice in a magnetic field*," Phys. Rev. B **79**, 195102 (2009).

[24] A. M. Läuchli, J. Sudan, and E. S. Sørensen, "*Ground-state energy and spin gap of spin-$\frac{1}{2}$ Kagomé-Heisenberg antiferromagnetic clusters: Large-scale exact diagonalization results*," Phys. Rev. B **83**, 212401 (2011).

[25] S. Capponi, O. Derzhko, A. Honecker, A. M. Läuchli, and J. Richter, "*Numerical study of magnetization plateaus in the spin-$\frac{1}{2}$ kagome Heisenberg antiferromagnet*," Phys. Rev. B **88**, 144416 (2013).

[26] S. Capponi and A. M. Läuchli, "*Phase diagram of interacting spinless fermions on the honeycomb lattice: A comprehensive exact diagonalization study*," Phys. Rev. B **92**, 085146 (2015).

[27] A. Wietek, A. Sterdyniak, and A. M. Läuchli, "*Nature of chiral spin liquids on the kagome lattice*," Phys. Rev. B **92**, 125122 (2015).

[28] A. Wietek and A. M. Läuchli, "*Chiral spin liquid and quantum criticality in extended $S = \frac{1}{2}$ Heisenberg models on the triangular lattice*," Phys. Rev. B **95**, 035141 (2017).

[29] N. Metropolis, A. W. Rosenbluth, M. N. Rosenbluth, A. H. Teller, and E. Teller, "*Equation of State Calculations by Fast Computing Machines*," J. Chem. Phys. **21**, 1087 (1953).

[30] U. Schollwöck, J. Richter, D. Farnell, and R. Bishop, "*Quantum Magnetism*", Lecture notes in physics (Springer, 2004).

[31] S.-i. Tomonaga, "*Remarks on Bloch's Method of Sound Waves applied to Many-Fermion Problems*," Progr. Theor. Exp. Phys. **5**, 544 (1950).

[32] J. M. Luttinger, "*An Exactly Soluble Model of a Many-Fermion System*," J. Math. Phys. **4**, 1154 (1963).

[33] D. C. Mattis and E. H. Lieb, "*Exact Solution of a Many-Fermion System and Its Associated Boson Field*," J. Math. Phys. **6**, 304 (1965).

[34] F. D. M. Haldane, "*General Relation of Correlation Exponents and Spectral Properties of One-Dimensional Fermi Systems: Application to the Anisotropic $S = \frac{1}{2}$ Heisenberg Chain*," Phys. Rev. Lett. **45**, 1358 (1980).

[35] F. D. M. Haldane, "*Effective Harmonic-Fluid Approach to Low-Energy Properties of One-Dimensional Quantum Fluids*," Phys. Rev. Lett. **47**, 1840 (1981).

[36] F. D. M. Haldane, "*'Luttinger liquid theory' of one-dimensional quantum fluids. I. Properties of the Luttinger model and their extension to the general 1D interacting spinless Fermi gas*," Journal of Physics C: Solid State Physics **14**, 2585 (1981).

[37] T. Giamarchi, "*Quantum Physics in One Dimension*" (Oxford University Press, Oxford, 2004).

[38] M. A. Cazalilla, R. Citro, T. Giamarchi, E. Orignac, and M. Rigol, "*One dimensional bosons: From condensed matter systems to ultracold gases*," Rev. Mod. Phys. **83**, 1405 (2011).

[39] T. Giamarchi, "*One-dimensional physics in the 21st century*," C. R. Phys. **17**, 322 (2016), physique de la matière condensée au XXIe siècle: l'héritage de Jacques Friedel.

[40] A. Griffin, D. W. Snoke, and S. Stringari, *Bose-Einstein Condensation* (Cambridge University Press, 1995).

[41] F. Dalfovo, S. Giorgini, L. P. Pitaevskii, and S. Stringari, "*Theory of Bose-Einstein condensation in trapped gases*," Rev. Mod. Phys. **71**, 463 (1999).

[42] A. J. Leggett, "*Bose-Einstein condensation in the alkali gases: Some fundamental concepts*," Rev. Mod. Phys. **73**, 307 (2001).

[43] T. Giamarchi, C. Rüegg, and O. Tchernyshyov, "*Bose-Einstein condensation in magnetic insulators*," Nat. Phys. **4**, 198 (2008).

[44] V. Zapf, M. Jaime, and C. D. Batista, "*Bose-Einstein condensation in quantum magnets*," Rev. Mod. Phys. **86**, 563 (2014).

[45] U. Schollwöck, "*The density-matrix renormalization group in the age of matrix product states*," Ann. Phys. **326**, 96 (2011).

[46] R. Orús, "*A practical introduction to tensor networks: Matrix product states and projected entangled pair states*," Ann. Phys. **349**, 117 (2014).

[47] S. R. White, "*Density matrix formulation for quantum renormalization groups*," Phys. Rev. Lett. **69**, 2863 (1992).

[48] S. R. White, "*Density-matrix algorithms for quantum renormalization groups*," Phys. Rev. B **48**, 10345 (1993).

[49] A. W. Sandvik and J. Kurkijärvi, "*Quantum Monte Carlo simulation method for spin systems*," Phys. Rev. B **43**, 5950 (1991).

[50] A. W. Sandvik, "*A generalization of Handscomb's quantum Monte Carlo scheme-application to the 1D Hubbard model*," J. Phys. A: Math. Gen. **25**, 3667 (1992).

[51] A. Paduan-Filho, R. D. Chirico, K. O. Joung, and R. L. Carlin, "*Field-induced magnetic ordering in uniaxial nickel systems: A second example*," J. Chem. Phys. **74**, 4103 (1981).

[52] H. Bethe, "*Zur Theorie der Metalle*," Zeitschrift für Physik **71**, 205 (1931).

[53] L. D. Faddeev, "*How Algebraic Bethe Ansatz works for integrable model*," arxiv:hep-th/9605187 (preprint) (1996).

[54] W. Marshall, "*Antiferromagnetism*," Proc. R. Soc. A **232**, 48 (1955).

[55] E. Lieb and D. Mattis, "*Ordering Energy Levels of Interacting Spin Systems*," J. Math. Phys. **3**, 749 (1962).

[56] E. Lieb, T. Schultz, and D. Mattis, "*Two soluble models of an antiferromagnetic chain*," Ann. Phys. **16**, 407 (1961).

[57] J. des Cloizeaux and J. J. Pearson, "*Spin-Wave Spectrum of the Antiferromagnetic Linear Chain*," Phys. Rev. **128**, 2131 (1962).

[58] I. Affleck, "*Exact correlation amplitude for the Heisenberg antiferromagnetic chain*," J. Phys. A: Math. Gen. **31**, 4573 (1998).

[59] J. Villain, "*Propagative spin relaxation in the Ising-like antiferromagnetic linear chain*," Physica B+C **79**, 1 (1975).

[60] N. Ishimura and H. Shiba, "*Dynamical Correlation Functions of One-Dimensional Anisotropic Heisenberg Model with Spin 1/2. Ising-Like Antiferromagnets*," Progr. Theor. Exp. Phys. **63**, 743 (1980).

[61] A. O. Gogolin, A. A. Nersesyan, and A. M. Tsvelik, "*Bosonization and strongly correlated systems*" (Cambridge University Press, Cambridge, 1999).

[62] P. Jordan and E. Wigner, "*Über das Paulische Äquivalenzverbot*," Zeitschrift für Physik **47**, 631 (1928).

[63] B. M. McCoy, "*Spin Correlation Functions of the $X-Y$ Model*," Phys. Rev. **173**, 531 (1968).

[64] H. Fröhlich, "*On the theory of superconductivity: the one-dimensional case*," Proc. R. Soc. A **223**, 296 (1954).

[65] R. Peierls, *Quantum Theory of Solids*, International series of monographs on physics (Clarendon Press, 1955).

[66] X. G. Wen, "*Electrodynamical properties of gapless edge excitations in the fractional quantum Hall states*," Phys. Rev. Lett. **64**, 2206 (1990).

[67] X. G. Wen, "*Chiral Luttinger liquid and the edge excitations in the fractional quantum Hall states*," Phys. Rev. B **41**, 12838 (1990).

[68] X. G. Wen, "*Gapless boundary excitations in the quantum Hall states and in the chiral spin states*," Phys. Rev. B **43**, 11025 (1991).

[69] S. Lukyanov and A. Zamolodchikov, "*Exact expectation values of local fields in the quantum sine-Gordon model*," Nucl. Phys. B **493**, 571 (1997).

[70] S. Lukyanov, "*Correlation amplitude for the XXZ spin chain in the disordered regime*," Phys. Rev. B **59**, 11163 (1999).

[71] A. Luther and I. Peschel, "*Calculation of critical exponents in two dimensions from quantum field theory in one dimension*," Phys. Rev. B **12**, 3908 (1975).

[72] I. Affleck, D. Gepner, H. J. Schulz, and T. Ziman, "*Critical behaviour of spin-s Heisenberg antiferromagnetic chains: analytic and numerical results*," J. Phys. A: Math. Gen. **22**, 511 (1989).

[73] T. Giamarchi and H. J. Schulz, "*Correlation functions of one-dimensional quantum systems*," Phys. Rev. B **39**, 4620 (1989).

[74] R. R. P. Singh, M. E. Fisher, and R. Shankar, "*Spin-1/2 antiferromagnetic XXZ chain: New results and insights*," Phys. Rev. B **39**, 2562 (1989).

[75] S. Eggert, I. Affleck, and M. Takahashi, "*Susceptibility of the spin 1/2 Heisenberg antiferromagnetic chain*," Phys. Rev. Lett. **73**, 332 (1994).

[76] T. Ami, M. K. Crawford, R. L. Harlow, Z. R. Wang, D. C. Johnston, Q. Huang, and R. W. Erwin, "*Magnetic susceptibility and low-temperature structure of the linear chain cuprate* Sr_2CuO_3," Phys. Rev. B **51**, 5994 (1995).

[77] S. Eggert, "*Accurate determination of the exchange constant in* Sr_2CuO_3 *from recent theoretical results*," Phys. Rev. B **53**, 5116 (1996).

[78] N. Motoyama, H. Eisaki, and S. Uchida, "*Magnetic Susceptibility of Ideal Spin 1 /2 Heisenberg Antiferromagnetic Chain Systems,* Sr_2CuO_3 *and* $SrCuO_2$," Phys. Rev. Lett. **76**, 3212 (1996).

[79] S. Suga, "*Tomonaga–Luttinger Liquid in Quasi-One-Dimensional Antiferromagnet* $BaCo_2V_2O_8$ *in Magnetic Fields*," J. Phys. Soc. Jpn. **77**, 074717 (2008).

[80] C. Rüegg, K. Kiefer, B. Thielemann, D. F. McMorrow, V. Zapf, B. Normand, M. B. Zvonarev, P. Bouillot, C. Kollath, T. Giamarchi, S. Capponi, D. Poilblanc, D. Biner, and K. W. Krämer, "*Thermodynamics of the Spin Luttinger Liquid in a Model Ladder Material*," Phys. Rev. Lett. **101**, 247202 (2008).

[81] F. D. M. Haldane, "*Nonlinear Field Theory of Large-Spin Heisenberg Antiferromagnets: Semiclassically Quantized Solitons of the One-Dimensional Easy-Axis Néel State*," Phys. Rev. Lett. **50**, 1153 (1983).

[82] F. Haldane, "*Continuum dynamics of the 1-D Heisenberg antiferromagnet: Identification with the O(3) nonlinear sigma model*," Phys. Lett. A **93**, 464 (1983).

[83] P. W. Anderson, "*An Approximate Quantum Theory of the Antiferromagnetic Ground State*," Phys. Rev. **86**, 694 (1952).

[84] R. Kubo, "*The Spin-Wave Theory of Antiferromagnetics*," Phys. Rev. **87**, 568 (1952).

[85] T. Oguchi, "*Theory of Spin-Wave Interactions in Ferro- and Antiferromagnetism*," Phys. Rev. **117**, 117 (1960).

[86] K. Nomura, "*Spin correlation function of the S=1 antiferromagnetic Heisenberg chain by the large-cluster-decomposition Monte Carlo method*," Phys. Rev. B **40**, 2421 (1989).

[87] S. Liang, "*Monte Carlo calculations of the correlation functions for Heisenberg spin chains at T=0*," Phys. Rev. Lett. **64**, 1597 (1990).

[88] S. R. White and D. A. Huse, "*Numerical renormalization-group study of low-lying eigenstates of the antiferromagnetic S=1 Heisenberg chain*," Phys. Rev. B **48**, 3844 (1993).

[89] H. Mutka, J. L. Soubeyroux, G. Bourleaux, and P. Colombet, "*Support for the Haldane conjecture: Gap for magnetic excitations in the quasi-one-dimensional S=1 Heisenberg antiferromagnet* $AgVP_2S_6$," Phys. Rev. B **39**, 4820 (1989).

[90] H. Mutka, C. Payen, P. Molinié, J. L. Soubeyroux, P. Colombet, and A. D. Taylor, "*Dynamic structure factor [S(Q,ω)] of the S=1 quasi-one-dimensional Heisenberg antiferromagnet: Neutron-scattering study on* $AgVP_2S_6$," Phys. Rev. Lett. **67**, 497 (1991).

[91] W. J. L. Buyers, R. M. Morra, R. L. Armstrong, M. J. Hogan, P. Gerlach, Hirakawa, and K., "*Experimental evidence for the Haldane gap in a spin-1 nearly isotropic, antiferromagnetic chain*," Phys. Rev. Lett. **56**, 371 (1986).

[92] J. P. Renard, M. Verdaguer, L. P. Regnault, W. A. C. Erkelens, J. Rossat-Mignod, and W. G. Stirling, "*Presumption for a Quantum Energy Gap in the Quasi-One-Dimensional S = 1 Heisenberg Antiferromagnet* $Ni(C_2H_8N_2)_2NO_2(ClO_4)$," EPL **3**, 945 (1987).

[93] M. Takigawa, T. Asano, Y. Ajiro, and M. Mekata, "*Static properties of the S=1 one-dimensional antiferromagnet* $AgVP_2S_6$," Phys. Rev. B **52**, R13087 (1995).

[94] T. K. Ng, "*Schwinger-boson mean-field theory for S=1 open spin chains*," Phys. Rev. B **45**, 8181 (1992).

[95] M. Hagiwara, K. Katsumata, I. Affleck, B. I. Halperin, and J. P. Renard, "*Observation of S=1/2 degrees of freedom in an S=1 linear-chain Heisenberg antiferromagnet*," Phys. Rev. Lett. **65**, 3181 (1990).

[96] S. H. Glarum, S. Geschwind, K. M. Lee, M. L. Kaplan, and J. Michel, "*Observation of fractional spin S=1/2 on open ends of S=1 linear antiferromagnetic chains: Nonmagnetic doping*," Phys. Rev. Lett. **67**, 1614 (1991).

[97] P. P. Mitra, B. I. Halperin, and I. Affleck, "*Temperature dependence of the electron-spin-resonance spectrum of the chain-end S=1/2 modes in an S=1 antiferromagnetic chain*," Phys. Rev. B **45**, 5299 (1992).

[98] F. Tedoldi, R. Santachiara, and M. Horvatić, "^{89}Y *NMR Imaging of the Staggered Magnetization in the Doped Haldane Chain* $Y_2BaNi_{1-x}Mg_xO_5$," Phys. Rev. Lett. **83**, 412 (1999).

[99] S. Miyashita and S. Yamamoto, "*Effects of edges in S=1 Heisenberg antiferromagnetic chains*," Phys. Rev. B **48**, 913 (1993).

[100] T. Asano, Y. Ajiro, M. Mekata, K. Kamishima, K. Koui, T. Goto, M. Furusawa, and H. Hori, "*The Haldane State in* $CsNiCl_3$ *Detected by Magnetization Measurements –Observation of Quantum-Classical Crossover and the Valence Bond Solid State–*," J. Phys. Soc. Jpn. **66**, 460 (1997).

[101] I. Affleck, T. Kennedy, E. H. Lieb, and H. Tasaki, "*Rigorous results on valence-bond ground states in antiferromagnets*," Phys. Rev. Lett. **59**, 799 (1987).

[102] I. Affleck, T. Kennedy, E. H. Lieb, and H. Tasaki, "*Valence bond ground states in isotropic quantum antiferromagnets*," Commun. Math. Phys. **115**, 477 (1988).

[103] T. Kennedy, "*Exact diagonalisations of open spin-1 chains*," J. Phys. Condens. Matter **2**, 5737 (1990).

[104] M. den Nijs and K. Rommelse, "*Preroughening transitions in crystal surfaces and valence-bond phases in quantum spin chains*," Phys. Rev. B **40**, 4709 (1989).

[105] Z.-C. Gu and X.-G. Wen, "*Tensor-entanglement-filtering renormalization approach and symmetry-protected topological order*," Phys. Rev. B **80**, 155131 (2009).

[106] F. Pollmann, A. M. Turner, E. Berg, and M. Oshikawa, "*Entanglement spectrum of a topological phase in one dimension*," Phys. Rev. B **81**, 064439 (2010).

[107] M. Z. Hasan and C. L. Kane, "*Colloquium*," Rev. Mod. Phys. **82**, 3045 (2010).

[108] X. Chen, Z.-C. Gu, and X.-G. Wen, "*Classification of gapped symmetric phases in one-dimensional spin systems*," Phys. Rev. B **83**, 035107 (2011).

[109] F. Pollmann, E. Berg, A. M. Turner, and M. Oshikawa, "*Symmetry protection of topological phases in one-dimensional quantum spin systems*," Phys. Rev. B **85**, 075125 (2012).

[110] M. Fruchart and D. Carpentier, "*An introduction to topological insulators*," C. R. Phys. **14**, 779 (2013), topological insulators / Isolants topologiques.

[111] N. Laflorencie, "*Quantum entanglement in condensed matter systems*," Phys. Rep. **646**, 1 (2016), quantum entanglement in condensed matter systems.

[112] C. Holzhey, F. Larsen, and F. Wilczek, "*Geometric and renormalized entropy in conformal field theory*," Nucl. Phys. B **424**, 443 (1994).

[113] P. Calabrese and J. Cardy, "*Entanglement entropy and quantum field theory*," J. Stat. Mech. Theory Exp. **2004**, P06002 (2004).

[114] P. Calabrese and J. Cardy, "*Entanglement entropy and conformal field theory*," J. Phys. A **42**, 504005 (2009).

[115] F. Verstraete, V. Murg, and J. Cirac, "*Matrix product states, projected entangled pair states, and variational renormalization group methods for quantum spin systems*," Adv. Phys. **57**, 143 (2008).

[116] J. I. Cirac and F. Verstraete, "*Renormalization and tensor product states in spin chains and lattices*," J. Phys. A **42**, 504004 (2009).

[117] M. Srednicki, "*Entropy and area*," Phys. Rev. Lett. **71**, 666 (1993).

[118] G. Vidal, J. I. Latorre, E. Rico, and A. Kitaev, "*Entanglement in Quantum Critical Phenomena*," Phys. Rev. Lett. **90**, 227902 (2003).

[119] M. B. Plenio, J. Eisert, J. Dreißig, and M. Cramer, "*Entropy, Entanglement, and Area: Analytical Results for Harmonic Lattice Systems*," Phys. Rev. Lett. **94**, 060503 (2005).

[120] Bose, "*Plancks Gesetz und Lichtquantenhypothese*," Zeitschrift für Physik **26**, 178 (1924).

[121] A. Einstein, "*Quantentheorie des einatomigen idealen Gases*," Sitzungsberichte/Physikalische Klasse, Preussische Akademie der Wissenschaften **22** (1924).

[122] A. Einstein, "*Quantentheorie des einatomigen idealen Gases ii*," Sitzungsberichte/Physikalische Klasse, Preussische Akademie der Wissenschaften **1** (1925).

[123] M. H. Anderson, J. R. Ensher, M. R. Matthews, C. E. Wieman, and E. A. Cornell, "*Observation of Bose-Einstein Condensation in a Dilute Atomic Vapor*," Science **269**, 198 (1995).

[124] K. B. Davis, M. O. Mewes, M. R. Andrews, N. J. van Druten, D. S. Durfee, D. M. Kurn, and W. Ketterle, "*Bose-Einstein Condensation in a Gas of Sodium Atoms*," Phys. Rev. Lett. **75**, 3969 (1995).

[125] S. Fujita, T. Kimura, and Y. Zheng, "*On the Bose-Einstein condensation of free relativistic bosons with or without mass*," Found. Phys. **21**, 1117 (1991).

[126] P. Kapitza, "*Viscosity of Liquid Helium below the λ-Point*," Nature **141**, 74 EP (1938).

[127] J. F. Allen and A. D. Misener, "*Flow of Liquid Helium II*," Nature **141**, 75 EP (1938).

[128] F. London, "*On the Bose-Einstein Condensation*," Phys. Rev. **54**, 947 (1938).

[129] L. Tisza, "*The Theory of Liquid Helium*," Phys. Rev. **72**, 838 (1947).

[130] P. Hohenberg and P. Martin, "*Microscopic theory of superfluid helium*," Ann. Phys. **34**, 291 (1965).

[131] A. J. Leggett, "*Superfluidity*," Rev. Mod. Phys. **71**, S318 (1999).

[132] V. G. Rousseau, "*Superfluid density in continuous and discrete spaces: Avoiding misconceptions*," Phys. Rev. B **90**, 134503 (2014).

[133] A. Miller, D. Pines, and P. Nozières, "*Elementary Excitations in Liquid Helium*," Phys. Rev. **127**, 1452 (1962).

[134] H. R. Glyde, S. O. Diallo, R. T. Azuah, O. Kirichek, and J. W. Taylor, "*Atomic momentum distribution and Bose-Einstein condensation in liquid* ^{4}He *under pressure*," Phys. Rev. B **84**, 184506 (2011).

[135] N. Bogoliubov, "*On the theory of superfluidity*," J. Phys **11**, 23 (1947).

[136] T. D. Lee, K. Huang, and C. N. Yang, "*Eigenvalues and Eigenfunctions of a Bose System of Hard Spheres and Its Low-Temperature Properties*," Phys. Rev. **106**, 1135 (1957).

[137] S. Giorgini, J. Boronat, and J. Casulleras, "*Ground state of a homogeneous Bose gas: A diffusion Monte Carlo calculation*," Phys. Rev. A **60**, 5129 (1999).

[138] R. Lopes, C. Eigen, N. Navon, D. Clément, R. P. Smith, and Z. Hadzibabic, "*Quantum Depletion of a Homogeneous Bose-Einstein Condensate*," Phys. Rev. Lett. **119**, 190404 (2017).

[139] A. Imamoğlu, R. J. Ram, S. Pau, and Y. Yamamoto, "*Nonequilibrium condensates and lasers without inversion: Exciton-polariton lasers*," Phys. Rev. A **53**, 4250 (1996).

[140] J. Kasprzak, M. Richard, S. Kundermann, A. Baas, P. Jeambrun, J. M. J. Keeling, F. M. Marchetti, M. H. Szymańska, R. André, J. L. Staehli, V. Savona, P. B. Littlewood, B. Deveaud, and L. S. Dang, "*Bose–Einstein condensation of exciton polaritons*," Nature **443**, 409 EP (2006).

[141] S. Utsunomiya, L. Tian, G. Roumpos, C. W. Lai, N. Kumada, T. Fujisawa, M. Kuwata-Gonokami, A. Löffler, S. Höfling, A. Forchel, and Y. Yamamoto, "*Observation of Bogoliubov excitations in exciton-polariton condensates*," Nat. Phys. **4**, 700 EP (2008).

[142] A. Oosawa, M. Ishii, and H. Tanaka, "*Field-induced three-dimensional magnetic ordering in the spin-gap system*," J. Phys. Condens. Matter **11**, 265 (1999).

[143] T. Nikuni, M. Oshikawa, A. Oosawa, and H. Tanaka, "*Bose-Einstein Condensation of Dilute Magnons in* $TlCuCl_3$," Phys. Rev. Lett. **84**, 5868 (2000).

[144] C. Rüegg, N. Cavadini, A. Furrer, H. U. Güdel, K. Krämer, H. Mutka, A. Wildes, K. Habicht, and P. Vorderwisch, "*Bose–Einstein condensation of the triplet states in the magnetic insulator* $TlCuCl_3$," Nature **423**, 62 EP (2003).

[145] T. Holstein and H. Primakoff, "*Field Dependence of the Intrinsic Domain Magnetization of a Ferromagnet*," Phys. Rev. **58**, 1098 (1940).

[146] T. Matsubara and H. Matsuda, "*A Lattice Model of Liquid Helium, I*," Prog. Theor. Phys. **16**, 569 (1956).

[147] T. Giamarchi and A. M. Tsvelik, "*Coupled ladders in a magnetic field*," Phys. Rev. B **59**, 11398 (1999).

[148] S. Wessel and S. Haas, "*Magnetic field induced ordering in quasi-one-dimensional quantum magnets*," Eur. Phys. J. B **16**, 393 (2000).

[149] S. Wessel and S. Haas, "*Three-dimensional ordering in weakly coupled antiferromagnetic ladders and chains*," Phys. Rev. B **62**, 316 (2000).

[150] I. Affleck, "*Bose condensation in quasi-one-dimensional antiferromagnets in strong fields*," Phys. Rev. B **43**, 3215 (1991).

[151] I. Affleck, "*Luttinger liquid parameter for the spin-1 Heisenberg chain in a magnetic field*," Phys. Rev. B **72**, 132414 (2005).

[152] A. K. Bera, B. Lake, A. T. M. N. Islam, and A. Schneidewind, "*Critical properties of coupled anisotropic Haldane spin chains in a magnetic field*," Phys. Rev. B **92**, 060412 (2015).

[153] T. Barnes, E. Dagotto, J. Riera, and E. S. Swanson, "*Excitation spectrum of Heisenberg spin ladders*," Phys. Rev. B **47**, 3196 (1993).

[154] S. Gopalan, T. M. Rice, and M. Sigrist, "*Spin ladders with spin gaps: A description of a class of cuprates*," Phys. Rev. B **49**, 8901 (1994).

[155] R. Chitra and T. Giamarchi, "*Critical properties of gapped spin-chains and ladders in a magnetic field*," Phys. Rev. B **55**, 5816 (1997).

[156] A. Furusaki and S.-C. Zhang, "*Dynamical spin correlations in the Heisenberg ladder under a magnetic field and correlation functions in the SO(5) ladder*," Phys. Rev. B **60**, 1175 (1999).

[157] M. P. A. Fisher, P. B. Weichman, G. Grinstein, and D. S. Fisher, "*Boson localization and the superfluid-insulator transition*," Phys. Rev. B **40**, 546 (1989).

[158] Y. Nambu, "*Quasi-Particles and Gauge Invariance in the Theory of Superconductivity*," Phys. Rev. **117**, 648 (1960).

[159] J. Goldstone, A. Salam, and S. Weinberg, "*Broken Symmetries*," Phys. Rev. **127**, 965 (1962).

[160] M. Matsumoto, B. Normand, T. M. Rice, and M. Sigrist, "*Magnon Dispersion in the Field-Induced Magnetically Ordered Phase of* $TlCuCl_3$," Phys. Rev. Lett. **89**, 077203 (2002).

[161] M. Matsumoto, B. Normand, T. M. Rice, and M. Sigrist, "*Field- and pressure-induced magnetic quantum phase transitions in* $TlCuCl_3$," Phys. Rev. B **69**, 054423 (2004).

[162] M. Jaime, V. F. Correa, N. Harrison, C. D. Batista, N. Kawashima, Y. Kazuma, G. A. Jorge, R. Stern, I. Heinmaa, S. A. Zvyagin, Y. Sasago, and K. Uchinokura, "*Magnetic-Field-Induced Condensation of Triplons in Han Purple Pigment* $BaCuSi_2O_6$," Phys. Rev. Lett. **93**, 087203 (2004).

[163] S. A. Zvyagin, J. Wosnitza, C. D. Batista, M. Tsukamoto, N. Kawashima, J. Krzystek, V. S. Zapf, M. Jaime, N. F. Oliveira, and A. Paduan-Filho, "*Magnetic Excitations in the Spin-1 Anisotropic Heisenberg Antiferromagnetic Chain System* $NiCl_2{-}4SC(NH_2)_2$," Phys. Rev. Lett. **98**, 047205 (2007).

[164] E. C. Samulon, Y.-J. Jo, P. Sengupta, C. D. Batista, M. Jaime, L. Balicas, and I. R. Fisher, "*Ordered magnetic phases of the frustrated spin-dimer compound* $Ba_3Mn_2O_8$," Phys. Rev. B **77**, 214441 (2008).

[165] H. Tanaka, A. Oosawa, T. Kato, H. Uekusa, Y. Ohashi, K. Kakurai, and A. Hoser, "*Observation of Field-Induced Transverse Néel Ordering in the Spin Gap System* $TlCuCl_3$," J. Phys. Soc. Jpn. **70**, 939 (2001).

[166] M. Klanjšek, H. Mayaffre, C. Berthier, M. Horvatić, B. Chiari, O. Piovesana, P. Bouillot, C. Kollath, E. Orignac, R. Citro, and T. Giamarchi, "*Controlling Luttinger Liquid Physics in Spin Ladders under a Magnetic Field*," Phys. Rev. Lett. **101**, 137207 (2008).

[167] B. Thielemann, C. Rüegg, K. Kiefer, H. M. Rønnow, B. Normand, P. Bouillot, C. Kollath, E. Orignac, R. Citro, T. Giamarchi, A. M. Läuchli, D. Biner, K. W. Krämer, F. Wolff-Fabris, V. S. Zapf, M. Jaime, J. Stahn, N. B. Christensen, B. Grenier, D. F. McMorrow, and J. Mesot, "*Field-controlled magnetic order in the quantum spin-ladder system* $(Hpip)_2CuBr_4$," Phys. Rev. B **79**, 020408 (2009).

[168] T. Kawamata, N. Sugawara, M. Uesaka, N. Kaneko, T. Kajiwara, H. Yamane, K. Koyama, K. Kudo, N. Kobayashi, and Y. Koike, "*Single-crystal growth of* $Pb_2V_3O_9$ *and the Bose-Einstein condensed state of triplons studied by thermal conductivity, specific heat and magnetization measurements*," J. Phys. Conf. Ser **150**, 042087 (2009).

[169] A. A. Aczel, Y. Kohama, C. Marcenat, F. Weickert, M. Jaime, O. E. Ayala-Valenzuela, R. D. McDonald, S. D. Selesnic, H. A. Dabkowska, and G. M. Luke, "*Field-Induced Bose-Einstein Condensation of Triplons up to* 8 K *in* $Sr_3Cr_2O_8$," Phys. Rev. Lett. **103**, 207203 (2009).

[170] A. A. Aczel, Y. Kohama, M. Jaime, K. Ninios, H. B. Chan, L. Balicas, H. A. Dabkowska, and G. M. Luke, "*Bose-Einstein condensation of triplons in* $Ba_3Cr_2O_8$," Phys. Rev. B **79**, 100409 (2009).

[171] D. Schmidiger, P. Bouillot, S. Mühlbauer, S. Gvasaliya, C. Kollath, T. Giamarchi, and A. Zheludev, "*Spectral and Thermodynamic Properties of a Strong-Leg Quantum Spin Ladder*," Phys. Rev. Lett. **108**, 167201 (2012).

[172] W. Keesom, *Helium* (Amsterdam, 1942).

[173] M. Jeong, H. Mayaffre, C. Berthier, D. Schmidiger, A. Zheludev, and M. Horvatić, "*Attractive Tomonaga-Luttinger Liquid in a Quantum Spin Ladder*," Phys. Rev. Lett. **111**, 106404 (2013).

[174] R. Blinder, M. Dupont, S. Mukhopadhyay, M. S. Grbić, N. Laflorencie, S. Capponi, H. Mayaffre, C. Berthier, A. Paduan-Filho, and M. Horvatić, "*Nuclear magnetic resonance study of the magnetic-field-induced ordered phase in the* $NiCl_2{-}4SC(NH_2)_2$ *compound*," Phys. Rev. B **95**, 020404 (2017).

[175] M. Campostrini, M. Hasenbusch, A. Pelissetto, and E. Vicari, "*Theoretical estimates of the critical exponents of the superfluid transition in* ^{4}He *by lattice methods*," Phys. Rev. B **74**, 144506 (2006).

[176] K. Huang and C. N. Yang, "*Quantum-Mechanical Many-Body Problem with Hard-Sphere Interaction*," Phys. Rev. **105**, 767 (1957).

[177] V. N. Popov, *Functional Integrals and Collective Excitations*, Cambridge Monographs on Mathematical Physics (Cambridge University Press, 1988).

[178] S. Sachdev, T. Senthil, and R. Shankar, "*Finite-temperature properties of quantum antiferromagnets in a uniform magnetic field in one and two dimensions*," Phys. Rev. B **50**, 258 (1994).

[179] I. P. McCulloch, "*From density-matrix renormalization group to matrix product states*," J. Stat. Mech. Theory Exp. **2007**, P10014 (2007).

[180] A. W. Sandvik, "*Computational Studies of Quantum Spin Systems*," AIP Conf. Proc. **1297**, 135 (2010).

[181] E. Pavarini, E. Koch, and U. Schollwöck, eds., *Emergent Phenomena in Correlated Matter*, Modeling and Simulation, Vol. 3 (Forschungszentrum Jülich Zentralbibliothek, Verlag, Jülich, 2013).

[182] E. Stoudenmire and S. R. White, "*Studying Two-Dimensional Systems with the Density Matrix Renormalization Group*," Annu. Rev. Condens. Matter Phys. **3**, 111 (2012).

[183] R. Penrose, "*Applications of negative dimensional tensors*," Combinatorial mathematics and its applications **1**, 221 (1971).

[184] G. M. Crosswhite and D. Bacon, "*Finite automata for caching in matrix product algorithms*," Phys. Rev. A **78**, 012356 (2008).

[185] G. M. Crosswhite, A. C. Doherty, and G. Vidal, "*Applying matrix product operators to model systems with long-range interactions*," Phys. Rev. B **78**, 035116 (2008).

[186] B. Pirvu, V. Murg, J. I. Cirac, and F. Verstraete, "*Matrix product operator representations*," New J. Phys. **12**, 025012 (2010).

[187] F. Fröwis, V. Nebendahl, and W. Dür, "*Tensor operators: Constructions and applications for long-range interaction systems*," Phys. Rev. A **81**, 062337 (2010).

[188] S. Singh, R. N. C. Pfeifer, and G. Vidal, "*Tensor network decompositions in the presence of a global symmetry*," Phys. Rev. A **82**, 050301 (2010).

[189] S. Singh, R. N. C. Pfeifer, and G. Vidal, "*Tensor network states and algorithms in the presence of a global U(1) symmetry*," Phys. Rev. B **83**, 115125 (2011).

[190] A. Weichselbaum, "*Non-abelian symmetries in tensor networks: A quantum symmetry space approach*," Ann. Phys. **327**, 2972 (2012).

[191] M. B. Hastings, "*An area law for one-dimensional quantum systems*," J. Stat. Mech. Theory Exp. **2007**, P08024 (2007).

[192] "*ITensor library*," http://itensor.org .

[193] M. Troyer and U.-J. Wiese, "*Computational Complexity and Fundamental Limitations to Fermionic Quantum Monte Carlo Simulations*," Phys. Rev. Lett. **94**, 170201 (2005).

[194] A. W. Sandvik, "*Finite-size scaling of the ground-state parameters of the two-dimensional Heisenberg model*," Phys. Rev. B **56**, 11678 (1997).

[195] A. W. Sandvik, "*Stochastic series expansion method with operator-loop update*," Phys. Rev. B **59**, R14157 (1999).

[196] N. Prokof'ev, B. Svistunov, and I. Tupitsyn, "*"Worm" algorithm in quantum Monte Carlo simulations*," Phys. Lett. A **238**, 253 (1998).

[197] N. V. Prokof'ev, B. V. Svistunov, and I. S. Tupitsyn, "*Exact, complete, and universal continuous-time worldline Monte Carlo approach to the statistics of discrete quantum systems*," J. Exp. Theor. Phys. **87**, 310 (1998).

[198] O. F. Syljuåsen and A. W. Sandvik, "*Quantum Monte Carlo with directed loops*," Phys. Rev. E **66**, 046701 (2002).

[199] K. Harada and N. Kawashima, "*Coarse-grained loop algorithms for Monte Carlo simulation of quantum spin systems*," Phys. Rev. E **66**, 056705 (2002).

[200] O. F. Syljuåsen, "*Directed loop updates for quantum lattice models*," Phys. Rev. E **67**, 046701 (2003).

[201] F. Alet and E. S. Sørensen, "*Directed geometrical worm algorithm applied to the quantum rotor model*," Phys. Rev. E **68**, 026702 (2003).

[202] M. V. Zyubin and V. A. Kashurnikov, "*Universal stochastic series expansion algorithm for Heisenberg model and Bose-Hubbard model with interaction*," Phys. Rev. E **69**, 036701 (2004).

[203] V. Ambegaokar and M. Troyer, "*Estimating errors reliably in Monte Carlo simulations of the Ehrenfest model*," Am. J. Phys. **78**, 150 (2010).

[204] M. Jeong, H. Mayaffre, C. Berthier, D. Schmidiger, A. Zheludev, and M. Horvatić, "*Magnetic-Order Crossover in Coupled Spin Ladders*," Phys. Rev. Lett. **118**, 167206 (2017).

[205] T. Hong, Y. H. Kim, C. Hotta, Y. Takano, G. Tremelling, M. M. Turnbull, C. P. Landee, H.-J. Kang, N. B. Christensen, K. Lefmann, K. P. Schmidt, G. S. Uhrig, and C. Broholm, "*Field-Induced Tomonaga-Luttinger Liquid Phase of a Two-Leg Spin−1/2 Ladder with Strong Leg Interactions*," Phys. Rev. Lett. **105**, 137207 (2010).

[206] D. Schmidiger, P. Bouillot, T. Guidi, R. Bewley, C. Kollath, T. Giamarchi, and A. Zheludev, "*Spectrum of a Magnetized Strong-Leg Quantum Spin Ladder*," Phys. Rev. Lett. **111**, 107202 (2013).

[207] D. Schmidiger, S. Mühlbauer, A. Zheludev, P. Bouillot, T. Giamarchi, C. Kollath, G. Ehlers, and A. M. Tsvelik, "*Symmetric and asymmetric excitations of a strong-leg quantum spin ladder*," Phys. Rev. B **88**, 094411 (2013).

[208] V. N. Glazkov, M. Fayzullin, Y. Krasnikova, G. Skoblin, D. Schmidiger, S. Mühlbauer, and A. Zheludev, "*ESR study of the spin ladder with uniform Dzyaloshinskii-Moriya interaction*," Phys. Rev. B **92**, 184403 (2015).

[209] M. Ozerov, M. Maksymenko, J. Wosnitza, A. Honecker, C. P. Landee, M. M. Turnbull, S. C. Furuya, T. Giamarchi, and S. A. Zvyagin, "*Electron spin resonance modes in a strong-leg ladder in the Tomonaga-Luttinger liquid phase*," Phys. Rev. B **92**, 241113 (2015).

[210] P. Bouillot, C. Kollath, A. M. Läuchli, M. Zvonarev, B. Thielemann, C. Rüegg, E. Orignac, R. Citro, M. Klanjšek, C. Berthier, M. Horvatić, and T. Giamarchi, "*Statics and dynamics of weakly coupled antiferromagnetic spin-$\frac{1}{2}$ ladders in a magnetic field*," Phys. Rev. B **83**, 054407 (2011).

[211] D. J. Scalapino, Y. Imry, and P. Pincus, "*Generalized Ginzburg-Landau theory of pseudo-one-dimensional systems*," Phys. Rev. B **11**, 2042 (1975).

[212] H. J. Schulz, "*Dynamics of Coupled Quantum Spin Chains*," Phys. Rev. Lett. **77**, 2790 (1996).

[213] V. Berezinskii, "*Destruction of long-range order in one-dimensional and two-dimensional systems having a continuous symmetry group I. Classical systems*," Sov. Phys. JETP **32**, 493 (1971).

[214] J. M. Kosterlitz and D. J. Thouless, "*Ordering, metastability and phase transitions in two-dimensional systems*," J. Phys. C **6**, 1181 (1973).

[215] J. M. Kosterlitz, "*The critical properties of the two-dimensional xy model*," J. Phys. C: Solid State Phys. **7**, 1046 (1974).

[216] M. Hasenbusch, "*The two-dimensional XY model at the transition temperature: a high-precision Monte Carlo study*," J. Phys. A **38**, 5869 (2005).

[217] Laflorencie, Nicolas, "*Sliding phase in randomly stacked 2d superfluids/superconductors*," EPL **99**, 66001 (2012).

[218] R. P. Feynman, *Statistical Mechanics: A Set of Lectures*, 2nd ed. (Advanced Book Classics, Perseus, New York, 1998).

[219] T. Sakai and M. Takahashi, "*The Ground State of Quasi-One-Dimensional Heisenberg Antiferromagnets*," J. Phys. Soc. Jpn. **58**, 3131 (1989).

[220] S. Lukyanov, "*Form Factors of Exponential Fields in the Sine–Gordon Model*," Mod. Phys. Lett. A **12**, 2543 (1997).

[221] M. Azzouz and B. Douçot, "*Effect of small interchain coupling on one-dimensional antiferromagnetic quantum Heisenberg spin systems: The integer-spin case*," Phys. Rev. B **47**, 8660 (1993).

[222] A. Parola, S. Sorella, and Q. F. Zhong, "*Realization of a spin liquid in a two dimensional quantum antiferromagnet*," Phys. Rev. Lett. **71**, 4393 (1993).

[223] I. Affeck, M. P. Gelfand, and R. R. P. Singh, "*A plane of weakly coupled Heisenberg chains: theoretical arguments and numerical calculations*," J. Phys. A **27**, 7313 (1994).

[224] T. Coletta, N. Laflorencie, and F. Mila, "*Semiclassical approach to ground-state properties of hard-core bosons in two dimensions*," Phys. Rev. B **85**, 104421 (2012).

[225] B. Bauer, L. D. Carr, H. G. Evertz, A. Feiguin, J. Freire, S. Fuchs, L. Gamper, J. Gukelberger, E. Gull, S. Guertler, A. Hehn, R. Igarashi, S. V. Isakov, D. Koop, P. N. Ma, P. Mates, H. Matsuo, O. Parcollet, G. Pawłowski, J. D. Picon, L. Pollet, E. Santos, V. W. Scarola, U. Schollwöck, C. Silva, B. Surer, S. Todo, S. Trebst, M. Troyer, M. L. Wall, P. Werner, and S. Wessel, "*The ALPS project release 2.0: open source software for strongly correlated systems*," J. Stat. Mech. Theory Exp. **2011**, P05001 (2011).

[226] A. W. Sandvik, "*Multichain Mean-Field Theory of Quasi-One-Dimensional Quantum Spin Systems*," Phys. Rev. Lett. **83**, 3069 (1999).

[227] S. R. White and A. L. Chernyshev, "*Neél Order in Square and Triangular Lattice Heisenberg Models*," Phys. Rev. Lett. **99**, 127004 (2007).

[228] B. N. Figgis and P. A. Reynolds, "*The charge density in dichlorotetrakis(thiourea)nickel(II),* $[NiSC(NH_2)_2 4Cl_2]$*: a contrast between spectroscopy and diffraction*," J. Chem. Soc., Dalton Trans. , 125 (1986).

[229] N. Tsyrulin, C. D. Batista, V. S. Zapf, M. Jaime, B. R. Hansen, C. Niedermayer, K. C. Rule, K. Habicht, K. Prokes, K. Kiefer, E. Ressouche, A. Paduan-Filho, and M. Kenzelmann, "*Neutron study of the magnetism in* $NiCl_2{-}4SC(NH_2)_2$," J. Phys. Condens. Matter **25**, 216008 (2013).

[230] V. S. Zapf, D. Zocco, B. R. Hansen, M. Jaime, N. Harrison, C. D. Batista, M. Kenzelmann, C. Niedermayer, A. Lacerda, and A. Paduan-Filho, "*Bose-Einstein Condensation of* $S = 1$ *Nickel Spin Degrees of Freedom in* $NiCl_2{-}4SC(NH_2)_2$," Phys. Rev. Lett. **96**, 077204 (2006).

[231] E. Wulf, D. Hüvonen, R. Schönemann, H. Kühne, T. Herrmannsdörfer, I. Glavatskyy, S. Gerischer, K. Kiefer, S. Gvasaliya, and A. Zheludev, "*Critical exponents and intrinsic broadening of the field-induced transition in* $NiCl_2{-}4SC(NH_2)_2$," Phys. Rev. B **91**, 014406 (2015).

[232] L. Yin, J. S. Xia, V. S. Zapf, N. S. Sullivan, and A. Paduan-Filho, "*Direct Measurement of the Bose-Einstein Condensation Universality Class in* $NiCl_2{-}4SC(NH_2)_2$ *at Ultralow Temperatures*," Phys. Rev. Lett. **101**, 187205 (2008).

[233] V. S. Zapf, V. F. Correa, C. D. Batista, T. P. Murphy, E. D. Palm, M. Jaime, S. Tozer, A. Lacerda, and A. Paduan-Filho, "*Magnetostriction in the Bose-Einstein condensate quantum magnet* $NiCl_2{-}4SC(NH_2)_2$," J. Appl. Phys **101**, 09E106 (2007).

[234] O. Chiatti, S. Zherlitsyn, A. Sytcheva, J. Wosnitza, A. A. Zvyagin, V. S. Zapf, M. Jaime, and A. Paduan-Filho, "*Ultrasonic investigation of* $NiCl_2{-}4SC(NH_2)_2$," J. Phys. Conf. Ser **150**, 042016 (2009).

[235] H. J. Schulz, "*Phase diagrams and correlation exponents for quantum spin chains of arbitrary spin quantum number*," Phys. Rev. B **34**, 6372 (1986).

[236] A. Langari, F. Pollmann, and M. Siahatgar, "*Ground-state fidelity of the spin-1 Heisenberg chain with single ion anisotropy: quantum renormalization group and exact diagonalization approaches*," J. Phys. Condens. Matter **25**, 406002 (2013).

[237] N. Papanicolaou, A. Orendáčová, and M. Orendáč, "*Electron-spin resonance in spin-1 planar magnetic chains*," Phys. Rev. B **56**, 8786 (1997).

[238] T. Hikihara and A. Furusaki, "*Spin correlations in the two-leg antiferromagnetic ladder in a magnetic field*," Phys. Rev. B **63**, 134438 (2001).

[239] T. Hikihara and A. Furusaki, "*Correlation amplitudes for the spin-*$\frac{1}{2}$ XXZ *chain in a magnetic field*," Phys. Rev. B **69**, 064427 (2004).

[240] E. L. Pollock and D. M. Ceperley, "*Path-integral computation of superfluid densities*," Phys. Rev. B **36**, 8343 (1987).

[241] E. Burovski, J. Machta, N. Prokof'ev, and B. Svistunov, "*High-precision measurement of the thermal exponent for the three-dimensional XY universality class*," Phys. Rev. B **74**, 132502 (2006).

[242] K. S. D. Beach, "*Comment on "High Precision Measurement of the Thermal Exponent for the three-dimensional XY Universality Class"*," arXiv:cond-mat/0507541 (2005).

[243] K. Harada, "*Bayesian inference in the scaling analysis of critical phenomena*," Phys. Rev. E **84**, 056704 (2011).

[244] K. Harada, "*Kernel method for corrections to scaling*," Phys. Rev. E **92**, 012106 (2015).

[245] V. Y. Irkhin and A. A. Katanin, "*Calculation of Neel temperature for* $S = 1/2$ *Heisenberg quasi-one-dimensional antiferromagnets*," Phys. Rev. B **61**, 6757 (2000).

[246] C. Yasuda, S. Todo, K. Hukushima, F. Alet, M. Keller, M. Troyer, and H. Takayama, "*Néel Temperature of Quasi-Low-Dimensional Heisenberg Antiferromagnets*," Phys. Rev. Lett. **94**, 217201 (2005).

[247] A. Furrer, T. Strässle, and J. Mesot, *Neutron Scattering in Condensed Matter Physics* (World Scientific, 2009).

[248] I. A. Zaliznyak and J. M. Tranquada, "*Neutron Scattering and Its Application to Strongly Correlated Systems*," in *Strongly Correlated Systems: Experimental Techniques*, edited by A. Avella and F. Mancini (Springer Berlin Heidelberg, Berlin, Heidelberg, 2015) pp. 205–235.

[249] A. Abragam and H. Carr, "*The principles of nuclear magnetism*," (1961).

[250] M. Horvatić and C. Berthier, "*NMR Studies of Low-Dimensional Quantum Antiferromagnets*," in *High Magnetic Fields*, Lecture Notes in Physics No. 595, edited by C. Berthier, L. P. Lévy, and G. Martinez (Springer Berlin Heidelberg, 2002) pp. 191–210.

[251] C. P. Slichter, *Principles of magnetic resonance*, Vol. 1 (Springer Science & Business Media, 2013).

[252] T. Jolicœur and O. Golinelli, "*σ-model study of Haldane-gap antiferromagnets*," Phys. Rev. B **50**, 9265 (1994).

[253] S. Sachdev and K. Damle, "*Low Temperature Spin Diffusion in the One-Dimensional Quantum $O(3)$ Nonlinear σ Model*," Phys. Rev. Lett. **78**, 943 (1997).

[254] S. C. Furuya and M. Sato, "*Electron Spin Resonance in Quasi-One-Dimensional Quantum Antiferromagnets: Relevance of Weak Interchain Interactions*," J. Phys. Soc. Jpn. **84**, 033704 (2015).

[255] K. R. Thurber, A. W. Hunt, T. Imai, and F. C. Chou, "*^{17}O NMR Study of $q = 0$ Spin Excitations in a Nearly Ideal $S = 1/2$ $1D$ Heisenberg Antiferromagnet, Sr_2CuO_3, up to 800 K*," Phys. Rev. Lett. **87**, 247202 (2001).

[256] J. Sirker, R. G. Pereira, and I. Affleck, "*Diffusion and Ballistic Transport in One-Dimensional Quantum Systems*," Phys. Rev. Lett. **103**, 216602 (2009).

[257] J. Sirker, R. G. Pereira, and I. Affleck, "*Conservation laws, integrability, and transport in one-dimensional quantum systems*," Phys. Rev. B **83**, 035115 (2011).

[258] E. Coira, *Numerical study of thermal effects in low dimensional quantum spin systems*, Ph.D. thesis, University of Geneva (2016).

[259] M. Jarrell and J. Gubernatis, "*Bayesian inference and the analytic continuation of imaginary-time quantum Monte Carlo data*," Phys. Rep. **269**, 133 (1996).

[260] A. W. Sandvik, "*Constrained sampling method for analytic continuation*," Phys. Rev. E **94**, 063308 (2016).

[261] Y. Q. Qin, B. Normand, A. W. Sandvik, and Z. Y. Meng, "*Amplitude Mode in Three-Dimensional Dimerized Antiferromagnets*," Phys. Rev. Lett. **118**, 147207 (2017).

[262] H. Shao, Y. Q. Qin, S. Capponi, S. Chesi, Z. Y. Meng, and A. W. Sandvik, "*Nearly Deconfined Spinon Excitations in the Square-Lattice Spin-1/2 Heisenberg Antiferromagnet*," Phys. Rev. X **7**, 041072 (2017).

[263] M. Suzuki, "*Relationship between d-Dimensional Quantal Spin Systems and (d+1)-Dimensional Ising SystemsEquivalence, Critical Exponents and Systematic Approximants of the Partition Function and Spin Correlations*," Progr. Theor. Exp. Phys. **56**, 1454 (1976).

[264] M. Suzuki, "*General theory of fractal path integrals with applications to many-body theories and statistical physics*," J. Math. Phys. **32**, 400 (1991).

[265] N. Hatano and M. Suzuki, "*Finding Exponential Product Formulas of Higher Orders*," in *Quantum Annealing and Other Optimization Methods*, edited by A. Das and B. K. Chakrabarti (Springer Berlin Heidelberg, Berlin, Heidelberg, 2005) pp. 37–68.

[266] G. Vidal, "*Efficient Simulation of One-Dimensional Quantum Many-Body Systems*," Phys. Rev. Lett. **93**, 040502 (2004).

[267] T. Barthel, "*Precise evaluation of thermal response functions by optimized density matrix renormalization group schemes*," New J. Phys. **15**, 073010 (2013).

[268] M. Binder and T. Barthel, "*Minimally entangled typical thermal states versus matrix product purifications for the simulation of equilibrium states and time evolution*," Phys. Rev. B **92**, 125119 (2015).

[269] J. Kokalj and P. Prelovšek, "*Finite-temperature dynamics with the density-matrix renormalization group method*," Phys. Rev. B **80**, 205117 (2009).

[270] F. Verstraete, J. J. García-Ripoll, and J. I. Cirac, "*Matrix Product Density Operators: Simulation of Finite-Temperature and Dissipative Systems*," Phys. Rev. Lett. **93**, 207204 (2004).

[271] S. R. White, "*Minimally Entangled Typical Quantum States at Finite Temperature*," Phys. Rev. Lett. **102**, 190601 (2009).

[272] E. M. Stoudenmire and S. R. White, "*Minimally entangled typical thermal state algorithms*," New J. Phys. **12**, 055026 (2010).

[273] C. Karrasch, J. H. Bardarson, and J. E. Moore, "*Reducing the numerical effort of finite-temperature density matrix renormalization group calculations*," New J. Phys. **15**, 083031 (2013).

[274] J. Hauschild, E. Leviatan, J. H. Bardarson, E. Altman, M. P. Zaletel, and F. Pollmann, "*Finding purifications with minimal entanglement*," arXiv:cond-mat/1711.01288 (2017).

[275] A. Weiße, G. Wellein, A. Alvermann, and H. Fehske, "*The kernel polynomial method*," Rev. Mod. Phys. **78**, 275 (2006).

[276] A. Holzner, A. Weichselbaum, I. P. McCulloch, U. Schollwöck, and J. von Delft, "*Chebyshev matrix product state approach for spectral functions*," Phys. Rev. B **83**, 195115 (2011).

[277] A. Braun and P. Schmitteckert, "*Numerical evaluation of Green's functions based on the Chebyshev expansion*," Phys. Rev. B **90**, 165112 (2014).

[278] F. A. Wolf, I. P. McCulloch, O. Parcollet, and U. Schollwöck, "*Chebyshev matrix product state impurity solver for dynamical mean-field theory*," Phys. Rev. B **90**, 115124 (2014).

[279] A. C. Tiegel, S. R. Manmana, T. Pruschke, and A. Honecker, "*Matrix product state formulation of frequency-space dynamics at finite temperatures*," Phys. Rev. B **90**, 060406 (2014).

[280] A. C. Tiegel, S. R. Manmana, T. Pruschke, and A. Honecker, "*Erratum: Matrix product state formulation of frequency-space dynamics at finite temperatures [Phys. Rev. B 90, 060406(R) (2014)]*," Phys. Rev. B **94**, 179908(E) (2016).

[281] A. Dorneich and M. Troyer, "*Accessing the dynamics of large many-particle systems using the stochastic series expansion*," Phys. Rev. E **64**, 066701 (2001).

[282] S. I. Kabanikhin, "*Definitions and examples of inverse and ill-posed problems*," Journal of Inverse and Ill-Posed Problems **16**, 317 (2008).

[283] C. E. Creffield, E. G. Klepfish, E. R. Pike, and S. Sarkar, "*Spectral Weight Function for the Half-Filled Hubbard Model: A Singular Value Decomposition Approach*," Phys. Rev. Lett. **75**, 517 (1995).

[284] O. Gunnarsson, M. W. Haverkort, and G. Sangiovanni, "*Analytical continuation of imaginary axis data for optical conductivity*," Phys. Rev. B **82**, 165125 (2010).

[285] C. Lawson and R. Hanson, *Solving Least Squares Problems*, Classics in Applied Mathematics (Society for Industrial and Applied Mathematics, 1995).

[286] N. V. Prokof'ev and B. V. Svistunov, "*Spectral analysis by the method of consistent constraints*," JETP Lett. **97**, 649 (2013).

[287] H. J. Vidberg and J. W. Serene, "*Solving the Eliashberg equations by means ofN-point Padé approximants*," J. Low Temp. Phys. **29**, 179 (1977).

[288] G. Baker and P. Graves-Morris, *Padé Approximants*, Encyclopedia of Mathematics an (Cambridge University Press, 1996).

[289] J. Schött, I. L. M. Locht, E. Lundin, O. Grånäs, O. Eriksson, and I. Di Marco, "*Analytic continuation by averaging Padé approximants*," Phys. Rev. B **93**, 075104 (2016).

[290] S. F. Gull and J. Skilling, "*Maximum entropy method in image processing*," IEE PROC-F **131**, 646 (1984).

[291] R. N. Silver, D. S. Sivia, and J. E. Gubernatis, "*Maximum-entropy method for analytic continuation of quantum Monte Carlo data*," Phys. Rev. B **41**, 2380 (1990).

[292] R. K. Bryan, "*Maximum entropy analysis of oversampled data problems*," Eur. Biophys. J. **18**, 165 (1990).

[293] J. E. Gubernatis, M. Jarrell, R. N. Silver, and D. S. Sivia, "*Quantum Monte Carlo simulations and maximum entropy: Dynamics from imaginary-time data*," Phys. Rev. B **44**, 6011 (1991).

[294] A. Dirks, P. Werner, M. Jarrell, and T. Pruschke, "*Continuous-time quantum Monte Carlo and maximum entropy approach to an imaginary-time formulation of strongly correlated steady-state transport*," Phys. Rev. E **82**, 026701 (2010).

[295] H. B. Schüttler and D. J. Scalapino, "*Monte Carlo studies of the dynamical response of quantum many-body systems*," Phys. Rev. B **34**, 4744 (1986).

[296] A. W. Sandvik, "*Stochastic method for analytic continuation of quantum Monte Carlo data*," Phys. Rev. B **57**, 10287 (1998).

[297] K. S. D. Beach, "*Identifying the maximum entropy method as a special limit of stochastic analytic continuation*," arXiv:cond-mat/0403055 (2004).

[298] O. F. Syljuåsen, "*Using the average spectrum method to extract dynamics from quantum Monte Carlo simulations*," Phys. Rev. B **78**, 174429 (2008).

[299] S. Fuchs, T. Pruschke, and M. Jarrell, "*Analytic continuation of quantum Monte Carlo data by stochastic analytical inference*," Phys. Rev. E **81**, 056701 (2010).

[300] M. Azuma, Z. Hiroi, M. Takano, K. Ishida, and Y. Kitaoka, "*Observation of a Spin Gap in* $SrCu_2O_3$ *Comprising Spin-½ Quasi-1D Two-Leg Ladders*," Phys. Rev. Lett. **73**, 3463 (1994).

[301] L. K. Alexander, J. Bobroff, A. V. Mahajan, B. Koteswararao, N. Laflorencie, and F. Alet, "*Impurity effects in coupled-ladder* $BiCu_2PO_6$ *studied by NMR and quantum Monte Carlo simulations*," Phys. Rev. B **81**, 054438 (2010).

[302] K. Magishi, S. Matsumoto, Y. Kitaoka, K. Ishida, K. Asayama, M. Uehara, T. Nagata, and J. Akimitsu, "*Spin gap and dynamics in* $Sr_{14-x}Ca_xCu_{24}O_{41}$ *comprising hole-doped two-leg spin ladders:* Cu *NMR study on single crystals*," Phys. Rev. B **57**, 11533 (1998).

[303] T. Shimizu, D. E. MacLaughlin, P. C. Hammel, J. D. Thompson, and S.-W. Cheong, "*Spin susceptibility and low-lying excitations in the Haldane-gap compound* Y_2BaNiO_5," Phys. Rev. B **52**, R9835 (1995).

[304] N. Ahmed, P. Khuntia, K. M. Ranjith, H. Rosner, M. Baenitz, A. A. Tsirlin, and R. Nath, "*Alternating spin chain compound* $AgVOAsO_4$ *probed by* ^{75}As *NMR*," Phys. Rev. B **96**, 224423 (2017).

[305] S. Sachdev, "*NMR relaxation in half-integer antiferromagnetic spin chains*," Phys. Rev. B **50**, 13006 (1994).

[306] A. W. Sandvik, "*NMR relaxation rates for the spin-1/2 Heisenberg chain*," Phys. Rev. B **52**, R9831 (1995).

[307] O. A. Starykh, A. W. Sandvik, and R. R. P. Singh, "*Dynamics of the spin-*$\frac{1}{2}$ *Heisenberg chain at intermediate temperatures*," Phys. Rev. B **55**, 14953 (1997).

[308] V. Barzykin, "*NMR relaxation rates in a spin-*$\frac{1}{2}$ *antiferromagnetic chain*," Phys. Rev. B **63**, 140412 (2001).

[309] M. Takigawa, O. A. Starykh, A. W. Sandvik, and R. R. P. Singh, "*Nuclear relaxation in the spin-*1/2 *antiferromagnetic chain compound* Sr_2CuO_3 : *Comparison between theories and experiments*," Phys. Rev. B **56**, 13681 (1997).

[310] T. Goto, T. Ishikawa, Y. Shimaoka, and Y. Fujii, "*Quantum spin dynamics studied by the nuclear magnetic relaxation of protons in the Haldane-gap system* $(CH_3)_4NNi(NO_2)_3$," Phys. Rev. B **73**, 214406 (2006).

[311] K. Izumi, T. Goto, Y. Hosokoshi, and J.-P. Boucher, "*Nuclear magnetic relaxation of* ^{19}F *in S=1/2 bond-alternating organic compound* F_5PNN," Physica B **329-333**, 1191 (2003).

[312] E. Orignac, R. Citro, and T. Giamarchi, "*Critical properties and Bose-Einstein condensation in dimer spin systems*," Phys. Rev. B **75**, 140403 (2007).

[313] H.-A. Krug von Nidda, N. Büttgen, and A. Loidl, "*Magnetic resonance in quantum spin chains*," Eur. Phys. J. Spec. Top. **180**, 161 (2009).

[314] Y. Ihara, P. Wzietek, H. Alloul, M. H. Rümmeli, T. Pichler, and F. Simon, "*Incidence of the Tomonaga-Luttinger liquid state on the NMR spin-lattice relaxation in carbon nanotubes*," EPL **90**, 17004 (2010).

[315] H. Z. Zhi, T. Imai, F. L. Ning, J.-K. Bao, and G.-H. Cao, "*NMR Investigation of the Quasi-One-Dimensional Superconductor* $K_2Cr_3As_3$," Phys. Rev. Lett. **114**, 147004 (2015).

[316] S. Mukhopadhyay, M. Klanjšek, M. S. Grbić, R. Blinder, H. Mayaffre, C. Berthier, M. Horvatić, M. A. Continentino, A. Paduan-Filho, B. Chiari, and O. Piovesana, "*Quantum-Critical Spin Dynamics in Quasi-One-Dimensional Antiferromagnets*," Phys. Rev. Lett. **109**, 177206 (2012).

[317] M. Klanjšek, D. Arčon, A. Sans, P. Adler, M. Jansen, and C. Felser, "*Phonon-Modulated Magnetic Interactions and Spin Tomonaga-Luttinger Liquid in the p-Orbital Antiferromagnet* CsO_2," Phys. Rev. Lett. **115**, 057205 (2015).

[318] M. Klanjšek, M. Horvatić, S. Krämer, S. Mukhopadhyay, H. Mayaffre, C. Berthier, E. Canévet, B. Grenier, P. Lejay, and E. Orignac, "*Giant magnetic field dependence of the coupling between spin chains in* $BaCo_2V_2O_8$," Phys. Rev. B **92**, 060408 (2015).

[319] M. Jeong, D. Schmidiger, H. Mayaffre, M. Klanjšek, C. Berthier, W. Knafo, G. Ballon, B. Vignolle, S. Krämer, A. Zheludev, and M. Horvatić, "*Dichotomy between Attractive and Repulsive Tomonaga-Luttinger Liquids in Spin Ladders*," Phys. Rev. Lett. **117**, 106402 (2016).

[320] C. Psaroudaki, J. Herbrych, J. Karadamoglou, P. Prelovšek, X. Zotos, and N. Papanicolaou, "*Effective* $S = \frac{1}{2}$ *description of the* $S = 1$ *chain with strong easy-plane anisotropy*," Phys. Rev. B **89**, 224418 (2014).

[321] C. J. Morningstar and M. Weinstein, "*Contractor renormalization group technology and exact Hamiltonian real-space renormalization group transformations*," Phys. Rev. D **54**, 4131 (1996).

[322] S. Capponi, A. Läuchli, and M. Mambrini, "*Numerical contractor renormalization method for quantum spin models*," Phys. Rev. B **70**, 104424 (2004).

[323] P. Bouillot, *Statics and dynamics of weakly coupled antiferromagnetic spin-1/2 ladders in a magnetic field*, Ph.D. thesis, University of Geneva (2011).

[324] T. Suzuki and S.-i. Suga, "*NMR relaxation of quantum spin chains in magnetic fields*," Phys. Rev. B **74**, 172410 (2006).

[325] S. Katsura, T. Horiguchi, and M. Suzuki, "*Dynamical properties of the isotropic XY model*," Physica **46**, 67 (1970).

[326] J. Stolze, A. Nöppert, and G. Müller, "*Gaussian, exponential, and power-law decay of time-dependent correlation functions in quantum spin chains*," Phys. Rev. B **52**, 4319 (1995).

[327] K. Fabricius and B. M. McCoy, "*Spin diffusion and the spin-1/2* XXZ *chain at* $T = \infty$ *from exact diagonalization*," Phys. Rev. B **57**, 8340 (1998).

[328] J. Sirker, "*Spin diffusion and the anisotropic spin-*$\frac{1}{2}$ *Heisenberg chain*," Phys. Rev. B **73**, 224424 (2006).

[329] V. Barzykin, "*Temperature-dependent logarithmic corrections in the spin-1/2 Heisenberg chain*," J. Phys. Condens. Matter **12**, 2053 (2000).

[330] K. Fabricius, U. Löw, and J. Stolze, "*Dynamic correlations of antiferromagnetic spin- XXZ chains at arbitrary temperature from complete diagonalization*," Phys. Rev. B **55**, 5833 (1997).

[331] T. Moriya, "*Nuclear magnetic relaxation in antiferromagnetics*," Progr. Theor. Exp. Phys. **16**, 23 (1956).

[332] E. Coira, P. Barmettler, T. Giamarchi, and C. Kollath, "*Temperature dependence of the NMR spin-lattice relaxation rate for spin-*$\frac{1}{2}$ *chains*," Phys. Rev. B **94**, 144408 (2016).

[333] A. Rançon and N. Dupuis, "*Kosterlitz-Thouless signatures in the low-temperature phase of layered three-dimensional systems*," Phys. Rev. B **96**, 214512 (2017).

[334] H. Mayaffre, M. Horvatić, C. Berthier, M.-H. Julien, P. Ségransan, L. Lévy, and O. Piovesana, "*NMR Evidence for a "Generalized Spin-Peierls Transition" in the High-Magnetic-Field Phase of the Spin Ladder* $Cu_2(C_5H_{12}N_2)_2Cl_4$," Phys. Rev. Lett. **85**, 4795 (2000).

[335] R. Blinder, *Etude par Résonance Magnétique Nucléaire de nouveaux états quantiques induits sous champ magnétique : condensation de Bose-Einstein dans le composé DTN*, Ph.D. thesis, Université Grenoble Alpes (2015).

[336] Y. Suzumura, "*Collective Modes and Response Functions for the BGD Model*," Progr. Theor. Exp. Phys. **61**, 1 (1979).

[337] P. Donohue, *Transition de Mott dans les échelles*, Ph.D. thesis, Paris XI University (2001).

[338] M. A. Cazalilla, A. F. Ho, and T. Giamarchi, "*Interacting Bose gases in quasi-one-dimensional optical lattices*," New J. Phys. **8**, 158 (2006).

[339] J.-S. You, H. Lee, S. Fang, M. A. Cazalilla, and D.-W. Wang, "*Tuning the Kosterlitz-Thouless transition to zero temperature in anisotropic boson systems*," Phys. Rev. A **86**, 043612 (2012).

[340] M. P. M. den Nijs, "*Derivation of extended scaling relations between critical exponents in two-dimensional models from the one-dimensional Luttinger model*," Phys. Rev. B **23**, 6111 (1981).

[341] M. Karowski and P. Weisz, "*Exact Form-Factors in (1+1)-Dimensional Field Theoretic Models with Soliton Behavior*," Nucl. Phys. **B139**, 455 (1978).

[342] F. H. L. Essler and R. M. Konik, "*Finite-temperature dynamical correlations in massive integrable quantum field theories*," J. Stat. Mech: Theory Exp. **2009**, P09018 (2009).

[343] A. H. Bougourzi, M. Couture, and M. Kacir, "*Exact two-spinon dynamical correlation function of the one-dimensional Heisenberg model*," Phys. Rev. B **54**, R12669 (1996).

[344] M. Karbach, G. Müller, A. H. Bougourzi, A. Fledderjohann, and K.-H. Mütter, "*Two-spinon dynamic structure factor of the one-dimensional s= Heisenberg antiferromagnet*," Phys. Rev. B **55**, 12510 (1997).

[345] J.-S. Caux, R. Hagemans, and J. M. Maillet, "*Computation of dynamical correlation functions of Heisenberg chains: the gapless anisotropic regime*," J. Stat. Mech. Theory Exp. **2005**, P09003 (2005).

[346] J.-S. Caux and R. Hagemans, "*The four-spinon dynamical structure factor of the Heisenberg chain*," J. Stat. Mech. Theory Exp. **2006**, P12013 (2006).

[347] T. Yamada, "*Fermi-Liquid Theory of Linear Antiferromagnetic Chains*," Progr. Theor. Exp. Phys. **41**, 880 (1969).

[348] R. G. Pereira, J. Sirker, J.-S. Caux, R. Hagemans, J. M. Maillet, S. R. White, and I. Affleck, "*Dynamical Spin Structure Factor for the Anisotropic Spin-*1/2 *Heisenberg Chain*," Phys. Rev. Lett. **96**, 257202 (2006).

[349] R. G. Pereira, J. Sirker, J.-S. Caux, R. Hagemans, J. M. Maillet, S. R. White, and I. Affleck, "*Dynamical structure factor at small q for the XXZ spin-1/2 chain*," J. Stat. Mech. Theory Exp. **2007**, P08022 (2007).

[350] M. Abramowitz and I. Stegun, eds., *Handbook of mathematical functions* (Dover, New York, 1972).

[351] M. Dupont, S. Capponi, and N. Laflorencie, "*Temperature dependence of the NMR relaxation rate* $1/T_1$ *for quantum spin chains*," Phys. Rev. B **94**, 144409 (2016).

[352] M. Suzuki, "*Static and Dynamic Finite-Size Scaling Theory Based on the Renormalization Group Approach*," Progr. Theor. Exp. Phys. **58**, 1142 (1977).

[353] P. C. Hohenberg and B. I. Halperin, "*Theory of dynamic critical phenomena*," Rev. Mod. Phys. **49**, 435 (1977).

[354] R. Folk and G. Moser, "*Critical dynamics: a field-theoretical approach*," J. Phys. A: Math. Gen. **39**, R207 (2006).

[355] M. Krech and D. P. Landau, "*Spin-dynamics simulations of the three-dimensional* XY *model: Structure factor and transport properties*," Phys. Rev. B **60**, 3375 (1999).

[356] L. M. Jensen, B. J. Kim, and P. Minnhagen, "*Dynamic critical behaviors of three-dimensional XY models related to superconductors/superfluids*," EPL **49**, 644 (2000).

[357] B. I. Halperin and P. C. Hohenberg, "*Hydrodynamic Theory of Spin Waves*," Phys. Rev. **188**, 898 (1969).

[358] A. Sen, H. Suwa, and A. W. Sandvik, "*Velocity of excitations in ordered, disordered, and critical antiferromagnets*," Phys. Rev. B **92**, 195145 (2015).

[359] M. Raczkowski and F. F. Assaad, "*Spinon confinement: Dynamics of weakly coupled Hubbard chains*," Phys. Rev. B **88**, 085120 (2013).

[360] M. Le Bellac, *Quantum and Statistical Field Theory* (Oxford University Press, Oxford, UK, 1992).

[361] S. Todo and K. Kato, "*Cluster Algorithms for General- S Quantum Spin Systems*," Phys. Rev. Lett. **87**, 047203 (2001).

[362] H. Nakano and A. Terai, "*Reexamination of Finite-Lattice Extrapolation of Haldane Gaps*," J. Phys. Soc. Jpn. **78**, 014003 (2009).

[363] J. Becker, T. Köhler, A. C. Tiegel, S. R. Manmana, S. Wessel, and A. Honecker, "*Finite-temperature dynamics and thermal intraband magnon scattering in Haldane spin-one chains*," Phys. Rev. B **96**, 060403 (2017).

[364] F. Lange, S. Ejima, and H. Fehske, "*Finite-temperature dynamic structure factor of the spin-1 XXZ chain with single-ion anisotropy*," Phys. Rev. B **97**, 060403 (2018).

[365] J. Sagi and I. Affleck, "*Theory of nuclear magnetic relaxation in Haldane-gap antiferromagnets*," Phys. Rev. B **53**, 9188 (1996).

[366] R. M. Konik, "*Haldane-gapped spin chains: Exact low-temperature expansions of correlation functions*," Phys. Rev. B **68**, 104435 (2003).

[367] K. Damle and S. Sachdev, "*Universal Relaxational Dynamics of Gapped One-Dimensional Models in the Quantum Sine-Gordon Universality Class*," Phys. Rev. Lett. **95**, 187201 (2005).

[368] R. Steinigeweg and R. Schnalle, "*Projection operator approach to spin diffusion in the anisotropic Heisenberg chain at high temperatures*," Phys. Rev. E **82**, 040103 (2010).

[369] C. Karrasch, J. E. Moore, and F. Heidrich-Meisner, "*Real-time and real-space spin and energy dynamics in one-dimensional spin-*$\frac{1}{2}$ *systems induced by local quantum quenches at finite temperatures*," Phys. Rev. B **89**, 075139 (2014).

[370] D. J. Scalapino, S. R. White, and S. Zhang, "*Insulator, metal, or superconductor: The criteria*," Phys. Rev. B **47**, 7995 (1993).

[371] G. Müller, "*Anomalous Spin Diffusion in Classical Heisenberg Magnets*," Phys. Rev. Lett. **60**, 2785 (1988).

[372] F. Carboni and P. M. Richards, "*Time Correlations and Magnetic-Resonance Linewidth in Finite Heisenberg Linear Chains*," J. Appl. Phys. **39**, 967 (1968).

[373] M. Böhm, V. S. Viswanath, J. Stolze, and G. Müller, "*Spin diffusion in the one-dimensional s=1/2 XXZ model at infinite temperature*," Phys. Rev. B **49**, 15669 (1994).

[374] M. Böhm, H. Leschke, M. Henneke, V. S. Viswanath, J. Stolze, and G. Müller, "*Spectral signature of quantum spin diffusion in dimensions d=1, 2, and 3*," Phys. Rev. B **49**, 417 (1994).

[375] H. Kühne, H.-H. Klauss, S. Grossjohann, W. Brenig, F. J. Litterst, A. P. Reyes, P. L. Kuhns, M. M. Turnbull, and C. P. Landee, "*Quantum critical dynamics of an* $S = \frac{1}{2}$ *antiferromagnetic Heisenberg chain studied by* ^{13}C *NMR spectroscopy*," Phys. Rev. B **80**, 045110 (2009).

[376] M. Takigawa, T. Asano, Y. Ajiro, M. Mekata, and Y. J. Uemura, "*Dynamics in the* $S = 1$ *One-Dimensional Antiferromagnet* $PAgV_2S_6$ *via* ^{31}P *and* ^{51}V *NMR*," Phys. Rev. Lett. **76**, 2173 (1996).

[377] Y. Itoh and H. Yasuoka, "*Interrelation between Dynamical and Static Spin Gaps in Quantum Spin Systems*," J. Phys. Soc. Jpn. **66**, 334 (1997).

[378] M. Takigawa, T. Asano, Y. Ajiro, and M. Mekata, "*Static properties of the S=1 one-dimensional antiferromagnet* $AgVP_2S_6$," Phys. Rev. B **52**, R13087 (1995).

[379] K. Ishida, Y. Kitaoka, K. Asayama, M. Azuma, Z. Hiroi, and M. Takano, "*Spin Gap Behavior in Ladder-Type of Quasi-One-Dimensional Spin (S=1/2) System* $SrCu_2O_3$," J. Phys. Soc. Jpn. **63**, 3222 (1994).

[380] H. Iwase, M. Isobe, Y. Ueda, and H. Yasuoka, "*Observation of Spin Gap in* CaV_2O_5 *by NMR*," J. Phys. Soc. Jpn. **65**, 2397 (1996).

[381] Y. Furukawa, A. Iwai, K. ichi Kumagai, and A. Yakubovsky, "31^P*-NMR Study of Low-Energy Spin Excitations in Spin Ladder* $(VO)_2P_2O_7$ *and Spin Dimer* $VO(HPO_4)0.5H_2O$ *Systems*," J. Phys. Soc. Jpn. **65**, 2393 (1996).

[382] J. Kikuchi, T. Yamauchi, and Y. Ueda, "*High-Temperature Spin Dynamics in the S=1/2 Spin Ladder* $(VO)_2P_2O_7$ *Studied by* ^{31}P *NMR*," J. Phys. Soc. Jpn. **66**, 1622 (1997).

[383] S. Fujimoto, "*Spin Transport Properties of the Quantum One-Dimensional Non-Linear Sigma Model: an Application to Haldane Gap Systems*," J. Phys. Soc. Jpn. **68**, 2810 (1999).

[384] C. S. Lue, C. N. Kuo, T. H. Su, and G. J. Redhammer, "*Spin gap behavior in* $Cu_2Sc_2Ge_4O_{13}$ *studied using* ^{45}Sc *nuclear magnetic resonance*," Phys. Rev. B **75**, 014426 (2007).

[385] P. W. Anderson, "*Absence of Diffusion in Certain Random Lattices*," Phys. Rev. **109**, 1492 (1958).

[386] E. Abrahams, P. W. Anderson, D. C. Licciardello, and T. V. Ramakrishnan, "*Scaling Theory of Localization: Absence of Quantum Diffusion in Two Dimensions*," Phys. Rev. Lett. **42**, 673 (1979).

[387] F. Evers and A. D. Mirlin, "*Anderson transitions*," Rev. Mod. Phys. **80**, 1355 (2008).

[388] A. Lagendijk, B. van Tiggelen, and D. S. Wiersma, "*Fifty years of Anderson localization*," Phys. Today **62**, 24 (2009).

[389] S. V. Kravchenko and M. P. Sarachik, "*Metal–insulator transition in two-dimensional electron systems*," Rep. Prog. Phys. **67**, 1 (2004).

[390] C. D'Errico, E. Lucioni, L. Tanzi, L. Gori, G. Roux, I. P. McCulloch, T. Giamarchi, M. Inguscio, and G. Modugno, "*Observation of a Disordered Bosonic Insulator from Weak to Strong Interactions*," Phys. Rev. Lett. **113**, 095301 (2014).

[391] M. Schreiber, S. S. Hodgman, P. Bordia, H. P. Lüschen, M. H. Fischer, R. Vosk, E. Altman, U. Schneider, and I. Bloch, "*Observation of many-body localization of interacting fermions in a quasirandom optical lattice*," Science **349**, 842 (2015).

[392] J.-Y. Choi, S. Hild, J. Zeiher, P. Schauß, A. Rubio-Abadal, T. Yefsah, V. Khemani, D. A. Huse, I. Bloch, and C. Gross, "*Exploring the many-body localization transition in two dimensions*," Science **352**, 1547 (2016).

[393] B. Sacépé, T. Dubouchet, C. Chapelier, M. Sanquer, M. Ovadia, D. Shahar, M. Feigel'man, and L. Ioffe, "*Localization of preformed Cooper pairs in disordered superconductors*," Nat. Phys. **7**, 239 (2011).

[394] C. Dasgupta and S.-k. Ma, "*Low-temperature properties of the random Heisenberg antiferromagnetic chain*," Phys. Rev. B **22**, 1305 (1980).

[395] D. S. Fisher, "*Random antiferromagnetic quantum spin chains*," Phys. Rev. B **50**, 3799 (1994).

[396] F. Iglói and C. Monthus, "*Strong disorder RG approach of random systems*," Phys. Rep. **412**, 277 (2005).

[397] R. Yu, S. Haas, and T. Roscilde, "*Universal phase diagram of disordered bosons from a doped quantum magnet*," EPL **89**, 10009 (2010).

[398] R. Yu, L. Yin, N. S. Sullivan, J. S. Xia, C. Huan, A. Paduan-Filho, N. F. Oliveira, Jr., S. Haas, A. Steppke, C. F. Miclea, *et al.*, "*Bose glass and Mott glass of quasiparticles in a doped quantum magnet*," Nature **489**, 379 (2012).

[399] R. Yu, C. F. Miclea, F. Weickert, R. Movshovich, A. Paduan-Filho, V. S. Zapf, and T. Roscilde, "*Quantum critical scaling at a Bose-glass/superfluid transition: Theory and experiment for a model quantum magnet*," Phys. Rev. B **86**, 134421 (2012).

[400] L. N. Bulaevskiĭ, A. V. Zvarykina, Y. S. Karimov, R. B. Lyubovskii, and I. F. Shchegolev, "*Magnetic Properties of Linear Conducting Chains*," JEPT **35**, 384 (1972).

[401] L. J. Azevedo and W. G. Clark, "*Very-low-temperature specific heat of quinolinium*$(TCNQ)_2$*, a random-exchange Heisenberg antiferromagnetic chain*," Phys. Rev. B **16**, 3252 (1977).

[402] J. Sanny, G. Grüner, and W. Clark, "*Observation of quasi-universal magnetic behavior in a random exchange Heisenberg antiferromagnetic chain: Neutron irradiated quinolinium* $(TCNQ)_2$," Solid State Commun. **35**, 657 (1980).

[403] H. M. Bozler, C. M. Gould, and W. G. Clark, "*Crossover Behavior of a Random-Exchange Heisenberg Antiferromagnetic Chain at Ultralow Temperatures*," Phys. Rev. Lett. **45**, 1303 (1980).

[404] L. C. Tippie and W. G. Clark, "*Low-temperature magnetism of quinolinium* $(TCNQ)_2$*, a random-exchange Heisenberg antiferromagnetic chain. I. Static properties*," Phys. Rev. B **23**, 5846 (1981).

[405] G. Theodorou and M. H. Cohen, "*Paramagnetic Susceptibility of Disordered* $N-$ methylphenazinium $-$ tetracyanoquinodimethanide," Phys. Rev. Lett. **37**, 1014 (1976).

[406] G. Theodorou, "*Hubbard model for a disordered linear chain: Probability distribution of exchange*," Phys. Rev. B **16**, 2254 (1977).

[407] G. Theodorou, "*Paramagnetic susceptibility of disordered* $N-$ methylphenazinium $-$ tetracyanoquinodimethanide," Phys. Rev. B **16**, 2273 (1977).

[408] A. W. Sandvik, D. J. Scalapino, and P. Henelius, "*Quantum Monte Carlo study of the one-dimensional Hubbard model with random hopping and random potentials*," Phys. Rev. B **50**, 10474 (1994).

[409] T. Masuda, A. Zheludev, K. Uchinokura, J.-H. Chung, and S. Park, "*Dynamics and Scaling in a Quantum Spin Chain Material with Bond Randomness*," Phys. Rev. Lett. **93**, 077206 (2004).

[410] T. Masuda, A. Zheludev, K. Uchinokura, J.-H. Chung, and S. Park, "*Erratum: Dynamics and Scaling in a Quantum Spin Chain Material with Bond Randomness [Phys. Rev. Lett. 93, 077206 (2004)]*," Phys. Rev. Lett. **96**, 169908(E) (2006).

[411] E. Westerberg, A. Furusaki, M. Sigrist, and P. A. Lee, "*Random Quantum Spin Chains: A Real-Space Renormalization Group Study*," Phys. Rev. Lett. **75**, 4302 (1995).

[412] T. N. Nguyen, P. A. Lee, and H.-C. z. Loye, "*Design of a Random Quantum Spin Chain Paramagnet:* $Sr_3CuPt_{0.5}Ir_{0.5}O_6$," Science **271**, 489 (1996).

[413] T. Hikihara, A. Furusaki, and M. Sigrist, "*Numerical renormalization-group study of spin correlations in one-dimensional random spin chains*," Phys. Rev. B **60**, 12116 (1999).

[414] N. Laflorencie, H. Rieger, A. W. Sandvik, and P. Henelius, "*Crossover effects in the random-exchange spin-$\frac{1}{2}$ antiferromagnetic chain*," Phys. Rev. B **70**, 054430 (2004).

[415] J. A. Hoyos, A. P. Vieira, N. Laflorencie, and E. Miranda, "*Correlation amplitude and entanglement entropy in random spin chains*," Phys. Rev. B **76**, 174425 (2007).

[416] Y.-R. Shu, D.-X. Yao, C.-W. Ke, Y.-C. Lin, and A. W. Sandvik, "*Properties of the random-singlet phase: From the disordered Heisenberg chain to an amorphous valence-bond solid*," Phys. Rev. B **94**, 174442 (2016).

[417] D. S. Fisher and M. P. A. Fisher, "*Onset of superfluidity in random media*," Phys. Rev. Lett. **61**, 1847 (1988).

[418] T. Giamarchi and H. J. Schulz, "*Localization and Interaction in One-Dimensional Quantum Fluids*," EPL **3**, 1287 (1987).

[419] T. Giamarchi and H. J. Schulz, "*Anderson localization and interactions in one-dimensional metals*," Phys. Rev. B **37**, 325 (1988).

[420] Z. Ristivojevic, A. Petković, P. Le Doussal, and T. Giamarchi, "*Phase Transition of Interacting Disordered Bosons in One Dimension*," Phys. Rev. Lett. **109**, 026402 (2012).

[421] Z. Ristivojevic, A. Petković, P. Le Doussal, and T. Giamarchi, "*Superfluid/Bose-glass transition in one dimension*," Phys. Rev. B **90**, 125144 (2014).

[422] E. V. H. Doggen, G. Lemarié, S. Capponi, and N. Laflorencie, "*Weak- versus strong-disorder superfluidBose glass transition in one dimension*," Phys. Rev. B **96**, 180202 (2017).

[423] J. P. Álvarez Zúñiga, D. J. Luitz, G. Lemarié, and N. Laflorencie, "*Critical Properties of the SuperfluidBose-Glass Transition in Two Dimensions*," Phys. Rev. Lett. **114**, 155301 (2015).

[424] R. Ng and E. S. Sørensen, "*Quantum Critical Scaling of Dirty Bosons in Two Dimensions*," Phys. Rev. Lett. **114**, 255701 (2015).

[425] V. Gurarie, L. Pollet, N. V. Prokof'ev, B. V. Svistunov, and M. Troyer, "*Phase diagram of the disordered Bose-Hubbard model*," Phys. Rev. B **80**, 214519 (2009).

[426] L. Pollet, N. V. Prokof'ev, B. V. Svistunov, and M. Troyer, "*Absence of a Direct Superfluid to Mott Insulator Transition in Disordered Bose Systems*," Phys. Rev. Lett. **103**, 140402 (2009).

[427] H. Rieger, "*Critical and off-critical singularities in disordered quantum magnets*," Ann. Phys. **7**, 564 (1999).

[428] K. Sheshadri, H. R. Krishnamurthy, R. Pandit, and T. V. Ramakrishnan, "*Superfluid and Insulating Phases in an Interacting-Boson Model: Mean-Field Theory and the RPA*," EPL **22**, 257 (1993).

[429] G. M. Falco, T. Nattermann, and V. L. Pokrovsky, "*Weakly interacting Bose gas in a random environment*," Phys. Rev. B **80**, 104515 (2009).

[430] L. Dell'Anna and M. Fabrizio, "*How localized bosons manage to become superfluid*," J. Stat. Mech. Theory Exp. **2011**, P08004 (2011).

[431] A. E. Niederle and H. Rieger, "*Superfluid clusters, percolation and phase transitions in the disordered, two-dimensional Bose–Hubbard model*," New J. Phys. **15**, 075029 (2013).

[432] S. Krinner, D. Stadler, J. Meineke, J.-P. Brantut, and T. Esslinger, "*Observation of a Fragmented, Strongly Interacting Fermi Gas*," Phys. Rev. Lett. **115**, 045302 (2015).

[433] S. Ospelkaus, C. Ospelkaus, O. Wille, M. Succo, P. Ernst, K. Sengstock, and K. Bongs, "*Localization of Bosonic Atoms by Fermionic Impurities in a Three-Dimensional Optical Lattice*," Phys. Rev. Lett. **96**, 180403 (2006).

[434] Barman, Apurba, Dutta, Sunayana, Khan, Ayan, and Basu, Saurabh, "*Understanding the Bose glass phase via a percolation scenario*," Eur. Phys. J. B **86**, 308 (2013).

[435] M. Gouker and F. Family, "*Evidence for classical critical behavior in long-range site percolation*," Phys. Rev. B **28**, 1449 (1983).

[436] M. B. Isichenko, "*Percolation, statistical topography, and transport in random media*," Rev. Mod. Phys. **64**, 961 (1992).

[437] H. Kuroyanagi, M. Tsukamoto, and M. Tsubota, "*Study of Kosterlitz–Thouless Transition of Bose Systems Governed by a Random Potential Using Quantum Monte Carlo Simulations*," J. Phys. Soc. Jpn. **80**, 034603 (2011).

[438] J. Saliba, P. Lugan, and V. Savona, "*Superfluid-insulator transition of two-dimensional disordered Bose gases*," Phys. Rev. A **90**, 031603 (2014).

[439] D. Finotello, K. A. Gillis, A. Wong, and M. H. W. Chan, "*Sharp Heat-Capacity Signature at the Superfluid Transition of Helium Films in Porous Glasses*," Phys. Rev. Lett. **61**, 1954 (1988).

[440] A. Goldman and Y. Liu, "*The two-dimensional superconductor-insulator transition*," Physica D **83**, 163 (1995), quantum Complexity in Mesoscopic Systems.

[441] B. C. Crooker, B. Hebral, E. N. Smith, Y. Takano, and J. D. Reppy, "*Superfluidity in a Dilute Bose Gas*," Phys. Rev. Lett. **51**, 666 (1983).

[442] J. D. Reppy, "*Superfluid helium in porous media*," J. Low Temp. Phys. **87**, 205 (1992).

[443] P. A. Crowell, J. D. Reppy, S. Mukherjee, J. Ma, M. H. W. Chan, and D. W. Schaefer, "*Critical behavior of superfluid* ^{4}He *films adsorbed in aerogel glass*," Phys. Rev. B **51**, 12721 (1995).

[444] P. A. Crowell, F. W. Van Keuls, and J. D. Reppy, "*Onset of superfluidity in* ^{4}He *films adsorbed on disordered substrates*," Phys. Rev. B **55**, 12620 (1997).

[445] D. Shahar and Z. Ovadyahu, "*Superconductivity near the mobility edge*," Phys. Rev. B **46**, 10917 (1992).

[446] B. Sacépé, C. Chapelier, T. I. Baturina, V. M. Vinokur, M. R. Baklanov, and M. Sanquer, "*Disorder-Induced Inhomogeneities of the Superconducting State Close to the Superconductor-Insulator Transition*," Phys. Rev. Lett. **101**, 157006 (2008).

[447] A. M. Finkel'stein, "*Superconducting transition temperature in amorphous films*," JETP Lett. **45** (1987).

[448] V. F. Gantmakher and V. T. Dolgopolov, "*Superconductor–insulator quantum phase transition*," Phys. Usp. **53**, 1 (2010).

[449] O. Nohadani, S. Wessel, and S. Haas, "*Bose-Glass Phases in Disordered Quantum Magnets*," Phys. Rev. Lett. **95**, 227201 (2005).

[450] K. Hida, "*Field-Induced Multiple Reentrant Quantum Phase Transitions in Randomly Dimerized Antiferromagnetic S=1/2 Heisenberg Chains*," J. Phys. Soc. Jpn. **75**, 074709 (2006).

[451] T. Roscilde and S. Haas, "*Bose–Einstein condensation versus localization of bosonic quasiparticles in disordered weakly-coupled dimer antiferromagnets*," J. Phys. B **39**, S153 (2006).

[452] A. Zheludev and T. Roscilde, "*Dirty-boson physics with magnetic insulators*," C.R. Phys. **14**, 740 (2013).

[453] T. Hong, A. Zheludev, H. Manaka, and L.-P. Regnault, "*Evidence of a magnetic Bose glass in* $(CH_3)_2CHNH_3Cu(Cl_{0.95}Br_{0.05})_3$ *from neutron diffraction*," Phys. Rev. B **81**, 060410 (2010).

[454] F. Yamada, H. Tanaka, T. Ono, and H. Nojiri, "*Transition from Bose glass to a condensate of triplons in* $Tl_{1-x}K_xCuCl_3$," Phys. Rev. B **83**, 020409 (2011).

[455] G. Kamieniarz, R. Matysiak, P. Gegenwart, A. Ochiai, and F. Steglich, "*Bose glass behavior in* $(Yb_{1-x}Lu_x)_4As_3$ *representing randomly diluted quantum spin-*$\frac{1}{2}$ *chains*," Phys. Rev. B **94**, 100403 (2016).

[456] E. Wulf, D. Hüvonen, J.-W. Kim, A. Paduan-Filho, E. Ressouche, S. Gvasaliya, V. Zapf, and A. Zheludev, "*Criticality in a disordered quantum antiferromagnet studied by neutron diffraction*," Phys. Rev. B **88**, 174418 (2013).

[457] K. Damle, O. Motrunich, and D. A. Huse, "*Dynamics and Transport in Random Antiferromagnetic Spin Chains*," Phys. Rev. Lett. **84**, 3434 (2000).

[458] O. Motrunich, K. Damle, and D. A. Huse, "*Dynamics and transport in random quantum systems governed by strong-randomness fixed points*," Phys. Rev. B **63**, 134424 (2001).

[459] T. Shiroka, F. Casola, V. Glazkov, A. Zheludev, K. Prša, H.-R. Ott, and J. Mesot, "*Distribution of NMR Relaxations in a Random Heisenberg Chain*," Phys. Rev. Lett. **106**, 137202 (2011).

[460] J. Herbrych, J. Kokalj, and P. Prelovšek, "*Local Spin Relaxation within the Random Heisenberg Chain*," Phys. Rev. Lett. **111**, 147203 (2013).

[461] J. E. Hirsch and R. Kariotis, "*Spin susceptibilities of a one-dimensional disordered quantum Heisenberg antiferromagnet*," Phys. Rev. B **32**, 7320 (1985).

[462] A. W. Sandvik, "*Classical percolation transition in the diluted two-dimensional* $S = \frac{1}{2}$ *Heisenberg antiferromagnet*," Phys. Rev. B **66**, 024418 (2002).

[463] A. Nocera and G. Alvarez, "*Symmetry-conserving purification of quantum states within the density matrix renormalization group*," Phys. Rev. B **93**, 045137 (2016).

[464] T. Barthel, "*Matrix product purifications for canonical ensembles and quantum number distributions*," Phys. Rev. B **94**, 115157 (2016).

[465] A. Zheludev, T. Masuda, G. Dhalenne, A. Revcolevschi, C. Frost, and T. Perring, "*Scaling of dynamic spin correlations in* $BaCu_2(Si_{0.5}Ge_{0.5})_2O_7$," Phys. Rev. B **75**, 054409 (2007).

[466] D. C. Johnston, "*Stretched exponential relaxation arising from a continuous sum of exponential decays*," Phys. Rev. B **74**, 184430 (2006).

[467] D. C. Johnston, "*Erratum: Stretched exponential relaxation arising from a continuous sum of exponential decays [Phys. Rev. B 74, 184430 (2006)]*," Phys. Rev. B **77**, 179901 (2008).

[468] M. Randeria, N. Trivedi, A. Moreo, and R. T. Scalettar, "*Pairing and spin gap in the normal state of short coherence length superconductors*," Phys. Rev. Lett. **69**, 2001 (1992).

[469] T. Shiroka, F. Casola, W. Lorenz, K. Prša, A. Zheludev, H.-R. Ott, and J. Mesot, "*Impact of strong disorder on the static magnetic properties of the spin-chain compound* $BaCu_2SiGeO_7$," Phys. Rev. B **88**, 054422 (2013).

[470] A. Paduan-Filho, X. Gratens, and N. F. Oliveira, "*Field-induced magnetic ordering in* $NiCl_2 \cdot 4SC(NH_2)_2$," Phys. Rev. B **69**, 020405 (2004).

[471] K. Y. Povarov, E. Wulf, D. Hüvonen, J. Ollivier, A. Paduan-Filho, and A. Zheludev, "*Dynamics of a bond-disordered* $S = 1$ *quantum magnet near* $z = 1$ *criticality*," Phys. Rev. B **92**, 024429 (2015).

[472] A. Orlova, R. Blinder, E. Kermarrec, M. Dupont, N. Laflorencie, S. Capponi, H. Mayaffre, C. Berthier, A. Paduan-Filho, and M. Horvatić, "*Nuclear Magnetic Resonance Reveals Disordered Level-Crossing Physics in the Bose-Glass Regime of the Br-Doped* $Ni(Cl_{1-x}Br_x)_2{-}4SC(NH_2)_2$ *Compound at a High Magnetic Field*," Phys. Rev. Lett. **118**, 067203 (2017).

[473] M.-H. Julien, Z. H. Jang, A. Lascialfari, F. Borsa, M. Horvatić, A. Caneschi, and D. Gatteschi, "*Proton NMR for Measuring Quantum Level Crossing in the Magnetic Molecular Ring* Fe_{10}," Phys. Rev. Lett. **83**, 227 (1999).

[474] E. Micotti, A. Lascialfari, F. Borsa, M. H. Julien, C. Berthier, M. Horvatić, J. van Slageren, and D. Gatteschi, "*Spin dynamics at the level crossing in the molecular antiferromagnetic ring* $[Cr_8F_8Piv_{16}]$ *from proton NMR*," Phys. Rev. B **72**, 020405 (2005).

[475] Y. Deng and H. W. J. Blöte, "*Monte Carlo study of the site-percolation model in two and three dimensions*," Phys. Rev. E **72**, 016126 (2005).

[476] I. M. Lifshitz, "*Energy spectrum structure and quantum states of disordered condensed systems*," Usp. Fiz. Nauk **83**, 617 (1964).

[477] R. Friedberg and J. M. Luttinger, "*Density of electronic energy levels in disordered systems*," Phys. Rev. B **12**, 4460 (1975).

[478] M. Sigrist and A. Furusaki, "*Low-Temperature Properties of the Randomly Depleted Heisenberg Ladder*," J. Phys. Soc. Jpn. **65**, 2385 (1996).

[479] A. Lavarélo, G. Roux, and N. Laflorencie, "*Magnetic responses of randomly depleted spin ladders*," Phys. Rev. B **88**, 134420 (2013).

[480] T. P. Eggarter and R. Riedinger, "*Singular behavior of tight-binding chains with off-diagonal disorder*," Phys. Rev. B **18**, 569 (1978).

[481] C. M. Soukoulis, I. Webman, G. S. Grest, and E. N. Economou, "*Study of electronic states with off-diagonal disorder in two dimensions*," Phys. Rev. B **26**, 1838 (1982).

[482] I. M. Lifshitz, "*Energy spectrum structure and quantum states of disordered condensed systems*," Sov. Phys. Usp. **7**, 549 (1965).

[483] W. Y. Ching and D. L. Huber, "*Numerical studies of energy levels and eigenfunction localization in dilute three-dimensional systems with exponential interactions*," Phys. Rev. B **25**, 1096 (1982).

[484] N. Laflorencie, D. Poilblanc, and A. W. Sandvik, "*Magnetic ordering in a doped frustrated spin-Peierls system*," Phys. Rev. B **69**, 212412 (2004).

[485] N. Laflorencie, S. Wessel, A. Läuchli, and H. Rieger, "*Random-exchange quantum Heisenberg antiferromagnets on a square lattice*," Phys. Rev. B **73**, 060403 (2006).

[486] S. Wessel, B. Normand, M. Sigrist, and S. Haas, "*Order by Disorder from Nonmagnetic Impurities in a Two-Dimensional Quantum Spin Liquid*," Phys. Rev. Lett. **86**, 1086 (2001).

[487] J. Bobroff, N. Laflorencie, L. K. Alexander, A. V. Mahajan, B. Koteswararao, and P. Mendels, "*Impurity-Induced Magnetic Order in Low-Dimensional Spin-Gapped Materials*," Phys. Rev. Lett. **103**, 047201 (2009).

[488] A. Priyadarshee, S. Chandrasekharan, J.-W. Lee, and H. U. Baranger, "*Quantum Phase Transitions of Hard-Core Bosons in Background Potentials*," Phys. Rev. Lett. **97**, 115703 (2006).

[489] P. B. Weichman and R. Mukhopadhyay, "*Critical Dynamics of the Dirty Boson Problem: Revisiting the Equality $z = d$*," Phys. Rev. Lett. **98**, 245701 (2007).

[490] H. Meier and M. Wallin, "*Quantum Critical Dynamics Simulation of Dirty Boson Systems*," Phys. Rev. Lett. **108**, 055701 (2012).

[491] A. B. Harris, "*Effect of random defects on the critical behaviour of Ising models*," J. Phys. C **7**, 1671 (1974).

[492] J. T. Chayes, L. Chayes, D. S. Fisher, and T. Spencer, "*Finite-Size Scaling and Correlation Lengths for Disordered Systems*," Phys. Rev. Lett. **57**, 2999 (1986).

[493] Z. Yao, K. P. C. da Costa, M. Kiselev, and N. Prokof'ev, "*Critical Exponents of the Superfluid-Bose-Glass Transition in Three Dimensions*," Phys. Rev. Lett. **112**, 225301 (2014).

[494] D. Hüvonen, S. Zhao, M. Månsson, T. Yankova, E. Ressouche, C. Niedermayer, M. Laver, S. N. Gvasaliya, and A. Zheludev, "*Field-induced criticality in a gapped quantum magnet with bond disorder*," Phys. Rev. B **85**, 100410 (2012).

[495] P. Hitchcock and E. S. Sørensen, "*Bose-glass to superfluid transition in the three-dimensional Bose-Hubbard model*," Phys. Rev. B **73**, 174523 (2006).

[496] R. Yu, V. Zapf, and T. Roscilde, "*Comment to "Critical Exponents of the Superfluid-Bose Glass Transition in Three-Dimensions" by Z. Yao et al.*" arXiv:1403.6059 (2014).

[497] J. Smith, A. Lee, P. Richerme, B. Neyenhuis, P. W. Hess, P. Hauke, M. Heyl, D. A. Huse, and C. Monroe, "*Many-body localization in a quantum simulator with programmable random disorder*," Nat. Phys. **12**, 907 EP (2016).

[498] P. Bordia, H. P. Lüschen, S. S. Hodgman, M. Schreiber, I. Bloch, and U. Schneider, "*Coupling Identical one-dimensional Many-Body Localized Systems*," Phys. Rev. Lett. **116**, 140401 (2016).

[499] J. Zhang, P. W. Hess, A. Kyprianidis, P. Becker, A. Lee, J. Smith, G. Pagano, I. D. Potirniche, A. C. Potter, A. Vishwanath, N. Y. Yao, and C. Monroe, "*Observation of a discrete time crystal*," Nature **543**, 217 EP (2017).

[500] S. Choi, J. Choi, R. Landig, G. Kucsko, H. Zhou, J. Isoya, F. Jelezko, S. Onoda, H. Sumiya, V. Khemani, C. von Keyserlingk, N. Y. Yao, E. Demler, and M. D. Lukin, "*Observation of discrete time-crystalline order in a disordered dipolar many-body system*," Nature **543**, 221 EP (2017).

[501] P. Jurcevic, H. Shen, P. Hauke, C. Maier, T. Brydges, C. Hempel, B. P. Lanyon, M. Heyl, R. Blatt, and C. F. Roos, "*Direct Observation of Dynamical Quantum Phase Transitions in an Interacting Many-Body System*," Phys. Rev. Lett. **119**, 080501 (2017).

[502] J. Zhang, G. Pagano, P. W. Hess, A. Kyprianidis, P. Becker, H. Kaplan, A. V. Gorshkov, Z. X. Gong, and C. Monroe, "*Observation of a many-body dynamical phase transition with a 53-qubit quantum simulator*," Nature **551**, 601 EP (2017).

[503] N. Fläschner, D. Vogel, M. Tarnowski, B. S. Rem, D. S. Lühmann, M. Heyl, J. C. Budich, L. Mathey, K. Sengstock, and C. Weitenberg, "*Observation of dynamical vortices after quenches in a system with topology*," Nat. Phys. **14**, 265 (2018).

[504] M. Mezard, G. Parisi, and M. Virasoro, *Spin Glass Theory and Beyond: An Introduction to the Replica Method and Its Applications*, World Scientific Lecture Notes in Physics (World Scientific, 1987).

[505] M. Kardar, G. Parisi, and Y.-C. Zhang, "*Dynamic Scaling of Growing Interfaces*," Phys. Rev. Lett. **56**, 889 (1986).

[506] T. Halpin-Healy and Y.-C. Zhang, "*Kinetic roughening phenomena, stochastic growth, directed polymers and all that. Aspects of multidisciplinary statistical mechanics*," Phys. Rep. **254**, 215 (1995).

[507] G. Roux, A. Minguzzi, and T. Roscilde, "*Dynamic structure factor of one-dimensional lattice bosons in a disordered potential: a spectral fingerprint of the Bose-glass phase*," New J. Phys. **15**, 055003 (2013).

[508] R. Nandkishore and D. A. Huse, "*Many-Body Localization and Thermalization in Quantum Statistical Mechanics*," Annu. Rev. Condens. Matter Phys. **6**, 15 (2015).

[509] F. Borgonovi, F. M. Izrailev, L. F. Santos, and V. G. Zelevinsky, "*Quantum chaos and thermalization in isolated systems of interacting particles*," Phys. Rep. **626**, 1 (2016).

[510] L. D'Alessio, Y. Kafri, A. Polkovnikov, and M. Rigol, "*From quantum chaos and eigenstate thermalization to statistical mechanics and thermodynamics*," Adv. Phys. **65**, 239 (2016).

[511] F. Alet and N. Laflorencie, "*Many-body localization: An introduction and selected topics*," C. R. Phys. (2018).

[512] F. Schindler, N. Regnault, and T. Neupert, "*Probing many-body localization with neural networks*," Phys. Rev. B **95**, 245134 (2017).

[513] D.-L. Deng, X. Li, and S. Das Sarma, "*Machine learning topological states*," Phys. Rev. B **96**, 195145 (2017).

[514] Y. Nagai, H. Shen, Y. Qi, J. Liu, and L. Fu, "*Self-learning Monte Carlo method: Continuous-time algorithm*," Phys. Rev. B **96**, 161102 (2017).

[515] E. Stoudenmire and D. J. Schwab, "*Supervised Learning with Tensor Networks*," in *Advances in Neural Information Processing Systems 29* (Curran Associates, Inc., 2016) pp. 4799–4807.

[516] E. M. Stoudenmire, "*Learning relevant features of data with multi-scale tensor networks*," Quantum Sci. Technol. **3**, 034003 (2018).

[517] Y. Liu, X. Zhang, M. Lewenstein, and S.-J. Ran, "*Entanglement-guided architectures of machine learning by quantum tensor network*," arXiv:1803.09111 (2018).

[518] W. Huggins, P. Patel, K. B. Whaley, and E. M. Stoudenmire, "*Towards Quantum Machine Learning with Tensor Networks*," arXiv:1803.11537 (2018).

[519] I. Glasser, N. Pancotti, and J. I. Cirac, "*Supervised learning with generalized tensor networks*," arXiv:1806.05964 (2018).

[520] Z.-Y. Han, J. Wang, H. Fan, L. Wang, and P. Zhang, "*Unsupervised Generative Modeling Using Matrix Product States*," Phys. Rev. X **8**, 031012 (2018).

List of Publications

[1] S. C. Furuya, M. Dupont, S. Capponi, N. Laflorencie, and T. Giamarchi"*Dimensional modulation of spontaneous magnetic order in quasi-two-dimensional quantum antiferromagnets*," Phys. Rev. B **94**, 144403 (2016).

[2] M. Dupont, S. Capponi, and N. Laflorencie, "*Temperature dependence of the NMR relaxation rate* $1/T_1$ *for quantum spin chains*," Phys. Rev. B **94**, 144409 (2016).

[3] R. Blinder, M. Dupont, S. Mukhopadhyay, M. S. Grbić, N. Laflorencie, S. Capponi, H. Mayaffre, C. Berthier, A. Paduan-Filho, and M. Horvatić, "*Nuclear magnetic resonance study of the magnetic-field-induced ordered phase in the* $NiCl_2{-}4SC(NH_2)_2$ *compound*," Phys. Rev. B **95**, 020404(R) (2017).

[4] A. Orlova, R. Blinder, E. Kermarrec, M. Dupont, N. Laflorencie, S. Capponi, H. Mayaffre, C. Berthier, A. Paduan-Filho, and M. Horvatić, "*Nuclear Magnetic Resonance Reveals Disordered Level-Crossing Physics in the Bose-Glass Regime of the Br-Doped* $Ni(Cl_{1-x}Br_x)_2{-}4SC(NH_2)_2$ *Compound at a High Magnetic Field*," Phys. Rev. Lett. **118**, 067203 (2017).

[5] M. Dupont, S. Capponi, and N. Laflorencie, "*Disorder-Induced Revival of the Bose-Einstein Condensation in* $Ni(Cl_{1-x}Br_x)_2{-}4SC(NH_2)_2$ *at High Magnetic Fields*," Phys. Rev. Lett. **118**, 067204 (2017).

[6] M. Dupont, S. Capponi, M. Horvatić, and N. Laflorencie, "*Competing Bose-glass physics with disorder-induced Bose-Einstein condensation in the doped* $S = 1$ *antiferromagnet* $Ni(Cl_{1-x}Br_x)_2{-}4SC(NH_2)_2$ *at high magnetic fields*," Phys. Rev. B **96**, 024442 (2017).

[7] Y.-R. Shu, M. Dupont, D.-X. Yao, S. Capponi, and A. W. Sandvik, "*Dynamical properties of the* $S = \frac{1}{2}$ *random Heisenberg chain*," Phys. Rev. B **97**, 104424 (2018).

[8] A. Orlova, H. Mayaffre, S. Krämer, M. Dupont, S. Capponi, N. Laflorencie, A. Paduan-Filho, and M. Horvatić, "*Detection of a disorder-induced Bose-Einstein condensate in a quantum spin material at high magnetic fields*," arXiv:1801.01445, preprint (2018).

[9] M. Dupont, S. Capponi, N. Laflorencie, and E. Orignac, "*Dynamical response and dimensional crossover for spatially anisotropic antiferromagnets*," arXiv:1806.04913, preprint (2018).

Résumé en Français[†]

Les travaux présentés dans ce manuscrit s'intéressent au magnétisme quantique, ou plus largement à la physique de la matière condensée et aux systèmes dits fortement corrélés. Dans ces systèmes, les interactions à plusieurs corps et corrélations entre les particules quantiques ne peuvent être négligées, sinon, les modèles échoueraient simplement à capturer les mécanismes physiques en jeu et les phénomènes qui en découlent. Bien que théoriques, il est intéressant de noter que ces travaux sont substantiellement reliés à des expériences. En effet, une grande partie a été réalisée dans le cadre d'une collaboration fructueuse avec le groupe de résonance magnétique nucléaire du Laboratoire National des Champs Magnétiques Intenses à Grenoble, en France. Cela permet à la fois une meilleure compréhension des observations expérimentales, mais aussi une vérification et comparaison expérimentale des prédictions théoriques.

Comprendre les effets des interactions à plusieurs corps dans des systèmes quantiques est un problème de longue date de la physique moderne. Essentiellement, décrire $\sim 10^{23}$ degrés de liberté couplés est un problème compliqué, impossible à résoudre exactement dans la plupart des cas. Ce qui le rend curieusement intéressant est que cette description intraitable est basée sur des modèles qui sont extrêmement simples à écrire. Malgré leur apparente simplicité, ils capturent et décrivent fidèlement une large gamme de propriétés et de phénomènes survenant dans des matériaux réalistes. Cela va des moins, aux plus exotiques phases de la matière, en passant par les transitions de phase. Le plus souvent, les modèles étudiés dans cette branche de la physique décrivent des degrés de liberté (électrons, ou plus particulièrement des spins ici, pour le magnétisme) couplés et contraints dans l'espace sur les sommets de structures géométriques appelées réseaux (par exemple carrés, cubiques, tétragonaux...), qui tirent leur origine de la structure microscopique sous-jacente des atomes dans les matériaux.

Ce résumé est organisé en trois parties, chacune reprenant un chapitre du texte principal. Les sections comprenant introductions, motivations, méthodes et détails techniques ne seront que très peu — voire pas du tout — discutées. Seule une partie des résultats sera présentée, s'articulant tout au plus autour d'une ou deux figures représentatives. La première partie concerne les aimants quantiques en dimensionalité réduite. Si géométriquement, des réseaux formant une chaîne ou échelle sont par définition en "basse dimension", car unidimensionnels (1D), des réseaux en dimension plus élevée peuvent aussi être considérés comme tels du moment que les forces des couplages entre les degrés de liberté sont fortement anisotropes, ou, autrement dit plus ou moins fortes dans les différentes directions de l'espace.

[†]This is a *not-so-short* summary, in French, of the work presented in this manuscript. Its length is constrained by administrative requirements.

La dimension est un paramètre ayant un contrôle important sur les phénomènes physiques. Par exemple, le théorème de Mermin-Wagner [17–20] établit que la brisure spontanée d'une symétrie continue dans le cadre d'une transition de phase est possible à n'importe quelle température T en trois dimensions (3D) et seulement à $T = 0$ pour des systèmes à deux dimensions — et ne peut pas avoir lieu dans des systèmes purement 1D, même à température nulle. Il est alors intéressant d'étudier l'effet de la modulation des forces de couplage sur les propriétés physiques, en particulier au regard de la température qui va servir de curseur. Dans le cas d'un système antiferromagnétique quasi unidimensionnel, à très basse température, on s'attend à une mise en ordre de type Néel ou XY en dessous d'une certaine température critique T_c. À plus haute température, loin de ce phénomène de transition de phase caractéristique en 3D, on peut s'attendre, du fait de la forte anisotropie du système, à avoir un régime où la physique si particulière du système purement 1D décrite par la théorie des champs du liquide de Tomonaga-Luttinger, caractérisée par deux paramètres u et K, se manifeste. Même si ce régime se développe *a priori* pour $T \gg T_c$, la température doit rester petite devant l'énergie caractéristique du système $T \ll J$ (J est la force de couplage le long de la direction 1D), de façon à ce que la physique quantique unidimensionnelle puisse émerger sans être masquée par des effets non universels à plus haute température. Derrière ces images qualitatives, une définition plus quantitative des différents régimes manque à plusieurs niveaux. Dans la première partie, on étudiera d'abord la modulation du paramètre d'ordre m^{AF} dans des plans antiferromagnétiques faiblement couplés. Ensuite, on discutera, en mêlant expériences et théorie, des approches basées sur la description liquide de Tomonaga-Luttinger pour rendre compte des propriétés d'un composé magnétique sous champ, "DTN", constitué de chaînes de spins $S = 1$ faiblement couplées. La seconde partie portera toujours sur l'effet de la modulation dimensionnelle d'aimants quantiques, mais dans le cadre de propriétés dynamiques cette fois. On s'intéressera notamment au taux de relaxation $1/T_1$ mesuré par résonance magnétique nucléaire (RMN) ainsi qu'au facteur de structure dynamique $S(\mathbf{q}, \omega)$ mesuré par diffusion inélastique de neutrons. Enfin, dans la dernière partie, on s'intéressera aux effets conjoints du désordre et des interactions dans le matériau dopé "DTNX" : plutôt qu'une phase de la matière dite localisée, appelée verre de Bose, attendue à fort champ magnétique, une phase ordonnée induite par le désordre lui-même est mise en lumière, avec une réapparition inattendue de la cohérence quantique dans ledit composé.

I. Aimants quantiques en dimensionalité réduite

La première sous-section s'intéressera à la modulation dimensionnelle du paramètre d'ordre antiferromagnétique, m^{AF}, associée à des plans magnétiques faiblement couplés. Dans ce travail, on a étudié comment le processus de mise en ordre du système tridimensionnel est modulé en celui du cas bidimensionnel par réduction de la dimensionalité dans la limite d'un couplage inter plan nul. Il est bien connu que dans un système pleinement 3D, le paramètre d'ordre montre une dépendance concave

avec la température ; cependant, il est fini uniquement à température nulle en deux dimensions. En utilisant une série de méthodes numériques et analytiques, complémentaires, on a montré que la courbe $m^{\mathrm{AF}}(T)$ est modifiée avec un changement non trivial de convexité en réduisant la force du couplage inter plan. Cela suppose l'existence d'une phase ordonnée quasi bidimensionnelle où le système se comporte comme s'il était bidimensionnel, sauf concernant la présence d'un paramètre d'ordre $m^{\mathrm{AF}}(T)$ très faible mais non nul. Ce travail a notamment été motivé par le composé $(C_7H_{10}N)_2CuBr_4$, aussi connu sous le nom de "DIMPY", fait d'échelles de spins $S = 1/2$ faiblement couplées. Dans ce matériau, les échelles sont d'abord couplées d'une façon bidimensionnelle, formant des plans, mais aussi en trois dimensions où ce couplage inter plan est la plus petite échelle d'énergie du système. Le paramètre d'ordre du matériau, expérimentalement mesuré par RMN a montré une telle modulation.

Dans un second temps, on se concentrera sur un composé antiferromagnétique fait de spins $S = 1$, $NiCl_2$-$4SC(NH_2)_2$, aussi appelé "DTN", au double chapeau intéressant. D'un côté, il est tridimensionnel et affiche donc une transition de phase à température finie, sous réserve qu'un champ magnétique suffisamment fort soit appliqué. D'un autre côté, ses faibles couplages tridimensionnels rendent *a priori* possible l'observation des propriétés universelles unidimensionnelles décrites par la théorie du liquide de Tomonaga-Luttinger. Les propriétés à haut champ magnétique de la phase ordonnée antiferromagnétique telles que le paramètre d'ordre et sa température critique ont été étudiées par RMN et directement comparées à diverses approches théoriques. Des simulations numériques de Monte Carlo quantique se sont montrées en parfait accord avec les données expérimentales. Nous les avons alors utilisées comme référence pour discuter de l'applicabilité d'approches approximatives et leur sensibilité à la force du couplage tridimensionnel. Nous avons trouvé que les prédictions analytiques basées sur la théorie unidimensionnelle du liquide de Tomonaga-Luttinger étaient très bonnes concernant la température critique du moment qu'une renormalisation du couplage 3D était appliquée, mais déviaient trop pour le paramètre d'ordre m^{AF}. La conclusion est que le composé DTN n'est en réalité "pas suffisamment unidimensionnel" pour être décrit par de telles approches.

1. Modulation dimensionnelle du processus de mise en ordre dans des plans magnétiques faiblement couplés

Adapté de Phys. Rev. B **94**, 144403 (2016)

Shunsuke C. Furaya, **Maxime Dupont**, Sylvain Capponi, Nicolas Laflorencie, and Thierry Giamarchi

Ce travail a donc été grandement motivé par des mesures expérimentales de RMN sous champ magnétique sur le matériau DIMPY, composé d'échelles de spins $S = 1/2$. Prises individuellement, les échelles de spins à deux montants ont un spectre en énergie présentant une bande d'énergie interdite entre l'état fondamental (singulet) et le premier état excité (triplet) à bas champ magnétique. À plus fort champ, ce gap se ferme et permet d'avoir une phase décrite par la physique du liquide de Tomonaga-Luttinger. Maintenant couplées en 3D, ces échelles peuvent s'ordonner en développant de l'ordre antiferromagnétique de type XY à basse température. Des

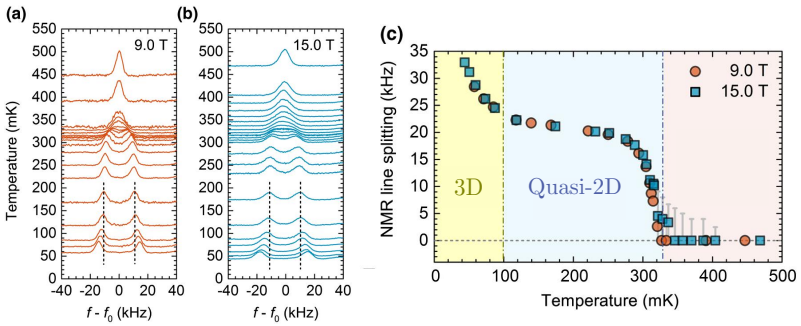

Figure 1: Spectre RMN du ^{14}N dans DIMPY en fonction de la température, pour deux valeurs du champ magnétique, **(a)** $H = 9.0$ T et **(b)** 15.0 T. Les traits pointillés verticaux correspondent à la première saturation de la séparation des lignes RMN autour de $T = 150$ mK. **(c)** La séparation de ces lignes est proportionnelle au paramètre d'ordre m^{AF}. En fonction de la température, trois régimes sont identifiés et représentés par trois couleurs différentes: 3D (jaune), quasi 2D (bleu) et désordonné (rouge). Adapté de la référence 204.

mesures RMN du paramètre d'ordre en fonction de la température, tel que montré dans la figure 1, montrent deux régimes distincts étiquetés — et interprétés comme — quasi 2D et 3D. Plus largement, DIMPY a récemment été activement étudié, aussi bien expérimentalement que théoriquement [171, 173, 205–209] en tant que premier composé d'échelle de spins avec une interaction le long des montants des échelles plus forte que le long des barreaux, $J_{\mathrm{montant}}/J_{\mathrm{barreau}} = 1.7$.

Étant donné que des échelles de spins couplées en 3D sujettes à un champ magnétique externe peuvent réaliser une phase ordonnée antiferromagnétique XY, les résultats observés sur la modulation du paramètre d'ordre ne devraient pas dépendre du modèle microscopique sous-jacent. C'est pourquoi par la suite, on s'éloigne un peu de la description réaliste de DIMPY en considérant des spins $S = 1/2$ sur un réseau orthorhombique, qui affiche la même phase ordonnée, avec des couplages anisotropes dans les trois directions de l'espace : J, J_1' et J_2' tels que $J \gg J_1' \gg J_2'$. La nature unidimensionnelle est masquée par les corrélations inter chaînes dans la phase quasi 2D ou 3D, et n'est donc pas essentielle dans l'étude de la modulation du paramètre d'ordre. Toujours est-il que c'est du point de vue technique intéressant pour se rapporter à des méthodes de la physique 1D. Le modèle est décrit par le Hamiltonien suivant,

$$\mathcal{H} = J \sum_{\langle ij \rangle_0} \left[\frac{1}{2} \left(S_i^+ S_j^- + S_i^- S_j^+ \right) + \Delta S_i^z S_j^z \right] - H \sum_i S_i^z + \mathcal{H}_{3\mathrm{D}}$$
$$\text{with } \mathcal{H}_{3\mathrm{D}} = J_1' \sum_{\langle ij \rangle_1} \mathbf{S}_i \cdot \mathbf{S}_j + J_2' \sum_{\langle ij \rangle_2} \mathbf{S}_i \cdot \mathbf{S}_j, \qquad (1)$$

avec $\langle ij \rangle_n$ restreignant la somme aux spins plus proches voisins dans les trois directions n de l'espace.

Approximation classique En utilisant la représentation de bosonisation des spins [37], le Hamiltonien du système dans la phase ordonnée XY amène à l'action euclidienne,

$$\mathcal{S} = \sum_{\mu,\nu}\Bigg\{ \frac{K}{2\pi u}\int \mathrm{d}\tau\mathrm{d}x\Big[(\partial_\tau\theta_{\mu,\nu})^2 + u^2\,(\partial_x\theta_{\mu,\nu})^2\Big] \\ - J_1' A_0\int \mathrm{d}\tau\mathrm{d}x\,\cos\left(\theta_{\mu,\nu}-\theta_{\mu+1,\nu}\right) - J_2' A_0\int \mathrm{d}\tau\mathrm{d}x\,\cos\left(\theta_{\mu,\nu}-\theta_{\mu,\nu+1}\right)\Bigg\}, \quad (2)$$

où le champ $\theta_{\mu,\nu}\equiv\theta_{\mu,\nu}(\tau,x)$ décrit l'ordre antiferromagnétique XY avec $m^{\mathrm{AF}}(T) = \sqrt{A_0}\langle\cos\theta_{\mu,\nu}\rangle$. Notons que quand $J_1' = J_2' = 0$, l'action représente un ensemble de liquides de Tomonaga-Luttinger mutuellement indépendants. Afin de décrire le processus de mise en ordre, on néglige la dépendance en temps imaginaire des champs $\theta_{\mu,\nu}(\tau,x)\simeq\theta_{\mu,\nu}(x)$, ce qui remplace donc le modèle quantique initial $(3+1)$-dimensionnel par un modèle classique $(3+0)$-dimensionnel. Cette approximation, dite classique, fonctionne bien proche de la température critique [21], et bien qu'il soit difficile d'en prédire exactement son domaine de validité, on peut s'attendre à ce qu'il soit très large dans la limite 2D, $J_2'/J_1'\to 0$, du fait que le système reste dans ce cas proche de la ligne critique à basse température. De plus, il est raisonnable de penser que dans la phase ordonnée, les fluctuations de chaînes voisines μ et $\mu+1$ au sein d'un même plan soient bien plus petites que celles entre chaînes voisines appartenant à des plans différents (ν et $\nu+1$) si $J_1'\gg J_2'$. De ce fait, on développe le terme en cosinus du couplage inter chaîne jusqu'au second ordre comme $\cos\left(\theta_{\mu,\nu}-\theta_{\mu+1,\nu}\right)\simeq 1-\frac{1}{2}\left(\theta_{\mu,\nu}-\theta_{\mu+1,\nu}\right)^2$. En omettant le terme constant et en considérant la limite du continu dans la direciton μ, $\left(\theta_{\mu,\nu}-\theta_{\mu+1,\nu}\right)^2\to(\partial_y\theta_\nu)^2$, où le champ classique dépend à présent du plan ν et des variables continues x et y, $\theta_\nu(x,y)$. La nouvelle action est donnée par,

$$\mathcal{S} = \sum_{\nu}\Bigg\{ \frac{K}{2\pi uT}\int \mathrm{d}x\mathrm{d}y\Big[u^2\,(\partial_x\theta_\nu)^2 + v_y^2\,(\partial_y\theta_\nu)^2\Big] \\ - \frac{J_2' A_0}{T}\int \mathrm{d}x\mathrm{d}y\,\cos\left(\theta_\nu-\theta_{\nu+1}\right)\Bigg\} \quad \text{with } v_y^2 = \frac{u^2 J_1' A_0}{2K}, \quad (3)$$

où nous avons utilisé $\int \mathrm{d}\tau = 1/T$ ainsi que la substitution $\sum_\mu\to\int \mathrm{d}y$ résultant du passage à la limite continue avec le pas du réseau pris égal à l'unité. Pour plus de commodité, on fait les changements de variables suivant, $y = v_y\tau'$, $K' = v_y K/T$ and $\tilde{J}_2' = v_y J_2'/T$, qui amènent à,

$$\mathcal{S} = \sum_{\nu}\Bigg\{ \frac{K'}{2\pi u}\int \mathrm{d}x\mathrm{d}\tau'\Big[u^2\,(\partial_x\theta_\nu)^2 + (\partial_{\tau'}\theta_\nu)^2\Big] \\ - \tilde{J}_2' A_0\int \mathrm{d}x\mathrm{d}\tau'\,\cos\left(\theta_\nu-\theta_{\nu+1}\right)\Bigg\}. \quad (4)$$

En comparant cette forme à l'action initiale, il est clair que le problème peut être vu à présent comme celui associé à un système quantique $(2+1)$-dimensionnel : des chaînes de spins avec des paramètres de Tomonaga-Luttinger K' et u, couplées en deux dimensions par $\tilde{J}_2'$ et où $K'\propto 1/T$.

Étude numérique Le modèle tridimensionnel initial avec $J \gg J_1' \gg J_2'$ est numériquement inaccessible du fait de la forte anisotropie entre les couplages, rendant les simulations de Monte Carlo quantique beaucoup trop coûteuses en temps pour accéder à des températures suffisamment basses et capturer la physique qui nous intéresse ici. En effet, une estimation grossière de la température critique de mise en ordre 3D est $T_c \sim \mathcal{O}(J_1')$, et nous devons aller bien en deçà de cette température pour capturer le régime quasi 2D puis 3D pour le paramètre d'ordre[1]. Cependant, l'approximation classique développée précédemment rend possible la simulation du Hamiltonien sous-jacent à l'action qui a été dérivée. En effet, simuler des chaînes couplées en deux dimensions, à température nulle, est bien moins gourmand en ressources. Le Hamiltonien considéré pour l'étude numérique est donc le suivant : des chaînes de spins $S = 1/2$ XXZ couplées,

$$\mathcal{H} = \sum_{i,n} \left\{ J \left[\frac{1}{2} \left(S^+_{i,n} S^-_{i+1,n} + S^-_{i,n} S^+_{i+1,n} \right) + \Delta S^z_{i,n} S^z_{i+1,n} \right] + J' \mathbf{S}_{i,n} \cdot \mathbf{S}_{i,n+1} \right\}, \quad (5)$$

où i et n représentent les sites le long et perpendiculaires aux chaînes. $\Delta \in [-1, 1]$ est une anisotropie de type Ising qui permet de moduler les paramètres du liquide de Tomonaga-Luttinger des chaînes isolées [71], et J' contrôle la force du couplage dans la direction transverse 2D. Dans la suite, le couplage le long des chaînes J est pris comme référence et égal à l'unité. Le but est d'étudier le paramètre d'ordre de l'état fondamental de ce Hamiltonien en fonction de l'inverse du paramètre K, jouant le rôle de température dans l'approximation classique.

Une première approche, de type champ moyen, ramène la description du couplage des chaînes ordonnées de façon antiferromagnétique à celle d'une seule chaîne, soumise à un champ magnétique alterné effectif, $\propto m^{\mathrm{AF}}$, couplé à la composante x du spin. Analytiquement, cela amène au modèle intégrable de sine-Gordon pour lequel le paramètre d'ordre m^{AF} peut être calculé de façon auto-cohérente. Une seconde approche vise à effectuer la même procédure numériquement, à l'aide du groupe de renormalisation de la matrice densité réduite (DMRG). Ces deux approches champ moyen sont en bon accord pour des petites valeurs de J', comme visible dans la figure 2. Le champ moyen numérique est cependant mieux contrôlé que son penchant analytique quand J' n'est pas "trop petit", dans le sens où la limite $m^{\mathrm{AF}} \leq 0.5$ est respectée, particulièrement proche du point ferromagnétique $1/K \to 0$. Par ailleurs, il ne prédit pas de divergence pour m^{AF} proche de $1/K \to 2$. Une autre approche, connue depuis longtemps est la théorie des ondes de spin d'Anderson [83], connue pour fournir une bonne estimation à l'ordre $1/S$ du paramètre d'ordre pour des systèmes antiferromagnétiques de spins S en dimensions $D \geq 2$, même pour $S = 1/2$. Dans la limite $1/K > 1$, le paramètre d'ordre des ondes de spin est fortement supprimé quand J' augmente et dévie énormément des résultats champ moyen. D'un autre côté, dans le régime $1/K < 1$, l'accord avec le champ moyen est remarquable, en particulier pour des petites valeurs de J'. Toutefois, on ne peut pas s'attendre à ce que la théorie des ondes de spin soit fiable pour des valeurs J' trop petites, étant donné que le développement sur laquelle elle est basée n'est pas justifié dans la limite unidimensionnelle $J' \to 0$. Pour aller au-delà de ces approches

[1] Nous avons tenté de simuler le modèle original avec $J_1' = J/10$ and $J_2' = J_1'/10$, à la limite de ce qui est numériquement accessible et n'avons pas pu observer le régime quasi 2D attendu pour le paramètre d'ordre. Nous pensons que le facteur 10 entre les couplages n'est pas suffisamment important pour l'observer.

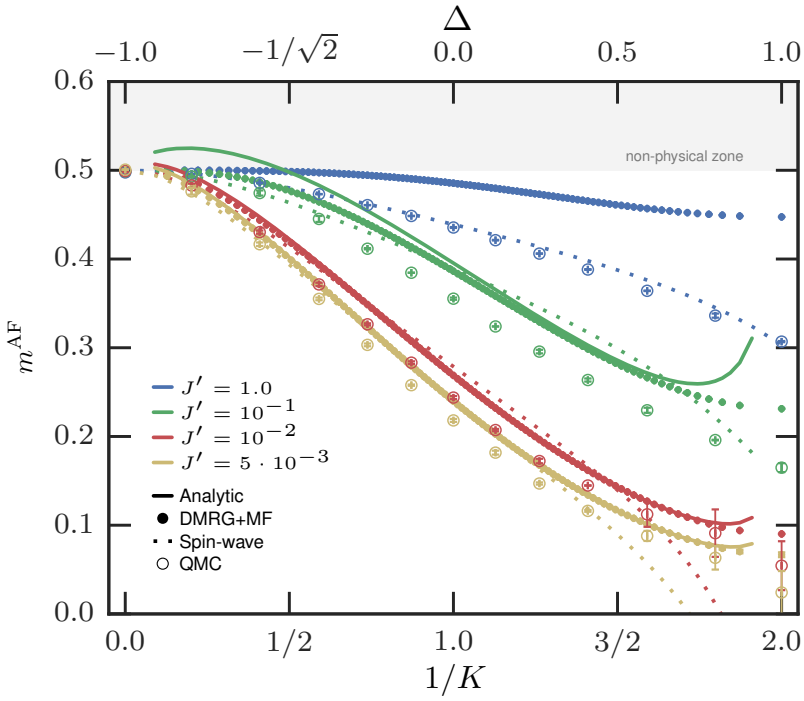

Figure 2: Paramètre d'ordre m^{AF} en fonction de l'inverse du paramètre de Tomonaga-Luttinger $1/K \propto T$, pour différentes valeurs du couplage inter chaîne J'/J et différentes approches : champ moyen analytique (*Analytic*) et numérique, basé sur le groupe de renormalisation de la matrice densité réduite (DMRG+MF), ondes de spin (*spin-wave*) et Monte Carlo quantique (QMC).

approximatives et prendre en compte exactement le couplage inter chaîne J', nous avons utilisé du Monte Carlo quantique [198,225] en s'assurant d'échantillonner l'état fondamental, en se positionnant à très basse température. Par ailleurs, le paramètre d'ordre a été calculé pour différentes tailles de systèmes et une valeur dans la limite d'un système infini a été extrapolée. Les résultats sont affichés dans la figure 2. On remarque que la valeur du paramètre d'ordre du Monte Carlo est toujours plus petite que celle donnée par le champ moyen : cette approximation a tendance à surestimer l'ordre du fait des fluctuations quantiques négligées.

Par le biais d'une approximation classique (d'autres ont été développées dans le texte principal), nous avons montré que le paramètre d'ordre $m^{\mathrm{AF}}(T)$ d'un système quasi 2D montre une dépendance convexe avec la température dans la limite $J'/J \to 0$, contrairement à la forme concave à laquelle on s'attend habituellement pour un système tridimensionnel.

2. Étude du composé magnétique "DTN" constitué de chaînes de spins S=1 faiblement couplées

Les propriétés magnétiques du composé "DTN" sont décrites par des degrés de liberté de spins $S = 1$, portés par les ions Ni^{2+}, et formant dans l'espace un réseau tétragonal. Deux atomes de chlore sont présents entre deux ions nickel le long de l'axe cristallographique c et sont responsables de l'anisotropie spatiale dans les couplages, comme montré dans la figure 3 (a). Les autres atomes ne jouent pas

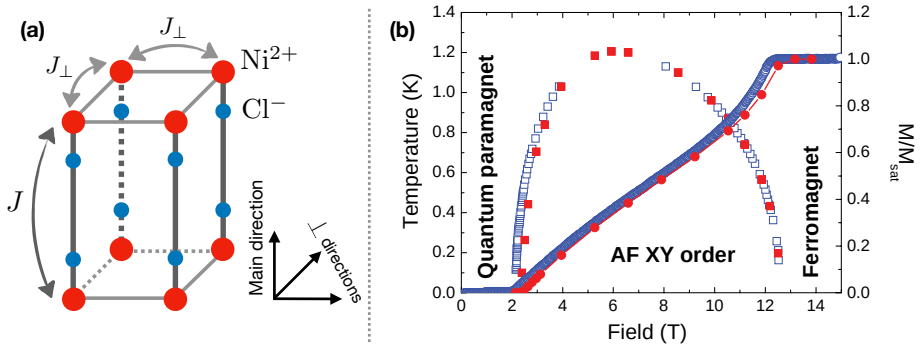

Figure 3: (a) Structure cristallographique du composé DTN. Les spins $S = 1$ sont portés par les ions Ni^{2+} (ronds rouges) et les atomes de chlores (ronds bleus) rendent le composé spatialement anisotrope (structure tétragonale). **(b)** Diagramme des phases température/champ magnétique, avec la détermination d'une phase ordonnée antiferromagnétique XY, sous le dôme, obtenue par des mesures magnétocaloriques (carrés ouverts). La courbe d'aimantation à $T = 16$ mK (cercles ouverts) est également montrée. Les résultats de simulations par Monte Carlo quantique concernant la température critique et l'aimantation sont représentés par les carrés et cercles pleins respectivement. Figure adaptée de la référence 163.

un rôle important en ce qui concerne la description des propriétés magnétiques et ne sont pas considérés. Les spins $S = 1$ interagissent au travers du Hamiltonien suivant [163, 230],

$$\mathcal{H} = \sum_i \left\{ \sum_m \left[J\mathbf{S}_{i,m} \cdot \mathbf{S}_{i+1,m} + D\left(S^z_{i,m}\right)^2 - g\mu_B H S^z_{i,m} \right] + \sum_{\langle m,n \rangle} J_\perp \mathbf{S}_{i,m} \cdot \mathbf{S}_{i,n} \right\}, \tag{6}$$

où le premier indice de l'opérateur de spin correspond à la position du spin sur la chaîne à laquelle il appartient, elle-même étiquetée par le second indice. Le symbole $\langle \cdot \rangle$ dans la dernière somme la restreint aux chaînes voisines. Les interactions d'échange entre spins sont de type Heisenberg, avec un couplage $J = 2.2$ K le long de la direction des chaînes et $J_\perp = 0.18$ K dans les directions transverses. Par ailleurs, chaque spin ressent une anisotropie de spin décrite par $D = 8.9$ K. Un champ magnétique externe H couplé aux spins est appliqué dans la même direction que l'anisotropie D de telle sorte que le Hamiltonien conserve sa symétrie U(1). Le facteur gyromagnétique prend la valeur $g = 2.31$. C'est assez inhabituel pour noter que toutes les échelles d'énergie sont connues exactement pour ce composé, le champ magnétique appliqué étant alors le seul paramètre ajustable.

Le diagramme des phases de ce matériau est affiché dans la figure 3 (b). À basse température, dans la limite $H \to +\infty$, le composé est dans un état ferromagnétique trivial, avec tous ses spins alignés le long de la direction du champ magnétique externe $|\uparrow\uparrow \cdots \uparrow\rangle$. En réduisant l'intensité du champ magnétique, la phase ferromagnétique va subister jusqu'à ce que le premier spin se retourne pour aller d'un état $|\uparrow\rangle$ à $|0\rangle$. Plus précisément, cela se passera lorsque l'énergie de l'état avec un spin retourné sera plus petite que celle de l'état entièrement polarisé. La valeur du champ magnétique

pour laquelle cela se produit définit un point critique quantique, nommé H_{c2} dont la valeur peut être exactement déterminée,

$$H_{c2} = (D + 4J + 8J_\perp)/g\mu_B = 12.3 \text{ T}. \tag{7}$$

Dans l'autre limite, pour $H = 0$, l'état fondamental du système est dans une phase de type grand-D [235], différente d'une phase de type Haldane. En effet, $D/J \simeq 4$ dans DTN, qui est plus grand que la valeur critique $D_c/J = 0.968$ [236], au-delà de laquelle le fondamental est dans une phase paramagnétique triviale (la phase grand D), séparée en énergie du premier état excité par une bande d'énergie interdite. C'est seulement en dessous de ce point critique, que le système subit une transition de phase vers une phase topologique de type Haldane. Dans cette phase grand D, l'état fondamental correspond à un état "habillé" où tous les spins vont avoir leur composante z selon $|00\cdots0\rangle$ pour minimiser l'énergie. Il est évident que la première excitation d'un tel état ne peut être associé qu'au retournement d'un spin, ce qui arrivera inévitablement en appliquant un champ magnétique suffisamment élevé, $H \geq H_{c1}$. La valeur de H_{c1}, un deuxième point critique quantique peut être obtenue en théorie des perturbations [237],

$$H_{c1} = \left[D - 2J - \frac{J^2}{D} + \frac{J^3}{2D^2} + \mathcal{O}\left(\frac{J^4}{D^5}\right) - 4J_\perp\right]/g\mu_B = 2.1 \text{ T}. \tag{8}$$

La région intermédiaire entre H_{c1} et H_{c2} correspond à une phase ordonnée XY (ordre antiferromagnétique) qui subsiste à température finie, en deçà de T_c, et brise spontanément la symétrie U(1) du système. La présence d'une bande d'énergie interdite dans le spectre en énergie des phases grand D et ferromagnétique est caractérisée par les plateaux d'aimantation affichés dans la figure 3 (b) pour $H \notin [H_{c1}, H_{c2}]$.

Du côté expérimental, ce travail contient les premières mesures de la valeur absolue (sans aucun ajustement) du paramètre d'ordre à basse température ($T = 0.12$ K). Du côté théorique, l'idée principale est de vérifier l'applicabilité et la précision d'une description basée sur le liquide de Tomonaga-Luttinger pour capturer les propriétés de la phase ordonnée XY, comme sa température critique et son paramètre d'ordre. La description liquide de Tomonaga-Luttinger étant pour des systèmes unidimensionnels, le couplage 3D est traité de manière champ moyen au travers de l'approximation de la phase aléatoire pour la température critique et le modèle de sine-Gordon pour le paramètre d'ordre. Ces approches nécessitent la connaissance *a priori* des paramètres A_0, K and u du liquide de Tomonaga-Luttinger. Des expressions analytiques de ces paramètres en fonction des paramètres microscopiques du modèle existent pour des chaînes XXZ de spins $S = 1/2$ grâce à l'ansatz de Bethe, mais pas pour le modèle spécifique de DTN sous champ. Une grande partie du travail consiste donc à les déterminer par le biais de simulations numériques. Notamment, ils apparaissent dans des quantités physiques comme la susceptibilité magnétique, $\chi = K/u\pi$ ou les fonctions de corrélations à deux corps, $\langle S_i^{\pm} S_{i+r}^{\mp}\rangle \sim (-1)^r A_0/|r|^{\frac{1}{2K}}$, qui peuvent être calculées par le biais du groupe de renormalisation de la matrice densité réduite puis *fittés* ensuite.

Tout d'abord, les mesures expérimentales de la température critique et du paramètre d'ordre m^{AF} sont comparées à des simulations de Monte Carlo quantique. Comme montré dans la figure 4, les estimations Monte Carlo sont en parfait accord avec les données expérimentales. Pour un système quasi unidimensionnel, une

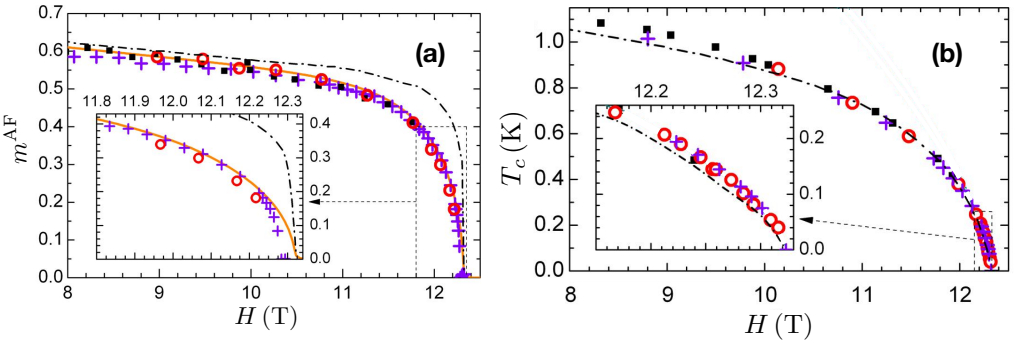

Figure 4: (a) Paramètre d'ordre de la phase ordonnée du composé DTN à $T = 0.12$ K déterminé par RMN (cercles), simulations Monte Carlo quantiques (croix). Les données RMN se superposent avec les données de diffraction de neutrons tirées de la référence 229 et réduites par un facteur -25% (carrés). La ligne pleine orange et la ligne pointillée noire sont les prédictions $T = 0$ du champ moyen numérique et analytique respectivement. L'encart est un zoom proche de H_{c2}. **(b)** Données RMN (cercles rouges) pour la température critique T_c, comparées aux prédictions théoriques : les simulations Monte Carlo quantiques sont représentées par les croix et la prédiction analytique basée sur l'approximation de la phase aléatoire par la ligne pointillée. Les carrés correspondent aux mesures magnétocaloriques tirées de la référence 230.

seconde approche, numériquement moins coûteuse pour décrire l'ordre à température nulle est de prendre en compte le couplage 3D dans une approximation champ moyen en négligeant des fluctuations quantiques. Cette méthode, déjà utilisée pour le travail présenté précédemment, ramène le problème tridimensionnel à celui d'une chaîne unique dans un champ magnétique effectif avec une composante transverse alterné en raison de l'ordre antiferromagnétique XY. Ce modèle est ensuite résolu numériquement de façon auto-cohérente en utilisant l'algorithme du groupe de renormalisation de la matrice densité réduite. Le résultat est affiché dans la figure 4 (a), et est très proche des résultats Monte Carlo à $T = 0.12$ K. La surestimation du paramètre d'ordre m^{AF} d'environ 3% est en partie due à la différence de température entre les différentes approches. L'approche champ moyen analytique dévie considérablement des résultats numériques, notamment proche du champ critique H_{c2} alors que les deux résultats devraient être identiques dans la limite $J_\perp/J \ll 1$. Apparemment, la valeur $J_\perp/J \simeq 0.08$ du matériau DTN n'est pas suffisamment petite pour considérer le composé comme fait de chaînes faiblement couplées, en particulier quand le couplage inter chaîne total $4J_\perp$ devient plus grand que l'échelle d'énergie à l'intérieur des chaîne, u, proche du point critique H_{c2}. Cette observation est à mettre en parallèle de composés similaires "plus unidimensionnels", comme $(C_5H_{12}N)_2CuBr_4$ où l'approche analytique pour le calcul du paramètre d'ordre était en très bon accord [166, 210] avec des approches plus exactes. La température critique peut aussi être décrite par une expression analytique basée sur l'approximation de la phase aléatoire de la susceptibilité d'une chaîne unique. Ce résultat est montré dans la figure 4 (b). Ici, nous avons explicitement inclus un paramètre de renormalisation α pour prendre en compte des effets de fluctuations de spins au-delà du traitement champ moyen de l'interaction inter chaînes, $J_\perp \to \alpha J_\perp$. Cette renormalisation a été discutée dans des travaux antérieurs, aussi bien analytiques 245 que numériques 246 où $\alpha = 0.695$

fut obtenu. Une valeur légèrement différente $\alpha = 0.74$ a été appliquée pour le composé $(C_5H_{12}N)_2CuBr_4$ [167, 210], alors que dans notre cas, pour DTN, on trouve $\alpha = 0.67(2)$. Cela pointe vers une valeur universelle de ce paramètre. Pour une valeur de champ magnétique donnée, la valeur de α a été déterminée de telle sorte que $T_c^{\text{Mont. Carl.}}(H) = T_c^{\text{Ch. moy.}}(H)$.

II. Propriétés dynamiques d'aimants quantiques

Le calcul de quantités dépendantes du temps, ou bien la réponse d'un système quantique au cours du temps à une perturbation initiale, constituent des problèmes très difficiles dans tous les champs de la physique, et notamment en théorie de la matière condensée. Il est cependant essentiel de comprendre ces effets sachant qu'ils se rapportent à des sondes expérimentales impliquées dans l'étude de systèmes quantiques. En particulier, je m'intéresserai dans cette partie aux fonctions spectrales mesurées dans des expériences de diffusion inélastique de neutrons [247, 248] ainsi qu'au taux de relaxation spin-réseau RMN [249–251]. Ils sont tous les deux des outils expérimentaux standards dans la communauté de la matière condensée pour étudier les sytèmes magnétiques quantiques. Ces quantités peuvent être reliées à des fonctions de corrélation dépendantes du temps comme

$$S^{\mu\upsilon}_{\mathbf{q}}(t) = \langle S^{\mu}_{-\mathbf{q}}(t) S^{\upsilon}_{\mathbf{q}}(0)\rangle - \langle S^{\mu}_{-\mathbf{q}}(t)\rangle\langle S^{\upsilon}_{\mathbf{q}}(0)\rangle, \tag{9}$$

où $\langle\rangle$ correspond à la moyenne à température finie, $\mathbf{S}_{\mathbf{r}}(t) = \mathrm{e}^{-i\mathcal{H}t}\mathbf{S}_{\mathbf{r}}\mathrm{e}^{i\mathcal{H}t}$ est l'opérateur de spin dépendant du temps dans la représentation de Heisenberg et l'index $\mu, \upsilon \in [x, y, z, +, -]$ est la composante du spin. L'opérateur de spin dans l'espace des $\mathbf{q}$ est relié par une transformée de Fourier discrète à l'espace réel par $S^{\mu}_{\mathbf{q}}(t) = \sum_{\mathbf{r}} \mathrm{e}^{i\mathbf{q}\cdot\mathbf{r}} S^{\mu}_{\mathbf{r}}(t)/\sqrt{N}$ où N est le nombre total de spins dans le système. En fonction de la dimension D du système, les vecteurs $\mathbf{r}$ et $\mathbf{q}$ sont D-dimensionnels et les composantes du vecteur d'onde sont $\in]-\pi, \pi]$ (le pas du réseau étant pris égal à l'unité). La transformée de Fourier pour passer du temps t à la fréquence ω donne le facteur de structure dynamique, aussi connu sous le nom de fonction spectrale,

$$S^{\mu\upsilon}_{\mathbf{q}}(\omega) = \int_{-\infty}^{+\infty} \mathrm{d}t\, \mathrm{e}^{i\omega t} S^{\mu\upsilon}_{\mathbf{q}}(t), \tag{10}$$

qui est la quantité principale ici, directement reliée aux expériences. Pour un Hamiltonien avec une symétrie U(1) où l'anisotropie est selon la composante de spin z, l'intensité de diffusion peut être séparée en deux parties, une longitudinale et l'autre transverse, $I = I^{\parallel} + I^{\perp}$,

$$I^{\parallel} = S^{zz}_{\mathbf{q}}(\omega), \quad \text{and} \quad I^{\perp} = \frac{1}{2}\Big[S^{+-}_{\mathbf{q}}(\omega) + S^{-+}_{\mathbf{q}}(\omega)\Big]. \tag{11}$$

Il en va de même pour le taux de relaxation RMN,

$$\frac{1}{T_1} = \frac{1}{T_1^{\perp}} + \frac{1}{T_1^{\parallel}}, \tag{12}$$

dont les composantes sont reliées aux fonctions de corrélation suivantes,

$$\frac{1}{T_1^{\parallel}} = S^{zz}_{\mathbf{r}=\mathbf{0}}(\omega_0), \quad \text{and} \quad \frac{1}{T_1^{\perp}} = \frac{1}{2}\Big[S^{+-}_{\mathbf{r}=\mathbf{0}}(\omega_0) + S^{-+}_{\mathbf{r}=\mathbf{0}}(\omega_0)\Big]. \tag{13}$$

où ω_0 correspond à la fréquence RMN, dont il est souvent théoriquement justifié de la considérer comme nulle étant donné qu'elle est de l'ordre de quelques dizaines ou centaines de MHz, correspondant à des températures de l'ordre du mK, la rendant de ce fait la plus petite échelle d'énergie du problème.

Une nouvelle fois, il est question dans cette partie de l'effet de la dimension. Pour un arrangement tridimensionnel de chaînes faiblement couplées, avec un couplage J le long des chaînes et $J_\perp \ll J$ dans les directions transverses, on s'attend à l'émergence d'un régime tridimensionnel pour $T \lesssim J_\perp$, avec la mise en place d'un ordre à longue distance. Cependant, à plus haute température, ce système devrait montrer des signatures de la physique unidimensionnelle, approximativement dans la fenêtre $J_\perp \ll T \ll J$. Ce régime 1D a été identifié dans plusieurs composés au travers de quantités thermodynamiques. Par exemple, la chaleur spécifique du matériau quasi unidimensionnel $BaCo_2V_2O_8$, fait de chaînes de spins $S = 1/2$ [79] et du matériau organique $(C_5H_{12}N)_2CuBr_4$ [80] ont montré une réponse linéaire avec la température $\propto T$, comme attendu pour un système purement unidimensionnel. Un autre cas intéressant concerne les corrections logarithmiques prédites par Eggert *et al.* [75] pour la susceptibilité magnétique de chaînes Heisenberg de spins $S = 1/2$, et qui ont été observées dans l'oxyde de cuivre Sr_2CuO_3 [76–78]. La question principale que l'on souhaite se poser ici concerne la signature de physique unidimensionnelle, au-dessus de T_c, et en particulier quelle est la fenêtre de température dans laquelle le régime universel du liquide de Tomonaga-Luttinger est attendu ? Comme vu dans le composé fait d'échelles $(C_5H_{12}N)_2CuBr_4$ [80], le régime 1D basé sur des mesures magnétocaloriques n'est pas distinctement défini. On peut donc se demander comment un tel régime se manifeste dans des *quantités dynamiques*, en étudiant des systèmes quasi unidimensionnels magnétiques en fonction de la température. L'idée principale développée par la suite est de définir une fenêtre de température à l'intérieur de laquelle les propriétés universelles unidimensionnelles sont visibles et expérimentalement accessibles. Cette fenêtre est définie à basse température pour que les propriétés quantiques émergent, mais pas à trop basse température non plus étant donné que l'on ne veut pas s'approcher de la transition qui mènerait à une mise en ordre qui masquerait le physique 1D. On cherche donc précisément à définir ce qu'on entend par *basse température*, mais *pas trop basse non plus*.

1. Temps de relaxation RMN dans des chaînes de spins

Adapté de Phys. Rev. B **94**, 144409 (2016)

Maxime Dupont, Sylvain Capponi, and Nicolas Laflorencie

Les liquides de Tomonaga-Luttinger sont des systèmes aux propriétés curieuses. Dans la limite de basse température, on s'attend à ce que leur taux de relaxation RMN diverge avec la température en suivant une loi de puissance [147] et dont l'exposant est fonction du paramètre K caractérisant le liquide. Ce premier travail vise à définir proprement ce qu'est cette "limite de basse température" entre un

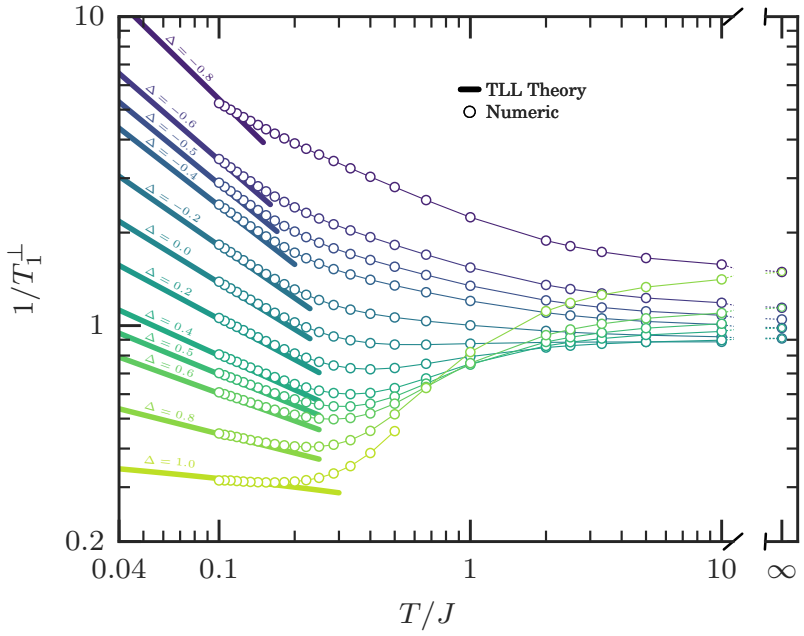

Figure 5: Composante transverse du taux de relaxation RMN, $1/T_1^\perp$, en fonction de la température réduite T/J pour des chaînes XXZ de spins $S = 1/2$ à différentes valeurs de l'anisotropie Δ à champ magnétique nul. Les résultats numériques utilisant une méthode basée sur le groupe de renormalisation de la matrice densité sont représentés par les cercles (de haut en bas: $\Delta = -0.8, -0.6, -0.5, -0.4, -0.2, 0.0, 0.2, 0.4, 0.5, 0.6, 0.8, 1$). Ces résultats numériques sont comparés aux prédictions analytiques de la théorie du liquide de Tomonaga-Luttinger à basse température (traits épais). Les traits fins entre les cercles sont des guides pour les yeux.

régime non universel à haute température et le régime universel unidimensionnel à basse température. Pour ce faire, on étudie des chaînes de spins $S = 1/2$ de type XXZ avec une anisotropie Ising $\Delta \in (-1, 1]$, mais aussi un système un peu plus réaliste, correspondant à une chaîne unique du matériau DTN sous champ, comme discuté dans la partie précédente.

Chaînes XXZ isolées Comme montré dans la figure 5, on observe un excellent accord entre les estimations numériques et les prédictions analytiques à suffisamment basse température. Ce régime asymptotique avec une loi de puissance caractéristique, $\propto T^{1/2K-1}$, n'apparaît seulement qu'en dessous de $T/J \sim 0.1 - 0.2$ suivant la valeur de l'anisotropie Δ. Il est intéressant de noter qu'en réalité, dans l'expression analytique, il n'y a pas de paramètre ajustable libre. Tout dépend, de façon connue, des paramètres du liquide Tomonaga-Luttinger. À température infinie, on observe que la valeur de $1/T_1^\perp$ ne dépend pas du signe de Δ, ce à quoi on s'attend du fait que le spectre du Hamiltonien $\mathcal{H}(\Delta)$ décrivant le système est une fonction impaire de Δ. Sa valeur est minimum pour $\Delta = 0$, et vaut exactement $1/T_1^\perp = \sqrt{\pi}/2J$ [330], puis augmente avec $|\Delta|$. À haute température, et au point $|\Delta| = 1$, on s'attend à ce que le taux de relaxation RMN diverge du fait d'un phénomène de diffusion se mettant en place dans la dynamique des fonctions de corrélations [327, 328]. Nos résultats à température infinie vont au-delà du développement de Baker-Campbell-Hausdorff, utilisé jusqu'à l'ordre $\mathcal{O}(t^2)$ dans la référence 331 pour calculer $\langle S_j^\pm(t) S_j^\mp(0)\rangle$ aux

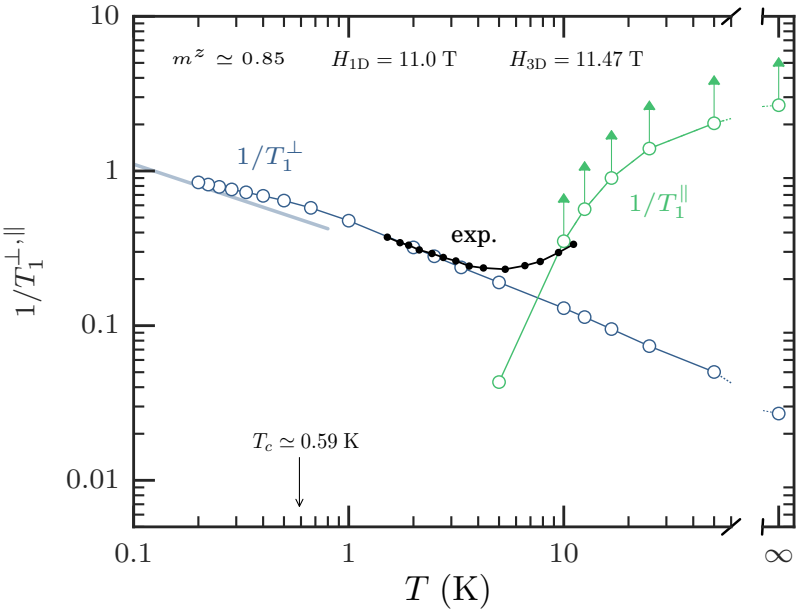

Figure 6: Composantes longitudinale $1/T_1^{\parallel}$ et transverse $1/T_1^{\perp}$ du taux de relaxation RMN pour une chaîne unique représentant le matériau DTN, de spins $S = 1$ sous champ magnétique $H = 11.0$ T, correspondant à une densité d'aimantation de l'échantillon le long du champ $m^z \simeq 0.85$. Étant donné que $1/T_1^{\parallel}$ ne peut être estimé de façon certaine, on ne fournit qu'une estimation basse ici. Le comportement non monotone observé expérimentalement à haute température dans la référence 316 provient apparemment de la contribution large de la composante longitudinale. Les données expérimentales sont tirées de la référence 316 à la même aimantation que le cas unidimensionnel pour mieux comparer aux résultats purement 1D numériques. Les résultats expérimentaux sont multipliés par un facteur adéquat pour se superposer aux résultats numériques à basse température. Dans le vrai matériau DTN, qui est tridimensionnel, la transition de phase XY intervenant à $T_c(m^z \simeq 0.85) \simeq 0.59$ K est également affichée (valeur tirée de la référence 174).

temps courts, et qui donnait $1/T_1^{\perp} \sim 1/J\sqrt{1+\Delta^2}$. Cette prédiction diffère avec ce que l'on trouve, notamment le fait que le taux de relaxation augmente avec $|\Delta|$. En effet, ce développement limité prédit le comportement gaussien, correct pour $\Delta = 0$, mais des termes d'ordre plus élevés doivent être pris en compte pour $|\Delta| > 0$ où les amplitudes des fonctions de corrélations transverses aux temps longs sont de plus en plus larges quand $|\Delta|$ augmente.

Composé unidimensionnel de spins S=1 "DTN" Nous avons également comparé le taux de relaxation RMN du composé DTN, mesuré expérimentalement dans le matériau [316] avec celui calculé numériquement pour une chaîne unique. Les résultats sont montrés dans la figure 6. Les deux composantes, transverse et longitudinale $1/T_1^{\perp,\parallel}$ sont montrées séparément concernant les résultats numériques. On ne peut pas précisément évaluer la valeur de $1/T_1^{\parallel}$ en raison de sa dépendance explicite avec la fréquence RMN ω_0 et ne fournissons donc qu'une estimation basse. Ceci est dû au phénomène de diffusion [327, 328]. Sa contribution à haute température au taux de relaxation RMN domine clairement sur la transverse et explique pourquoi un

régime non monotone est observé expérimentalement à haute température. Peut-être plus important, la mise en ordre antiferromagnétique XY observée dans le matériau [174, 230] pour une densité d'aimantation $m^z \simeq 0.85$ se situe à une température $T_c \simeq$ 0.59 K. Cette dernière se situe au-dessus du régime asymptotique, où les propriétés universelles (dépendance en loi de puissance) du liquide te Tomonaga-Luttinger se manifestent. Il est donc impossible de directement extraire le paramètre K en ajustant le taux de relaxation dans DTN, du fait des couplages inter chaînes qui entraînent une mise en ordre. Idéalement, on s'attendrait à ce que pour des composés quasi unidimensionnels, la description du liquide de Tomonaga-Luttinger pour le taux de relaxation RMN, soit valide pour un régime de température $J \gg T \gg J_\perp$. En conséquent, il reste expérimentalement difficile d'explorer le régime unidimensionnel dans des composés quasi unidimensionnels lorsque J est petit et que la mise en ordre antiferromagnétique empêche la présence d'une fenêtre large en température pour observer le régime du liquide de Tomonaga-Luttinger. Précisément, pour le composé DTN, nous avons montré que la température critique de mise en ordre est plus grande que la température $T/J \sim 0.1$, en dessous de laquelle on peut s'attendre à voir le régime 1D.

2. Réponse dynamique dans des chaînes de spins faiblement couplées

Adapté de arXiv:1806.04913 (2018)

Maxime Dupont, Sylvain Capponi, Nicolas Laflorencie, and Edmond Orignac

Prolongeant notre travail précédent sur des systèmes purement unidimensionnels, on s'intéresse maintenant à la question de la réponse dynamique dans des aimants quantiques faits de chaînes de spins faiblement couplées. En effet, une interaction résiduelle est toujours présente dans la nature, nous éloignant du monde unidimensionnel et de ses descriptions. En particulier, nous avons présenté dans ce travail une étude théorique complète basée à la fois sur des calculs analytiques et des simulations numériques, nous permettant de décrire le régime de températures complet du taux de relaxation RMN : de la physique unidimensionnelle du liquide de Tomonaga-Luttinger au régime tridimensionnel ordonné, et ce, en fonction de la force du couplage inter chaînes. Ceci est intéressant pour déterminer expérimentalement le paramètre du liquide de Tomonaga-Luttinger K : comme vu précédemment, on s'attend à ce que le taux de relaxation RMN diverge de façon algébrique à basse température comme $1/T_1 \propto T^{1/2K-1}$ [166, 210]. Une première limite de la fenêtre a pu être posée grâce au travail précédent où dans un système purement unidimensionnel, la dépendance en loi de puissance est observée à basse température $T \lesssim J/10$ uniquement. Pour un système en trois dimensions, on s'attend à ce que la réponse dynamique change lorsque l'on s'approche de T_c. Pa exemple, le taux de relaxation RMN diverge comme $1/T_1 \propto |T - T_c|^{-\nu(z_t-1-\eta)}$, où l'exposant $\nu(z_t - 1 - \eta) > 0$ est caractéristique de la transition de phase. Ces différents régimes pour $T > T_c$ sont résumés dans la figure 7 (c–e).

La prédiction associée au liquide de Tomonaga-Luttinger est souvent utilisée pour ajuster expérimentalement les données RMN en fonction de T et ainsi obtenir le paramètre K, mais une définition quantitative de ce régime en température fait défaut.

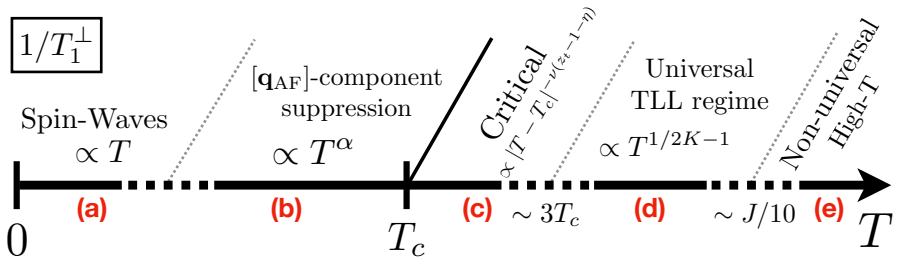

Figure 7: Différents régimes en température pour la composante transverse du taux de relaxation RMN $1/T_1^\perp$ pour un système antiferromagnétique anistrope et tridimensionnel, fait de chaînes de spins faiblement couplées avec une température critique T_c. La force de couplage est J le long des chaînes et $J_\perp$ dans les directions transverses. **(a)** Loin dans la phase ordonnée, le taux de relaxation RMN augmente linéairement $\propto T$ depuis le zéro absolu du fait des contributions des ondes de spin. **(b)** Juste en dessous de la température critique T_c, le taux de relaxation RMN subit une suppression algébrique $\propto T^\alpha$ ($\alpha \simeq 4-5$) du fait de la "suppression de sa composante antiferromagnétique $\mathbf{q}_{\rm AF}$". **(c)** À l'approche de la transition, par dessus la température critique, le taux de relaxation RMN diverge $\propto |T-T_c|^{-\nu(z_t-1-\eta)}$ avec des exposants critiques ν, η and z_t caractéristiques de la classe d'universalité de la transition de phase. La divergence associée à la transition est observée jusqu'à approximativement $\simeq 3T_c$. **(d)** Pour $J_\perp/J \ll 1$, on s'attend à avoir un régime où la physique unidimensionnelle prédomine avec le taux de relaxation RMN divergeant comme $\propto T^{1/2K-1}$, où K est le paramètre du liquide de Tomonaga-Luttinger. **(e)** À haute température, plus grande que $\sim J/10$, le comportement du $1/T_1^\perp$ n'est pas universel. Notons que si $3\mathrm{T}_c \gtrsim J/10$, alors la région (d) est réduite à zéro et aucune physique unidimensionnelle ne peut être observée, en tout cas en ce qui concerne le taux de relaxation RMN.

Précédemment, nous avons montré par exemple que pour le composé, pourtant quasi unidimensionnel DTN [316], la température critique est plus grande que celle en deçà de laquelle la physique unidimensionnelle émerge, empêchant toute observation. En d'autres termes, la région (d) de la figure B.7 est réduite à zéro pour DTN. Et ce, bien que ce matériau ait montré d'autres empreintes unidimensionnelles (voir la deuxième section du premier chapitre). Un autre matériau intéressant, avec un couplage tridimensionnel plus petit (résultant en une T_c plus petite) est DIMPY [171, 173] où le $1/T_1$ a été ajusté pour obtenir K en fonction du champ magnétique H, mais qui a tout de même montré des différences avec la valeur de $K(H)$ attendue, calculée numériquement. Notre travail révèle notamment que la fenêtre expérimentale de *fit* en température, $2T_c < T < 3T_c$ est trop proche de la transition pour être fiable.

Par ailleurs, dans des expériences de RMN, une façon de déterminer la position de la transition entre une phase ordonnée et désordonnée est de déterminer la température T_c à laquelle la division hyperfine de "la ligne RMN" dans le spectre du noyau visé disparaît [166, 174, 204]. Une autre façon de faire et de mesurer le $1/T_1$ en fonction de la température T, pour lequel on s'attend à ce qu'il diverge à la transition, et résultant en pratique en une forte augmentation [173, 204, 317, 318]. En dessous de T_c, les observations expérimentales du taux de relaxation RMN montrent qu'il est grandement supprimé avec la température, *fittant* empiriquement une dépendance

en loi de puissance $1/T_1 \propto T^\alpha$ où $\alpha \simeq 4-5$, comme observé dans le composé $Cu_2(C_5H_{12}N_2)_2Cl_4$ [334], le DTN [335] ou encore DIMPY [204]. Ce comportement visible dans la figure B.7 (b), vient du fait qu'en dessous de T_c, la composante antiferromagnétique $\mathbf{q}_{\mathrm{AF}}$ n'est plus capturée. Enfin, bien que cela reste difficile à observer, tant expérimentalement que numériquement, étant donné que cela se passe à très basse température, loin dans la phase ordonnée, on s'attend à ce que le taux de relaxation RMN augmente linéairement avec T du fait de contributions ondes de spin.

III. Effets conjoints du désordre et des interactions dans un aimant quantique: DTN*X*

Adapté de Phys. Rev. Lett. **118**, 067203 (2017),

Anna Orlova, Rémi Blinder, Edwin Kermarrec, **Maxime Dupont**, Nicolas Laflorencie, Sylvain Capponi, Hadrien Mayaffre, Claude Berthier, Armando Paduan-Filho, and Mladen Horvatić

Phys. Rev. Lett. **118**, 067204 (2017),

Maxime Dupont, Nicolas Laflorencie, and Sylvain Capponi

Phys. Rev. B **96**, 024442 (2017),

Maxime Dupont, Sylvain Capponi, Mladen Horvatić, and Nicolas Laflorencie

et arXiv:1801.01445 (2018)

Anna Orlova, Hadrien Mayaffre, Steffen Krämer, **Maxime Dupont**, Nicolas Laflorencie, Sylvain Capponi, Armando Paduan-Filho, and Mladen Horvatić

Dans cette série de travaux, nous avons étudié les effets conjoints du désordre et des interactions pour des degrés de liberté bosoniques émergents, induits par un champ magnétique externe dans le composé antiferromagnétique quasi unidimensionnel $Ni(Cl_{1-x}Br_x)_2$-4SC$(NH_2)_2$ (DTNX). Ce matériau a été introduit dans la première partie pour le cas sans désordre $x = 0$. En dopant le composé avec des impuretés Br, DTNX développe des propriétés fascinantes [398] : il a été rapporté comme un candidat potentiel présentant une phase de la matière dite verre de Bose [397–399]. Contrairement au cas sans impureté, la phase grand-D à bas champ est substituée par cette phase verre de Bose en présence de désordre. Par ailleurs, elle émerge à plus haut champ entre la phase ordonnée XY[2] et la phase triviale ferromagnétique. La phase verre de Bose du DTNX peut être définie de la manière suivante : co-existants dans un environnement possédant une bande d'énergie interdite, des états

[2]Bien que non discuté ici, on peut montrer qu'une phase ordonnée antiferromagnétique de type XY, comme dans le cas du DTN, partage de nombreuses propriétés avec les condensats de Bose-Einstein que l'on retrouve dans des expériences d'atomes froids. De ce fait, par la suite, la phase XY sera notée "BEC" pour *Bose-Einstein Condensation*, terme anglais pour condensat de Bose-Einstein.

magnétiques localisés prennent place autour des impuretés et développent localement une susceptibilité finie. Ces degrés de liberté localisés sont spatialement séparés et leur corrélation décroît exponentiellement, empêchant toute cohérence globale et mise en ordre dans le système. Ultérieurement à nos travaux, il a été proposé dans la référence 398 que la phase verre de Bose à haut champ magnétique est ininterrompue entre la phase ordonnée et ferromagnétique. À la place, nous trouvons que les degrés de liberté associés aux impuretés développent un phénomène de délocalisation à plusieurs corps très net avec une apparition d'ordre induit par le désordre [449, 450]. Le composé pur et désordonné peut être décrit par le modèle suivant de spins $S = 1$ sur un réseau tétragonal,

$$\mathcal{H}_{\mathrm{DTN}X} = \sum_i \Bigg\{ \sum_m \Big[J_{i,m} \mathbf{S}_{i,m} \cdot \mathbf{S}_{i+1,m} + D_{i,m} \left(S^z_{i,m}\right)^2 - g\mu_B H S^z_{i,m} \Big] + \sum_{\langle m,n \rangle} J_\perp \mathbf{S}_{i,m} \cdot \mathbf{S}_{i,n} \Bigg\}, \tag{14}$$

où dans le cas du DTN pur, le couplage d'échange antiferromagnétique le long de la direction des chaînes est $J_{i,n} = J = 2.2$ K, le terme grand D est $D_{i,n} = D = 8.9$ K, et le couplage entre les chaînes voisines (noté par le symbole $\langle m, n \rangle$) est $J_\perp = 0.18$ K. H est un champ magnétique extérieur appliqué selon la même direction que l'anisotropie D pour conserver la symétrie U(1) du système. Nous utilisons $g = 2.31$ pour le facteur gyromagnétique. Dans le composé dopé DTNX, un des deux ions Cl^- dans le couplage intra chaîne de lien J peut être substitué par une impureté Br^-, introduisant ainsi du désordre dans le système. Comme annoncé, nous avons dans un premier temps, à l'aide des expériences de RMN à fort champ magnétique, totalement caractérisé le modèle microscopique du composé DTNX en présence d'impuretés. En effet, ces résultats expérimentaux peuvent être interprétés et compris par de la physique à une impureté, ce qui rend possible des calculs analytiques et de diagonalisation exacte sur de grands systèmes. En supposant que le dopage introduit uniquement une perturbation locale, nous avons montré qu'une impureté Br modifie le couplage d'échange du lien par $J' = 2.42J$ et l'anisotropie D de l'ion Ni le plus proche par $D' = 0.36D$, sans rien affecter d'autre.

De plus, cette description simple fournit de précieuses informations sur une image du matériau DTNX à haut champ magnétique : les états des impuretés sont fortement localisés et les degrés de liberté non affectés par le désordre se polarisent le long du champ pour un champ magnétique inférieur à celui des impuretés. En conséquence, une image simple du DTNX à fort champ consiste en un fond magnétique polarisé et gelé avec un ensemble d'impuretés, qui sont distribuées spatialement aléatoirement et pour le moment non polarisées. Une continuité naturelle a été d'étudier l'effet mutuel de deux impuretés. Au moyen de diagonalisation exacte, nous avons révélé que, en dépit de la forte localisation des états des impuretés, il existe une interaction de paire, non frustrante entre les degrés de liberté associés aux impuretés. Dans le but de développer une description physique simple à basse température, nous avons construit un modèle effectif de bosons sur un réseau dilué (certains sommets sont occupés par un degré de liberté et d'autres non) avec des interactions qui décroissent exponentiellement avec la distance entre les particules. Ce modèle suggère que les degrés de liberté bosoniques peuvent s'ordonner à suffisamment basse température, ce qui est confirmé par des simulations de Monte Carlo quantique. Cela ouvre la voie

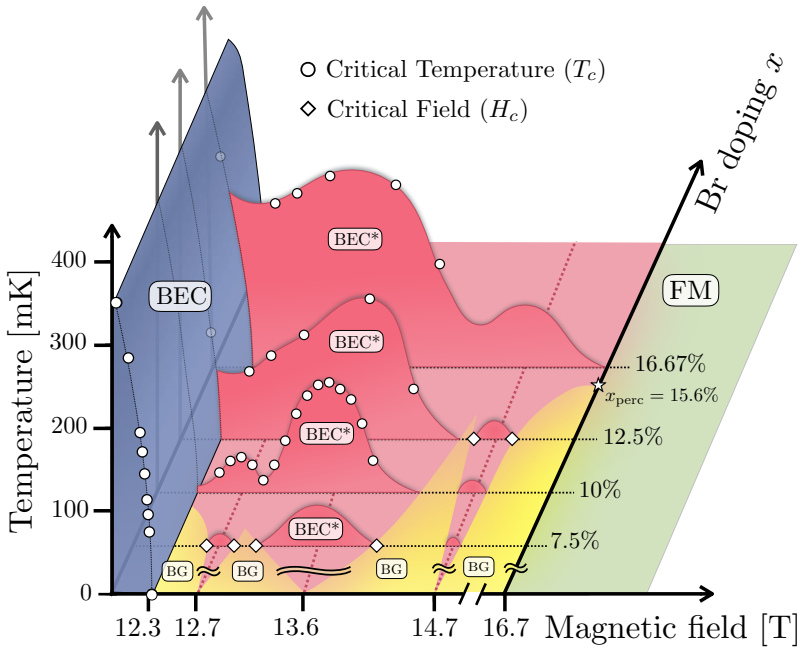

Figure 8: Diagramme des phases global champ magnétique – température pour le matériau DTNX, basé sur des résultats numériques de Monte Carlo quantique (cercles et diamants), pour différentes valeurs de dopage en Brome x. À petit dopage x, et au-delà de la phase ordonnée AF (dôme bleu, BEC) à $H > 12.3$ T, une succession de phases ordonnées, induites par le désordre (dômes roses, BEC*) sont stabilisées avec entre deux des régions avec une présence d'une phase verre de Bose (jaune, notée "BG"), avant d'arriver vers la phase ferromagnétique totalement polarisée par le champ (région verte, notée "FM"). On s'attend à ce que cette série de dômes disparaisse lorsque le dopage x augmente, pour finalement avoir une seule phase ordonnée induite par le désordre, qui vient par ailleurs se chevaucher avec la phase ordonnée principale en bleu. Au-delà du seuil de percolation tridimensionnel, $x_{\text{perc}} = 15.6\%$, le système sera ordonnée à toutes les valeurs du champs jusqu'à sa polarisation complète.

à une résurgence globale de la cohérence quantique dans DTNX, en fort contraste avec la phase verre de Bose qui a été rapportée dans la référence 398. En effet, en étendant notre étude au modèle initial réaliste du DTNX, nous avons montré que ce scénario est vérifié par des simulations de Monte Carlo quantique pour un dopage $x = 10\%$.

Pour cette concentration, le dôme de la phase ordonnée induite par le désordre BEC* est connecté au dôme principal BEC sans aucune phase verre de Bose intermédiaire. De plus, nous montrons que la phase BEC* n'est pas constituée d'un seul dôme, mais deux distincts : le premier attendu à $H^* \sim 13.6$ T qui correspond à des degrés de liberté associés à des impuretés uniques, et un nouveau, centré autour de $H \sim 12.7$ T. Le nouveau dôme peut être compris comme la mise en ordre d'objets constitués de plusieurs impuretés. Cela étend considérablement l'image actuelle du diagramme des phases du DTNX à haut champ magnétique : à faible concentration de dopage, les mini-dômes consécutifs d'ordre par le désordre sont séparés par des phases localisées verre de Bose qui viennent s'intercaler. Un résumé de nos résultats

est montré dans la figure 8, qui est une représentation complète, en trois dimensions, du diagramme des phases “champ magnétique/température/concentration de Br” du DTNX à fort champ magnétique. Nous nous sommes aussi intéressés à la physique à température nulle $T = 0$ pour $x = 7.5\%$, en se concentrant sur la transition de phase quantique entre la phase ordonnée BEC et la phase verre de Bose, dans le but de déterminer les exposants critiques de cette classe d'universalité, qui se sont trouvés en accord avec ceux obtenus dans d'autres travaux [399, 493, 495].

Dynamics and disorder in quantum antiferromagnets

Condensed matter physics, and especially strongly correlated systems provide some of the most challenging problems of modern physics. In these systems, the many-body interactions and correlations between quantum particles cannot be neglected; otherwise, the models would simply fail to capture the relevant physics at play and phenomena ensuing. In particular, the work presented in this manuscript deals with quantum magnetism and addresses several distinct questions through computational approaches and state-of-the-art numerical methods. The interplay between disorder (*i.e.* impurities) and interactions is studied regarding a specific magnetic compound, where instead of the expected many-body localized phase at high magnetic fields, a novel disorder-induced ordered state of matter is found, with a resurgence of quantum coherence. Furthermore, the dynamical response of quantum magnets to an external perturbation, such as it is accessed and measured in nuclear magnetic resonance and inelastic neutron scattering experiments is investigated.

Keywords: quantum physics · condensed matter theory · strongly correlated systems · quantum magnetism · disordered systems · time evolution · advanced numerical methods

Dynamique et désordre dans des aimants quantiques

La physique de la matière condensée, et notamment les systèmes fortement corrélés, amènent à des problèmes parmi les plus stimulants et difficiles de la physique moderne. Dans ces systèmes, les interactions à plusieurs corps et les corrélations entre les particules quantiques ne peuvent être négligées, sinon, les modèles échoueraient simplement à capturer les mécanismes physiques en jeu et les phénomènes qui en découlent. En particulier, le travail présenté dans ce manuscrit traite du magnétisme quantique et aborde plusieurs questions distinctes à l'aide d'approches computationnelles et méthodes numériques à l'état de l'art. Les effets conjoints du désordre (*i.e.* impuretés) et des interactions sont étudiés concernant un matériau magnétique spécifique : plutôt qu'une phase de la matière dite localisée, attendue à fort champ magnétique, une phase ordonnée induite par le désordre lui-même est mise en lumière, avec une réapparition inattendue de la cohérence quantique dans ledit composé. Par ailleurs, la réponse dynamique d'aimants quantiques à une perturbation externe, comme celle mesurée dans des expériences de résonance magnétique nucléaire ou de diffusion inélastique de neutrons est étudiée.

Mots-clés: physique quantique · théorie de la matière condensée · systèmes fortement corrélés · magnétisme quantique · systèmes désordonnés · évolution dans le temps · méthodes numériques avancées